

Inkjet deposition of low-dimensional materials for flexible healthcare electronics

Charles Edward David Heaton

Thesis submitted to the University of Nottingham for the degree of Doctor of Philosophy

March 2026

Abstract

This work targets the development of printed electronic devices with high degrees of flexibility and stretchability, capable of performing complex simultaneous sensing operations and detecting stimuli relevant to healthcare applications. Where existing technologies are largely constrained by conventional manufacturing processes and rigid materials, not well suited for wearable devices.

Inkjet printing provides a versatile platform for the fabrication of flexible and wearable electronics, enabled by diverse printable materials and substrates. Conventional thermal post-processing methods rely on high temperatures, limiting use with thermally sensitive polymers required for stretchable devices. This work develops low temperature, photonic post-processing using intense pulsed light (IPL) and UV irradiation to functionalise graphene, graphene oxide (GO), graphene/PEDOT:PSS, and metal nanoparticle (MeNP) inks on polymer films and textiles. IPL annealing was used to develop graphene-based conductive films with sheet resistance as low as 191 Ω/sq., comparable to thermal annealing, whilst maintaining performance under 40% elongation and cyclic mechanical deformation. Device design permitted decoupling of elongation effects and enabled directional strain sensing. Textile based graphene devices demonstrated sensing capabilities whilst a multimaterial graphene–polymer heterostructure enabled simultaneous detection and differentiation between multiple stimuli. Breath analysis was investigated on printed graphene devices, where acetone response was distinguishable under dynamic humidity, replicating exhaled breath, with sensitivity exceeding alternative printed devices. Graphene devices also detected quorum signalling molecules at picomolar concentrations, while capacitive measurements of NaCl in hydrogels revealed sensitivity to compositional changes.

Publications, Conferences and Awards

Publications:

Inkjet-printed Multifunctional Graphene Sensors for Flexible and Wearable Electronics. F. Wang, **C. E. D. Heaton**, N. D. Cottam, J. S. Austin, J. Im, T. M. Fromhold, R. D. Wildman, R. J. M. Hague, C. J. Tuck, O. Makarovsky and L. Turyanska. *Adv. Electron. Mater.* 2025, 11 2400689. https://doi.org/10.1002/aelm.202400689

On-demand sintering of gold nanoparticles via controlled removal of o-nitrobenzyl thiol ligands under ultralow-power UV for conductive patterns. J. Im, **C. E. D. Heaton**, N. R. E. Putri, C. Liu, J. Usuba, K. Butler, M. Fay, G. G. D. Han, H. Hooshmand, A. Thompson, R. Wildman, R. Hague, L. Turyanska and C. Tuck. *Adv. Sci.,* 2025, 12 2415496. https://doi.org/10.1002/advs.202415496

Photonic Annealing of Inkjet-printed Graphene for Stretchable Wearable Healthcare Monitoring Devices. **C. E. D. Heaton**, J. S. Austin, L. Ruer, N. D. Cottam, F. Wang, Y. He, G. A. Rance, F. R. A. J. Rose, R. D. Wildman, R. J. M. Hague, O. Makarovsky and L. Turyanska. Adv. Mater. Technol. 2025, 10 e00913. https://doi.org/10.1002/admt.202500913

Multimaterial additive manufacturing of GelMA hydrogel-based structures with tuneable compositional and mechanical properties. K. Joderi, S. Santoni, **C. E. D. Heaton**, F. Wang, N. Carpentier, L. Jiang, F. R. A. J. Rose, R. Wildman and L. Turyanska. *In submission to Mater. Adv. (2025)*

Inkjet printed graphene strain sensors. **C. E. D. Heaton**, et al., *In preparation (2026).*

Conferences:

Celebrating Engineering Research, Nottingham (18 June 2025). Poster presentation. Functional Materials for Additively Manufactured Electronics. **C. E. D. Heaton,** F. Wang, N. Weston, F. R. A. J. Rose, R. D. Wildman, R. J. M. Hague, O. Makarovsky, L. Turyanska.

European Materials Research Society Fall meeting, Warsaw (15-18 September 2025). Oral presentation. *Inkjet-Printing of LowD Materials: towards flexible and wearable healthcare sensing devices.* **C. E. D. Heaton**, F. Wang, J. Im, J. S. Austin, N. D. Cottam, R. D. Wildman, R. J. M. Hague, O. Makarovsky, L. Turyanska.

Graphene Week, Vicenza (22-26 September 2025). Poster presentation. *Inkjet-Printed Multifunctional Graphene Sensors: towards flexible and wearable healthcare devices*. **C. E. D. Heaton**, F. Wang, J. S. Austin, N. D. Cottam, R. D. Wildman, R. J. M. Hague, O. Makarovsky, L. Turyanska.

Awards:

E-MRS Young Researcher Award in recognition of the work: *"Inkjet Printing of LowD Materials: towards flexible and wearable healthcare sensing devices"* in contribution to Symposium K (3D and Additive Manufacturing of Organic Materials and Nanocomposites for Advanced Applications), European Materials Research Society Fall Meeting (17th September 2025)

Individual Travel Grant; EU - Graphene Flagship (£300), Graphene week, Vicenza (22-26 September 2025)

Individual Travel Grant; Researcher Academy, University of Nottingham (£500 award)

Acknowledgements

First and foremost, I have to give my absolute thanks to my supervisor, Prof. Lyudmila Turyanska, without her limitless knowledge, support, time and encouragement, there is no doubt that the completion of this work would have been a monumental challenge. I am deeply grateful for the countless hours dedicated to developing my skills and providing advice. And lastly, for her understanding, care and empathy when the going has not been so easy.

To my co supervisors, Prof. Richard Hague, Prof. Ricky Wildman and Prof. Felicity Rose, the depth of knowledge between them is simply overwhelming, and I am truly grateful to have been a recipient of that. The ideas and guidance I have received from them has been invaluable throughout this work.

I am eternally grateful to everyone within the Centre for Additive Manufacturing who has been there to help me throughout this journey. Firstly to Dr. Feiran Wang, the encyclopaedia for inkjet printing, always happy to help however small the problem, and demonstrating such patience when things haven't gone to plan. To Dr. Geoffrey Rivers, I extend my thanks for the time spent training me on numerous pieces of equipment and, perhaps even more importantly, for troubleshooting when they did not work as intended; your enthusiasm and knowledge have been truly inspiring. To my friends and colleagues, past and present: Ashleigh Murray, Dr. Oliver Nelson-Dummett, Dr. Jonathan Austin, Dr. Negar Gilani, Dr. Jisun Im, Dr. Bruno Vuillod, Alisdair Bulloch, Dr. Sebastien Faron, Daniel Spragg, Katherine George, William Pritchard, Dr. Diego Della Crociata, Dr. Francisco Reyes, Dr. Maria Inês Evangelista Barreiros, Ryan McMullen, Dr. Thomas Girerd, Dr. Keyvan Joderi and Dr. Amin

Askari, for those I've worked with it has truly been a pleasure, and to the rest I am deeply grateful for their friendship.

I am grateful for Mark East, Mark Hardy and Adam Whitbread, whose technical support has been essential in overcoming the countless challenges I have faced in the lab with difficult pieces of equipment, and who seem to possess every tool under the sun. Further thanks go to Mirela Axinte and Flavia Guzman Villarroel, their administrative support has guided me through even the most challenging of paperwork.

I would like to thank Prof. Oleg Makarovsky and Dr. Nathan Cottam from the School of Physics and Astronomy, with whom I thoroughly enjoyed collaborating, and look forward to our future work together.

From the Nanoscale and Microscale Research Centre, I would like to acknowledge Dr. Graham Rance for his awesome knowledge on Raman spectroscopy, and the essential data he provided to my studies. I would also like to thank Dr. Nicola Weston, for the many hours spent with me on the SEM, demonstrating such patience whilst helping to uncover the smallest of details.

Finally, my utmost and heartfelt thanks go to my family. Firstly, to my Uncle David, for his continued interest and enthusiasm in my studies, as well as the 'beer' money to get me through my undergraduate years. To my brother William, sister-in-law Rachael, and their beautiful children, Maggie and Bonnie, thank you for being such a joyful distraction throughout this journey. And to my parents, for their support appears to be endless, as well as their patience for my eternal studying, and for that I thank them deeply.

Table of Contents

Abstract i
Publications, Conferences and Awards ii
Acknowledgements iv
List of acronyms and variables ix
1 Introduction 1
2 Literature Review 6
2.1 Inkjet-printed electronics 6
2.2 Printed sensing devices 7
2.2.1 Methods for device manufacture 8
2.2.2 Flexible and stretchable electronics 12
2.2.3 Printed healthcare devices 16
2.3 Functional materials for inkjet printing 21
2.3.1 0D materials 21
2.3.2 2D materials 25
2.3.3 Conductive and insulating polymers 31
2.3.4 Hydrogels 34
2.3.5 Hybrid inks 36
2.4 Inkjet printing 38
2.5 Post-processing methods for printed functional materials 47
2.5.1 Thermal post-processing 47
2.5.2 Alternative post-processing methods 49
2.5.3 Photonic post-processing methods 50
2.6 Inkjet-printed sensor devices 54
2.6.1 Environmental sensing 55
2.6.2 Chemical sensing 58
2.6.3 Biological biomarkers 60
2.7 Summary 63
3 Aims and Objectives 66
4 Materials and Experimental Methods 67
4.1 Printing materials 67
4.1.1 Inks and substrates 67
4.1.2 Cartridges for inkjet printing 68

4.1.3 Ink formulations and modification for inkjet printing 69
4.2 Ink characterisation techniques 71
4.2.1 Viscosity measurements 71
4.2.2 Surface tension and contact angle measurements 72
4.2.3 Thermogravimetric analysis 74
4.2.4 Physical properties 75
4.3 Inkjet printing 76
4.4 Post-deposition processing methods 79
4.4.1 Thermal annealing and sintering 79
4.4.2 Intense pulsed light 79
4.4.3 UV annealing, sintering and curing 80
4.5 Optical and morphological characterisation 81
4.5.1 Optical microscopy 81
4.5.2 Optical profilometry 81
4.5.3 Scanning Electron Microscopy (SEM) 81
4.5.4 Transmission Electron Microscopy (TEM) 83
4.5.5 Raman spectroscopy 83
4.5.6 Ultraviolet-visible spectroscopy 85
4.6 Electrical measurements 86
4.6.1 Sample preparation for electrical measurements 86
4.6.2 Device performance under mechanical deformation 88
4.7 Sensing performance 89
4.7.1 Temperature dependent measurements 89
4.7.2 Humidity sensing 91
4.7.3 Pressure dependent measurements 91
4.7.4 Measurements of sensing response to multiple stimuli 92
4.7.5 Chemical sensing 94
5 Inkjet printing and post-processing of functional materials 97
5.1 Inkjet printing of functional materials 97
5.1.1 Graphene ink 97
5.1.2 Graphene/PEDOT:PSS deposition 98
5.1.3 Nitschke cage ink 103
5.2 Post-processing of printed materials 104

5.2.1 Thermal annealing of iGr-fabric 105
5.2.2 IPL annealing of iGr 110
5.2.3 UV annealing of graphene/PEDOT:PSS 121
5.2.4 UV annealing of GO 122
5.2.5 UV sintering of AuNPs 124
5.3 Material suitability for printed wearable electronics 129
6 Substrates for inkjet-printed electronics 132
6.1 Flexible and stretchable devices 132
6.1.1 AuNPs deposited on PEN 132
6.1.2 Graphene deposited on Kapton film 134
6.1.3 IPL-graphene on stretchable Beyolex 135
6.1.4 Stretch response of Gr/PEDOT:PSS on Beyolex 137
6.2 3D printed stretchable substrates 141
6.2.1 Printed silicone substrate 141
7 Multifunctional sensing devices 144
7.1 Developing simultaneous detection 144
7.2 iGr devices on textile substrates 148
8 Chemical and environmental sensing 153
8.1 Temperature dependence of IPL annealed graphene 153
8.2 Sensing performance of IPL annealed graphene under strain 155
8.3 Acetone and humidity sensing 159
9 Sensing of biologically relevant molecules 162
9.1 Temperature dependence of Gr/PEDOT:PSS 162
9.2 Detection of Quorum signalling molecules 164
9.3 Chemical sensing through a hydrogel medium 171
10 Conclusions and future work 176
11 References 181

List of acronyms and variables

Acronyms

0D = 0 dimensional
1D = 1 dimensional
2D = 2 dimensional
3D = 3 dimensional
AgNP = silver nanoparticle
AM = additive manufacture
AuNP = gold nanoparticle
BSE = backscattered electrons
BSED = BSE detector
CaPNPs = calcium phosphate nanoparticles
CE = counter electrode
CIJ = continuous inkjet
CNT = carbon nanotubes
CuNP = copper nanoparticle
CVD = chemical vapour deposition
DLP = digital light processing
DOD = drop on demand
DSA = drop shape analyser
DVLO = Derjaguin-Landau-Verwey-Overbeek
EC = ethyl cellulose
ECG = electrocardiography
ESEM = environmental scanning electron microscopy
GNP = graphene nanoplatelets
GO = graphene oxide
Gr/PEDOT:PSS = graphene/PEDOT:PSS ink
h-BN = hexagonal boron nitride
HHQ = nonyl-4-hydroxyquinoline
HQNO = 2-heptyl-4-hydroxyquinoline N-oxide
IDE = interdigitated electrode
iGr = graphene ink
IoT = Internet of Things
IPL = intense pulsed light
LAP = lithium phenyl (2,4,6-trimethylbenzoyl) phosphinate
LFD = large field detector
lowD = low-dimensional
LOx = lactate oxidase
MeNP = metallic nanoparticles
MOC = metal organic cages
N-cages = Nitschke cages
NHQ = 2-heptyl-4(1H)-quinolone
NIR = near infrared
NP = nanoparticle
NT-AuNP = o-nitrobenzyl thiol functionalised gold nanoparticles
OT-AuNP = Octane thiol functionalised gold nanoparticles
PANI = polyaniline
PCB = printed circuit board
PDMS = polydimethylsiloxane
PEDOT:PSS = poly(3,4-ethylenedioxythiophene) polystyrene sulfonate
PEGDA = poly(ethylene glycol) diacrylate
PEN = polyethylene naphthalate
PEO = poly(ethylene oxide)
PET = polyethylene terephthalate
poly-ACMO = poly-4-acryloylmorpholine
PPC = post-print-cure
PPy = polypyrrole
PQS = Pseudomonas quinoline signal 2-heptyl-3-hydroxy-4(1H)-quinolone
PT = polythiophene
PVC = poly(vinyl chloride)
PVP = polyvinylpyrrolidone
QSM = quorum signalling molecule
RE = reference electrode
rGO = reduced graphene oxide

RH = Relative humidity
SBS = scan-by-scan
SE = secondary electrons
SED = secondary electron detector
SEM =scanning electron microscopy
SLA = stereolithography
SLG = Single layer graphene
SLS = selective laser sintering
SWCNT = single walled carbon nanotube
TA = thermally annealed
TEM = transmission electron microscopy
TGA = thermogravimetric analysis
TPGDA = tripropylene glycol diacrylate
TPU = thermoplastic polyurethane
UV = ultraviolet
UV-vis = ultraviolet-visible spectroscopy
VOC = volatile organic compound
WE = working electrod

Variables

ΔL = elongation/strain
A = Absorbance
C = concentration
CA = contact angle
d = dielectric thickness
E = Young's modulus
E_a = activation energy
I = current
I_{sd} = source-drain current
$k_{substrate}$ = thermal conductivity
k_B = Boltzmann constant
L = length
l_p = path length
n_C = number of cycles
n_{drople} = number of droplets
n_f = number of IPL flashes
n_L = number of printed layers
Oh = Ohnesorge number
P = Pressure
P_d = power density
R = resistance
R_{4t} = 4 terminal resistance
Re = Reynolds number
R_S = sheet resistance
T = temperature
t = time
T_{anneal} = annealing temperature
t_{anneal} = annealing time
$T_{chamber}$ = chamber temperature
t_{flash} = IPL flash time
T_{glass} = glass temperature
T_M = Mott temperature
$T_{melting}$ = melting temperature
T_{nozzle} = nozzle temperature
$t_{response}$ = response time
T_{sample} = sample temperature
$T_{substrate}$ = substrate temperature
t_{UV} = UV irradiation time
V = voltage
V_{4t} = 4 terminal voltage
V_{sd} = source-drain voltage
V_{xx} = longitudinal voltage
V_{xy} = transverse voltage
W = width
We = Weber number
Z = Z number
γ = surface tension
ε = molar absorptivity
η = viscosity
θ = angle
μ = carrier mobility
σ = electrical conductivity
τ = exponential time constant
$\varphi_{droplet}$ = droplet diameter

1 Introduction

Inkjet printing is fast becoming a popular method for the deposition of functional materials, enabling electronic devices with a plethora of applications, including sensors,[1–6] optoelectronics,[7,8] displays,[9–11] energy storage[12–14] and more.[15,16] To facilitate the manufacture of these devices, a range of functional materials is available for deposition, often via complex and expensive processes, such as chemical vapour deposition (CVD) or photolithography. Commonly featured materials include graphene, graphene oxide (GO), silver nanoparticles (AgNPs), gold nanoparticles (AuNPs), conductive polymers (e.g., poly(3,4-ethylenedioxythiophene):poly (styrene sulfonate) (PEDOT:PSS)), quantum dots, and perovskites.[17]

Inkjet printing offers significant advantages over conventional silicon-chip-based electronics manufacturing, particularly in its compatibility with a broad range of flexible and stretchable substrates such as polyimide, polyethylene terephthalate (PET), thermoplastic polyurethane (TPU), textiles and many more.[18–20] Unlike lithographic or printed circuit board (PCB) based fabrication methods, which are constrained to rigid substrates, inkjet printing enables non-contact patterning of electronics onto materials well-suited for flexible and wearable applications.

However, a key challenge in the deposition of functional materials is the need for post-processing to achieve the desired electrical properties. This often requires thermal treatment(s) to achieve electrical conductivity in the deposited layer, where the temperatures involved in these processes (> 150 °C)[21,22] frequently exceed the thermal limits of the flexible substrates used in wearable devices. A range of alternative methods exists, with photonic techniques being the most promising due to their ability

to mitigate substrate degradation, operate at relatively low power (1-10 J/cm^2)[23,24] and significantly reduce processing times. Techniques such as Intense Pulsed Light (IPL)[23] and ultraviolet (UV)[24] irradiation have demonstrated effective sintering and annealing of carbon and metallic-based inks whilst preserving the integrity of temperature-sensitive substrates.

The suitability of functional materials for sensing applications further motivates the development of low-temperature post-processing methods to advance wearable electronics within healthcare. Graphene and GO exhibit strong response to a broad range of stimuli, including temperature, humidity, strain, pressure, chemicals and gases due to their high surface area.[16,25–27] Metallic Nanoparticles (MeNPs) have been successfully inkjet-printed with high resolution and electrical conductivity, demonstrating strong potential for use as electrodes and interconnects in sensing devices.

As such, graphene (or a graphene-based hybrid) was selected as the primary material of interest for sensing applications in this work. Its high carrier mobility and large surface-to-volume ratio enable sensitive detection of chemical, thermal and mechanical stimuli, which is essential for applications such as breath analysis and infection monitoring where stimuli concentrations are low.[28] The exceptional mechanical properties of graphene and the ability to maintain conductivity under bending and stretching also make it well-suited to conformal, skin-mounted devices and textile-based sensors. Importantly, the low-temperature post-processing of graphene inks has been shown in the literature, ensuring compatibility of this material with soft polymeric substrates with high degrees of flexibility and stretchability.[23] Whilst other 2D materials are available, graphene is the most mature in its

development with regards to inkjet printing, and as such is the most readily available as well as best documented.[17]

Despite the growing variety of inkjet-printed sensors, challenges remain when using them in complex environments with multiple stimuli and in decoupling sensor responses.[29,30] Furthermore, systems for wearable devices must be able to withstand repeated bending and stretching without degrading sensing performance. As such, devices must consider implementing selectivity, enabling distinguishability between multiple stimuli and decoupling of strain effects. Finally, the detection of biologically relevant molecules, including quorum-signalling molecules associated with bacterial infection and ionic changes in hydrogels are all highly relevant to wound monitoring. These studies extend the multifunctional sensing strategies developed earlier to clinically meaningful biomarkers.

Wearable healthcare technologies are well-poised to benefit from the advances offered from printed electronics. For instance, devices must operate on soft, flexible and stretchable, thermally sensitive substrates, capable of withstanding repeated mechanical deformation, as well as operate in complex physiological environments. These constraints motivates the development of low-temperature manufacturing processes, as well as establishing multifunctional sensing platforms and selective devices.

This thesis addresses the following research questions:

1. What low-temperature, photonic post-processing methods are available, how do they compare to conventional thermal processes and what is their effectiveness across different substrates and inks?

2. Can inkjet-printed low-dimensional materials deliver mechanically robust and reliable sensing performance when subjected to bending, stretching, and other forms of mechanical deformation?
3. To what extent can printed devices detect clinically relevant biomarkers, including volatile breath analytes and quorum-signalling molecules associated with infection?

Therefore, presented is the development of low-temperature techniques for post-processing of inkjet-printed functional materials alongside exploration of the sensing capabilities of these materials is detailed, alongside suitability for performance in complex environments.

- **Chapter 1** provides an introduction to the thesis, as well as an overview of the chapters.
- **Chapter 2** details a literature review on the technical details of inkjet printing and functional materials available for electronic devices, as well as their application to healthcare monitoring applications. Comparison is provided towards alternative fabrication methods (additively manufactured (AM) and non-AM).
- **Chapter 3** outlines the aims and objectives for this work.
- **Chapter 4** details the materials and methods used for the development of inkjet-printed electronics. Including ink formulation, ink characterisation, printing parameters, post-processing techniques, optical and morphological characterisation and methods for analysis of electrical performance.
- **Chapter 5** established the electrical properties of functional materials used in this work, as well as the effectiveness of thermal and photonic post-processing methods.

- **Chapter 6** evaluates the substrates available for inkjet-printed electronics, especially those now usable due to low-temperature post-processing methods. As such, the performance under mechanical deformation is investigated, as well as the suitability of AM materials for use as substrates.
- **Chapter 7** explores the capability of device design to achieve simultaneous sensing in a multi-material graphene-based device. With further work investigating the response of textile-based inkjet-printed graphene to temperature, pressure, and humidity, determining whether device function is transferable towards more challenging substrates.
- **Chapter 8** details the suitability of inkjet-printed graphene towards breath monitoring. Determining whether chemical species can be detected in an environment with varying humidity.
- **Chapter 9** investigates the detection of biological biomarkers with two focuses. Firstly, using a cross-AM method, overprinting hydrogels onto graphene/PEDOT:PSS IDEs, and determining the capability to measure compositional changes of NaCl content. Secondly, the ability to detect infection-related biomarkers, present in the growth of biofilms, with multi-material inkjet-printed devices.
- **Chapter 10** reports on the conclusions of this thesis and considers future work to continue this direction of research.

2 Literature Review

2.1 Inkjet-printed electronics

Expansion of the Internet of Things (IoT) has led to a shift in focus towards advances in wearable electronics, with the realisation of effective interactions between electronic devices and the human body.[20,31] Wearable electronics serve numerous functions; the smartwatch is a salient example of such technology, with strong uptake.[32] Whether users are logging activity or monitoring their health, it is evident that the use of wearable electronics, whether worn on the skin or through clothing, is becoming increasingly desirable. Furthermore, the widespread desire for increasingly personalised healthcare is as a driving factor in the development of wearable electronics for medical applications.[33]

Much of the currently available technology is produced using conventional manufacturing techniques and materials that are not necessarily well-suited to wearable devices. Available manufacturing techniques are primarily limited to fabrication on rigid materials, thereby constraining material choice and design flexibility.[34] Additive manufacturing (AM) of such devices boasts considerable benefits, particularly for end-use applications. For instance, it offers greater design freedom than traditional manufacturing techniques and the ability to vary features on a print-by-print basis is significant for prototyping.[35]

Whilst inkjet printing is not a new technology, the inclusion of functional materials in inks has enabled the fabrication of 3-dimensional (3D) structures by depositing materials (via inks) layer by layer.[36] It is the primary AM technique for the fabrication of electronics, and an excellent choice for the production of flexible devices.[37] This

technique enables the deposition of functional inks containing conductive materials with a high degree of freedom and precision in design, with feature size down to ~100 μm possible as well as film thicknesses of < 1 μm. [38–40] The ability for the deposition of thin films with high resolution is suitable for a range of substrates with specific material compatibility dependent on the ink formulation used and any post-processing requirements. Compared with conventional electronics manufacturing methods, inkjet printing can utilise highly flexible substrates, such as polyethene naphthalate (PEN) and Kapton, which are well-suited for wearable devices.[20,41] Whilst printing onto textiles currently remains challenging, strategies can be implemented to improve surface characteristics, thereby advancing wearable electronics.[42,43]

Due to its scalability, inkjet printing also has significant potential for commercial production, making it an attractive technology for manufacturing flexible electronics. Electronic components, such as capacitors and transistors, have exemplified this scalability, with production initially achieved on laboratory-scale printers and subsequently with industrial print heads that enable high quality, yield, and batch size.[44]

2.2 Printed sensing devices

The progress achieved in inkjet-printing of electronics in recent years has broadened the range of potential applications for healthcare devices, including sensors,[1–6,45] thin-film transistors,[46–48] photovoltaic cells[15] and displays.[9–11] Unlike conventional electronics fabrication techniques, ink jetting permits the use of a diverse range of substrates, such as flexible and stretchable polymers, which are well suited to wearable healthcare devices. The conventional methods, including photolithography, chemical

vapour deposition (CV) and PCB-based processes, are ill-suited to wearable electronics due to inherent constraints, such as the reliance on high temperatures, rigid substrates and multi-stage workflows.[49] These constraints prevent their use in wearable systems, where conformability to the human body and the ability to perform under mechanical deformation are critical. Traditional, rigid fabrication technologies thus fall short in the desire for wearable electronic devices, motivating new methods for developing flexible approaches.[50]

2.2.1 Methods for device manufacture

Multiple techniques have been demonstrated for the successful fabrication of functional materials-based electronics, including inkjet printing, screen printing, photolithography, and chemical vapour deposition (CVD).[51–56] When evaluating the value of inkjet printing in this context, it is important first to understand the alternative processes, the advantages they offer, and their limitations.

Inkjet printing is a non-contact deposition method for the manufacture of electronic devices, with a broad range of functional materials available by use. Liquid inks can be loaded with functional materials and deposited using digitally defined patterns, enabling design variation on a print-by-print basis.[35] Due to the non-contact nature of this process, a wide variety of substrates are available, including flexible and stretchable polymers as well as textiles.[57] Loading of solid material into inks typically remains low not to exceed viscosity requirements and avoid nozzle occlusion, whilst careful formulation is required to tune surface tension and wetting characteristics required for achieving high resolution devices.[17]

Furthermore, this introduces the requirement for post processing for many formulated inks, as they are not electrically conductive in their printed form.[58,59] For instance,

many graphene-based inks contain additives to prevent flake agglomeration, which improves dispersion stability and printing performance, however, can inhibit electrical transport and therefore require removal or decomposition after deposition. Inkjet-printed MeNPs similarly require a sintering stage after printing to remove NP surface coatings and to provide fusion forming a continuous electrically conductive film. These objectives are commonly achieved through the application of thermal energy, typically by heating the printed material to elevated temperatures (> 150 °C). [17] More recently, alternative approaches have been developed that utilise photonic methods for the application of energy, such as intense pulsed light or UV irradiation.[60] These techniques provide the necessary post-processing, whilst minimising heating, broadening the range of substrates available for use.

Screen printing is, in some respects (namely, materials), the most similar to inkjet among the listed methods, with both processes capable of utilising conductive particle-based inks. This process operates by pushing ink through a purpose-made stencil onto the substrate, achieving resolution down to 50 μm in feature size, and post-processing required to harness the material's electrical conductivity. It enables highly reproducible, large-scale production of electronic devices, such that screen-printed electrodes have been widely used in research,[61,62] as well as being used commercially for the manufacture of end-use products. Screen printing has been applied to a range of electrical devices, including supercapacitors, resistors, inductors and electrochemical sensors.[51,63,64]

A number of functional materials have been deposited via screen printing, including graphene, AgNPs and liquid metals, such as gallium indium (GaIn, $T_{melting}$ = 15.7 °C). Screen printing can handle high viscosity inks (> 5000 cP[63]), and as such is capable of including high concentrations of the functional material. For example, Kim et al

printed a graphene formulation of 47.5 mg/mL.[65] This high-viscosity potential permits screen printing to be applied to textile-based device manufacturing, where high substrate porosity can be countered by deposition of large quantities of functional materials being deposited, thereby enabling devices with high electrical conductivity. For example, Islam et al fabricated a graphene pattern onto a cotton substrate, achieving a resistivity of 62.5 Ω/cm.[66] However, it is not a digital process (one of the primary advantages of inkjet printing) where each individual device requires a unique stencil for the correct design to be printed. This inflexibility reduces its suitability for purposes such as prototyping, where frequent design changes may be required, as well as its potential for manufacturing a diverse product line.

Photolithography is a multistep process that requires detailed preparation and execution of each stage and is capable of producing features with very high resolution, reportedly approaching or even reaching the nanoscale.[67,68] Common materials used in photolithography for electronics include PEDOT:PSS, gold and graphene, enabling the fabrication of a range of devices, such as transistors and microprocessors.[56,69,70] Disadvantages of lithography techniques arise from slow processing times, due to multiple complex steps, high fabrication costs associated with extremely clean operating conditions and the mask-based, non-digital nature which limits design flexibility and ability for rapid prototyping.

Vat photopolymerisation (e.g. laser-based stereolithography (SLA) and digital light processing (DLP)) is an AM process that involves photosensitive resins cured layer-by-layer. SLA utilises a UV laser to trace a layer, whilst DLP uses a projected light source to cure a whole layer at once, both capable of creating highly detailed 3D objects, with feature size down to 25 μm.[71] The inclusion of conductive materials, such as PEDOT:PSS, CNTs and graphene, into these resins has permitted the development

of 3D printed geometries with unique electrical properties.[72] However, as the resins require the application of UV light for curing to occur, there is a limit on the amount of conductive material that can be included, as it can scatter or absorb the incident light. As such, the conductivities of these structures remain low compared to other methods for printing electronics(~ 10^{-2} S/m).[72]

A systematic comparison of the presented printing technologies is offered below, in **Table 2-1**.

Table 2-1 An overview of the reviewed printing technologies for 3D printing electronics.

Method	Feature size	Accuracy & reproducibility	Key functional materials	Substrate compatibility	Design flexibility
Inkjet printing	20-100 µm	Moderate, sensitive to print parameters and ink formulation	Graphene, GO, CNTs, MeNP, PEDOT:PSS	Broad; flexible polymers, textiles, non-contact deposition	High – digital patterns
Screen printing	50-100 µm	Good, consistent film thickness from stencil, used commercially	Graphene, AgNPs, liquid metals (GaIn)	Good, high viscosity inks are compatible with porous substrates	Low – stencil based
Photo-lithography	<1 µm	Very high, used for precision electronics. Batch level production in cleanrooms.	PEDOT:PSS, gold, graphene	Rigid/planar surfaces only	Low – mask based
SLA/ DLP	25 µm	High, layer by layer curing enables high 3D detail, but resin batch variation can cause issues.	PEDOT:PSS, CNTs, graphene	Enables complex 3D geometries	High – digital 3D designs

Among these alternative fabrication methods, inkjet printing offers clear benefits.[73,74] Versatility is the standout feature of inkjet: due to its digital, drop-on-demand nature, the pattern can be reprogrammed for each individual print with ease,[75] thereby negating the requirement for pattern-specific equipment, such as a screen-printing and

lithographic masks. This drop-on-demand method also offers cost-effectiveness by using material more efficiently than other methods, since only the necessary material is deposited.[36] Moreover, the availability of multi-material inkjet printing systems facilitates upscaling of more complex device manufacturing, enabling the fabrication of complete devices within a single system.[76]

However, several challenges remain. For instance, the reliable deposition of graphene has been difficult to achieve without nozzle clogging and the occurrence of the coffee ring effect[20,77] and the resolution of jetted electronics is constrained by nozzle dimensions, which dictate droplet size.[78] Despite these limitations, inkjet printing offers significant advantages, including low-cost, reconfigurable, scalable and mask-free fabrication, making it well-suited towards large-area and wearable electronics where ultra-high resolution is not critical. Ongoing developments in ink formulation and printing strategies work to mitigate these challenges, supporting the viability of this approach.

2.2.2 Flexible and stretchable electronics

Inkjet- and screen-printed devices have been successfully deposited onto polymeric substrates with high flexibility and stretchability. Among these materials, Kapton, PEN, polyurethane, TPU, and polydimethylsiloxane PDMS are widely used in flexible and stretchable electronic devices.

Inkjet printing, coupled with low-temperature photonic annealing, has enabled the fabrication of graphene-based electronics on thermally sensitive, highly flexible substrates such as PET and PEN.[79] For example, Secor et al demonstrated inkjet printing of a graphene/ethyl cellulose (EC) ink onto PET with high electrical conductivity (2.56×10^4 S/m), enabling large-scale fabrication of conductive patterns

(**Figure 2-1 a**).[23] It is a concern that the rapid nature of IPL annealing may induce local stresses and unique morphological features. To investigate these effects, the IPL-annealed graphene was subject to 1000 cycles of bending with radii of 8.1 and 1.3 mm, with little variation in resistance (≤ 10 %). It was observed that a lower pulse energy for IPL yielded a lower increase in resistance, perhaps due to a more uniform surface morphology. Stretchable substrates are also applicable for inkjet printing, with materials such as TPU, polyurethane and PDMS commonly used. Material adhesion to these substrates is considered in tandem with the ink formulations, but remains challenging. PEDOT:PSS has been inkjet-printed upon PDMS, exhibiting low sheet resistance (58 Ω/sq.) whilst being capable of accommodating mechanical deformation up to 50 % strain.[80] This study addresses ink formulation for stretchable devices, where the addition of the soft polymer, poly(ethylene oxide) (PEO), improves the elasticity of the inkjet-printed film but does increase the sheet resistance from 58 Ω/sq. to 84 Ω/sq depending on the volume added. Strain sensitivity was drastically reduced, as well as the maximum elongation, more than doubling through the addition of PEO (**Figure 2-1 b**).

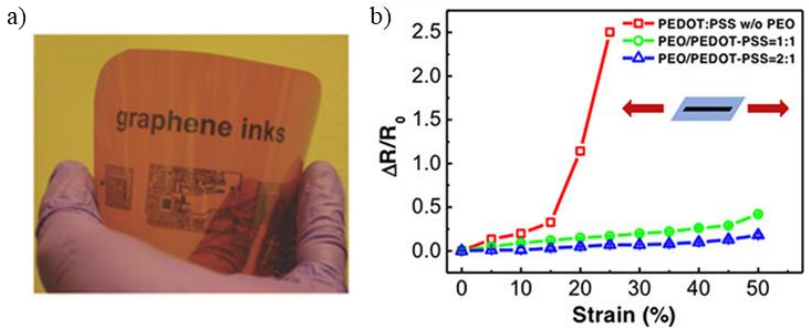


Figure 2-1 a) Large-area inkjet-printed graphene patterns on polyimide. Reproduced from Secor et al.[23] **b)** Relative change in resistance plotted as a function of tensile strain for the PEDOT:PSS thin film with various amounts of PEO. Reproduced from Lo et al.[80]

Kim et al. fabricated a graphene sensor via screen printing, achieving high electrical conductivity (1.49×10^4 S/m) and good mechanical flexibility.[65] The device consisted of a graphene layer measuring 20 – 41 μm in thickness, deposited on a PET substrate. Bending was performed up to 1400 cycles, demonstrating little to no change in resistance throughout (**Figure 2-2 a**).

A liquid GaIn ink was screen-printed onto a stretchable, commercially available TPU substrate, forming a conductive network with high electrical conductivity (7.32×10^5 S/m) (**Figure 2-2 b**).[81] The device exhibited impressive resistance to strain, with electrical conductivity remaining largely unaffected until 800 % elongation, whilst resistance decreased < 2 % at 200 % strain. When subjected to 500 stretching cycles at up to 50 % strain, the device exhibited a 10 % increase in resistance. The low strain sensitivity and excellent stretchability can be explained by the merging of liquid metal particles, which reduces defect formation within the film and enables recovery to a continuous state.

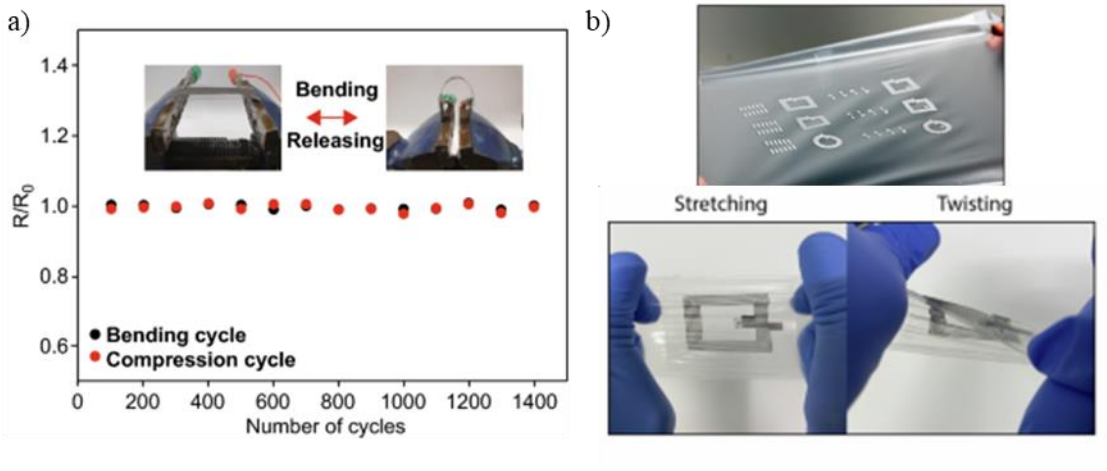


Figure 2-2 a) Electrical conductivity of screen-printed graphene on PET subject to fatigue test for evaluating resistance to bending over 1400 cycles. Reproduced from Kim et al.[65] **b)** Screen-printed liquid GaIn on TPU subject to stretching and twisting. Reproduced from Shang et al.[81]

Photopolymerisation methods have alternatively been used to fabricate flexible electronic devices using AM, such as DLP and SLA. Functional materials, such as PEDOT:PSS, can be dispersed in photocurable resins, enabling the fabrication of 3D conductive composite parts with highly customisable geometry. During resin formulation, optical transparency must be considered to ensure sufficient light penetration throughout; otherwise, incomplete curing may occur.

Lopez-Larrea et al utilised PEDOT:PSS dispersed in a poly(ethylene glycol) diacrylate (PEGDA) resin to print hydrogels using DLP (**Figure 2-3 a,b**).[82] Devices were capable of monitoring electrocardiography (ECG) whilst withstanding strain > 20% without degradation. Single-walled carbon nanotubes (SWCNT) dispersed in functionalised vegetable oil up to a concentration of 1.0 wt% were used in the preparation of soft-robotics for fabrication via DLP (**Figure 2-3 c**).[83] Printed samples demonstrated electrical conductivity between 10^{-3} – 10^{2} S/m and could withstand between 5 to 17.5 % elongation before failure, depending on SWCNT concentration. Increasing the concentration would improve electrical conductivity but reduce the ability to withstand mechanical deformation, highlighting a consideration for resin formulation. SLA has been used to print a PEODT:PSS-PEGDA ink onto a variety of flexible and stretchable substrates (**Figure 2-3 d**) with a sub 100 μm resolution. Microstructures were printed with relatively low impedance (< 200 kΩ) and used in bioelectronic applications such as electromyography measurements.

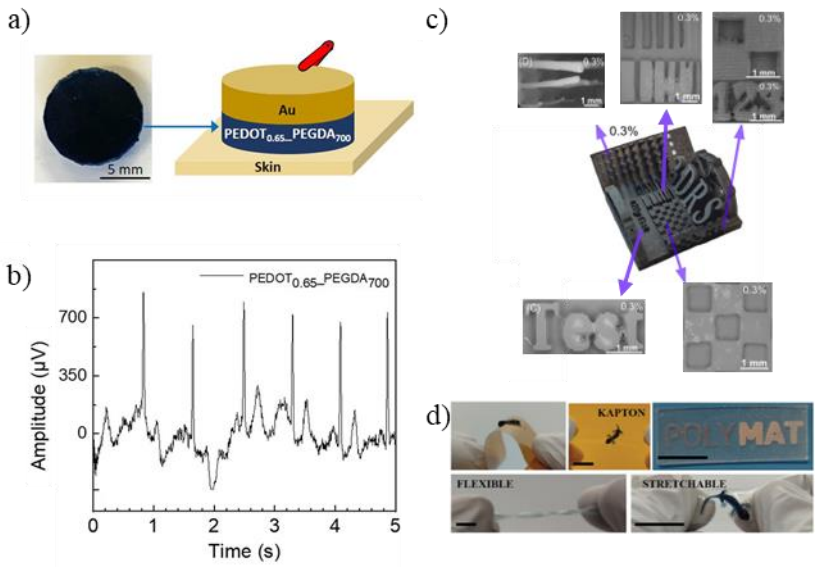


Figure 2-3 a) Optical image of the DLP 3D printed PEODT:PSS-PEGDA$_{700}$ hydrogels, with a round shape for ECG monitoring, and schematic representation of the built-up electrode. **b)** ECG signals recorded with PEDOT:PSS-PEGDA hydrogels. Reproduced from Lopez-Larrea et al.[82] **c)** DLP 3D printed resolution check of CWNT-vegetable oil resin. Reproduced from Jurinovs et al.[83] **d)** PEDOT:PSS/PEGDA ink is printed on top of Kapton film, and multi-layered on top of a flexible or stretchable material, demonstrating the possibility to create highly stretchable and flexible complex multi-materials (scale bar: 1 cm). Reproduced from Dominguez-Alfaro et al.[84]

2.2.3 Printed healthcare devices

There has been increased demand for patient data in healthcare, where greater information can lead to a more personalised approach to patient therapy, with benefits for diagnostic, treatment, and prognostic accuracy.[33]

A wide range of wearable healthcare devices has emerged in recent years, with development driven by data collection, leading to progress in breath analysis, sleep monitoring, hydration, movement detection, sweat analysis and infection detection.[85] Yet many existing systems face limitations, constrained by the available materials and manufacturing procedures which are governed by rigid materials and high temperature processes which translate to operating requirements. For instance, breath analysis devices, used for monitoring volatile organic compounds, often employ metal-oxide

sensors which require operating temperatures >200 °C, resulting in poor compatibility as a skin mounted system.[86] Infection monitoring devices, particularly those targeting wound healing often depend on optical or biochemical assays, which are difficult to implement as a point of care diagnostic device, challenged especially through miniaturisation and disposability.[87] Across these devices, common requirements emerge, where conformability to the human body is highly desired, as well as low power, low operating temperature and low cost to improve disposability, whilst also being capable of delivering highly accurate diagnostics.[88] The existing technology falls short of these requirements, and as such the previously discussed capabilities in 3D-printed electronics show strong applications in healthcare, where flexibility and customisability have significant potential for devices. The integration of printed electronics into medical devices showcases the strengths of this suite of manufacturing techniques, enabling devices to be produced with high flexibility and stretchability to fit the form and function of the human body.[89]

Wound dressings have attracted particular focus from printed devices, as the flexibility offered by printed electronics improves conformability to the human body. Prominent techniques include inkjet printing, screen printing, SLA and DLP.[90–92] For example, screen printing has been used to deposit a carbon electrode onto the skin-facing side of a plaster in an interdigitated pattern (IDE) pattern (**Figure 2-4 a**, Inset).[93] The capacitive field created by the printed pattern exhibited a response to blood and sweat, responding to fluids of differing volumes and demonstrating distinguishability for presence at a wound location (**Figure 2-4 a**). In a similar fashion, Nga et al fabricated an inkjet-printed AgNP parallel plate capacitor with a PET dielectric layer (**Figure 2-4 b**) and attached it to a dressing.[94] Information on wound pressure is valuable, as it can inform treatment decisions and prevent further damage from sustained mechanical

load (e.g., pressure ulcers). The device was shown to be responsive over the range 0.7 Pa – 2 kPa, with a sensitivity of 0.08 kPa^{-1}. A comparable device was produced by Ju et al. using inkjet printing, with TPU as the spacer between silver electrodes, which were deposited directly onto a non-woven textile.[95]

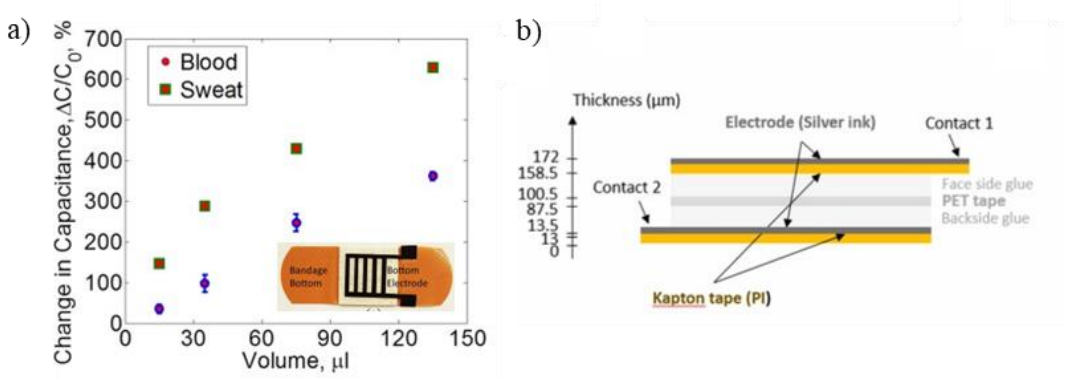


Figure 2-4 a) Dependence of capacitance on volume of blood and sweat mimicking fluids for a screen-printed carbon IDE (Inset: Carbon-based IDE screen-printed onto a plaster). Reproduced from Farooqui et al.[93] **b)** Schematic for the design of a silver electrode parallel plate capacitor. Reproduced from Nga et al.[94]

A novel approach to temperature sensing was demonstrated using DLP printing, in which a hollow microneedle array (1 mm in height) was fabricated from a clear, acrylate-based microfluidic resin. PEDOT:PSS was then cast in the hollow structure, and thermally insulated from the back side (**Figure 2-5 a**).[96] The microneedle device exhibited a change in resistance of > 40 % across a temperature range of 25 – 50 °C, whilst on-body temperature monitoring was performed on euthanised rats. It was found that the calibrated response of the device matched that of a syringe-type temperature probe (**Figure 2-5 b**).

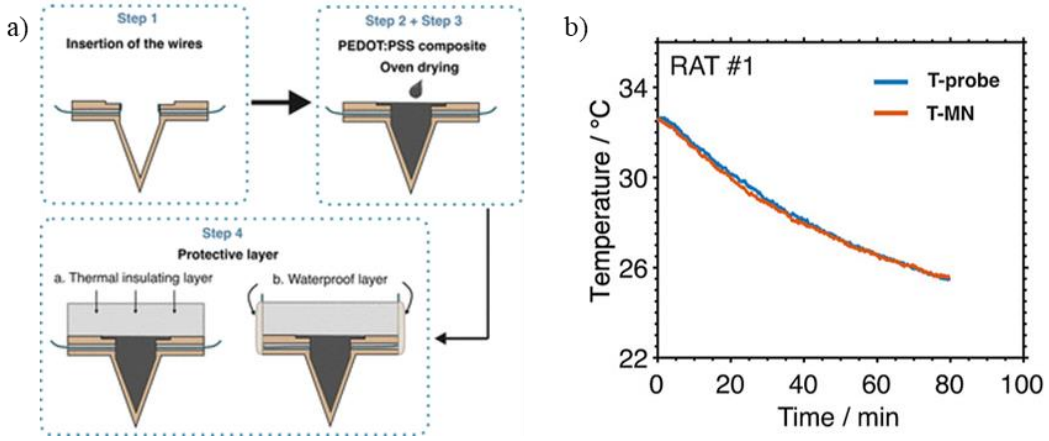


Figure 2-5 a) Schematic illustration of the preparation process for microneedle-PEDOT:PSS temperature-sensitive microneedle array. **b)** Temperature profiles obtained with the microneedle temperature device and the temperature probe in the investigated rat. Reproduced from Wei et al.[96]

Wound healing is a complex process, with multiple analytes indicating healing status. This is especially relevant for chronic wounds, where enhanced diagnostic information could better inform treatment and encourage healing. As such, Nga et al. developed a multifunctional sensing device capable of detecting pressure, pH, humidity, and lactate levels.[97] The device utilised inkjet-printed AgNP and AuNP electrodes on top of Kapton film, in combination with additional functional materials for specific stimuli sensing. It demonstrated the following sensitivities towards each stimulus: pressure – 0.5 kPa^{-1} (0.7 - 150 Pa), pH – 66.9 mV/pH unit, humidity – quick response time ($t_{response}$ < 5 s) to 100 % RH. Whilst no sensitivity towards lactate was calculated, the magnitude of signal change increased with concentration. Pressure and humidity devices were demonstrated in situ by attaching them to wound dressings and by a volunteer wearing them. However, this study does not demonstrate simultaneous sensing; thus, sensor operation in the presence of multiple stimuli may be compromised.

The addition of wireless technology could further improve the integration of printed electronic sensors into wound dressings. 3D-printed antennas are not a new phenomenon; numerous examples appear in the literature over the last 10 years, with AgNP inks being the common choice.[98–100] Chen et al demonstrated a screen-printed silver antenna, deposited upon a Tegaderm™ hydrocolloidal, moisture-retentive wound dressing, with a bandwidth of 3.2 - 4.6 GHz.[101] The antenna was shown to be unaffected by bending and to transmit sensor information, enabling remote wound monitoring via 3D-printed devices.

Hydrogels have also demonstrated application in wound dressings, firstly through therapeutic aid, providing a moist environment for healing, and secondly through the addition of responsive features and drug release.[102] Healthy skin has a weakly acidic pH (4 - 6), whereas the excretion of wound exudate can raise this (> 7). As such, pH-responsive hydrogels have been developed and printed using SLA, where a colour change will occur when critical ranges are reached.[103] Further functionality has been introduced by doping antimicrobial agents (calcium phosphate nanoparticles, CaPNPs) with a triggered release mechanism based on a shift in pH toward a more alkaline environment.[104] The addition of CaPNPs exhibited further benefit, improving the tensile strength and maximum elongation of the hydrogels, which are notoriously fragile.

Pharmaceutical tablets have been fabricated using inkjet printing. Multimaterial inkjet printing was used to fabricate a tablet with a specific geometry to control the release of a water-soluble poly (4-acryloylmorpholine) (poly-ACMO) that encapsulates aspirin.[76] The architecture of the tablet's insoluble structure would control surface area exposure of the aspirin-loaded poly-ACMO, with the drug release and dosage

managed. High scalability was demonstrated through a single-batch production of 56 tablets.

2.3 Functional materials for inkjet printing

Functional materials are defined as specifically engineered materials capable of executing a specific function in response to certain stimuli.[105] Graphene, MeNPs, quantum dots, carbon nanotubes (CNT), metal organic frameworks (MOFs) and hexagonal boron nitride (hBN) are just a few of this collection of materials, and have a significant impact in novel applications such as semiconductors, sensors, biomedical applications and energy storage.[106–108]

Functional materials often possess one or more features on the nanoscale, giving them unique properties that make their application so exciting, as well as appropriate for use in inkjet printing. These can also be called low-dimensional (lowD) materials and are classified by the number of dimensions present on the nanoscale, possessing at least one. Zero-dimensional (0D) materials can be classified on the nanoscale in three dimensions and consist of quantum dots and nanoparticles. One-dimensional (1D) materials possess two dimensions in the nanoscale and, due to this, often provide extraordinary length-to-width ratios. Common structures include nanotubes, nanowires and nanorods. Two-dimensional (2D) materials have just one nanoscale dimension, often taking the form of nanofilms or flakes.

2.3.1 0D materials

0D materials, such as nanoparticles and quantum dots, feature prominently in inkjet-printed electronics, with applications in printed circuitry and contacts, sensing and

emissive devices; they offer unique advantages due to their tuneable properties and high surface-area-to-volume ratio.[17,109–111] Metallic nanoparticles possess remarkably low sintering temperatures compared with their bulk counterparts (e.g., for AgNPs: $T_{NP,sinter}$ = 200 – 300 °C,[112] $T_{bulk,sinter}$ = 960 °C), making them well-suited for the low-temperature manufacture of electronic devices. The high surface-area-to-volume ratio means that surface-driven processes dominate sintering behaviour, thereby lowering the energy barrier to nanoparticle (NP) coalescence. Quantum dots boast a wide variety of tuneable properties, including their size, morphology, light emission spectrum, photostability and thermal conductivity.[113,114] These materials are widely used in inkjet printing, enabling the fabrication of a range of sensing devices through their incorporation into heterostructures. Quantum dots have been developed and inkjet-printed with photoluminescence exhibited upon exposure to UV and near infrared (NIR) light, whilst graphene quantum dots have been demonstrated with photo detecting properties.[8,115] The small size of 0D materials reduces the risk of nozzle occlusion during jetting, enabling the formulation of highly printable dispersions.[17] Combined, these properties make 0D materials versatile tools for the development of printed electronic devices.

Silver (Ag) and gold (Au) nanoparticles (**Figure 2-6**) appear to be the most prevalent in terms of inkjet-printed MeNPs, owing to their ease of synthesis, low toxicity, good electrical properties and strong applications to biomedicine.[116–119] MeNPs are well-suited for inkjet printing due to their small diameter (typically < 100 nm) and narrow size distribution, therefore reducing the risk of nozzle blockages as nozzle dimensions typically range from 10 – 100 μm in diameter. Both silver and gold nanoparticles have been produced, with AgNPs synthesised with 50 nm diameter,[109] and AuNPs with a distribution range of 6 - 50 nm.[120] On a larger scale, printable inks are commercially

available, with nanoparticles sized at < 100 nm[121] and 500 - 1000 nm[122] for Ag and Au respectively. Copper nanoparticles have been synthesised, but there is considerable difficulty in preventing oxidation before and during printing, thereby making their use challenging.[17]

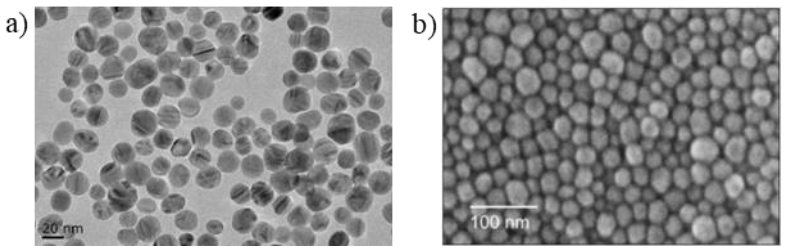


Figure 2-6 a) Transmission electron microscope (TEM) image of AgNPs. Reproduced from Huang et al.[123] **b)** SEM image of gold nanoparticles. Reproduced from Benkovičová et al.[124]

One distinct advantage of metallic nanoparticles is the low sintering temperature, T_{sinter}, compared with the bulk material. Sintering temperature is reported to decrease with nanoparticle size, and is significantly lower than that of bulk materials due to the high surface-to-volume ratio.[125] The reduction in sintering temperature arises from the increased fraction of surface atoms in nanoparticles, whose lower coordination and weaker binding energies reduce the thermal energy required for atomic rearrangement. For instance, the sintering temperatures of bulk silver and gold range between 600 °C and 900 °C, respectively; however, AgNPs and AuNPs can be sintered at temperatures down to 150 °C, due to the thermodynamic size effect.[126,127] Sintering of nanoparticles results in fusion between them (**Figure 2-7**), providing pathways for electron transport. Conductivities have been achieved close to the bulk material, e.g., AgNPs were inkjet-printed, sintered at 300 °C and had a resistivity of 3 μΩ/cm,[128] whilst AuNPs have been sintered at 180 °C, achieving a resistivity of 5 μΩ/cm. These values are within a factor of three for the bulk resistivity of silver (1.6 μΩ/cm) and gold (2.2 μΩ/cm),[129,130]

demonstrating the excellent retention of electrical properties of inkjet-printed nanoparticle films. The decrease in electrical conductivity of MeNPs compared to bulk material can be attributed to an enhanced scattering of charge carriers at grain boundaries and surfaces, as well as the presence of defects within the film.[131] Furthermore, anisotropic electrical conductivity has been observed in inkjet-printed AgNPs, where the presence of organic stabilisers increases resistance.[132]

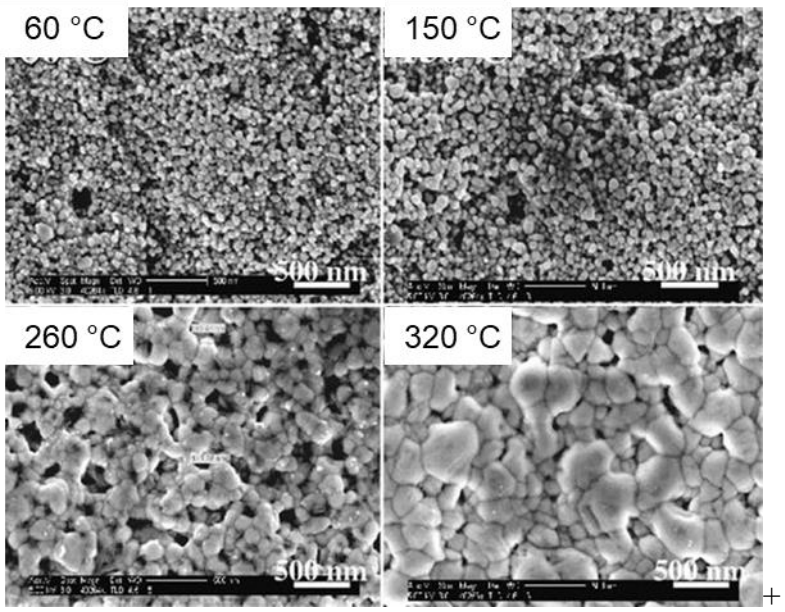


Figure 2-7 SEM images of silver nanoparticles dispersed on a glass slide and sintered at increasing temperatures. All scale bars are 500 nm. Reproduced from Kamyshny et al.[109]

Both of these materials have strong potential for biomedical device applications, beyond the scope of printed electronics. AgNPs are already widely used in healthcare due to their potent antimicrobial properties, as well as their capacity for drug delivery.[133] AuNPs, known for their excellent biocompatibility, are well-suited for intrusive medical treatments such as diagnostics, cancer therapies and drug delivery.[134]

2.3.2 2D materials

2D materials such as graphene, GO, MXenes, tungsten disulfide (WS_2) and hBN (**Figure 2-8**) exhibit promising functionality, in terms of mechanical, electrical and chemical properties due to the strength of carrier confinement and high surface area.[135,136] Inkjet printed 2D material based devices were successfully demonstrated. including transistors, sensors and superconductors.[137] 2D materials were produced with high electrical conductivity (Graphene and MXenes), as well as semiconductors (WS_2, In Se) and insulators (hBN), enabling realisation of multimaterial inkjet printing to produce heterostructure devices with multiple functionalities. The novelty of 2D materials extends beyond electrical properties, including high mechanical strength, optical tunability and chemical versatility, providing a broad range of applications.[138]

Liquid exfoliation is a common method for producing 2D materials, providing a scalable and versatile pathway for synthesis.[138] This method involves dispersing bulk material (e.g., graphite) into a solvent and applying energy, usually by ultrasonication or shear mixing, which separates them into few-layer or monolayer nanosheets.[139] Solvents are selected to match the surface energy of the 2D material selected, aiding stability of the produced dispersion, as well as preventing aggregation.[140] This is well-suited to the production of inks for inkjet printing, as it not only provides stable dispersions but is also highly scalable, capable of producing material at the gram scale, bridging the gap between lab-scale synthesis and industry.[141] Further ink modification may be required to tune viscosity, surface tension and stability for specific inkjet printing systems.

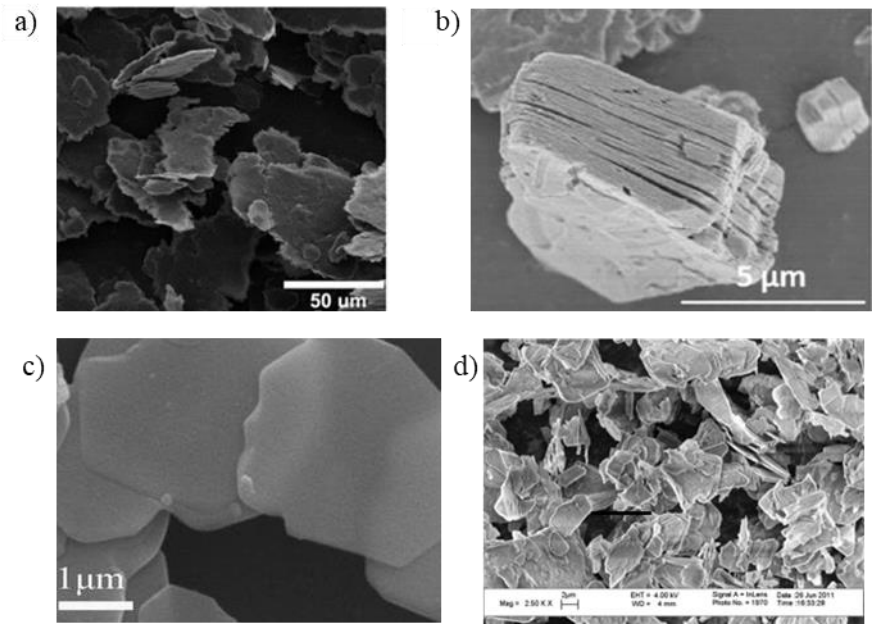


Figure 2-8 a) SEM micrograph of graphene nanoflakes, reproduced from Sengupta et al.[142] **b)** SEM visualisation of chemically exfoliated titanium carbide MXene nanostructures. Reproduced from Krishnamoorthy et al.[143] **b)** SEM image of exfoliated WS_2 nanosheets. Reproduced from Huang et al. **d)** SEM image of h-BN platelets, reproduced from Lin et al.[144]

Graphene is a 2D material that has attracted considerable interest in recent years, following its discovery by Novoselov and Geim in 2004 via mechanical exfoliation.[145,146] It can be synthesised as single-layer graphene (SLG), with flake sizes varying from 100 nm to 1000 µm.[147,148] Graphene can be synthesised via mechanical or liquid exfoliation or CVD.[149] Graphene inks are commercially available and typically consist of 1 - 3 layers, with lateral flake dimensions of 50 - 100nm.[150] For such dispersions, flakes are often synthesised through chemical liquid exfoliation.

The properties of graphene are quite remarkable, with high electron mobility (200,000 cm^2/Vs),[151] exceptional mechanical strength (Young's modulus, E = 1 TPa) and high thermal conductivity (3000 - 5000 W/m.K).[152,153] These properties pertain to a single graphene flake and change when translated to a network of inkjet-printed graphene flakes. Carrier mobility in inkjet-printed graphene films is 1 - 13 cm^2/Vs,[154]

with some state-of-the-art devices reaching up to 100 cm^2/Vs.[154–156] The thermal conductivity also reduces when presented in inkjet-printed form, with values at room temperature typically ranging from 1 - 10 W/m.K.[157,158]

This change in properties arises from several factors. When inkjet-printed, the stacking and alignment of graphene flakes cannot be controlled, resulting in a disordered network with defects and impurities introduced during ink formulation and processing. Consequently, interflake electrical conductivity is reduced, and charge transport is dominated by electron hopping between flakes. Annealing of printed graphene samples can improve electrical conductivity through the removal of residual solvents and additives, improving the interflake contact. Studies also suggest that annealing increases the packing density of graphene flakes in the deposited ink, improving conductivity through reduction in the distance required for inter-flake charge transport (**Figure 2-9 a**).[159] Furthermore, it was demonstrated that increasing both the number of printed layers and annealing temperature decreased the sheet resistance (**Figure 2-9 b,c**). Increasing the number of layers improves graphene coverage across the printed film, whilst higher annealing temperature, T_{anneal}, enhances EC decomposition into carbon char, which has been suggested to improve film electrical conductivity by connecting neighbouring flakes.[160] EC is also important in graphene ink formulation, as it aids in ink stability and prevents flake agglomeration, improving printability.

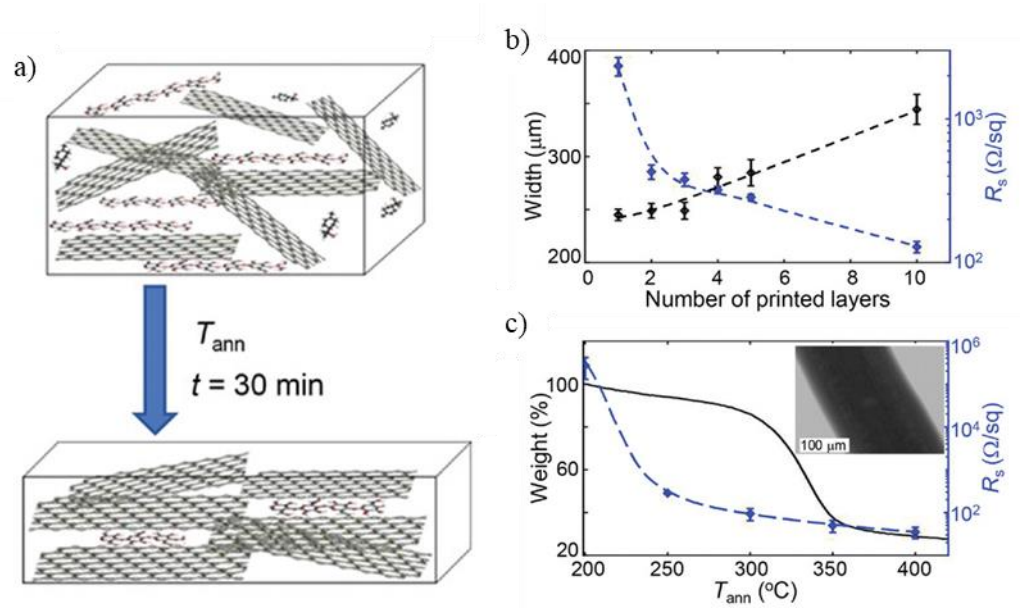


Figure 2-9 a) Schematic for packing of inkjet-printed graphene flakes and ink additives before and after thermal annealing. **B)** Printed line width and sheet resistance measured versus the number of inkjet-printed layers of graphene (10 lines, T_{anneal} = 250 °C). **c)** Thermal gravimetric analysis (TGA) of the ink and corresponding sheet resistance measured versus annealing temperature (5 layers/10 lines). (Inset: The scanning electron microscopy image of a graphene sample (5 layers/6 lines on Si/SiO_2, T_{anneal} = 250 °C)). Reproduced from Wang et al.[159]

The properties of inkjet-printed graphene are still excellent with low sheet resistance (< 500 Ω/sq.[154,161]) and high sensitivity to a range of external stimuli, including temperature,[162] humidity,[163] pressure,[164] gases[165] and chemicals[166] making it well-suited towards sensor devices.

The temperature-dependence of graphene has been shown to follow an Arrhenius-like behaviour, whereby the electrical conductivity, σ, is proportional to the temperature (**Equation (2-1)**) for ranges exceeding 250 K.[167,168]

$$\sigma \propto \exp\left(\frac{-E_a}{k_B T}\right) \qquad \textbf{(2-1)}$$

where σ is the electrical conductivity at temperature T, E_a is the activation energy and k_B is the Boltzmann constant.

Graphene flakes are subject to types of scattering that are a result of imperfections, defects, impurities and flake edges. The imperfections allow thermally activated charge carriers to increase electrical conductivity with temperature increase.[169] Thus, as the temperature increases, the likelihood of electron transfer to the conduction band increases and consequent hopping between the graphene flakes to carry charge.[169] The activation energy is indicative of the required for thermal energy transfer, which will permit the electrons to transfer bands, thus lowering $E_a$results in greater electrical conductivity.[26]

Graphene flake networks also exhibit strong sensitivity towards humidity, whereby increased humidity will reduce network electrical conductivity. This occurs due to the obstruction of flake-to-flake junctions by water molecules, as well as increased separation of flakes, both of which increase the difficulty for electron hopping.[6] There may also be charge transfer to water molecules, further impeding electron transport. It has been suggested that this response has two stages; at low relative humidity (*RH*), resistance increase is small due to graphene-water molecule interactions occurring at the surface level. As *RH* increases, sensitivity increases because molecules penetrate deeper into the graphene flake network, resulting in reduced packing density, as was reported for graphene devices.[26,170]

The study of graphene's sensitivity to chemicals and gases is well documented, with the detection mechanism similar to that for humidity. The stimuli molecule can block the flake-to-flake junctions as well as increase the inter-flake spacing. The target molecule can also affect charge distribution throughout the graphene network, depending on whether it is an electron donor or acceptor.[171] For instance, one study investigated the response of graphene to a number of different gases: NH_3, CO, H_2O and NO_2 (**Figure 2-10**).[172] The results observed an increase in resistivity for NH_3 and

CO, which are electron donors, whilst NO_2 and H_2O are electron receptors, causing a decrease in resistivity.

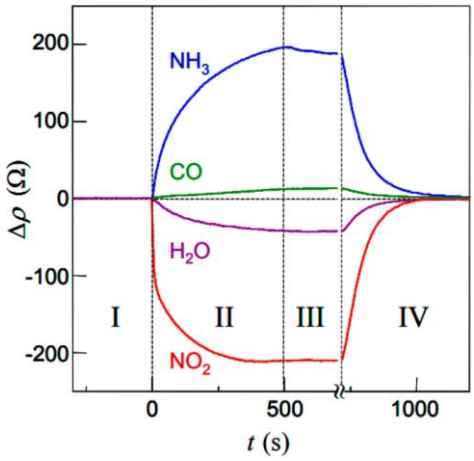


Figure 2-10 Changes in the electrical resistivity of graphene over time by various gases diluted to 1 ppm. Reproduced from Shedin et al.[172]

GO is a notable derivation of graphene, consisting of a hexagonal lattice of carbon atoms with oxygen-based functional groups, produced commonly by oxidative reduction of graphite through the Hummers or modified Hummers method.[173] This involves oxidising graphite with strong chemicals, such as potassium permanganate in sulfuric acid, which introduces oxygen-containing functional groups onto the surface and edges.[174] This method presents high efficiency and shorter reaction time than previous strategies, and modified versions have been developed with improved yield.[175] GO is inherently hydrophilic, exhibiting excellent dispersibility in water and polar solvents without the need for additives, facilitating straightforward formulation for ink jet printing.[176,177] As printed GO presents weak electrical conductivity, acting more like an insulator, thus a reduction stage is implemented through thermal, chemical or photonic processes (**Figure 2-11 a**),[178] yielding reduced graphene oxide (rGO) with improved conductivity (4.32×10^{-5} S/m).[179–182] In its reduced form, GO

has demonstrated many similar sensing capabilities to graphene, with sensitivity exhibited towards temperature, humidity (**Figure 2-11 b**), chemicals and gases.[183–188]

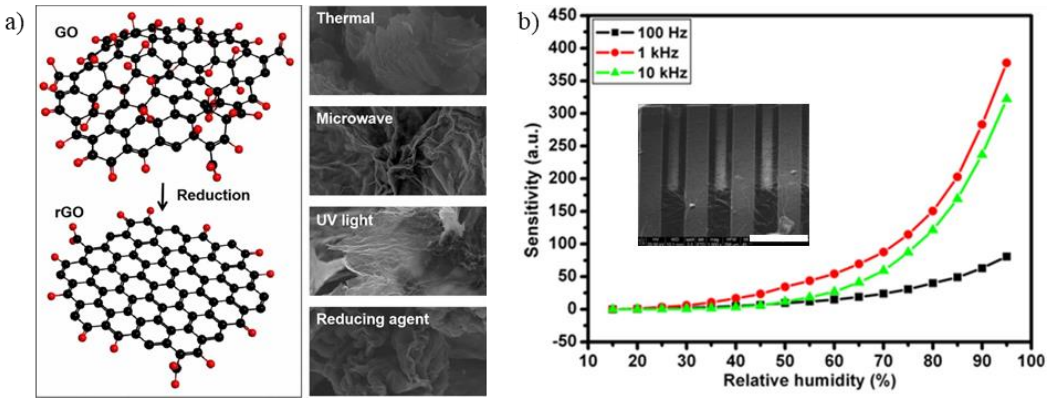


Figure 2-11 a) Schematic of reduction of GO and SEM images of rGO using different methods. Reproduced from Xiang et al.[178] **b)** Humidity dependence of graphene oxide capacitive device with Au interdigitated electrodes at 100 Hz, 1 kHz and 10 kHz. (Inset: SEM image of graphene oxide film on Au electrodes) Reproduced from Bi et al.[184]

2.3.3 Conductive and insulating polymers

Polymers have a significant presence in the materials library for inkjet printing, for both conducting and insulating purposes. Conjugated polymers are organic macromolecules with a backbone of alternating single and double bonds, which enable electron movement.[189] This unique structure gives them interesting electrical properties, well-suited for flexible sensing devices, whilst the high solubility and small size of the molecules enable efficient inkjet printing. Commonly featured conductive polymers include PEDOT:PSS, polyaniline (PANI), polythiophene (PT) and polypyrrole (PPy) (**Figure 2-12**).[190]

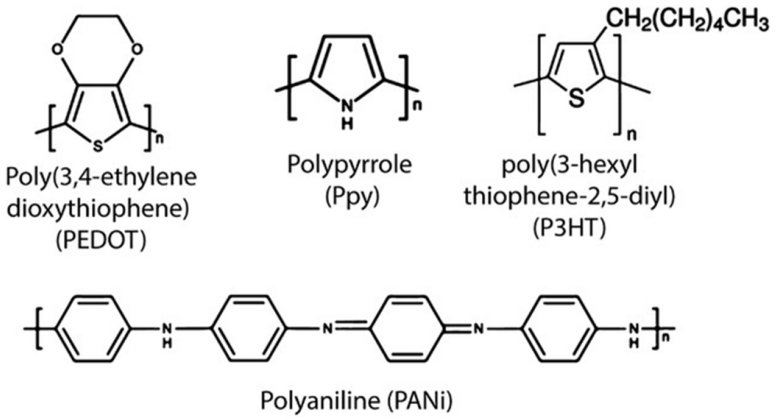


Figure 2-12 Chemical structures of conjugated polymers. Reproduced from Liu et al.[190]

PEDOT:PSS has gained significant attention in recent years for inkjet-printed electronics due to its low sheet resistance (< 125 Ω/sq.[191]) and the ability to form aqueous ink formulations.[192] Other interesting properties of PEDOT:PSS include its optical transparency, with high transmission across the visible light spectrum[193] (**Figure 2-13 a**) and the ability to form thin films with low surface roughness (root-mean-square roughness of 1.7 nm, (**Figure 2-13 b**)[194].

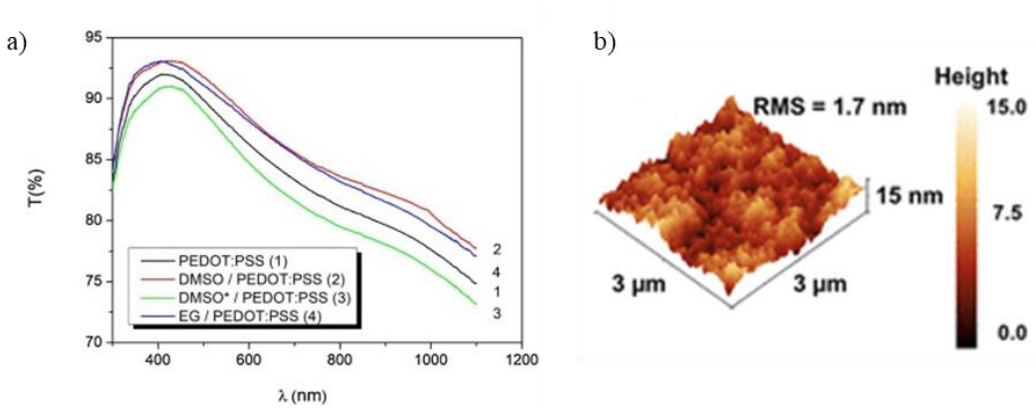


Figure 2-13 a) Transmission spectra for PEDOT: PSS, dimethyl sulfoxide (DMSO) and ethylene glycol (EG) sensitised PEDOT:PSS thin films on glass. Reproduced from Girtan et al.[193] **b)** Morphology of PEDOT:PSS film obtained with tapping mode atomic force microscopy (AFM). Reproduced from Lo et al.[80]

Hence, the application of conductive polymers to a wide range of electrical devices is seen. Due to its ability to form thin, conductive films, PEDOT:PSS is widely used in inkjet-printed electronics, offering high flexibility and stretchability without degrading electrical properties.[80,191,195,196] Sensitivity towards environmental stimuli, such as temperature and humidity,[197,198] low toxicity[199] and the ability to conduct ions as well as electrons, enabling electrical interaction with biological tissue,[200] sees a variety of biomedical devices produced.

Insulating, or dielectric, polymers have been well demonstrated in inkjet printing, serving as structural supports, encapsulants, and dielectric layers. These materials are characterised by strong electrical insulating properties, UV curability, and thermal stability.[201,202] Commonly used materials include tripropylene glycol diacrylate (TPGDA), polyimide and polyvinylpyrrolidone (PVP).[13,201,203] TPGDA is a UV-curable monomer that can be rapidly polymerised post-printing to form a rigid dielectric structure (**Figure 2-14 a**). These insulating polymers have been demonstrated in tandem use with conductive materials, such as silver, and processed with multi-material inkjet printing, enabling fabrication of fully encapsulated electrical devices (**Figure 2-14 b,c**). [132]

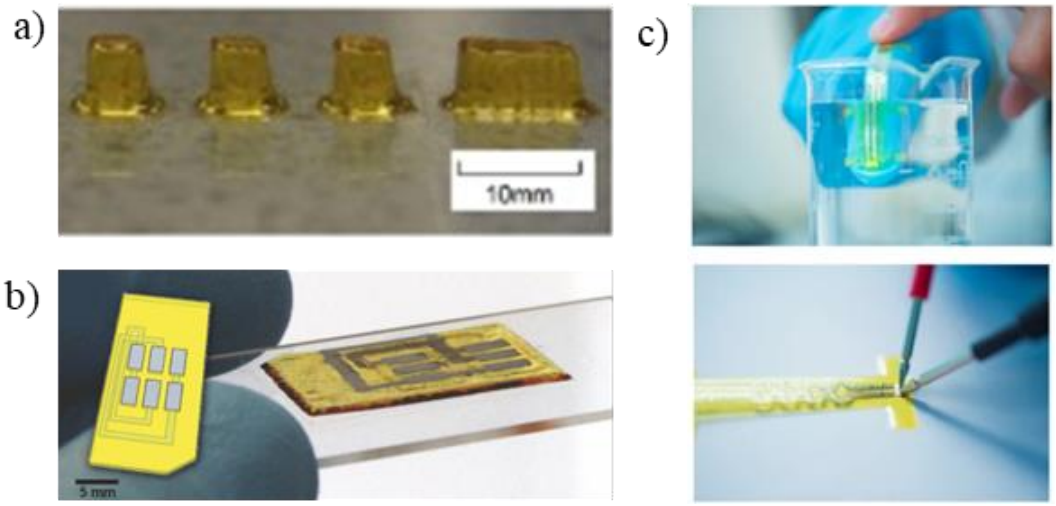


Figure 2-14 a) Cubic TPGDA structures inkjet-printed and UV irradiated. Reproduced from He et al.[203] **b)** Demonstrator of insulating polymeric (TPGDA) and conductive metallic materials inkjet-printed in one structure forming a chip with specific conductive layout. Reproduced from Saleh et al.[204] **c)** Inkjet-printed encapsulated silver patterns in TPGDA with residual PVP permitting anisotropic conductivity. Reproduced from Trinidade et al.[132]

2.3.4 Hydrogels

Hydrogels are insoluble 3D polymer networks, capable of absorbing water or other biological fluids whilst maintaining their structural integrity. A cross-linker is required to connect individual polymer chains, thereby providing rigidity and elasticity and preventing the gel from collapsing upon water absorption.[205] Depending on the degree of crosslinking, hydrogels can be composed of up to 90 % of their weight in water, making them highly versatile for medical applications.[206] Crosslinking can be activated by a variety of methods, including optical polymerisation, enzymatic reactions, and changes in temperature and pH.[205] Hydrophilic groups within the polymer network can facilitate swelling, the extent of which can be controlled by the degree of crosslinking, and consequent mechanical stiffness of the gel. Superabsorbent hydrogels have been synthesised that can swell by more than 5000 g/g, enabling applications in drug delivery, wound dressings, and tissue engineering.

Hydrogels can be formed from a variety of naturally occurring and synthetic materials. Biopolymers such as gelatin, collagen and chitosan, derived from natural sources, are prevalent choices in the literature. Hydrogels produced from these materials are non-toxic, biocompatible, biodegradable and cost-effective, making them an excellent choice for healthcare applications.[207] Synthetic-based hydrogels provide some advantages over naturally occurring materials in terms of their highly tuneable properties, reproducibility and improved mechanical strength. Commonly used materials include polyethylene glycol (PEG), poly(vinyl alcohol) and poly(meth)acrylates.[208] Hybrid hydrogels incorporate both naturally occurring and synthetic materials, combining the advantages presented by each group with a strong applications in medicine.[209]

Further functionality has been embedded into hydrogels through the addition of functional materials, drug-loaded molecules and selection of pH or temperature-responsive materials. Electrical conductivity can be achieved through the addition of functional materials, permitting the fabrication of 3D charge-carrying structures. PEDOT:PSS is a popular material due to its high dispersibility in water, with application demonstrated in use as strain gauge devices, where a change in electrical conductivity is related to the experienced mechanical deformation (**Figure 2-15 a**).[210] AgNPs have been included in hydrogel formulations, lending their antimicrobial properties to medical applications (**Figure 2-15 b**). Silver ions are released within the gel and help to disrupt bacterial formation and promote tissue regeneration.[211] Similar behaviours have been observed through the addition of AuNPs capped with anticancer agents, where healing could be triggered by irradiation with an infrared laser (**Figure 2-15 c**).[212] pH and temperature have also been demonstrated as effective mechanisms for stimulating and controlling drug release from hydrogels.[213,214]

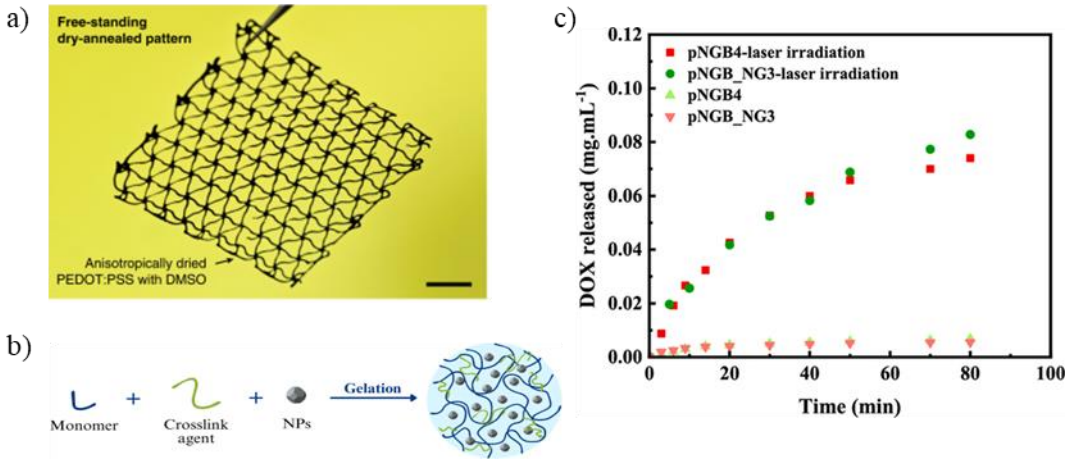


Figure 2-15 a) Free standing, electrically conductive PEDOT:PSS hydrogel for strain sensing. Reproduced from Lu et al.[210] **b)** Schematic for polymerisation of nanoparticles in polymer suspension. Reproduced from Albao et al.[211] **c)** Drug release from AuNP infused hydrogels triggered by infrared irradiation. Reproduced from Khodami et al.[212]

2.3.5 Hybrid inks

The formulation of hybrid inks has been reported to provide highly sensitive electronic devices through the combination of metallic nanoparticles[45,215] and conductive polymers[216] to graphene flakes and CNTs. The conductive polymer PEDOT:PSS is commonly found hybridised with graphene.[17] It is suggested that in graphene-based hybrid inks the PEDOT:PSS forms a connective glue between the graphene flakes through non-covalent bonding.[217] This mechanism of film formation supports a stronger interpenetrating structure and should benefit the electrical conductivity of the printed material, greater than that of graphene alone. It has also been reported that the addition of PEDOT:PSS into graphene inks results in a greater packing density of the graphene flakes, resulting in a more conductive network.[218] It is understood that the presence of graphene flakes in a PEODT:PSS film greatly enhances sensitivities towards external stimuli, with reports of up to 60 % higher response for hybrid inks when subject to humidity changes.[219]

Gas-based sensing can also be significantly improved due to the increase in surface area gained by the addition of graphene flakes, promoting interaction between molecules and the printed material. Graphene-PEDOT:PSS hybrid inks have also been formulated using polar solvents, including but not limited to ethanol, DMF and DMSO, and inkjet-printed to form a range of sensing devices with similar functionalities to those previously described for graphene-based devices.[166,220,221]

2D materials have often been combined with MeNPs, yielding performance improvements for both materials. The addition of AgNPs to a graphene dispersion has been shown to result in an increase in electrical conductivity from 51 S/m to 180 S/m (**Figure 2-16 a**).[222] Enhancement of the optical properties of MeNP-based inks has been demonstrated by adding graphene nanoplatelets (**Figure 2-16 b,c**). When added to a zinc oxide dispersion, photoresponsivity to UV light has been shown to increase by a factor of 10. [223]

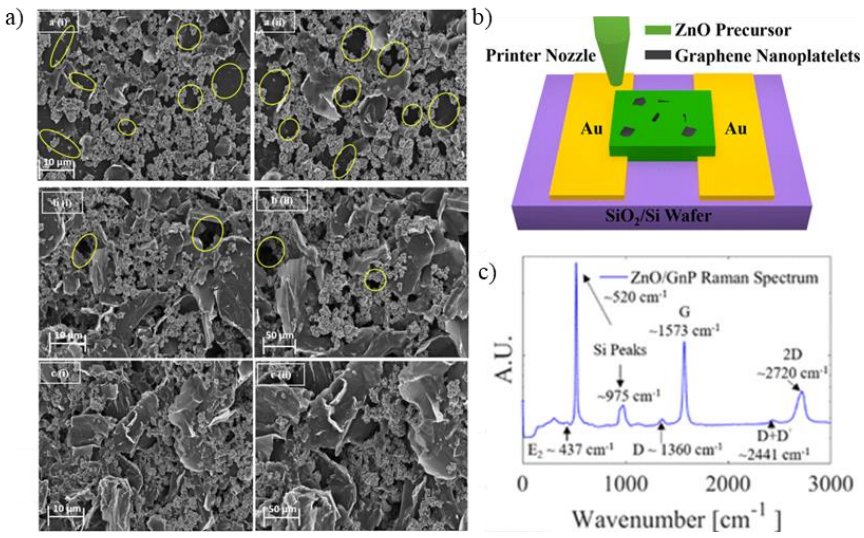


Figure 2-16 a) SEM micrographs of graphene/AgNPs hybrid ink deposited with increasing number of printed layers (top = 1, middle = 5, bottom = 10). Reproduced from Htwe et al.[222] **b)** Schematic for deposition of zinc oxide/graphene nanoplatelet ink. **c)** Raman spectrum of zinc oxide/graphene nanoplatelet film, confirming the presence of graphene. Reproduced from Cook et al.[223]

Non-conductive polymers have been added to inks, providing a range of benefits for the final printed electronics. A polyurethane dispersion was added to a PEDOT:PSS ink for deposition on PDMS, reducing the change in electrical properties when subject to strain and bending.[224] Further material combinations have been demonstrated with this purpose, such as the addition of PVP to AgNPs, which also improved adhesion of functional materials when deposited onto textile substrates.[43] Nitrocellulose has been added to a liquid metal ink for improved device electrical conductivity. During sintering, an exothermic reaction was induced, releasing additional energy into the deposited film and further enhancing the annealing effects, resulting in a electrical conductivity increase of over 60 % compared with the liquid metal ink formulation alone.[225] This has also demonstrated effectiveness in graphene-based inks, where low-power photonic annealing methods have been shown to be comparable to high-temperature thermal processes.[226]

2.4 Inkjet printing

Commercial inkjet printing came to prominence in the 1970s through the form of Continuous Inkjet (CIJ) technology, with its primary function being the deposition of ink onto paper to convey information.[75] The working principle behind CIJ involves a continuous stream of ink that is forced from a nozzle under pressure, before separating into droplets due to either its natural instability or disturbances from an imposed waveform (**Figure 2-17**).[227,228] Charged plates deflect droplets, electrostatically steering them toward the desired position on the substrate, thereby producing the printed pattern, text, or image. Droplets that are not desired for the pattern are directed

to a gutter and recycled for later use.[229] The capability for high jetting frequency (80 - 100 kHz)[230] of CIJ permits fast printing speeds whilst maintaining precision.

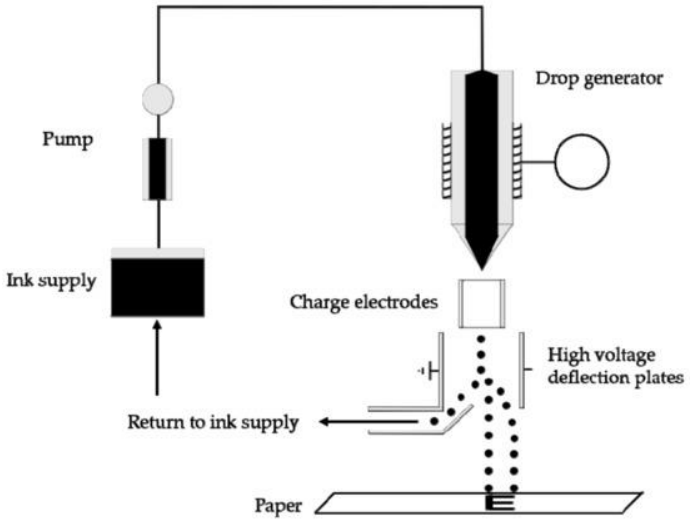


Figure 2-17 Schematic detailing the working principles of CIJ. Reproduced from Ansell.[228]

The next development in jetting technology arrived with the invention of Droplet-On-Demand (DOD) printers. DOD printers do not emit a continuous stream of ink; instead, they produce a droplet only when required, hence the term drop-on-demand.[231] There are several advantages and disadvantages of the two methods, better suited to differing purposes. Firstly, there is a reduced waste output with DOD, due to droplets only being produced with the intention of being deposited,[232] also simplifying equipment requirements by eliminating the need for a gutter and recycling system or conductive inks. The recycling system in CIJ presents a risk for ink contamination through its exposure to the environment during jetting, before being reintroduced to the ink reservoir, a problem that DOD does not face.[229] CIJ operates at a comparatively high jetting frequency, thereby increasing droplet velocity, but this comes at the cost of reduced resolution, whereas DOD produces higher-resolution prints, albeit at a slower speed.

DOD printers utilise a pressure pulse to eject an ink droplet from the nozzle, typically via a heated plate or a piezoelectric material.[233] Thermal DOD uses a heated plate to vaporise the local ink into steam, which expands in volume. This in turn creates a positive pressure, pushing ink through the nozzle (**Figure 2-18 a**). The second key DOD technology uses a piezoelectric element to force ink out through the nozzle, where the element will experience mechanical stress or deformation when a voltage is applied, forcing ink out of the nozzle at the desired moment (**Figure 2-18 b**).

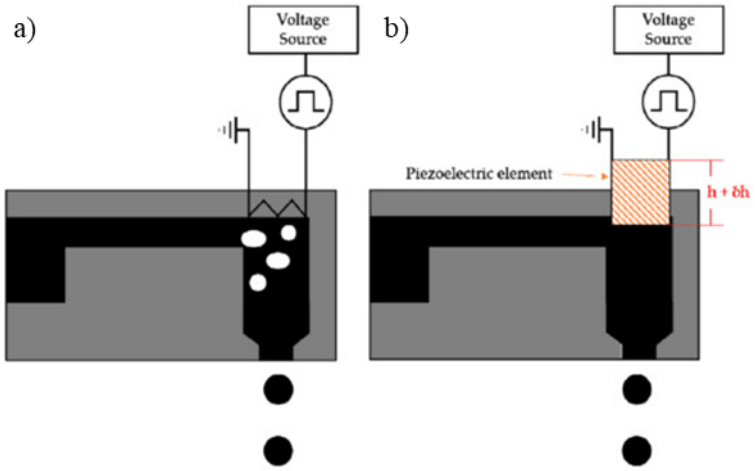


Figure 2-18 Schematic detailing the working principles of **a)** Thermal DOD and **b)** Piezo DOD. Reproduced from Ansell.[228]

The piezo method can provide further benefit to the ejection process through tuning of the applied voltage waveform (**Figure 2-19**), broken into the three stages of droplet production. First, the voltage is reduced, causing the piezo element to retract, drawing ink into the chamber. The next stage sees the voltage pulse, which generates a pressure that ejects ink from the nozzle. Then, the voltage returns to its initial position, which removes the pressure ejecting ink, causing the ink in the nozzle to retreat and preventing any further jetting in this cycle through the formation of a meniscus. A step can be added between stages 2 and 3 to aid in the meniscus production as well as

prevent air being drawn into the nozzle.[234] The voltage magnitude and pulse durations can be tuned to control the droplet formation, velocity, tail, and volume. Thus, making it a key part of the inkjet deposition set up procedure.

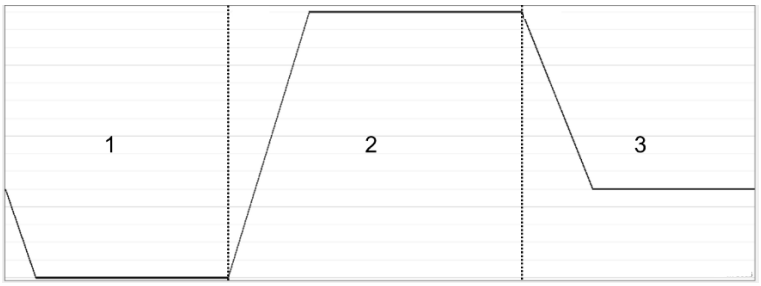


Figure 2-19 Waveform applied to a piezoelectric element in a Dimatix printhead whilst jetting a conductive graphene ink, where segment 1 represents the retraction stage, segment 2 is the voltage pulse, and segment 3 causes the droplet to pinch off.

Once ink is jetted from the nozzle, droplet formation must succeed to ensure accurate print quality. There are several key stages throughout the droplet's production and ejection from the nozzle that are indicative of the resulting print's quality. The ink will be pinched from the nozzle by stage 3 in the piezo waveform (**Figure 2-19**), causing the formation of a droplet head with a tail. At this point, the tail will either coalesce with the droplet or separate into a string of satellite droplets (**Figure 2-20**), due to the Rayleigh-Plateau instability.[75] This is a fluid-dynamics phenomenon in which small disturbances in a liquid jet grow over time, causing it to break down into droplets as surface tension reduces the total surface area. There is a later opportunity for satellites to combine with the droplet head; however, if this does not occur, there is a possibility of loss of resolution in the final print. It is preferable for the tail to immediately join the droplet head, as this shows the best promise for accurate deposition.

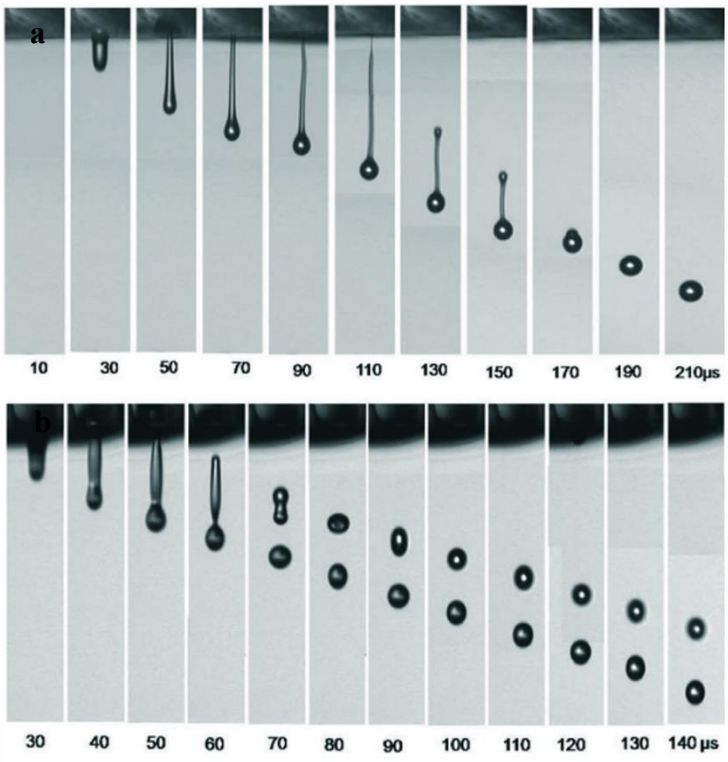


Figure 2-20 High-speed photographic images of droplets ejected from a DOD printhead at consecutive stages of drop formulation. **a)** The tail of the droplet successfully coalesces with the head. **b)** The tail forms a satellite droplet which remains separate. Reproduced from Li et al.[235]

Other important droplet characteristics include its path, size, and velocity. It is important that the droplet travels in a straight line from the nozzle and does not deviate from the course to preserve print accuracy. Droplet diameter should remain small in DOD, to ensure high precision printing is achieved, which is limited by the hardware used. Lastly, the velocity should remain low to prevent 'splashing' occurring when it contacts the substrate. This can be influenced by the jetting frequency, which also determines the speed at which a print will be completed. Whilst higher jetting frequencies increase productivity they can adversely affect droplet formation and thus quality. For high-precision applications, the DOD jetting frequency is currently limited to 40 kHz, with a corresponding reduction in print accuracy above this. Recent work

has investigated the optimisation of the voltage waveform, which may mitigate the issues encountered when jetting at higher frequencies.[74]

These factors can be controlled in several ways: by modifying the ink composition, tuning the voltage waveform sent to the piezoelectric element and optimising the jetting frequency. The velocity and drop diameter are key variables for the dimensionless parameters that can be used to give an indication of an ink's printability, the Weber number (WE), Reynolds number (Re) and Ohnesorge number (Oh). These are related as shown by **Equation (2-2)** below.

$$Oh = \frac{We}{\sqrt{Re}} = \frac{viscous\ forces}{intertia \times surface\ tention} \qquad \textbf{(2-2)}$$

The Ohnesorge number and Reynolds number can be related in such a way that allows for the determination of an ink's printability (**Figure 2-21**).

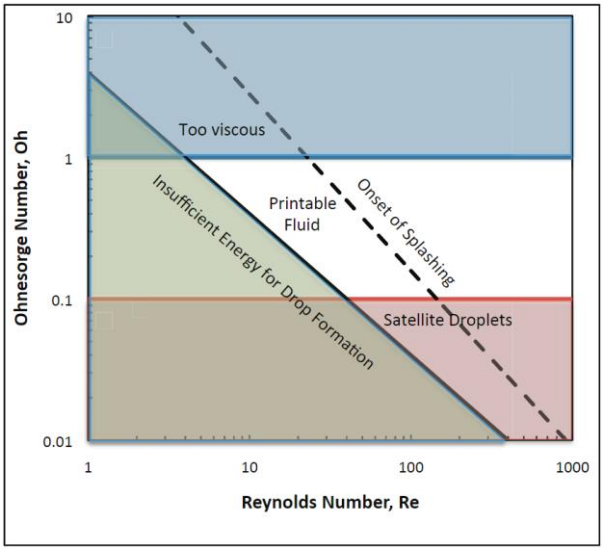


Figure 2-21 A schematic diagram illustrating the operation regime for inks to be used in DOD inkjet printing. Reproduced from McKinley and Renardy[236]

Lastly, the inverse of the Ohnesorge number can be taken, commonly referred to as the Z number (**Equation (2-3)**). This is commonly used to predict the jetting

performance for inks used in DOD inkjet printing. Z is normally required to be in the range of $1 < Z < 14$ to facilitate proper droplet formation.[237]

$$Z = \frac{1}{Oh} \quad \textbf{(2-3)}$$

Once deposited on the substrate, several critical factors can still influence printing performance. The droplet's impact velocity can affect the extent of spreading upon contact with the substrate. This spreading should be kept to a minimum to preserve the print accuracy. A study by Hoath et al[231] further explored this interaction, and identified the role of kinetic energy, a function of velocity, in droplet spreading mechanics. Thus, by reducing impact velocity, spreading could be kept to a minimum by following the laws of conservation of energy and momentum. One key finding in this study was the effect of viscosity on spreading, with higher-viscosity inks exhibiting lower spreading. This is due to the higher shear force encountered between the droplet and the substrate. The droplet's adhesion to the substrate is key to print accuracy, which is governed by the wetting behaviour. The substrate surface energy and the droplet surface tension regulate the wetting regime and the degree of spreading.[238]

The wetting behaviour of a droplet can be largely understood through measurement of its contact angle, which is a function of surface interfacial energies, or surface tension, γ (**Figure 2-22**). The contact angle is a result of three interfaces, solid-liquid (SL), solid-vapour (SV) and liquid-vapour (LV). They can be related in such a way that allows for the calculation of the contact angle θ_c (Equation **(2-4)**).

$$\cos(\theta) = \frac{\gamma_{SV} - \gamma_{SL}}{\gamma_{LV}} \quad \textbf{(2-4)}$$

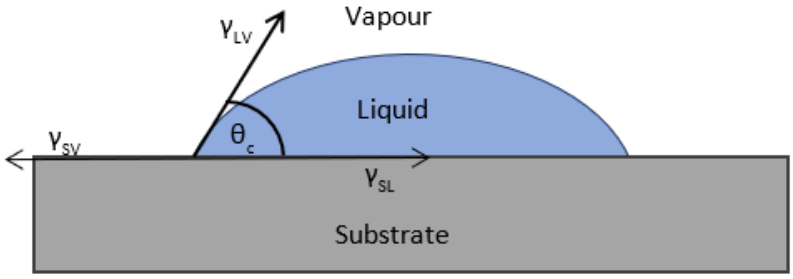


Figure 2-22 Representation of a liquid droplet with contact angle on the three-phase contact line.

The inclusion of lowD materials such as gold and silver nanoparticles, CNTs and graphene flakes into colloidal dispersion inks facilitates the printing of conductive pathways onto the selected substrate.[239,240] Dispersions of 2D materials have a tendency to agglomerate and the stability can be predicted using the Derjaguin-Landau-Verwey-Overbeek (DVLO) theory which can estimate the particle aggregation.[241] The primary forces concerned with the stability of the ink are the Van der Waals attractive and electrostatic repulsive, which are combined within the DVLO theory. Gravitational sedimentation can also pose a risk to ink stability, especially if the ink is stored for an extended period of time after formulation, as exhibited by **Figure 2-23**.

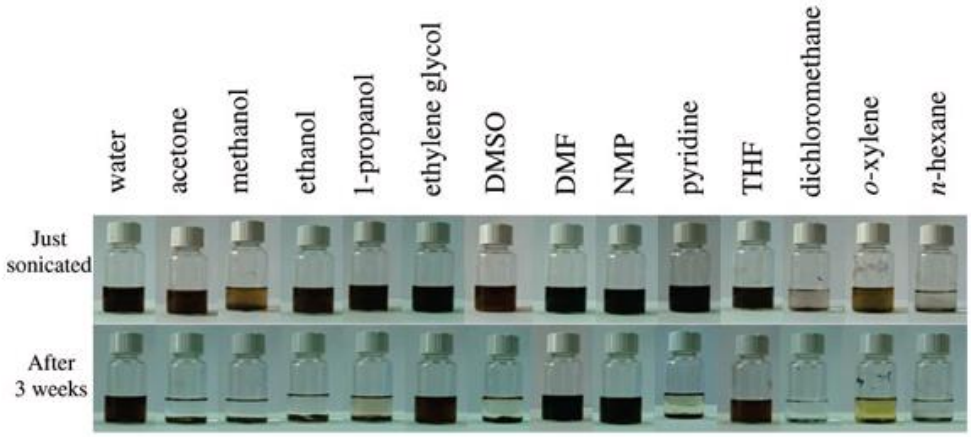


Figure 2-23 Graphene oxide inks prepared with water and a range of solvents shown immediately after sonification and 3 weeks after sonification. Reproduced from Parades et al.[176]

Additives can be used to further improve ink stability; for instance EC is commonly featured in graphene-based inks, preventing agglomeration.[160] The choice of solvent is also critical, as some materials disperse preferentially in specific solvents – for example, Graphene oxide readily disperses in solvents due to its abundant oxygen-containing functional groups, which increase its hydrophilicity and facilitate interactions with water molecules. Furthermore, the rheological properties of the solvent will significantly affect the printability of an ink, influencing viscosity, surface tension, and evaporation rate.[77,242,243]

Once the droplet has been deposited onto the substrate, the solvent evaporates, with the functional material remaining. Print defects can occur at this point through a phenomenon known as the coffee ring effect. The coffee ring effect occurs during the droplet drying process due to the solvent evaporation, resulting in an uneven particle distribution with a higher concentration towards the edge of the circle. When the solvent evaporates, an internal flow is driven radially outward towards the contact line of the droplet, causing transport of the suspended particles in the same direction.[75] This flow rate is governed by the solvent's rate of evaporation and evaporation temperature, which determines the ultimate thickness of the ring. The dark lines towards the edges of each printed shape show the increased particle density in these locations (**Figure 2-24**).

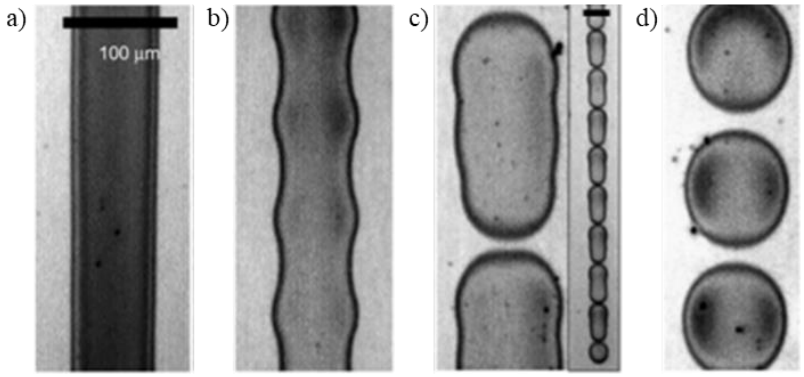


Figure 2-24 Jetted PEDOT:PSS ink exhibiting the coffee ring effect in **a)** a straight line 50 µm drop spacing; **b)** a straight line with 75 µm drop spacing; **c)** pairs of drop spacing 84 µm; **d)** isolated drops with spacing 100 µm drop spacing. Reproduced from Soltman and Subramanian.[244]

2.5 Post-processing methods for printed functional materials

Many graphene-based and MeNP inks require a post-processing stage to achieve the desired electrical conductivity, with specific requirements dependent on ink formulation and functional material. Currently, a range of methods are present in the literature, including thermal and photonic techniques. When selecting a post-processing method, it is important to consider substrate properties to ensure that the chosen method does not degrade the substrate and is effective for the intended purpose.

2.5.1 Thermal post-processing

The most widely used technique is thermal annealing/sintering, with good reliability and accessibility.[17,245] The as-printed material will likely have very high electrical resistance and thus requires a sintering process to improve electrical conductivity. Graphene ink often include polymeric additives, such as EC, to enhance ink stability and prevent agglomeration, necessitating post-processing to achieve high electrical conductivity by degradation of these additives. Conventional methods for post-

processing of graphene inks require thermal annealing at high temperatures (T_{anneal} = 250 °C).[150]

Thermal sintering, a common process for MeNPs-based inks, involves surface ligand desorption and particle fusion at temperatures much lower than the bulk sintering point ($T_{sintering}$), due to the significant decrease in $T_{sintering}$ with sub-micron particle sizes. Thermally sintered MeNP printed patterns can achieve electrical conductivities of 10^6 to 10^7 S m^{-1} at a sintering temperature between 130 to 300 °C for 30–60 minutes.[17,246] Although thermal sintering is effective and widely adopted, it can deform flexible, heat-sensitive polymer substrates with low glass transition temperatures (T_{glass}), causing cracks and delamination in printed material. The temperatures required for these thermal processes are often high with respect to the thermal properties of polymeric materials, often desired for substrate choice, thus limiting material selection via these methods.

Table 2-2 presents a summary of commonly inkjet-printed conductive materials and their corresponding thermal post-processing temperatures.

Table 2-2 Thermal processing requirements for different inkjet-printed materials.

Ink	Required Temperature	Reference
Graphene flakes	200 - 350 °C	[247]
AgNPs	150 - 240 °C	[248]
AuNPs	200 °C	[249]
PEDOT:PSS	120 °C	[250]

2.5.2 Alternative post-processing methods

Flexibility and stretchability are highly desirable substrate properties for healthcare devices, enabling function on nonlinear, nonstationary surfaces; however, such materials often lack sufficient thermal resistance for thermal annealing, such as PEN (T_{glass} = 120 °C). Notable efforts have been observed in recent years towards the development of alternative techniques aimed at preserving substrate functionality at lower temperatures. Such processes include low-temperature plasma, Ohmic sintering, and microwave heating; however, these are less widely used, owing to increased costs, limited success, high power requirements, and scalability issues (**Table 2-3**).

Table 2-3 Alternative post-processing methods and their working principles.

Process	Material	*T* (°C)	Working principles	Limitations
Low-temperature plasma reduction[251]	GO	138	Plasma treatment in an Argon environment (99.9999% purity)	Vacuum system is expensive regarding assembly and maintenance, as well as limitations in terms of batch size
Dry hydrogen plasma reduction[252]	GO	- 93	Removal of oxygen using Hydrogen plasma treatment	
Ohmic sintering[253,254]	AgNPs	200	Exposure to electrical current to heat conductive track and local substrate only	Only effective on structures > 100 µm, smaller structures fail due to induced thermal stresses.
Microwave heating[255]	AgNPs	N/A	Maxwell-Wagner polarization of NPs interacting with microwave radiation resulting in coupling	Low electrical conductivity of printed material vs bulk when compared with alternate methods
Room temperature sintering ink[256]	Graphene nanoplatelets (GNPs)	-	Ink composition using Oleic modified graphene	Additional complexity required in ink formulation

2.5.3 Photonic post-processing methods

One particular group of processes that demonstrates significant promise and application is photonic annealing, which includes the use of IPL, laser sintering and UV exposure.[257]

IPL presents an effective, low-temperature alternative using intense pulsed light.[258] A Xenon flash lamp delivers a short pulse of high-energy light to the printed material, causing localised heating and providing the desired annealing effects, without causing substrate degradation (**Figure 2-25 a, b, c**).[259] IPL also reduces process duration, enabling annealing in milliseconds ($t_{flash} < 1$ s),[260] with compatibility for in situ printing/annealing supporting high-throughput manufacturing. Excessive pulse energy in IPL treatment can cause defects, including morphological variations, cracks, delamination, inhomogeneous shrinkage in the printed film, and substrate damage.[261–264] To mitigate these issues, pulsed sintering parameters such as energy, pulse duration, peak power, and number of pulses must be carefully controlled and optimised for different inks and substrates to ensure uniform sintering.[265] It has been deduced that certain substrates are not suitable for IPL due to the materials' high thermal conductivity, which results in a rapid dissipation of heat away from the printed material and incomplete annealing.[259] Photonic annealing can produce unique, high-surface-area morphologies on iGr films, increasing porosity via rapid solvent evaporation and thus improving device sensitivity.[257]

IPL annealing has been shown to produce graphene samples with electrical properties comparable with those achieved by thermal annealing,[225,257,261,262,266–270] with pulse energy (3 - 10 J.cm^{-2}) achieving sheet resistance $R_S = 200\ \Omega$/sq. (**Figure 2-25 d**).[23,271,272] Polymeric additives, such as EC, also offer enhanced print electrical

conductivity where, after photonic decomposition, they are thought to improve the connection of the graphene flake network.[160] Exothermic binders have been used, resulting in high energy release during photonic annealing and high electrical conductivity (> 10^4 S/cm).[226]

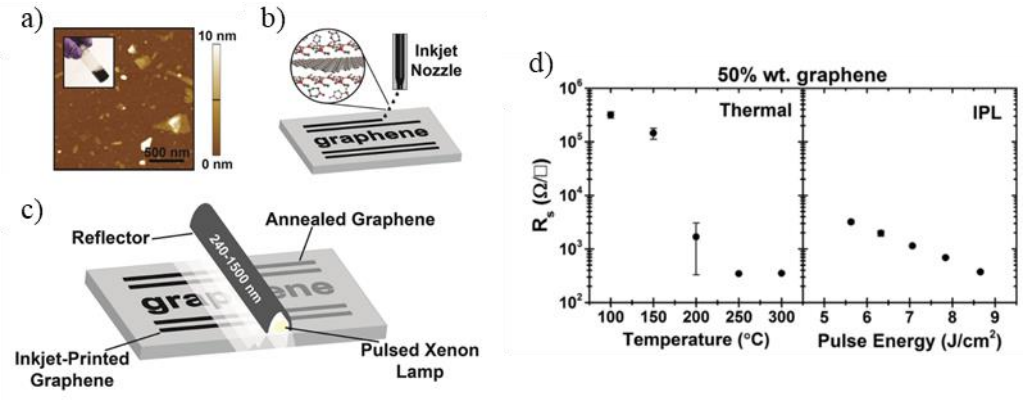


Figure 2-25 Inkjet printing and IPL annealing of graphene **a)** Atomic force microscopy image of graphene flakes (Inset: image of graphene ink vial). b) Schematic illustration of inkjet printing of graphene. c) Schematic illustration of IPL annealing applied to graphene patterns. Reproduced from Secor et al.[23]

Light-based sintering techniques have proved effective on a range of MeNPs, including the use of IPL, selective laser sintering (SLS), NIR and UV irradiation. Broad range IPL treatment is an effective method for sintering copper nanoparticles (CuNP), achieving electrical conductivity of 20 % of bulk copper with a pulse energy of 6.5 J/cm^2.[266] CuNPs were synthesised with a cuprous oxide shell, which, when subject to IPL, are reduced to copper and aid in forming connections between larger particles. This method was shown to exhibit high electrical conductivity (1.43 × 10^6 S/m, 25 % of bulk), obtained with a power density of 3.08 J/cm^2.[273] It should be noted that although the power density in this case was low, successive flashes were required (n_f > 5), with a relatively long duration of exposure (t_f = 2 s). IPL has been further demonstrated on AgNP inks, where a pulse energy of 10 J/cm^2 induced high

temperatures within the printed film (448 K), but the polymer substrate remained at room temperature, and produced printed silver patters with high electrical conductivity (1.31×10^7 S/m).[274]

Alternative, narrowband photonic methods have also been successfully demonstrated for the sintering of MeNPs. Laser sintering (808 nm) has been demonstrated to be highly effective on copper films, with one study achieving electrical conductivity 25 % of the bulk value.[275] However, this required a significantly higher energy density of 64.9 J/cm^2. Near infrared (NIR) (1100 nm) sintering has been applied to AgNPs, in a highly scalable roll-to-roll printing system, enabling manufacturing of metal patters with low sheet resistance (0.288 Ω/sq.).[262] However this process requires relatively long exposure times (~ 10.8 s) and can induce substrate heating, thereby potentially limited its use for printing onto polymer substrates with low T_{glass}, such as PEN.

UV photonic post-processing (300 - 700 nm) has been demonstrated on nickel NPs with silver shell structures, using low-power (2.90 mW/cm^2) and achieving electrical conductivity ~ 30 % of bulk nickel (**Figure 2-26**).[276] However, this study would imply that there are significant heating effects incurred, as a cooling strategy was implemented to preserve substrate integrity during a long exposure time of 90 minutes.

An AgNP ink was inkjet-printed upon polyethylene terephthalate, and irradiated with UV light (365 nm), obtaining a low electrical resistivity of 5.44×10^{-6} Ω/cm (~1/3 bulk silver).[277] This study utilised a high-power UV-LED (300 mW/cm^2) with a long exposure duration of 50 minutes, resulting in a relatively high power density required to achieve the observed electrical conductivity. It appears that the application of UV sintering to MeNPs faces two challenges: long exposure times result in high power densities, whilst NP synthesis and structure requirements can become more complex.

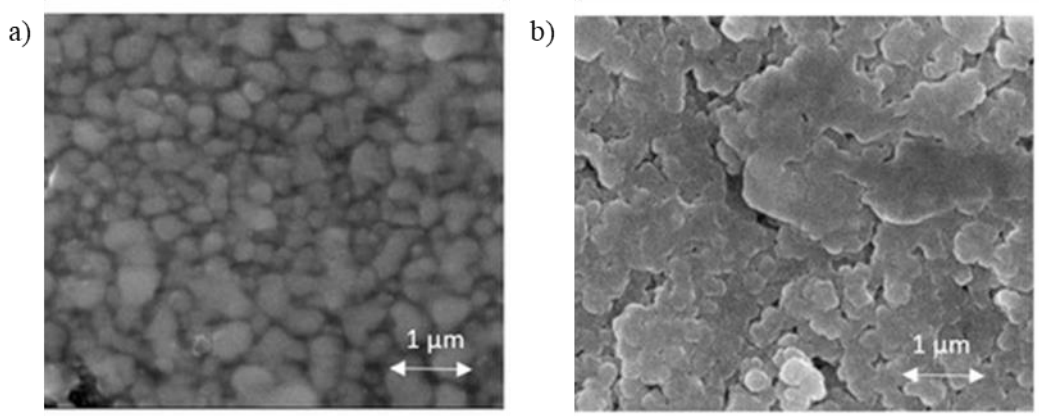


Figure 2-26 SEM images of silver coated nickel nanoparticles **a)** before and **b)** after UV irradiation. Reproduced from Pajor-Świerzy et al.[276]

UV exposure has also shown to enhance the electrical conductivity of non-metallic functional materials. GO possesses significant absorbance at the start of the UV region (~ 250 nm), which decreases with wavelength,[182,278,279] and can be reduced through UV irradiation within 5 minutes.[181] Conventional methods for reducing GO are chemical and thermal. Chemical reduction can vary in quality, with residues left from the process,[280,281] whilst thermal reduction requires high temperatures (> 500 °C) and can be time consuming.[282] As such, UV treatment has demonstrated reduction of GO to produce electrically conductive films, with a sheet resistance of ~10^2 kΩ/sq.[283]

The electrical properties of PEDOT:PSS can be enhanced by the application of UV irradiation.[24] It has been found to cause a reduction in sheet resistance from 2.5 to 1.5 kΩ/sq. when irradiated for 10 minutes, which then increases again for t_{UV} > 10 minutes.[284] It has been suggested that UV irradiation will increase the grain size (**Figure 2-27**), reducing porosity of the film and improving electrical conductivity.

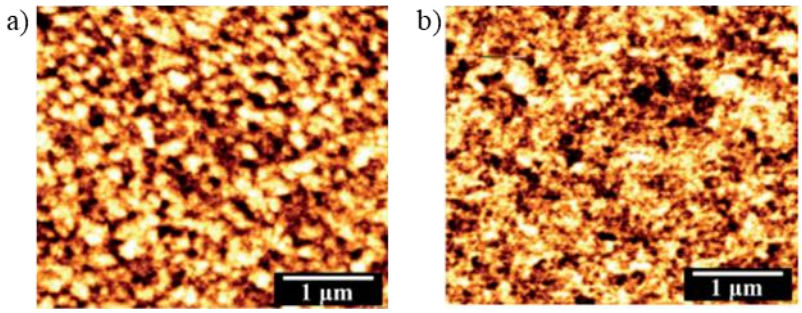


Figure 2-27 AFM images of PEDOT:PSS surfaces irradiated by UV lights under **a)** 0 and **b)** 60 min. Reproduced from Tang et al.[285]

2.6 Inkjet-printed sensor devices

Inkjet printing is an attractive technology for sensor manufacturing due to the excellent device properties it enables, such as low power consumption, low cost, and small footprint, which are made possible through the use of low-dimensional materials.[286]

There are many approaches to sensor patterning, with prominent choices including the serpentine, meander and interdigitated electrode (IDE) patterns (**Figure 2-28**). The high surface area provided by the serpentine-like patterns increases device sensitivity through the improved probability of material-parameter interactions occurring. Moreover, this pattern improves device performance under bending and stretching by reducing the risk of microcracks that impair functionality.[287] Huang et al demonstrated a GO serpentine electrode (**Figure 2-28 a**) with electrical properties remaining unchanged after being subject to 100 bending cycles of 75°.[288]

IDEs are formed of two closely spaced, interlaced, comb-like structures (**Figure 2-28 b, c**). These electrodes can detect stimuli via changes in current/resistance as well as changes in capacitance. Concerning the former, whilst there is no electrical contact between the two sides, devices have been produced with silver or gold electrodes and a conductive film that covers both electrodes, often graphene, GO, or CNTs.[289] Thus,

electrical changes in the overlapping film will alter the device's overall resistance. IDEs also have the ability to form a capacitive field between the electrodes, where disturbances by stimuli can be used to provide sensing measurements. These are common for the detection of humidity, chemicals, gases and touch.[290–292]

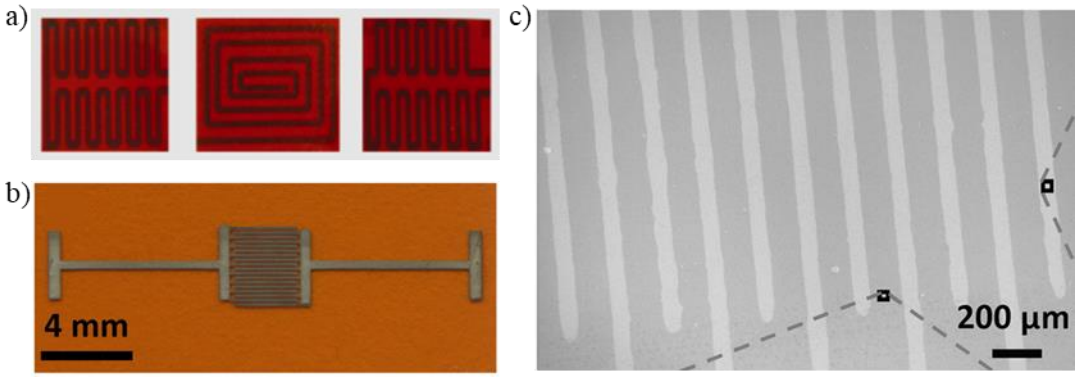


Figure 2-28 a) Patterns for flexible electronics formed of inkjet-printed GO on PET. Reproduced from Huang et al.[288] **a)** Optical and **b)** SEM images of inkjet-printed AgNP IDE on Kapton film. Reproduced from Fang et al.[289]

Achieving sensor selectivity is a significant challenge within inkjet-printed devices. For example, graphene, as previously discussed, exhibits high sensitivity to multiple stimuli, making it difficult to distinguish the desired response. There are various strategies to combat this, including device architecture, capping with selective membranes, microfluidic channels, and enzyme immobilisation, all of which permit selective sensing.[161,293,294]

2.6.1 Environmental sensing

Stimuli of interest regarding environmental sensing include temperature, humidity, pressure and strain. The high thermal sensitivities of graphene, GO, and PEDOT:PSS enable detection of local temperature changes, making them suitable for sensing devices. [162,185,295] For instance, a temperature sensor produced by Vuorinen et al was

formed of a graphene/PEDOT:PSS meander atop silver flake electrodes (**Figure 2-29 a**).[221] The silver electrodes were screen-printed onto a polyurethane film, and subsequently, the graphene/PEDOT:PSS layer was inkjet-printed. The device exhibited a high temperature sensitivity of 0.06 %/°C. Liew et al inkjet-printed a hybrid GO/AgNP ink onto PET (**Figure 2-29 b**).[45] Over a temperature range of 25 - 100 °C, the device exhibited an exceptionally high sensitivity of 0.14 %/°C. This high sensitivity could be explained by the large number of defects present in the GO flakes, which produce strong temperature-dependent transport between them.[296] Being printed onto PET permits flexibility of the device, and as such, was subject to bend testing with a radius of 20 mm, where a very small change in device resistance was observed (< 0.5 %).

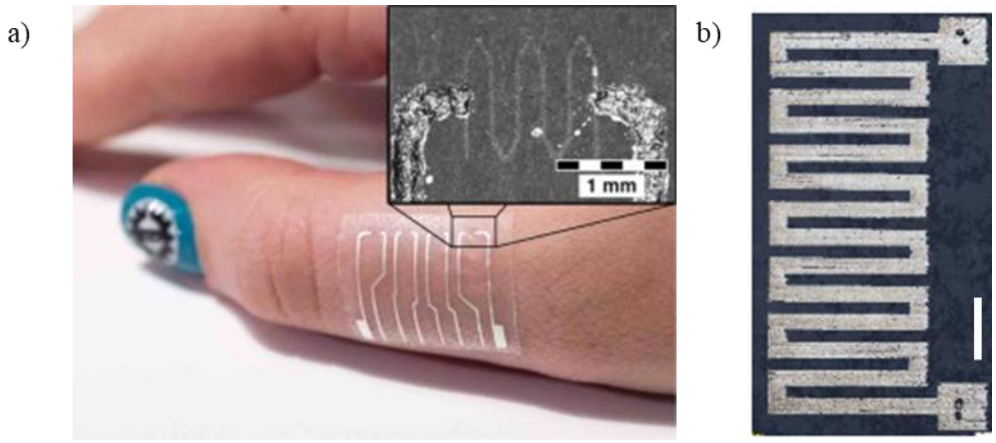


Figure 2-29 a) Optical image of inkjet-printed graphene/silver temperature sensor. Reproduced from Vuorinen et al.[221] **b)** Microscopic image of inkjet-printed rGO/AgNP temperature sensor (Scale bar = 2 mm). Reproduced from Lee et al.[45]

A humidity sensor produced by Lim et al. was fabricated as an inkjet-printed graphene IDE deposited on a paper-based flexible substrate.[297] The device, placed inside a tube, would monitor disruptions to the capacitive field generated by the graphene IDE due to local changes in humidity when a student volunteer would blow into the tube.

Sensitivity was observed across the region of 1 - 70 % *RH*, with application towards real-time breath monitoring studied on three modes of breathing (normal, deep and coughing), where a significant difference in the capacitance was observed for each (**Figure 2-30 a**). A similar device was produced by Lu et al, whereby an inkjet-printed graphene film sat atop a silver IDE, and resistance change in the film due to humidity change from breathing was detected (**Figure 2-30 b**).[298]

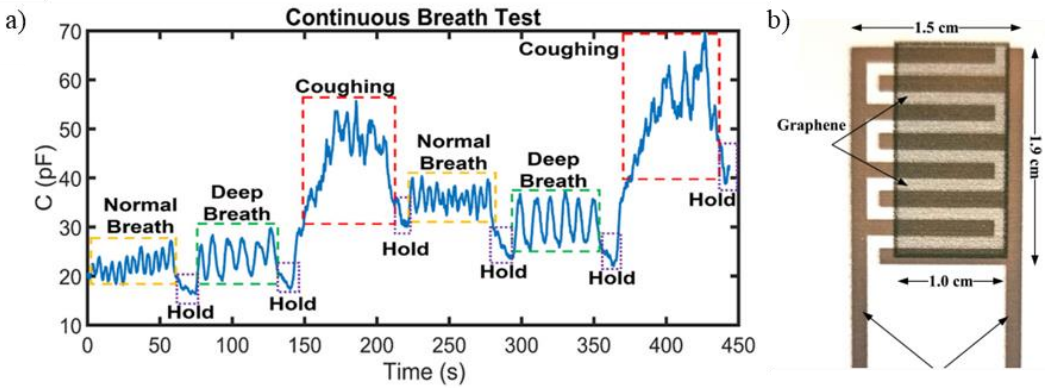


Figure 2-30 a) Continuous breath monitoring of graphene IDE for normal breathing, deep breathing and coughing. Reproduced from Lim et al.[297] **b)** Inkjet-printed AgNP IDE with graphene film utilised for humidity sensing. Reproduced from Lu et al.[298]

Pressure is another environmental stimulus of interest, with multiple viable mechanisms for detection. A sensor was developed using inkjet-printed AgNPs on PDMS, encapsulated with acrylic foam tape.[299] Application of pressure would cause microcracks in the printed AgNP pattern, resulting in a change in resistance, thus, the longevity of such a device is questionable if undergoing repeated degradation. Application towards wearable devices was shown in the form of accurate pulse rate detection when placed on the wrist (**Figure 2-31 a**).

An approach by Sun et al. demonstrated the fabrication of a graphene-based flexible bend sensor using a novel pre-deposition method.[164] The sensor was formed from a graphene IDE inkjet-printed onto a PET substrate. Prior to printing, the PET was

covered in a layer of ethanol, which acted to pin the graphene ink droplets upon deposition, whilst also reducing the risk of the coffee ring effect. When graphene ink contacts ethanol, solvents within the ink infiltrate the fixing layer, allowing the graphene sheets to compact and form a film. The work presented printing with and without this method, demonstrating enhanced resolution from the pre-deposition strategy. The device demonstrated a clear response to an increasing degree of bending when attached to a human finger and bent (**Figure 2-31 b**).

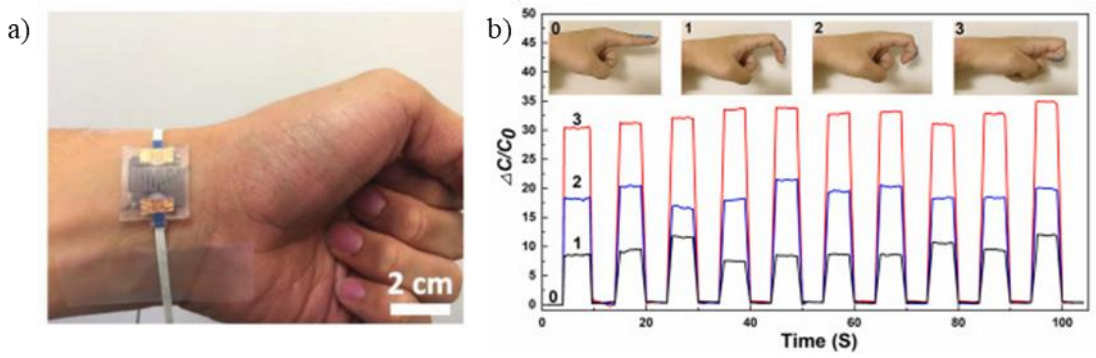


Figure 2-31 a) Optical image of inkjet-printed AgNP-PDMS pressure sensor. Reproduced from Lo et al.[299] **b)** Relative changes of capacity from inkjet-printed graphene IDE subject to increasing degrees of bending. Reproduced from Sun et al.[164]

2.6.2 Chemical sensing

Inkjet-printed sensors have seen extensive development for the detection of chemical species, particularly gases and volatile organic compounds (VOCs). Chemical sensing is of significant interest for healthcare monitoring, as variations in local chemical composition can indicate a range of conditions. One non-invasive diagnostic option is breath analysis, in which chemicals such as acetone, ammonia, and CO_2 correlate with metabolic disorders, kidney function, and respiratory function. As such, recent studies have demonstrated inkjet-printed gas sensors capable of detecting clinically relevant analytes with high sensitivity and integration for flexible, wearable devices.

High levels of CO_2 are clinically relevant in both the breath and wound exudate, where it can be indicative of respiratory issues, where the body is not expelling enough CO_2; in wounds, high levels of CO_2 are actually indicative of regeneration, a positive diagnostic. Graphene is sensitive to CO_2 due to its large surface area, which make its electrical properties highly susceptible to gas molecule absorption; inkjet-printed graphene has demonstrated responsivity to CO_2 of 45 μΩ/ppm, with a limit of detection of 100 ppm (**Figure 2-32 a**).[3] Whilst this sensitivity appears low, it is more than adequate for detecting exhaled breath concentrations exceeding 25,000 ppm, which is high relative to atmospheric conditions (400 ppm).[300]

Acetone is another analyte of significant interest in breath monitoring, with a normal concentration is 0.8 - 2.0 ppm.[301] Whereas high levels (75 - 1250 ppm) are associated with diabetic ketoacidosis,[302] a life-threatening complication caused by a severe lack of insulin. Wu et al. inkjet-printed a graphene/zinc-oxide device, which was capable of acetone detection for a clinically relevant range of 1 - 4 ppm and sensitivity of 5.54 %/ppm (**Figure 2-32 b**).[303] It should be noted that the device also presented sensitivity towards ammonia, posing risk for false positives. Acetone is also relevant to wounds, where it has been detected in the exudate of a range of bacteria known to cause infections.[304]

Current methods for ammonia (NH_3) detection use metal oxide or polymer-based gas sensors, these are costly, possess slow desorption characteristics and require high operating temperatures. Graphene offers an alternative approach, with inkjet printing proving to be cost-effective for manufacture, as well as presenting high sensitivity and long-term stability. Inkjet-printed graphene devices have been shown to provide a response down to 10 ppm NH_3, with a relatively fast response time (~ 100 s) (**Figure 2-32 c**).[165] However, the recovery time of the presented device is considerably slower,

requiring approximately 30 minutes to return to the original resistance. However, whilst the operating temperatures used in this study exceed those suitable for wearable healthcare devices, it still demonstrates the applicability of printed graphene for gas sensing, and further work should be conducted to investigate room-temperature functionality.

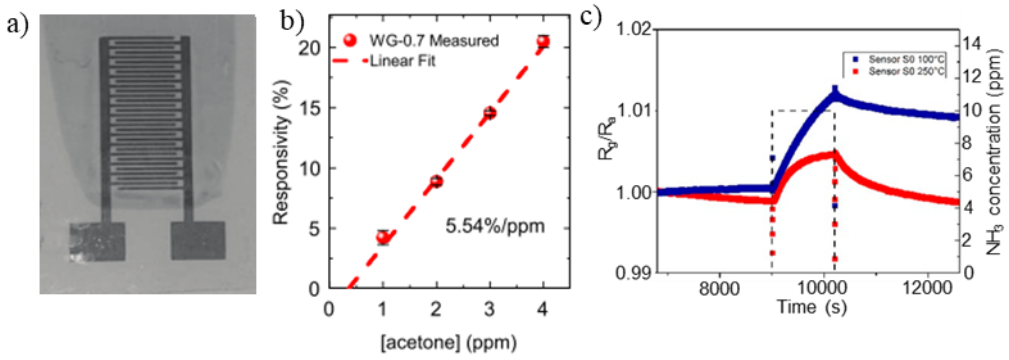


Figure 2-32 a) Inkjet-printed graphene CO_2 sensor. Reproduced from Andò et al.[3] **b)** Responsivity as a function of acetone concentration for an inkjet-printed graphene-zinc oxide device. Reproduced from Wu et al.[303] **c)** Temporal response of inkjet-printed graphene film to ammonia (10 ppm) at different temperatures. Reproduced from Travan et al.[165]

2.6.3 Biological biomarkers

Beyond sensing physical and chemical stimuli, inkjet-printed devices have been increasingly developed to detect biological analytes within epidermal fluids, such as sweat and wound exudate. Sweat-based sensors are currently more focused on a sports setting, where on-demand feedback can monitor and improve athlete performance,[305] whilst wound exudate offers high value to inform clinical decisions regarding wound care.[306] Both media contain a number of interesting analytes reflecting the condition of the human body, these include lactate, electrolytes, metabolites and inflammatory markers, offering an opportunity for non-invasive health monitoring.

Lactate has been an analyte of interest for inkjet-printed devices, where the enzymatic oxidation of lactate releases an electron, and provides the mechanism for detection for inkjet-printed sensors (**Equation (2-5)**, **Equation (2-6)**).[307,308]

$$Lactate + O_2 \xrightarrow{LO_x} pyruvate + H_2O_2 \quad \textbf{(2-5)}$$

$$H_2O_2 \rightarrow O_2 + 2H^+ + 2e^- \quad \textbf{(2-6)}$$

Payne et al demonstrated a strategy for lactate sensing using inkjet-printed, 3-electrode devices. containing: a working electrode (WE), reference electrode (RE) and counter electrode (CE).[309] The WE was formed of inkjet-printed AuNPs, with a CNT dispersion and lactate oxidase (LO_x) sequentially deposited on top (**Figure 2-33 a, b**). When a voltage was applied across the WE and RE, the oxidation of lactate occurs, initiating the reaction presented previously (**Equation (2-5)**, **Equation (2-6)**), and as such produces an electron altering the current characteristics of the devices. A linear response was exhibited up to 24 mM lactate, with a sensitivity of ~ 3 μA/mM. A non-enzymatic method for lactate detection was demonstrated using a two-electrode device; a nickel oxide (NiOx)/nafion WE and Ag/AgCl RE.[310] All materials were inkjet-printed onto Kapton film, providing a highly flexible composite device. Performance was investigated at low (< 0.3 mM) and medium (0.5 - 4 mM) concentrations of lactate, exhibiting a different linear response for each region (**Figure 2-33 c**).

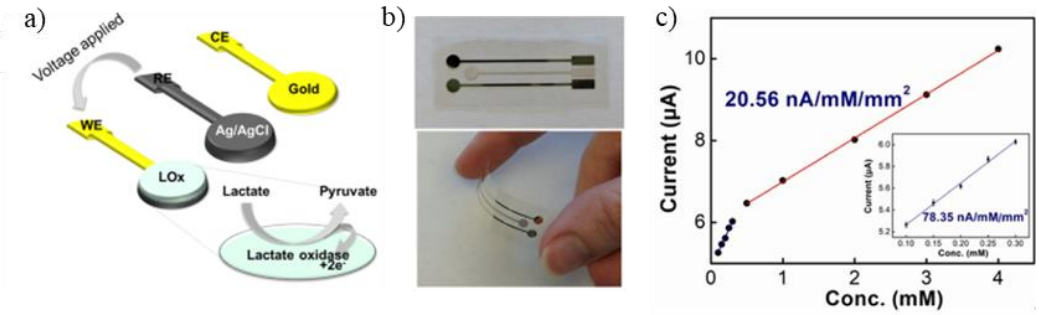


Figure 2-33 a) A schematic of a 3-electrode lactate sensor indicating chemical reactions occurring on the WE **b)** optical images of printed gold and Ag/AgCl electrodes prior to deposition of working electrode layers, with electrodes of 3 mm diameter, pictured straight and flexed. Reproduced from Payne et al.[309] **c)** Potentiostatic analysis of the inkjet-printed NiOx/nafion composite electrode when subject to increasing concentrations of lactate. Reproduced from Tsou et al.[310]

The concentration of electrolytes, or salt ions, within sweat can be indicative of multiple health conditions – for example, for an athlete, low potassium can be a precursor to reduced performance, whilst high levels might be signalling the onset of severe medical conditions such as kidney failure. He et al. developed an ion-selective electrode based on inkjet-printed graphene.[311] After fabrication of the highly conductive printed graphene (172.7 Ω/sq.), a poly(vinyl chloride) (PVC) membrane and potassium-selective ionophore were deposited, providing ionic selectivity (**Figure 2-34 a**). The electrode displayed a wide response range to potassium ions (0.001 – 100 mM), with a very low limit of detection (7 µM). Performance was examined towards a more complex situation, testing sweat containing a wide range of ions; NaCl, Na_2SO_4, $NaHCO_3$, KCl, $MgCl_2$, NaH_2PO_4, $CaCO_3$, and NH_4Cl at physiological concentrations. The device demonstrated sustainable selective performance towards potassium under the previously described mixture of ions. Devices have also been developed to not only analyse sweat composition but also measure perspiration rate. Microfluidic channels have been incorporated into an inkjet-printed carbon electrode device (**Figure 2-34 b**)[312] where resistance of the carbon electrode would change

depending on the volume of sweat occupying the channel, thus enabling measurement of sweat rate.

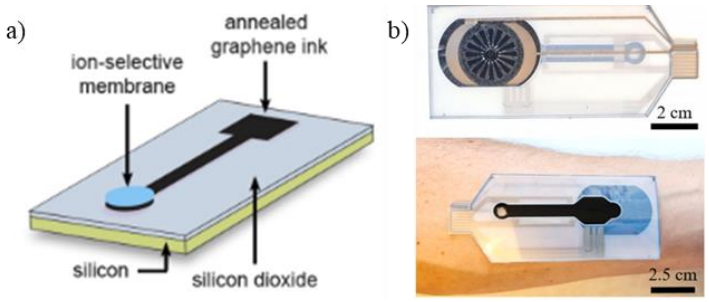


Figure 2-34 a) Schematic of an inkjet-printed graphene electrode with an ion-selective membrane. Reproduced from He et al.[311] **b)** Device design and optical image of in situ placement for carbon-based sweat rate sensor. Reproduced from Yang et al.[312]

2.7 Summary

Inkjet printing presents a low-cost, highly scalable and effective method for the manufacture of electronic devices. It is notable as an efficient way to manufacture LowD materials, such as graphene and MeNPs, with high precision on a wide range of substrates that are ill-suited for conventional manufacturing methods. A broad range of functional materials has been developed for inkjet-printed electronics spanning diverse applications, utilising 0D and 2D materials as well as polymers with electrically conductive and insulating properties.[17]

Inkjet printing of 0D materials is widespread, with commercially available inks for metallic nanoparticles such as AgNPs and AuNPs, enabling fabrication of highly conductive electronics. There is considerable variety among 2D materials, with graphene being a prominent feature in printed electronics since its discovery in 2004.[145] 2D flakes are deposited to form a network with interesting charge transport properties, not only being electrically conductive but also highly sensitive to external

stimuli.[162,313,314] Polymers offer a wide range of applications for printed devices; conductive polymers such as PEDOT:PSS combine low electrical resistance with optical transparency and smooth film morphology, making them well-suited for flexible devices; insulating polymers provide the dielectric component in devices, enabling the fabrication of devices with multiple electronic components. Hybrid inks combine functional materials to enhance the electrical properties of printed films.[218,315]

Formulation of these materials into printable inks requires the consideration of a number of features. Ink rheology (viscosity and surface tension) plays a significant role in droplet formation and ejection, but it is also required for precise control over deposition and high-resolution printed patterns.[229] The addition of solvents, surfactants and additives all influence the stability and printability of an ink, whilst also helping to mitigate the occurrence of material agglomeration and the coffee ring effect.[75]

The inclusion of these components presents the requirement for post-processing in printed inks, which is often performed at high temperatures (> 150 °C).[150,316] This becomes problematic if deposition is required upon flexible substrates, which seldom possess the thermal properties to withstand high temperatures. Recent efforts have been focused on the development of low-temperature sintering and annealing techniques. These primarily employ photonic methods, with IPL and UV exposure demonstrated to yield highly conductive inkjet-printed films from graphene, AgNPs, AuNPs, and PEDOT:PSS.[23,277,317] These low-temperature methods permit deposition onto highly flexible polymeric substrates, such as PET, PEN, and TPU, which are well-suited for wearable devices.

One popular application for inkjet printing of functional materials is the development of sensors for wearable devices, driven by the demand for personalised

healthcare.[318,319] Inkjet-printed sensors have been demonstrated with a wide array of sensing capabilities, including temperature, humidity, pressure, strain, gases, chemicals and biological biomarkers such as lactate and electrolytes.[3,163,166,215,221,299,310] One distinct challenge in the application of printed electronic sensors is achieving selectivity, whereby, when multiple stimuli are present, the received data can be influenced by factors other than the target of interest.[320,321] For chemical and biological analytes, this has been mitigated by incorporating selective membranes or immobilising enzymes on the electrode surface. However, this remains problematic for detecting environmental stimuli, for which such methods are not applicable. Whilst broader applications for printed

Progression towards wearable electronics has included the use of textile substrates, where achieving high electrical conductivity is challenging due to the rough, porous nature of fabrics.[322] This requires the deposition of large amounts of functional materials, for which screen printing is well-suited but entails drawbacks due to its rigid manufacturing process. Inkjet printing on textiles has been achieved through strategies that more precisely control material deposition, as well as through substrate pretreatments.[323] Still, the presence of textile-based sensing devices remains low in the literature.

To summarise, inkjet printing is established as a prominent method for fabricating next-generation flexible electronic devices. It presents strengths in material versatility, both in printable inks and substrate choice, as well as high scalability for commercialisation. However, challenges still remain in achieving devices well-suited for wearable applications, as well as providing selective sensing in dynamic and complex environments, where there are limited devices present.

3 Aims and Objectives

This literature review has outlined the significant potential of inkjet-printed graphene in flexible electronics, whilst also highlighting challenges in achieving simultaneous, multifunctional sensing and deposition onto materials for wearable devices.

The overall aim of this PhD is to establish functional materials and AM processes for the fabrication of flexible, wearable devices for healthcare monitoring applications. To achieve this, the following objectives were set:

1. Develop a multi-material inkjet printing strategy for flexible and textile-based electronics. This includes the reduction of surface roughness and porosity, thereby improving surfaces for the deposition of functional materials (MeNPs, graphene, Nitschke cages) as well as the evaluation of their electrical properties on flexible/stretchable substrates under bending, stretching, and real-use conditions.

2. Establish and optimise low-temperature photonic annealing (IPL/UV) methods for functional materials (MeNPs and graphene-based), enabling deposition onto thermally sensitive polymeric substrates. Provide a comparison of the achieved electrical properties with those obtained by conventional thermal post-processing methods.

3. Develop inkjet printing and device designs (multimaterial and single material) to produce fully printed sensors for simultaneous detection of multiple stimuli, including environmental conditions (temperature, pressure, humidity), gas sensing, strain sensing, chemical species in breath and infection-specific biomarkers for smart healthcare devices.

4 Materials and Experimental Methods

4.1 Printing materials

4.1.1 Inks and substrates

A number of inks were used in this work, some commercially available, whilst others were formulated in-house. Commercial inks include Graphene ink (iGr), Graphene(Gr)/PEDOT:PSS, GO and AgNPs (**Table 4-1**).

Table 4-1 Summary of the commercially available inks used in this work.

Ink	Formulation	Supplier	Product number(s)
iGr	2.4 wt% solid (graphene flakes and ethyl cellulose) suspended in cyclohexanone/terpineol (85:15)	Merck	793663
Graphene (Gr)/PEDOT:PSS	0.1 wt% graphene flakes, 0.02 wt% PEDOT:PSS suspended in dimethylformamide (DMF)	Merck	900442
GO	0.4 wt% GO flakes suspended in deionised water	Merck	777676
AgNPs	30 wt% AgNPs suspended in triethylene glycol monoethyl ether	Advanced Nano Products	DGP-40LT-15C

A range of substrates was used for inkjet deposition, including Prime-grade silicon wafers (200 nm SiO2 thickness, PI-KEM), sapphire substrates Al2O3, 0.8 mm thickness, PI-KEM), and Borosilicate glass microscope slides (1 mm thickness, Fisher Scientific). These substrates were cleaned by sonicating in acetone for 30 minutes at room temperature followed by washing with Isopropyl Alcohol (IPA) and drying with N_2. For printing on flexible substrates, polyimide (Kapton® HN with thickness 250 μm, DUPONT) and PEN (75 μm thickness, GTS Flexible Materials Ltd.) were used

and rinsed with acetone and IPA, then subsequently dried under N_2 prior to material deposition. Stretchable Beyolex (Panasonic Industry) was printed upon as received, after removal of the protective film. A polyester:cotton blend (65:35 respectively) was used as the fabric substrate for textile-based devices.

4.1.2 Cartridges for inkjet printing

A DOD Fujifilm Dimatix DMP-2800 printer (**Figure 4-1 a**) was used for ink deposition. Inks were loaded into cartridges prior to printing using a syringe and needle (**Figure 4-1 b**). The printer featured a cleaning pad, which could be used to run cleaning operations during printing (**Figure 4-1 c**) Two piezo-driven printheads used were compatible with this system, the first being a Fujifilm DMC-11610, featuring 10 pL drop volume and 16 nozzles of 21.5 μm diameter (**Figure 4-1 d,e**). The ideal viscosity and surface tension for the DMC-11610 printheads is 2 - 30 cP and 25 - 50 mN/m. The second printhead used was a Fujifilm Samba cartridge, with a 2.4 pL drop volume and 12 nozzles of 17 μm diameter (**Figure 4-1 f, g**). The required viscosity and surface tension for the Samba printheads is 4 - 8 cP and 28 - 32 mN/m.

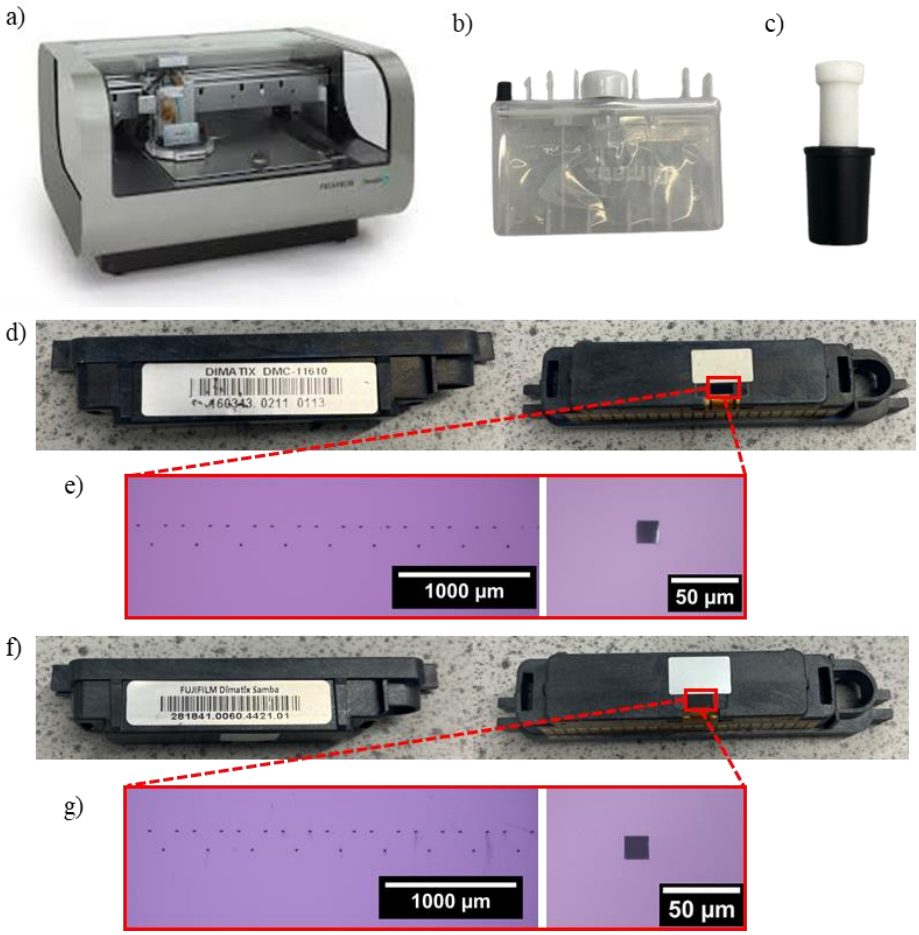


Figure 4-1 Optical images of **a)** Dimatix DMP-2800 inkjet printer, **b)** Dimatix inkjet cartridge, **c)** Dimatix printhead cleaning pad. **d)** Optical and **e)** optical microscope images of Dimatix DMC printhead and nozzles. **f)** Optical and **g)** optical microscope images of Dimatix Samba printhead and nozzles.

4.1.3 Ink formulations and modification for inkjet printing

Inks were formulated to enable the inkjet printing of low-dimensional materials. Some of the purchased inks required modification to promote colloidal stability or to ensure rheological properties were within a printable range for inkjet deposition.

Graphene ink: The as-purchased iGr ink was diluted with a mixture of cyclohexanone and terpineol (85:15 V/V), reducing the solid loading to 1.2 wt%. The mixture was

sonicated in a water bath for 45 minutes to ensure complete mixing and homogenisation.

Gold nanoparticle ink: AuNP inks were formulated with a solid loading of 30 wt% in 2-butoxyethly acetate provided by Dr Jisun Im (University of Warwick). The particles were dispersed in the solvent using a bath sonicator for 20 minutes and stored in the dark at ambient temperature before use. The AuNPs were synthesised by Dr Jisun Im using the Brust method[324] and were functionalised with the UV-cleavable ligand *o*-nitrobenzyl thiol (NT), ligand exchange reaction.

Graphene oxide: The commercially available aqueous GO dispersion (4 mg/mL, product number: 777676, Sigma-Aldrich), composed of GO flakes (0.4 wt%) and deionised water (99.6 wt%), was purchased. IPA (20 wt%) was added to the GO dispersion in order to adjust the surface tension to within a printable range. EC (0.02 wt%) was added to the formulation to aid GO flake dispersion and prevent agglomerations from occurring. The ink formulation was stirred with a magnetic mixer bar for 12 hours to ensure incorporation of the solid EC powder.

Nitschke-cages: Tetrahedral iron (Fe) – ligand (L) Fe_4L_6 N-cages were synthesised by Mr Adam Holt (University of Nottingham). In these cages, four iron ions are located at the vertices of the tetrahedron, whilst 6 ligands span the edges, forming Fe_4L_6 N-cages. The cages were dispersed at 10 wt% in; deionised water (88.5 wt%), IPA (8.84 wt%) and butanol (2.66 wt%). Polyvinylpyrrolidone (PVP) was added at 0.86 mg/mL to aid in particle dispersion.

Tripropylene glycol diacrylate (TPGDA): TPGDA monomer (product number: 246832), 2,4-diethyl-9Hthioxanthen-9-one (DETX, product number: 406368) and ethyl 4-dimethylamino benzoate (EDB, product number: E24905) were purchased

from Merck. TPGDA monomer (92 wt%), DETX (4 wt%) and EDB (4 wt%) were mechanically mixed with a magnetic stirrer bar for 12 hours, ensuring incorporation of all solid material, in the dark.

Summary of ink formulations:

Table 4-2 In-house ink formulations

Ink	Formulation
iGr diluted	1:1 (m/m) iGr ink and cyclohexanone/terpineol (85:15 V/V)
GO	80 wt% GO ink, 20 wt% IPA/EC dispersion (0.1 wt%)
AuNPs	30 wt% AuNPs suspended in 2-butoxyethyl acetate
Nitschke cages	10 wt% Fe_4L_6 Nitschke cages suspended in deionised water (88.5 wt%), IPA (8.84 wt%) and butanol (2.66 wt%)
TPGDA	92 wt% TPGDA monomer, 4 wt% 2,4-diethyl-9Hthioxanthen-9-one, 4 wt% ethyl 4-dimethylamino benzoate

4.2 Ink characterisation techniques

A series of complementary analytical techniques and measurements was performed on formulated inks to ensure compliance with inkjet-printing requirements. These included measurement of viscosity, surface tension, contact angle and density, relevant for the printability of an ink. Whilst thermogravimetric analysis (TGA) was used to determine the solid content of the inks.

4.2.1 Viscosity measurements

Viscosity is a physical property which quantifies the resistance of a liquid to deformation when subject to shear or tensile stresses. Precise control of viscosity in inkjet printing is critical to maintain good droplet formation and high print resolution.

Viscosity was measured using a Kinexus prime pro rheometer (Netzsch Group, Selb, Germany) (**Figure 4-2 a**). A standardised procedure was used across all inks, whereby

they were subjected to shear rates ranging from 1 to 1000 s^{-1} at 25 °C. Flat plate-to-plate geometries were used for all measurements, with a plate separation of 0.25 mm (**Figure 4-2 b**). Viscosity measurements were performed across a varied temperature range, up to 60 °C (**Equation (4-1)**).[325]

$$\eta = \eta_0 \exp\left(\frac{E}{k_B(T + T_0)}\right) \quad \textbf{(4-1)}$$

Where η is viscosity, η_0 is a pre-exponential factor, E represents the activation energy, k_B is the Boltzmann constant, T is the absolute temperature and T_0 is the introduced correction term.

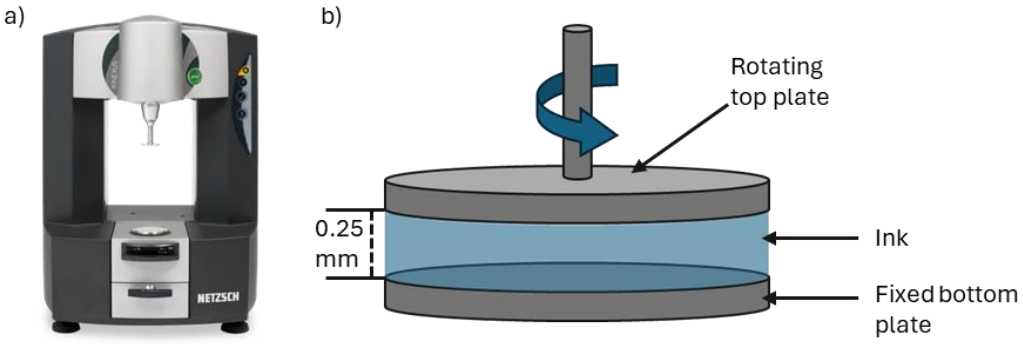


Figure 4-2 a) Image of the Kinexus Prime Pro rheometer used in this work. **b)** Schematic detailing of plate-to-plate geometry for rheometer set up with working distance of 0.25 mm

4.2.2 Surface tension and contact angle measurements

Surface tension is the cohesive force at the liquid-air interface, which causes liquids to resist external forces and reduce to the minimum surface area possible. This governs the stability of inks during jetting, including droplet formation and satellite separation. Contact angle is the angle formed between a droplet and the substrate it has been deposited on, reflecting the balance of liquid-air and liquid-substrate forces.

A Kruss drop shape analyser (DSA) 100 (**Figure 4-3 a**) was used to investigate both surface tension and contact angle. Surface tension measurements were performed automatically in the pendant droplet mode. Ink was loaded into a 1 mL syringe with a 1.2 mm diameter needle. Droplets were ejected from the needle at a continuous rate of 30 µL/min, whilst silhouetted against a bright background (**Figure 4-3 b**). A camera continuously took images of the droplet stream at a rate of 15/second, permitting measurement of droplet characteristics such as volume and diameter, which in turn enabled calculation of surface tension using the Young-Laplace model.[326] In inkjet printing, the Young-Laplace model governs the pressure inside droplets as well as meniscus formation at the nozzle orifice, influencing droplet formation, detachment and stability. Surface tension was evaluated as an average of the measurements of at least 10 droplets.

Contact angle was measured by depositing sessile droplets onto the desired substrate, which was prepared using the same cleaning process as previously described, and by recording video footage of droplet spreading until it was stable. Frames were then extracted from video footage at the point of droplet stabilisation, and contact angle measurements were performed using ImageJ and the contact angle plugin (**Figure 4-3 c**).[327–329] The contact angle was calculated using (**Equation (4-2)**).

$$CA = 180 - \bar{\theta} \qquad \textbf{(4-2)}$$

where CA is the contact angle, and $\bar{\theta}$ is the mean value of θ_L and θ_R.

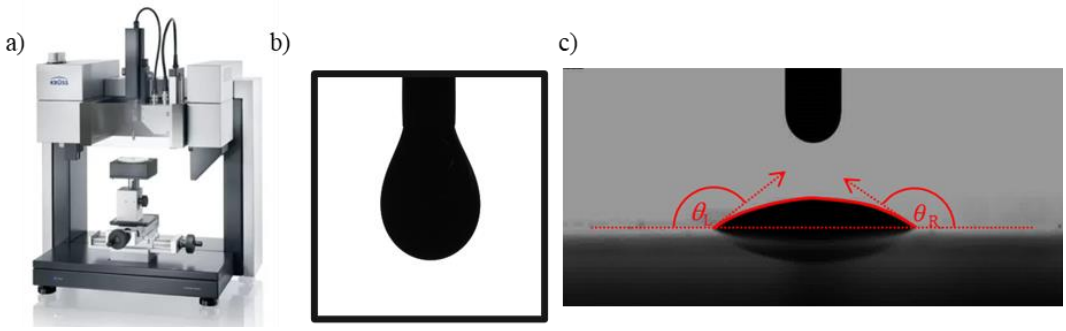


Figure 4-3 a) Image of Kruss DSA100. **b)** Image of pendant droplet suspended during interfacial surface tension measurements. **c)** Schematic depicting method for contact angle measurement and calculation.

4.2.3 Thermogravimetric analysis

In order to quantify the composition of inks used in this work TGA was used. TGA enables measurement of mass change as a function of temperature, thereby allowing determination of the thermal degradation temperature. These measurements are used to quantify sample composition, such as solvent content and organic materials. TGA 4000 (Perkin Elmer, Massachusetts, United States) was used for analyses. Heating profiles were tailored to the analysis required for each ink. To quantify ink composition, temperature holds were used for 1 hour at critical temperatures for the individual components (e.g., solvent boiling point). A low scan rate of 3 - 5 °C/min was used when heating liquid samples, to ensure uniform sample heating as well as to prevent boiling over.

To eliminate any inconsistencies in measurements of inks and to determine the accuracy of the method, samples of EC in a dispersion of cyclohexanone and terpineol (85:15 volume ratio) were prepared at concentrations of 0.25, 1.44 and 3.44 wt%. Samples were exposed to a scan rate of 3 °C/min across a temperature range of 30 - 700 °C. The boiling points for cyclohexanone and terpineol are 155.6 °C and

219 °C respectively. The thermal decomposition of EC occurs between 250 - 400 °C.[330] The wt% remaining at 240 °C was taken to be the measured solid content of each solution and compared to the expected value from formulation. This measurement was repeated 3 times for each concentration, where an average error of 0.069 ± 0.008 mg was deduced. As such, all measurements using TGA set this value as the equipment error.

TGA was used to analyse iGr, GO, Gr/PEDOT:PSS and AuNP inks. The heating profiles for each can be seen below **Figure 4-4**.

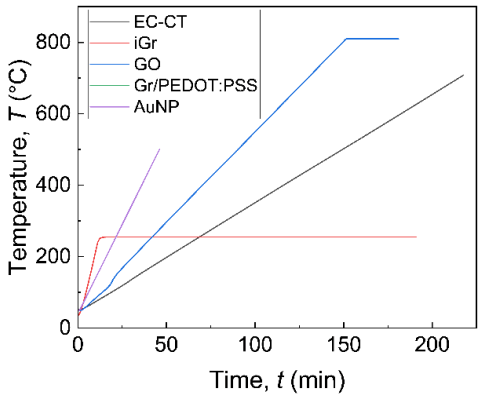


Figure 4-4 TGA time-temperature profiles used in this work.

4.2.4 Physical properties

Rheological measurements were performed on formulated inks to investigate composition, viscosity, surface tension, contact angle and density, used to inform printing parameters needed for high quality inkjet printing. Formulated inks were loaded into cartridges and stored wrapped in Parafilm in a refrigerator (T = 4 °C).

Table 4-3 Rheological properties of both commercially available and in-house formulated inks.

Ink	Physical properties			
	Solid content (wt%)	η (cP)	Surface tension (mN/m)	Contact angle (°)
iGr	2.4	11.3	33	-
iGr	1.2	3.7	29	14.6
Gr/PEDOT:PSS	0.12	0.8	46	-
GO	0.34	8.5	17.3	53.8
AuNPs	30	-	-	-
AgNPs	30	-	-	-
N-cage	10			
TPGDA	-	1.2	29	14.3

4.3 Inkjet printing

Prior to printing, optimal droplet formation was achieved through the drop watcher present on the DMP-2800 printer. It was desired for droplets to possess a thin tail which would coalesce with the main body, forming a uniform spherical shape (**Figure 4-5 a**). In some instances, the tail of the droplet formed a separate satellite droplet, which would either rejoin (**Figure 4-5 b**) or remain separate (**Figure 4-5 c**). The voltage waveform was used to control droplet formation and ejection. Blockages in the printhead nozzles were cleared by syringing air into the cartridge, forcefully expelling ink from the printhead. Further steps to clear blockages included purging with isopropyl alcohol (IPA).

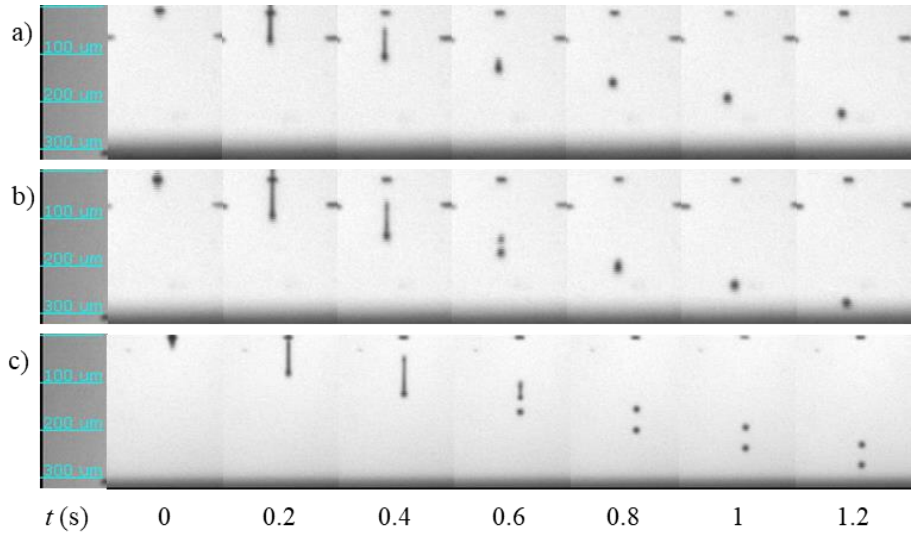


Figure 4-5 View of droplets forming in the Dimatix DMP 2800 drop watcher. **a**) Correct formation of droplet whereby tail does not separate and combines with the main droplet. **b)** Separation of tail and consequent rejoining with the main droplet. **c)** The tail of the does not rejoin the main droplet and instead forms a satellite droplet.

With respect to the viscosity and surface tension measurements, the nozzle temperature, T_{nozzle}, can be controlled up to 60 °C on the Dimatix DMP-2800. Increasing the nozzle temperature will reduce the viscosity of the ink, facilitating printing of inks with higher room temperature viscosity. Substrate temperature, $T_{substrate}$, can also be controlled, effecting both the wetting and drying characteristics of deposited ink. A warmer substrate can accelerate solvent evaporation and reduce spreading, improving print resolution. When printing an ink, the diameter of the printed droplets must be known. This enables control of the drop spacing, which is the physical distance between the centre of adjacently deposited droplets (**Figure 4-6**). If the drop spacing is too large, then droplets fail to coalesce and form a uniform film. However, if it is too small, then excess ink will accumulate, and as such, print resolution will be reduced due to spreading.

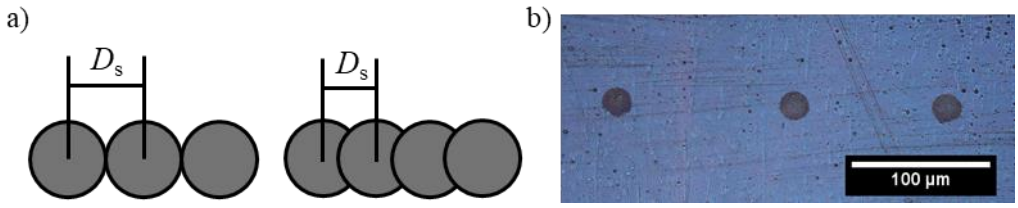


Figure 4-6 a) Schematic detailing influence of droplet spacing upon printed droplets. **b)** Inkjet-printed single droplets of graphene ink (1.2 wt%, Samba) on glass, measuring 20.4 ± 0.4 µm.

To improve print quality, a 1 mm leader bar was included in all prints, separated from the main print by 1 mm. This improves pattern quality by "pre-firing" nozzles before reaching the desired droplet speed and shape. Details of the optimised print parameters can be seen in **Table 4-4**.

Table 4-4 Printing parameters for the inks used in this work, both the commercially available and formulated.

Ink	**Printing parameters**			
	Printhead	T_{nozzle} *(°C)*	$T_{substrate}$ *(°C)*	*Drop spacing (µm)*
iGr	DMC	30	60	20
iGr	Samba	30	60	10
Gr/PEDOT:PSS	Samba	30	30-60	10
GO	Samba	25	45	20
AuNPs	DMC	35	60	10
AgNPs	Samba	30	90	10
N-cage	Samba	25	25	10
TPGDA	Samba	25	25	10

4.4 Post-deposition processing methods

Once printed, some of the inks featured in this work require an additional processing step, either to achieve their optimal properties (e.g., electrical conductivity) or to complete solidification.

4.4.1 Thermal annealing and sintering

Thermal annealing was performed either in air in a natural convection oven (Carbolite Gero PN), or under 1 mbar vacuum in a Thermo Scientific™ Vacutherm vacuum heating and drying oven. A list of the inks which required thermal annealing and the applied parameters is provided below (**Table 4-1**).

Table 4-5 Thermal annealing conditions used for relevant inks within this work.

Ink	**Thermal annealing conditions**	
	Temperature (°C)	*Duration* (hrs)
iGr (1.2 wt%)	250	2
iGr (1.2 wt%)	250	2
Gr/PEDOT:PSS	100	0.5
AgNPs	150	1

4.4.2 Intense pulsed light

A custom-built IPL system was developed to provide annealing specifically for iGr inks. The IPL had a broad spectral range of 550 – 900 nm with maximum intensity at 600 nm, and several peaks between 800 and 950 nm (**Figure 4-7 a**). The pulse duration was ~ 4 ms (**Figure 4-7 b**) with a flash power of 5.4 J/cm^2. After printing, samples were placed 10 mm away from the light source and flashed a number of times, n_f.

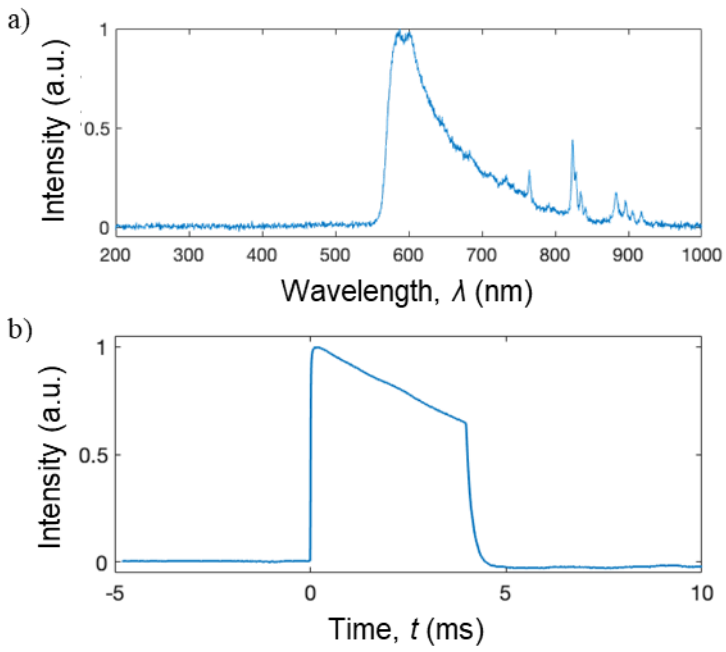


Figure 4-7 a) Emission spectrum of light emitted by IPL annealing system and **b)** light intensity as a function of time during IPL flash.

4.4.3 UV annealing, sintering and curing

Multiple UV post-processing sources were used in this work. Firstly, the Dimatix DMP-2800 printer is equipped with a 365 nm UV LED mounted on the printhead carriage assembly. This enabled *in situ*, swathe-by-swathe application of UV light to printed material. Two *in situ* strategies were applied for UV curing of polymers (e.g., TPGDA). The first strategy, scan-by-scan (SBS), exposed each ink swathe to UV light during deposition. The second strategy, post-print-cure (PPC), deposited all of the ink before curing. Once deposition was complete, the appropriate number of UV passes was completed.

UV post-deposition processing was also applied directly via a clamp-stand-mounted light source (36 nm, 282 mW/cm2; Phoseon Technology, FireFly UV lamp). This

enabled the adjustment of the distance between the UV lamp and the printed pattern (e.g., AuNPs)and hence power density, as well as precise control over exposure time.

4.5 Optical and morphological characterisation

4.5.1 Optical microscopy

Optical microscopy was used to examine the surface of printed films and to perform dimensional measurements, thereby verifying the printed patterns against the intended design. In this work, a Nikon Eclipse LV100ND optical microscope with Nikon NIS-Elements software was used, equipped with 5x, 10x, 20x, 50x and 100x lenses.

4.5.2 Optical profilometry

Optical profilometry is a non-contact measurement technique which uses light to create a detailed 3D map of a surface's topography. It enables the measurement of surface roughness, feature size, and defects with high accuracy. A Bruker ContourX-200 3D optical profilometer was used to investigate the thickness and surface morphology of inkjet-printed films.

4.5.3 Scanning Electron Microscopy (SEM)

SEM enables visualisation of features at the nanometre to micrometre scale across a wide range of materials. Analysis is performed through the application of a focused beam of electrons onto the sample surface in high vacuum (10^{-6} torr). Electrons are elastically scattered out of the sample after interacting with the atoms within, these are called backscattered electrons (BSE) and are the primary form of imaging in SEM. BSE can be used to determine material composition, whereby elements with higher atomic numbers scatter electrons more strongly because they have larger, denser

nuclei. BSE images are imaged using the backscattered electron detector (BSED). Secondary electrons (SE) are a result of inelastic interactions between target atoms and incident electrons. These reveal details of the sample's surface morphology and can be imaged using the secondary electron detector (SED). Some SEMs are equipped with a large-field detector (LFD), which enables the acquisition of a wide range of signals, often combining BSE and SE. The LFD facilitates SEM imaging over a larger area at reduced magnification, increasing efficiency. SEM can be used to both analyse surface morphology and sample composition.[331] Environmental SEM (ESEM) is a specialised form of SEM which enables imaging of non-conductive samples without the need for coating via operation in a low-pressure (0.2-20 torr) gaseous environment. The choice of gas is critical because it will amplify the signal and neutralise the sample's charge. Common gases include water vapour, nitrogen, helium and oxygen.

An FEI Quanta 650 ESEM was used to investigate the deposition of TPGDA and graphene onto the fabric. Samples were fixed onto stubs via carbon tape. Cross-sectioning of samples was performed by first freezing ($T_{chamber}$ = -31 °C, T_{sample} = -25 °C) and then slicing using Leica 3050S cryostat. This produced very thin (50 µm) samples absent of mechanical damage. Cross-sectioned samples were then mounted on the vertical face of a 90° stub using carbon tape. ESEM was used due to the absence of a requirement for sample coating as well as charge mitigation. ESEM and sample sectioning were performed by Dr Nicola Weston (University of Nottingham). Due to the excellent conductive properties of graphene, as already discussed, there is a significant build-up of charge during SEM imaging, resulting in distortions in the produced images. ESEM possesses the necessary tools to mitigate charge buildup, such as electron flood guns and low-energy electron beams. Both LFD and BSE detectors were utilised. Low vacuum mode was used within the range of 40 - 80 Pa,

allowing for contrast and resolution adjustment for optimal clarity. Observation of samples was performed at intervals over the magnification range of 500x – 10000x. A Hitachi TM3030Plus Tabletop SEM was used to capture high-resolution surface images of inkjet-printed samples on polymer and rigid substrates. Samples were held in place using electrically conductive, non-porous, adhesive carbon disks.

4.5.4 Transmission Electron Microscopy (TEM)

TEM is a powerful characterisation technique that uses a high-intensity electron beam to examine the internal structure of materials down to the atomic scale. An electron beam is focused on the sample, resulting in elastic and inelastic scattering of the electrons by sample nuclei and electrons.[332] Transmitted electrons are used to form a magnified and focused image, capable of producing extremely high-resolution images (< 1nm), offering detail down to the atomic level.

AuNP samples were prepared for TEM analysis by dispersing at ultra-low concentrations in Toluene (1 μg/mL) and depositing upon TEM support grids (Agar Scientific). TEM studies were performed by Dr Michael Fay (University of Nottingham) on JEOL 2100F FEG TEM operating at an accelerating voltage of 200 kV and equipped with a Gatan K3-IS camera. Images were analysed using ImageJ.[327]

4.5.5 Raman spectroscopy

Raman spectroscopy is a spectral technique for measuring samples based on the inelastic scattering of light. Energy exchange between the photon and target molecule decree that the scattered photon is of either higher or lower energy than the incident. This difference in energy is a result of vibrational or rotational modes of motion of the molecule, which is called Raman scattered light and is collected by a detector,

revealing information regarding its energy levels.[333] Scattering can occur in three modes (**Figure 4-8**), 1) Rayleigh scattering (elastic), in which the molecule is excited to the virtual state, and relaxes immediately back with no net energy transfer with the photon. 2) Stokes Raman scattering (inelastic), where the excited molecule relaxes to a higher vibrational energy level than its original state. 3) Anti-Stokes Raman scattering (inelastic), where the excited molecule relaxes to a lower vibrational energy level than its original state. The most common mode is Stokes scattering, and the one which is most often measured in Raman spectroscopy.[334]

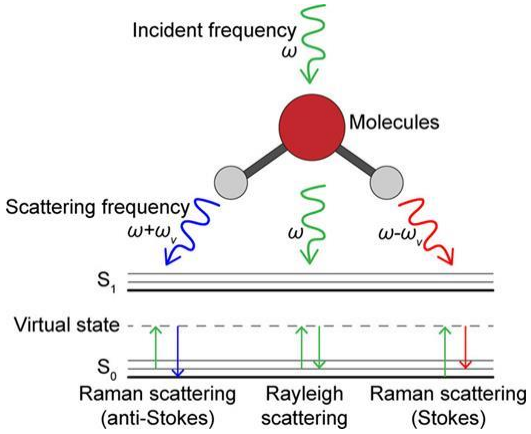


Figure 4-8 Schematic and Jablonski diagram depicting Raman and Rayleigh scattering. Reproduced from Lin et al.[334]

Samples for Raman spectroscopy were prepared by inkjet printing or drop casting the material of interest (e.g., iGr, Gr/PEDOT:PSS) onto a substrate and then applying any required post-processing procedures. Micro Raman spectroscopy was performed by Dr Graham Rance using a HORIBA LabRAM HR Raman spectrometer. Spectra were collected using a 532 nm laser (at ~0.3 mW power), a 100x objective and a 200 µm confocal pinhole. To simultaneously scan a range of Raman shifts, a 300 lines/mm rotatable diffraction grating along a path length of 800 mm was employed. Spectra were acquired using a Synapse CCD detector (1024 pixels) thermoelectrically cooled

to −60 °C. Before spectra collection, the instrument was calibrated using the zero-order line and a standard Si(100) reference band at 520.7 cm^{-1}. Raman spectroscopic maps were acquired over the range 450 - 3400 cm^{-1} (1 spectral window) at 5 µm steps within a square 50 x 50 µm.

4.5.6 Ultraviolet-visible spectroscopy

Ultraviolet-visible (UV-Vis) spectroscopy is an analytical technique which measures the absorbance of UV and visible light by a sample.[335] A white light source is passed through a sample, and the intensity of light is measured at specific wavelengths, giving a measure of absorption at that specific wavelength. A typical UV-Vis spectrometer includes a light source, often a deuterium lamp for UV or tungsten lamp for visible light, and a monochromator to select narrow wavelengths of light, as well as the detector to measure the absorbance or transmittance. The Beer-Lambert law[336] (**Equation (4-3)**) is used to relate the measured absorbance to sample concentration, making it very useful for quantitative analysis.

$$A = \varepsilon c l_p \qquad \textbf{(4-3)}$$

where A is the measured absorbance, ε is the molar absorptivity, c is the sample concentration and l_p is the path length.

A Tecan Infinite M nano UV-Vis spectrometer was used to analyse samples across a broad range of wavelengths 230 nm - 1000 nm. Samples were placed in a quartz cuvettes of 3 mL volume, with capability to read 4 samples at a time.

4.6 Electrical measurements

Electrical measurements were performed on printed devices to obtain *I-V* characteristics and sheet resistance. The length, L, and width, W, of samples were measured by optical microscopy (**Chapter 4.5.1**).

4.6.1 Sample preparation for electrical measurements

In order to provide electrical contact to inkjet-printed samples without risk of damage to the thin films, silver paste (RS Pro Conductive Silver Paint) was manually deposited to the sample edges. A multi-terminal micropositioner system (Micromanipulator, model 450PM) was used to hold samples in place and provide electrical contact. The micropositioners featured tungsten probes (Micromanipulator, model 7B-5) with tip radius of 0.5 mm, which were used to provide electrical contact with samples. The micropositioner tips could be viewed through a microscope, enabling precise and careful placement onto samples. The system is equipped with a vacuum pump, which enables firm placement of the micropositioners and holds the sample on the stage. The micropositioners were connected to a Keithley-2400 Source-Meter for electrical measurements (**Figure 4-9**).

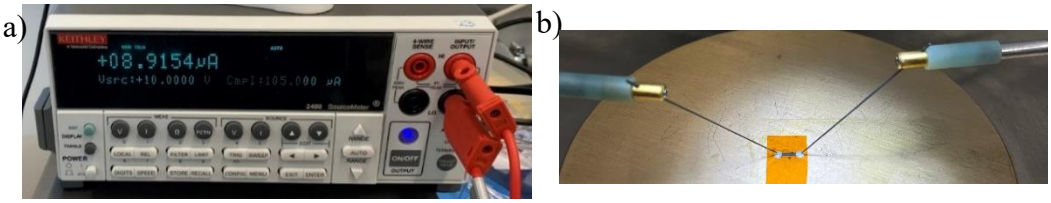


Figure 4-9 Equipment setup for electrical characterisation. Photographs of **a)** the Keithley 2401 source meter and **b)** printed graphene sample printed on Kapton. Micromanipulators make contact with silver paste pads in a 2-terminal geometry setup.

Sheet resistance measurements: To access the sheet resistance, R_S, of printed films, samples of varying dimensions were printed. Current-voltage dependencies, *I(V)*, were measured using a Keithley-2400 Source-Meter. Both 2-terminal and 4-terminal geometries were used (**Figure 4-9**).

In 2-terminal geometry, manipulator tips are placed at opposing ends of the printed material (**Figure 4-10 a**), from where a voltage, V_{sd}, can be applied between the source-drain contacts and current measured, I_{sd}. The electrical resistance of the sample is calculated using Ohm's law. 4-terminal geometry is required when measuring highly conductive samples (< 100 Ω) to eliminate the effect of contact resistance. 4 electrical contacts are spread out evenly along the length of the sample (**Figure 4-10 b**). A voltage, V_{sd}, is applied between the outermost, source-drain contacts and current I_{sd} is measured. Voltage between the innermost two contacts is measured, V_{4t}, and used in conjunction with Ohm's law to calculate resistance, R_{4t}.

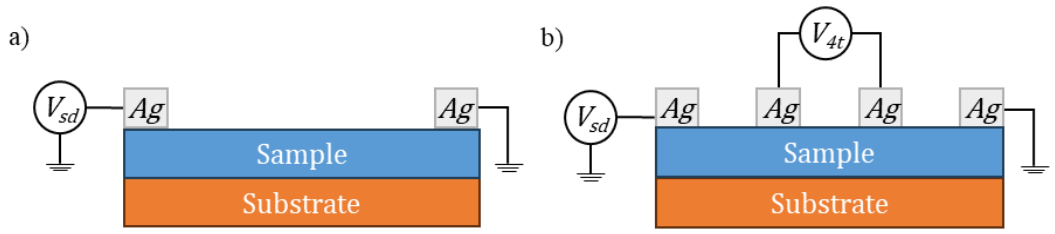


Figure 4-10 Schematic of electrical characterisation techniques for **a)** 2-terminal geometry and **b)** 4-terminal geometry.

A voltage was applied for the source-drain contacts in each geometry setup and swept over a defined range, ensuring the current is below 1 mA preventing device damage. Current was measured during this process, and each sweep repeated three times. The length between contacts, *L*, and width of lines, *W*, were measured using an optical microscope to enable the calculation of sheet resistance using (**Equation (4-4)**).

Measurements in 4-terminal geometry use the value of L to be measured in between the innermost two contact points. Note, sheet resistance measurements were only used for samples, where $W < 0.5L$.

$$R_s = R\frac{W}{L} \quad \textbf{(4-4)}$$

4.6.2 Device performance under mechanical deformation

For samples intended for mechanical testing, the Micropositioner system was not suitable due to the movement that would occur during measurements. Furthermore, silver paste could not be used to enhance contacts, due to its tendency to crack and lose adhesion to the substrate under strain and bending. Instead, connections were provided through fixing wire to sample edges and holding in place with aluminium tape. Wires were then soldered to onto circular electrical header pins, which in turn would be connected with the source meter.

To investigate the response of the devices to mechanical deformation and durability of printed samples under stretching or bending, a custom built set up was used (**Figure 4-11**). Printed samples were held in place by a pair of grippers, where a stepper motor and lead screw were used to provide linear oscillation both incrementally and cyclically. The separation distance between the two grippers was changed incrementally, allowing evaluation of device performance with regards to elongation or bending, with *I(V)* measurements performed at different deformations. This action could also be performed cyclically, enabling sample durability to repeated deformation to be investigated. The maximum travel distance of the rig was 22 mm, which enables a range of bend angles and elongations to be achieved, depending on the set separation distance of the grippers.

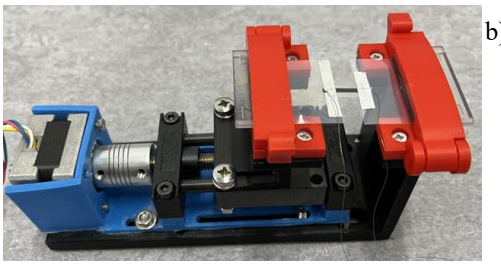
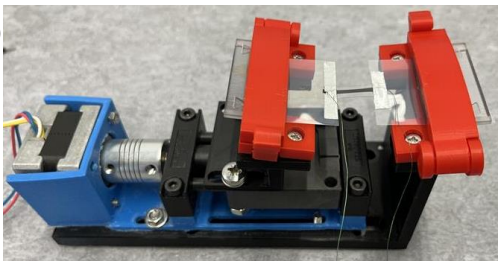
a)  b) 

Figure 4-11 Custom built Mechanical deformation rig with iGr-Beyolex sample shown in a) zero deformation and b) stretched state.

4.7 Sensing performance

4.7.1 Temperature dependent measurements

To investigate the response to temperature, samples were mounted in a cryostat chamber connected to a Pfieffer HiCube^{TM} Eco Dry Pumping Station and equipped with a temperature controller (Lakeshore Cryotonics Model 336) (**Figure 4-12**). The cryostat was sealed and brought to low pressure, then the sample stage was heated to 290 < T < 370 K. The temperature induced change of electrical conductivity, $\Delta\sigma$, was calculated using **Equation (4-5)**.

$$\Delta\sigma/\ \sigma_{RT} = \frac{\sigma - \sigma_{RT}}{\sigma_{RT}} \qquad \textbf{(4-5)}$$

where σ is the measured electrical conductivity and σ_{RT} is the electrical conductivity measured at room temperature.

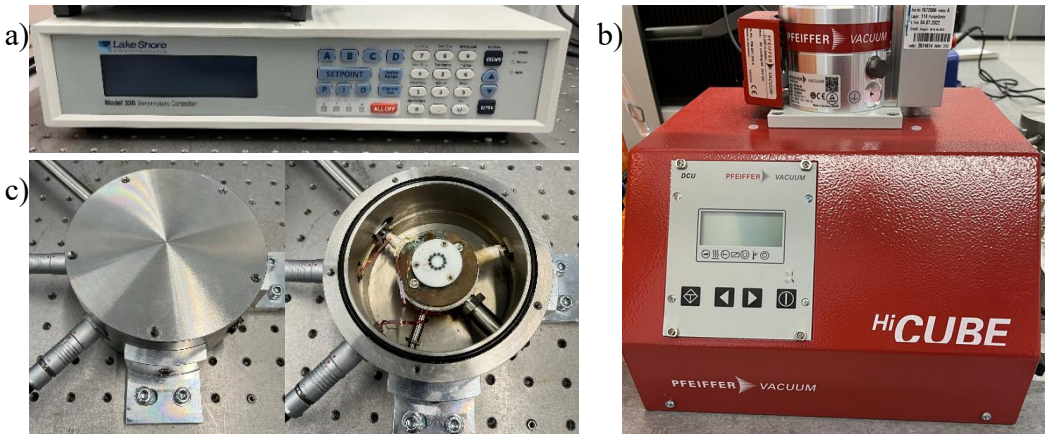


Figure 4-12 Equipment used for temperature dependence investigations, **a)** Lakeshore Cryotonics Model 336 temperature controller. **b)** Pfieffer HiCube^{TM} Eco Dry Pumping Station. **c)** Cryostat to provide low pressure environment for temperature measurements, in closed and open states, featuring header fixture to enable sample mounting.

For extended temperature range measurements and for investigations of carrier concentration and mobility, Hall bar shaped devices were used (**Figure 4-13**-b). Measurements were performed in a helium atmosphere in a cryofree magnetocryostat at 2 K < T < 300 K and magnetic field B < 16 T. A Keithley-2400 sourcemeter and two Keithley-2010 multimeters were used for the transport measurement of longitudinal, V_{xx}, and transverse, V_{xy}, voltages in the DC mode. Lakeshore 340 Temperature controller was used to control T in the system. As depicted in **Figure 4-13 a**, V_{xx} is measured between points 2 and 3, V_{xy} is measured between points 2 and 6 whilst a current is applied across points 1 and 4. Low-temperature measurements on Hall bar devices were performed by Dr Nathan Cottam.

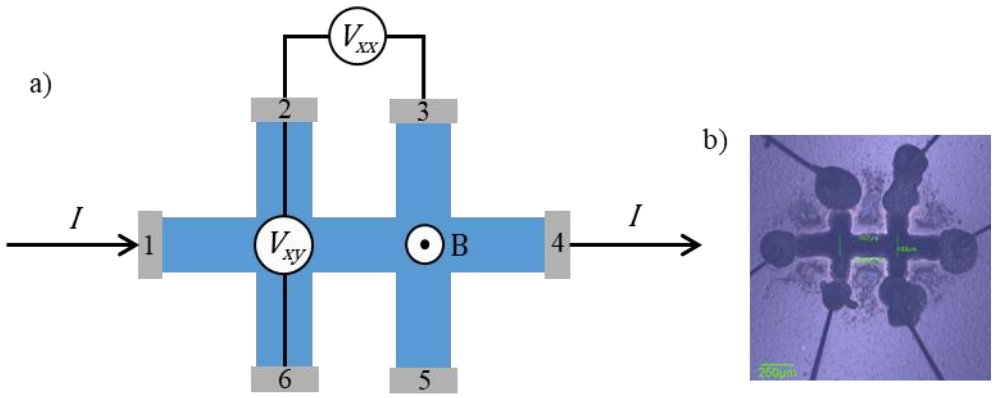


Figure 4-13 a) Schematic of Hall bar geometry, where I is current applied, V_{xx} is the longitudinal voltage measurement, V_{xy} is the transverse voltage measurement and B is the applied magnetic field perpendicular to the direction of the applied current. **b)** An iGr Hall bar device (n_L = 5, n_F = 10) with silver paste contacts on Kapton film.

4.7.2 Humidity sensing

Humidity sensing was performed by several methods. The immediate response to humidity change was measured by breathing onto the devices. A constant voltage was applied across the sample, whilst the temporal change of current was recorded. Whilst the humidity of exhaled breath varies depending on local conditions and the individual, it is expected to be in the range of $RH = 76.8 \pm 5.9$ %[337] and a temperature of about 34 °C.[338] Laboratory conditions were 18 °C and < 50 % *RH*.

4.7.3 Pressure dependent measurements

A custom setup was developed and printed using Anycubic – Normal UV Resin and an Anycubic Photon Mono X SLA printer to investigate the effects of increased pressure on the printed graphene. The setup consisted of a free moving shaft with a tray to hold mass, located within a stand. Mass could be added to the tray, changing the downwards force onto the sample (**Figure 4-14**). The shaft was lubricated to reduce friction during vertical movement. Current-voltage (*I(V)*) measurements were performed at different pressures.

Pressure testing was also investigated in an ON/OFF manner, where a mass was loaded into the tray and then removed. A constant voltage was applied across the sample, whilst current was continuously recorded against time.

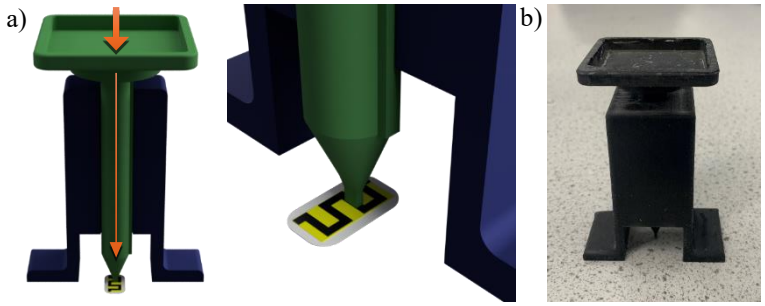


Figure 4-14 Custom test equipment for pressure testing, **a)** design and depiction of function **b)** SLA printed set up from Anycubic black UV curable resin.

4.7.4 Measurements of sensing response to multiple stimuli

A specific device design was developed for simultaneous measurement of response to temperature, pressure and humidity. To achieve this, a graphene-TPGDA heterostructure device was printed by Dr Feiran Wang (University of Nottingham), comprising two sets of graphene tracks with a dielectric separating layer. Using the Fujifilm DMP-2810 printer with DMC printheads, the top and bottom graphene tracks (1.2 cm × 0.12 cm) separated by 0.15 cm gap were printed using the graphene ink with a drop spacing of 10 µm and n_L = 10, and annealed at 250 °C in vacuum for 1 h. The dielectric separation layer consisting of 25 printed layers was printed using TPGDA monomer, with a drop spacing of 10 µm, and cured *in situ* using 365 nm UV LED during printing. Electrical contact was provided by the addition of inkjet-printed AgNPs on the bottom iGr tracks, and silver paste applied to the top.

Two Keithley 2401 source meters were used in order to perform simultaneous measurement of current variation to temperature and humidity, and temperature and

pressure respectively. To simultaneously measure the changes in temperature and humidity, a constant voltage was applied to both the top and bottom tracks, whilst recording the current. The device was placed on a hotplate, and the temperature was increased from 30 to 40 to 50 °C. Once the temperature had reached each step, the top tracks were blown upon, increasingly the local humidity distinctly. This was repeated 3 times at each temperature stage. The readouts for both the top and bottom tracks were normalised against the respective initial sheet resistance value. The device design would prevent exposure of the bottom track to humidity, whilst both tracks would experience a response to temperature changes. Thus, the normalised response of the bottom track could be subtracted from the top in order to isolate the humidity response.

Acetone sensing was performed in a low oxygen (< 1 %) atmosphere glovebox. Samples were placed in a sealable glass container along with MQ135 and DHT22 sensors, which in turn was situated on a 60 °C hotplate (**Figure 4-15**). Readout of the MQ135 and DHT22 sensors was characterised using an Arduino uno board. Acetone and deionised water were added in a range of concentrations to achieve up to 3.2 ppm acetone and 100 % RH, and the container was then sealed. A constant voltage of 1 V was applied across samples, enabling measurement of resistance change due to gas presence. Both acetone and deionised water were applied to the container to investigate multiple stimuli sensing.

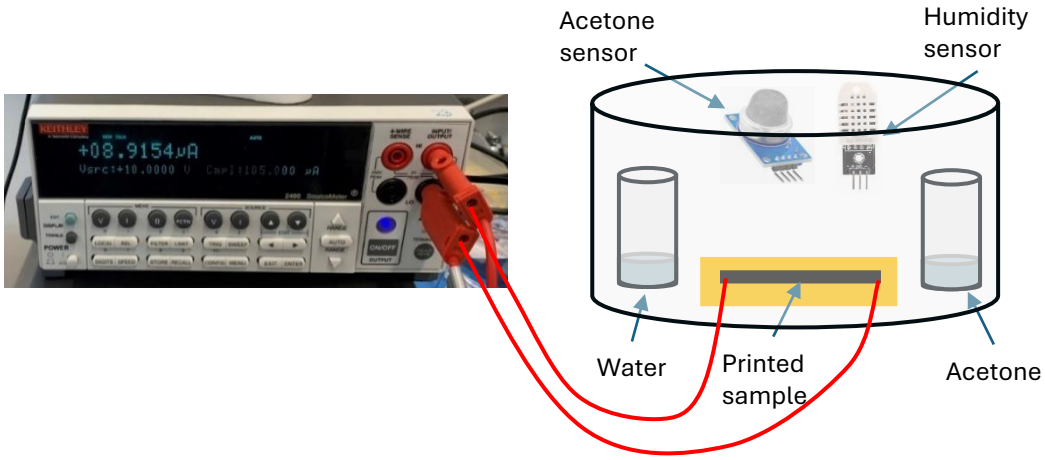


Figure 4-15 Schematic illustration of the equipment setup used for acetone and humidity sensing of printed devices.

4.7.5 Chemical sensing

In order to investigate the detection of quorum signalling molecules, molecules were first dispersed in methanol across a range of concentrations (1 mg/mL – 1 pg/mL). 4 quorum molecules were investigated for the work: Pseudomonas quinoline signal 2-heptyl-3-hydroxy-4(1H)-quinolone (PQS), 2-heptyl-4(1H)-quinolone (NHQ), 2-nonyl-4-hydroxyquinoline (HHQ) and 2-heptyl-4-hydroxyquinoline N-oxide (HQNO) (**Figure 4-16**). The quorum molecules (PQS, NHQ, HHQ and HQNO) were received from Dr Nigel Halliday (University of Nottingham). These molecules were selected as they are all produced during biofilm growth of the bacteria pseudomonas aeruginosa.[339]

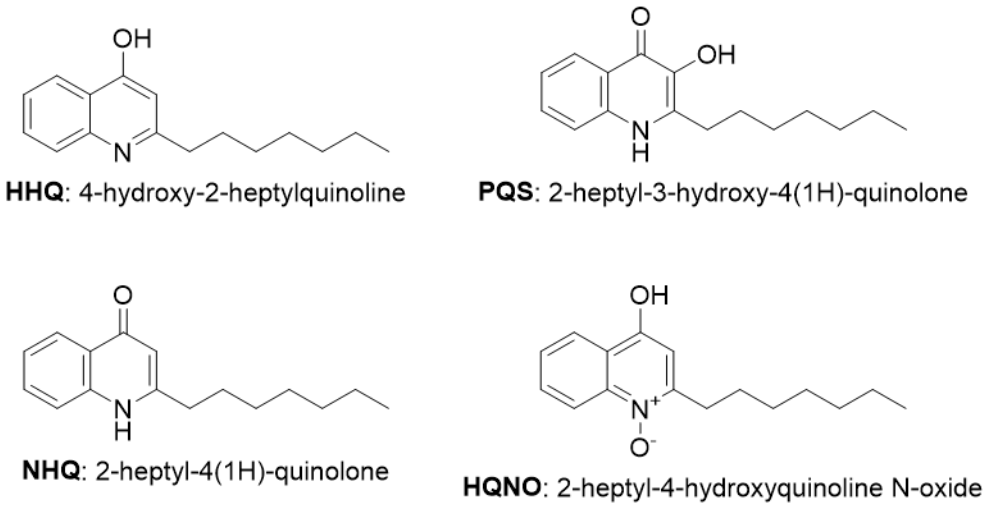


Figure 4-16 Chemical structure of quorum signalling molecules used.

AgNP contacts were first printed onto Kapton film (n_L = 1), with the Gr/PEDOT:PSS film (15 x 3 mm, n_L = 20) deposited on top. A TPGDA overlay was printed (10 x 1.5 mm, n_L = 5) to control the region of the Gr/PEDOT:PSS film available for exposure to the quorum molecule solution (**Figure 4-17 a**). The Gr/PEDOT:PSS devices were placed in a curved sample holder (**Figure 4-17 b**) – printed in-house using FDM. This would prevent the accumulation of the deposited molecules at the edge of the Gr/PEDOT:PSS-TPGDA interface. Devices were placed in a low oxygen (< 1 %) atmosphere glovebox on a 60 °C hotplate. Inkjet-printed AgNPs and silver paste were used to provide electrical contact to samples.

To investigate the response to different quorum molecules at different concentrations, a 2 µL droplet of the selected dispersion (molecule and concentration) was deposited on the centre of the Gr/PEDOT:PSS (**Figure 4-17**). Constant voltage was supplied and output current measured. A delay of 100 s was allowed between repeats with the heated substrate aiding methanol evaporation and device recovery. 3 repeats were performed for each solution. Different samples of Gr/PEDOT:PSS were used for each

molecule type to prevent any contamination effects, with concentration in ascending order to reduce effects from the accumulation of remaining molecules on the sensor surface.

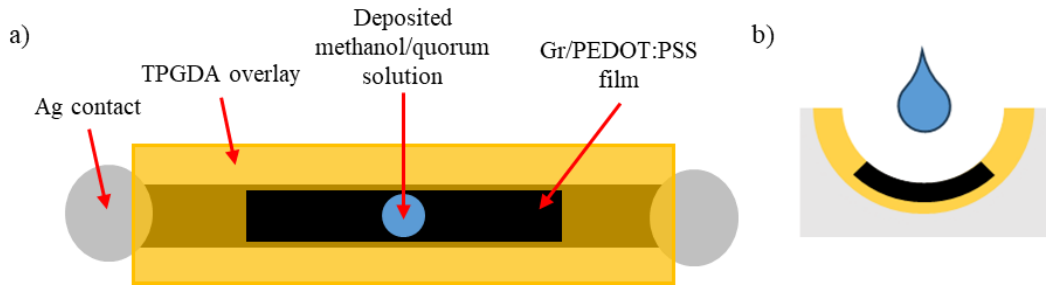


Figure 4-17 Schematic of printed Gr/PEDOT:PSS – TPGDA devices showing the **a)** device design with sensing window and **b)** placement in the curved sample holder.

5 Inkjet printing and post-processing of functional materials

A range of inks utilising functional materials was used in this work. This chapter details the printing process and optimisation for electrical characterisation of printed inks. In some cases, post-processing methods were required to improve electrical conductivity, and the effectiveness of these strategies is discussed.

The work included in this chapter is based on the characterisation of graphene ink printed onto textiles published in *Wang et al., "Inkjet-printed Multifunctional Graphene Sensors for Flexible and Wearable Electronics", Adv. Electron. Mater., 2025, 11, 2400689*. The work included in this chapter based on printed AuNPs is published in *Im et al., "On-demand sintering of gold nanoparticles via controlled removal of o-nitrobenzyl thiol ligands under ultralow-power UV for conductive patterns", Adv. Sci., 2025, 12, 2415496*. The results on investigations of IPL annealed iGr is published in *Heaton et al., "*Photonic Annealing of Inkjet-printed Graphene for Stretchable Wearable Healthcare Monitoring Devices*", Adv. Mater. Technol., 2025, 10, e00913*.

5.1 Inkjet printing of functional materials

5.1.1 Graphene ink

The commercially available iGr ink used in this work is already well established in previous studies, with a good understanding of its electrical properties and applications towards sensing.[159,161] Current work uses thermal annealing at high temperatures (T_{anneal} = 250 °C, $t_{anneal} \geq 30$ mins) for post-processing to achieve high-quality printed

films, exhibiting sheet resistance, R_S values in the range of 102 – 103 Ω/sq..[159] Low-temperature post-processing methods are yet to be explored with this ink, which would be more suited towards printing onto highly flexible polymer substrates, better suited towards wearable electronics.

5.1.2 Graphene/PEDOT:PSS deposition

The electrical properties of the commercially available graphene/PEDOT:PSS (Gr/PEDOT:PSS) ink used in this work are not well established. Current literature is limited to spray-coated photodetectors,[217] supercapacitors[340] and drop cast electrochemical sensors.[341] There is no evidence of inkjet printing of this hybrid ink, and thus it is important to establish the printing process and electrical properties of the printed layers. The effect of the number of printed layers on sheet resistance was investigated, as well as printing and post-processing parameters on the quality and properties of Gr/PEDOT:PSS printed on different substrates.

The Gr/PEDOT:PSS ink was printed onto Kapton and Beyolex substrates with n_L = 1, 3, 5, 10 and 20 and $T_{substrate}$ = 35 °C. Samples were left to air dry for 30 minutes after printing, and then electrical measurements were performed, with electrical contact provided by the application of silver paste. It was observed that for both substrates, the sheet resistance decreased with increasing number of printed layers as well as a linear current-voltage dependence in both directions, indicating Ohmic behaviour (**Figure 5-1 a, b**). The relationship between the number of printed layers and electrical resistance is presented in **Figure 5-1 c**. It reveals that the electrical conductivity decreases by > 2 orders of magnitude with n_L increases to n_L = 3 and begins to saturate after $n_L > 5$ with $R_S \sim 10^3$ Ω/sq.. This suggests that after a certain number of layers, there is no enhancement of electrical properties, in agreement with parallel studies on

inkjet printing alternative conductive materials.[159] There is no discernible difference between the conductivities achieved on Kapton and Beyolex (**Figure 5-1 c**), suggesting the compatibility of the Gr/PEDOT:PSS ink for different substrates. Optical microscopy was performed on printed samples to measure width and length as well as to provide visual inspection (**Figure 5-1 d**). For $n_L < 10$, prints appear to be faint in colour, likely due to the low solid content of the Gr/PEDOT:PSS ink (0.12 wt%). When $n_L = 10$ or 20, prints appear much darker, indicating an increased coverage and thickness of Gr/PEDOT:PSS. This is predominantly due to the deposited graphene in the composite ink, as there is a higher content of solid graphene (1 mg/mL) compared to PEDOT:PSS (0.2 mg/mL). The pattern observed by the optical microscopy supports the electrical measurements, as it would be expected that more solid material deposited would lead to the formation of graphene networks with higher packing density, hence improving the electrical resistance. [159]

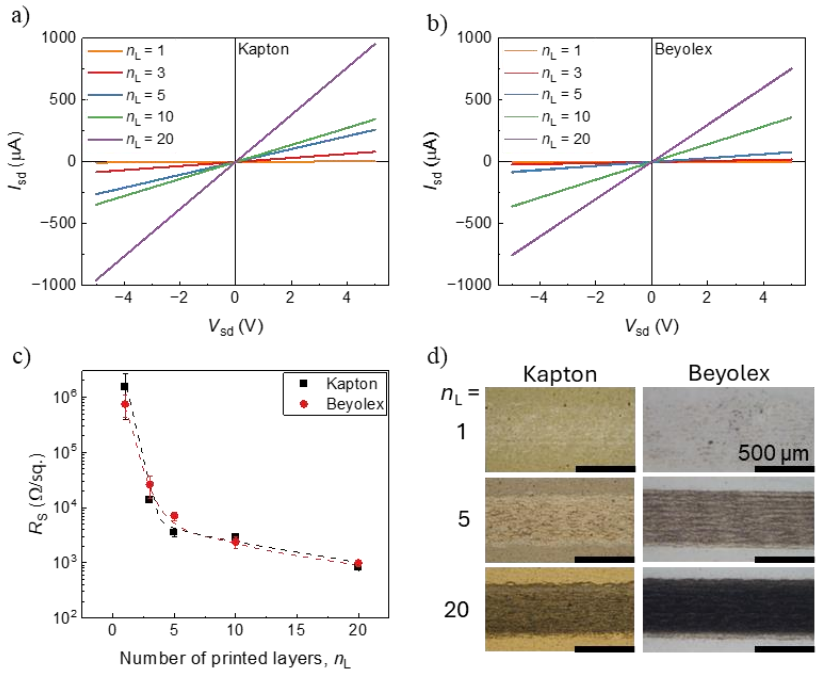


Figure 5-1 Representative I(V) characteristics of inkjet-printed Gr/PEDOT:PSS films ($T_{substrate}$ = 35 °C) on **a)** Kapton and **b)** Beyolex with number of printed layers n_L = 1, 3, 5, 10 and 20. **c)** Dependence of sheet resistance of Gr/PEDOT:PSS inkjet-printed on Kapton and Beyolex films. Error bars represent the standard deviation between sampes used for measurement. The dashed lines provide a guide to follow for each trend. **d)** Representative optical images of Gr/PEDOT:PSS inkjet-printed onto Kapton and Beyolex films at 1, 5 and 20 layers ($T_{substrate}$ = 35 °C) (Scale bar is 500 µm).

To further optimise printing parameters for the Gr/PEDOT:PSS ink, the effects of substrate temperature, thermal annealing, and substrate choice were investigated. Samples were printed (n_L = 10, 3 x 0.4 mm) at substrate temperatures of 25, 30, 40, 50, and 60 °C on Beyolex. It was observed that the sheet resistance increased with the increasing substrate temperature (**Figure 5-2 a**). Optical microscopy was performed on the printed samples at $T_{substrate}$ = 25 °C and 50 °C (**Figure 5-2 b**), which indicated better print definition at higher $T_{substrate}$ = 50 °C. It was observed that the line width, decreased with an increase of $T_{substrate}$, which can be attributed to droplet drying mechanics where, at increased temperature, there is faster solvent evaporation, reducing the time available for the droplet to spread. Furthermore, rapid evaporation of the solvent also induces the early onset of pinning, where the contact line of the

deposited droplet solidifies before the droplet fully spreads. These effects help to improve the resolution of printed lines.

The electrical resistance of samples was also measured after 3 months of storage to investigate the stability of the printed material (**Figure 5-2 a**). The printed Gr/PEDOT:PSS samples were stored in air, at room temperature (~ 20 °C) and in a dark container. Electrical measurements revealed a small, insignificant increase in sheet resistance after storage; for example, for $n_L = 20$, $T_{substrate} = 25$ °C, an increase of ~ 850 Ω/sq. (23 %) from 3739 ± 83 Ω/sq. to 4605 ± 308 Ω/sq. was observed, indicating a high stability of this ink and suitability for long-term operation.

The effects of post-deposition thermal annealing were investigated on printed Gr/PEDOT:PSS ($n_L = 10$, $T_{substrate} = 30$ °C) on Beyolex. It was found that after annealing the prints for 1 hour at 100 °C there was a small, insignificant change in electrical resistance, increasing by 40 Ω/sq. (~ 1 %) from 2721 ± 200 Ω/sq. to 2760 ± 236 Ω/sq. (**Figure 5-2**-c). This highlights the suitability of the Gr/PEDOT:PSS ink for the manufacture of flexible and stretchable devices, permitting high electrical conductivity printed films onto substrates with a low thermal resistance.

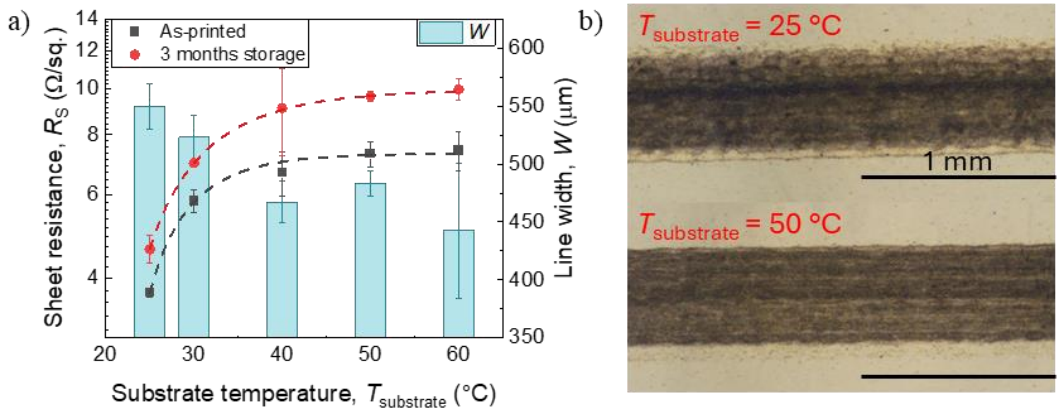


Figure 5-2 a) Sheet resistance of Gr/PEDOT:PSS printed onto Beyloex at increasing substrate temperature in as-printed and 3 months post printing, stored in in air, at room temperature (~20 °C) and in a dark container, with comparison of the measured line width at the time of printing. Error bars represent the standard deviation across all samples used. The dashed lines provide a guide to follow for each trend. **b)** Optical images of Gr/PEDOT:PSS (n_L = 10) on Beyolex printed at $T_{substrate}$ = 25 °C and 50 °C. (Scale bare = 1 mm) **c)** Sheet resistance for Gr/PEDOT:PSS inkjet-printed on Beyloex ($T_{substrate}$ = 35 °C) as printed and after 30 minutes of thermal annealing at 100 °C.

To examine the effect of substrate properties on the sheet resistance of Gr/PEDOT:PSS, printed samples were evaluated upon a range of substrates from flexible and stretchable polymers (Beyolex) to rigid materials (Si/SiO_2, glass) (**Figure 5-3**). There is no defined relationship between thermal conductivity of the substrate, $k_{substrate}$, and R_S observed, as the range of values obtained is relatively narrow (385 – 1821 Ω/sq.). However, the width of printed lines does directly scale with the thermal conductivity of the substrate used. This can be attributed to the more thermally insulating materials (PEN, Kapton, Beyolex) having a lower surface temperature despite the applied $T_{substrate}$. These results are in agreement with the trend observed in the investigation of the effect of $T_{substrate}$ (**Figure 5-2 a**). Hence, it can be concluded that for higher resolution printing, either substrates with higher thermal conductivity, such as glass, or higher $T_{substrate}$ should be used.

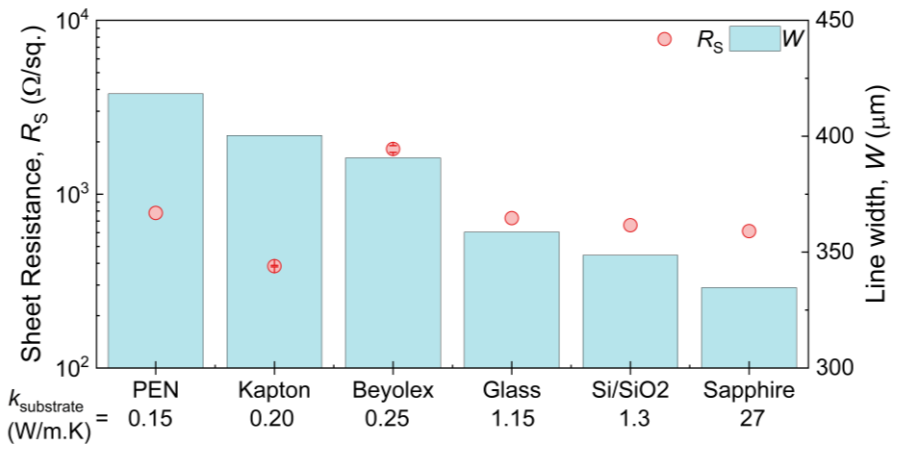


Figure 5-3 Sheet resistance (red circles) obtained from Gr/PEDOT:PSS (n_L = 20, $T_{substrate}$ = 50 °C, 3 x 0.3 mm) on different substrates compared with the width of printed lines (blue bars). Thermal conductivity, $k_{substrate}$, values have been provided for each substrate in ascending order.

5.1.3 Nitschke cage ink

N-cages are self-assembled molecular structures composed of metal ions on the vertices and connecting ligands, with the cavity suitable for encapsulation of specific molecules,[342] and could offer a route for surface functionalization of graphene-based sensors for selectivity and specificity to chemical stimuli. Printed N-cages could form a capping layer to iGr, enabling sensitivity towards a specific chemical through discrimination of the stimuli available to contact the graphene sublayer.

The tetrahedral iron (Fe) – ligand (L) Fe_4L_6 N-cages ink (**Chapter 4.1.1**) was deposited n_L = 1, 5 and 10 printed layers upon 10 layers of iGr (2.4 wt%) (**Figure 5-4 a-c**). Upon deposition, the N-cage ink was dried in a natural convection oven (Carbolite Gero PN) at 100 °C for 1 hour. It was observed that for samples produced with n_L = 5 and 10, severe cracking occurred in the N-cage film. For n_L = 10, this cracking resulted in removal of the iGr sublayer. Electrical measurements were performed on n_L = 0, 1 and 5 N-cages (**Figure 5-4 d**). A small increase in resistance was noted between 0 and 1 layers (200 Ω/sq.). When $n_{L,N\text{-}cage}$ = 5, there was a large

increase in sheet resistance (18 kΩ/sq.), likely a result of the mechanical damage due to the cracking seen in the printed layer (**Figure 5-4 c**), disrupting the continuity of the graphene network in the iGr film beneath.

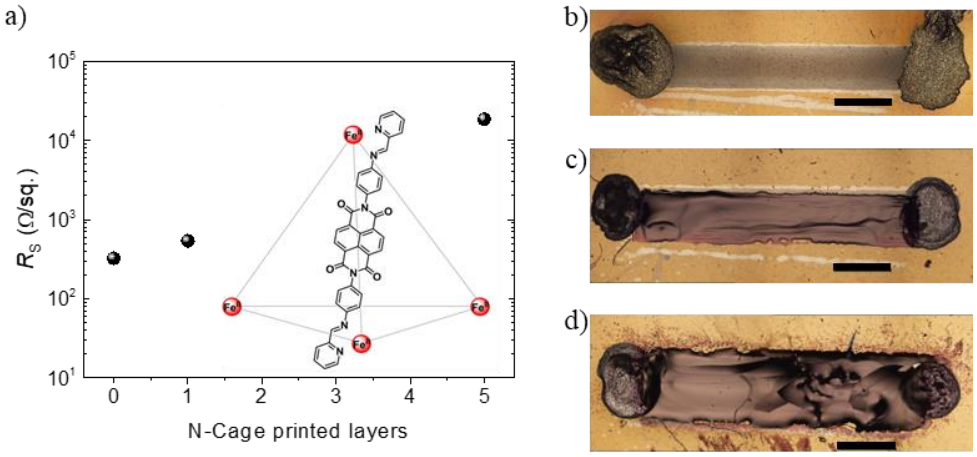


Figure 5-4 a) Dependence of sheet resistance of iGr-Nitschke cage devices on the number of printed Nitschke cage layers (Inset: structure of Fe_4L_6 Nitschke cages). **b)** An optical image of as printed iGr sample ($n_{L\text{-}iGr}$ = 10, $T_{substrate}$ = 60 °C, T_{anneal} = 250 °C, t_{anneal} = 1 hour). Optical images of Fe_4L_6 Nitschke cages deposited ($T_{substrate}$ = 30 °C, T_{anneal} = 100 °C, t_{anneal} = 1 hour) onto 10 printed layers iGr with **c)** $n_{L\text{-}Nitschke}$ = 1 and **d)** $n_{L\text{-}Nitschke}$ = 5. (scale bars = 1000 µm).

5.2 Post-processing of printed materials

Existing work detailing the production of fabric-based electronics manufactured by inkjet printing is limited. Current textile-based devices are often produced via screen printing, as this enables deposition of highly concentrated inks.[51,63] This presents a challenge for graphene formulations for inkjet printing, where the solid content of the ink is usually very low (0.5 - 6 wt%).[343–345] Printed inks often require a post-processing step to achieve electrical conductivity. The specific requirements of this stage vary depending on the material, both in terms of its purpose and the available techniques. Graphene-based inks typically contain additives and high boiling-point solvents to maintain printability; however, these components must be removed after printing. Therefore, an annealing stage is necessary to enable electrical conductivity. MeNP

inks require a sintering stage, which serves two key purposes: firstly, to remove solvents and particle coatings, secondly, to promote fusion of the MeNPs, forming a conductive network through particle-to-particle contact. Both annealing and sintering of inks is conventionally achieved with thermal processes, heating the printed materials at high temperatures (T_{anneal} > 250 °C, T_{sinter} > 150 °C)[17,159], for sustained periods of time. However, recent work has developed the use of photonic, low-temperature methods, which enable printing onto polymeric substrates with a low thermal degradation point.

5.2.1 Thermal annealing of iGr-fabric

iGr ink patterns printed directly onto textile substrates and thermally annealed (T_{anneal} = 250 °C, t_{anneal} = 4 hours) have no measurable electrical conductivity, likely due to wettability of the substrate and penetration of graphene flakes through fibres, limiting opportunity for formation of conductive graphene networks. Thus, a strategy is required to improve surface quality prior to iGr deposition. The high surface roughness of fabrics can be mitigated by adding a polymeric interface layer, thereby improving surface uniformity for the subsequent printed layer.[346] Current work is limited to evaluating the viability of functional materials printed onto textile substrates; however, there is a need to explore performance and the sensing capabilities of such devices.

In order to reduce the surface roughness and porosity, an interface layer of TPGDA was deposited onto fabric substrates prior to printing of graphene. Initial investigations were conducted to establish the appropriate n_L for the interface layer. As such, textile substrates were prepared with $n_{L\text{-}TPGDA}$ = 0, 1, 2, 3, 4, 5, 10, 20, 50 (**Figure 5-5 a**). The initial UV-curing strategy employed the scan-by-scan method, in which UV light is applied during the printing of each swathe of TPGDA. Next, 50 layers of the iGr ink

(1.2 wt%, Samba) were deposited upon the prepared textile-TPGDA substrates, and subsequently thermally annealed (T_{anneal} = 250 °C, t_{anneal} = 4 hours). Previous work at the University of Nottingham (Dr Feiran Wang), determined that applying the same t_{anneal} for iGr on Kapton (1 hour) was not sufficient, and prints had very high resistance (> 10^9 Ω). Some change in the fabric colour was observed after thermal annealing. Electrical measurements were performed, where it was established that n_L = 2 of TPGDA provides a sufficient interface layer, though no significant benefit was achieved with additional layers (**Figure 5-5 d**). However, for all samples there was large uncertainty observed in the electrical measurements. Optical microscopy was used to provide further comparison between samples (**Figure 5-5 c, b**). Samples were imaged with $n_{L\text{-}TPGDA}$ = 5, 50. With increasing thickness of the TPGDA layer (↑n_L), there was a significant change in macroscopic appearance and 3D features on the textile surface.

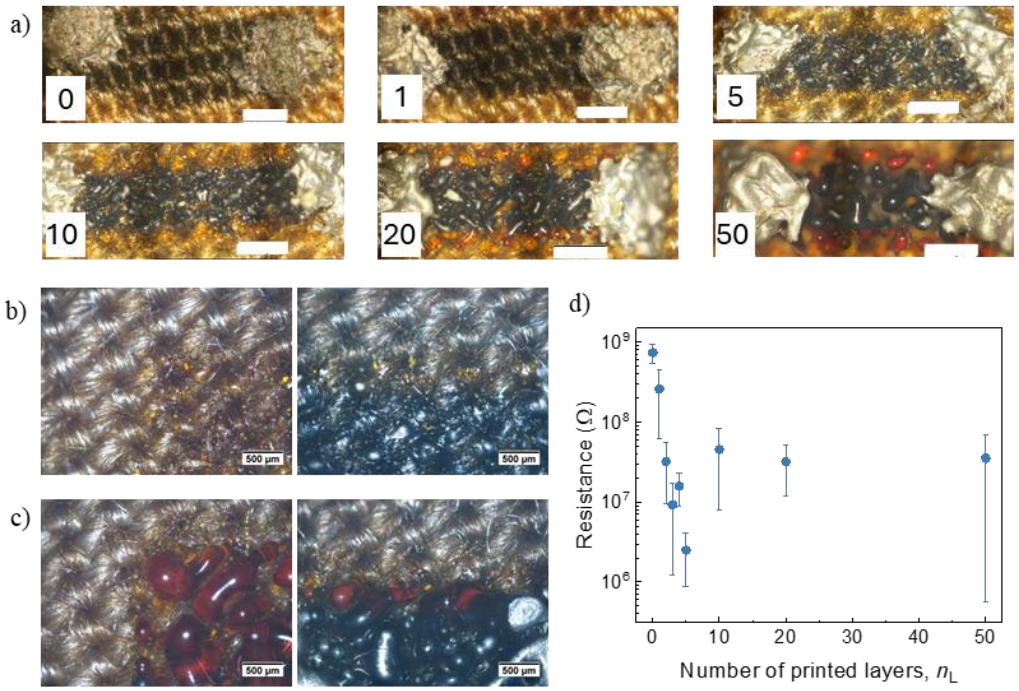


Figure 5-5 Optical microscopy for iGr-TPDGDA-textile samples ($n_{L\text{-}iGr}$ = 50, T_{anneal} = 250 °C, t_{anneal} = 4 hours) for **a)** $n_{L\text{-}TPGDA}$ = 0, 1, 5, 10, 20 and 50 (Scale bars = 1 mm).Optical microscopy images of textile substrates before and after iGr deposition **b)** $n_{L\text{-}TPGDA}$ = 5 **c)** $n_{L\text{-}TPGDA}$ = 50. **d)** Dependence of resistance on the number of printed TPGDA layers (SBS) for iGr ($n_{L\text{-}iGr}$ = 50, T_{anneal} = 250 °C, t_{anneal} = 4 hours). Error bars represent the standard deviation between samples used for measurement.

To improve the previous method for deposition of the TPGDA interface layer, a UV curing strategy was implemented, where UV light was applied after all ink was deposited, PPC. The rationale behind this approach was that a large volume of monomer ink can spread over the textile surface, reducing surface roughness, by occupying the textile structure with uncured ink and being allowed to flow into gaps before curing and solidification. To investigate the effectiveness of this strategy, samples were produced with $n_{L\text{-}TPGDA}$ = 5, 50 and $n_{L\text{-}iGr}$ = 50 (1.2 wt%, Samba) onto the textile substrate. Samples were thermally annealed at 250 °C for 4 hours. Electrical measurements were performed on the printed samples. Linear *I-V*s were observed for the PPC samples (**Figure 5-6 a**). In contrast, the *I-V* measurements for the SBS samples proved to possess high electrical resistance, this could be indicative of a less

uniform distribution of graphene flakes throughout the fabric structure (**Figure 5-6 a**, Inset). The PPC UV curing strategy, where $n_{\text{L-TPGDA}}$ = 50, achieved the lowest resistance. This can be attributed towards the effectiveness of the interface layer, which provided a more consistent and less porous surface for deposition (**Figure 5-6 e**).

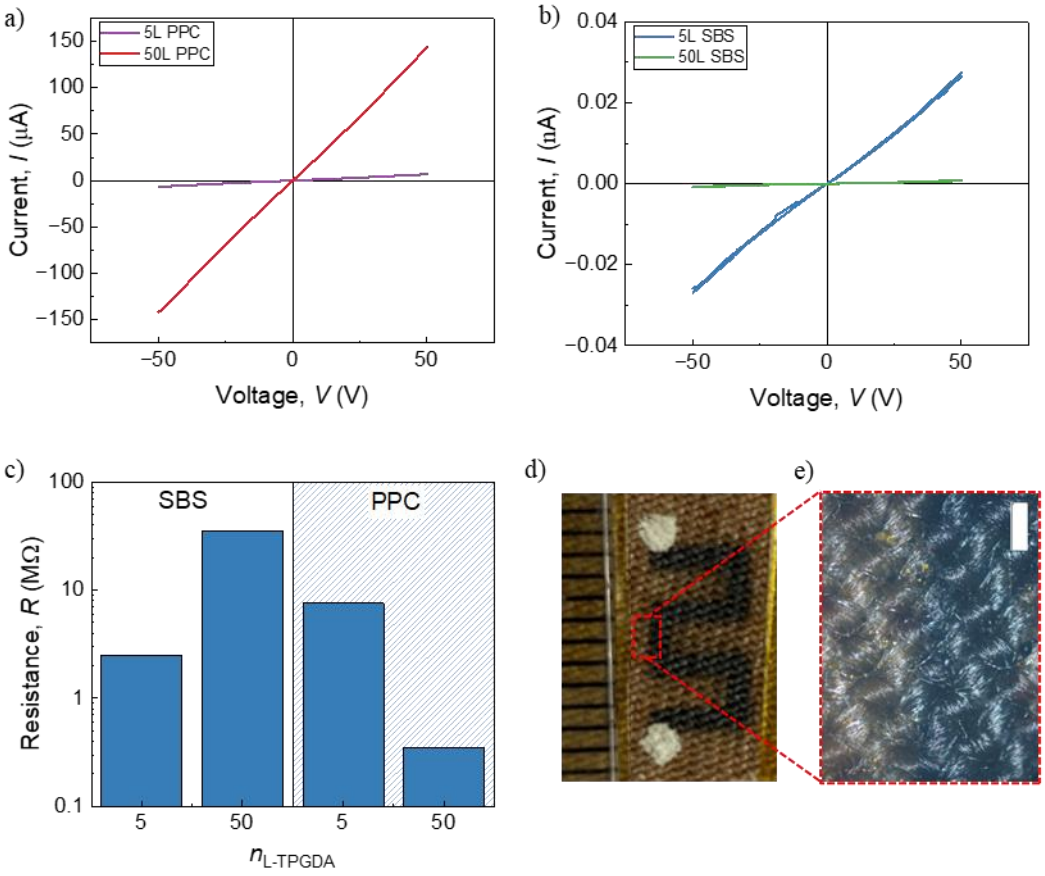


Figure 5-6 Current-voltage dependence for iGr-TPGDA-textile samples ($n_{\text{L-TPGDA}}$ = 5, 50, $n_{\text{L-iGr}}$ = 50, 1.2 wt% Samba) for **a)** PPC and **b)** SBS UV curing strategies. **c)** Resistance measurements for iGr-TPGDA-textile samples produced using different UV curing strategies. **d)** Optical image and **e)** optical microscope image of iGr-TPGDA-textile sample ($n_{\text{L-TPGDA}}$ = 50, $n_{\text{L-iGr}}$ = 50).

An FEI Quanta 650 ESEM was used to investigate the material deposition, of both TPGDA and graphene onto the fabric, as well as to better understand the substrate morphology. Samples were fixed onto stubs via carbon tape.

Three samples were prepared for ESEM; this included a textile sample, TPGDA printed onto fabric, TPGDA then graphene printed onto fabric. Both printed samples were produced with $n_{\text{L-TPGDA-PPC}} = 50$, $n_{\text{L-iGr}} = 50$ (1.2 wt% Samba). ESEM imaging of the untreated fabric cross-sectioned sample revealed that each bundle of strands possesses a loose and spacious structure, with the distance between strands taking an average value of 15.7 ± 7.8 μm (**Figure 5-7 a**). The bundles of strands had an average width of 320 ± 34 μm. It appeared that the TPGDA layer provides a coating on the individual strands, which is smooth in appearance, presenting an improved surface for the deposition and adhesion of graphene flake (**Figure 5-7 b**). Cross-sectioning of the fabric-TPGDA sample revealed that the inter-strand spacing within bundles is completely filled with the printed polymer (**Figure 5-7 c**), where the gaps observed were reduced to 3.9 ± 3.4 μm. This is a result of the PPC strategy, which allows the TPGDA ink to remain in liquid form during printing and occupy the spaces within the bundles of fibres prior to polymerisation. The fabric-TPGDA-iGr sample reveals coverage of graphene flakes on the TPGDA-coated fabric strands. This is seen by the rough surface texture on the strands compared to the previously smooth coating from the TPGDA (**Figure 5-7 d**). It is possible to resolve several large agglomerations of graphene flakes, approximately 2 μm across, which is a result of the high layer count of iGr. For reference, the graphene flake size in suspension, prior to printing, is 2590 nm^2.

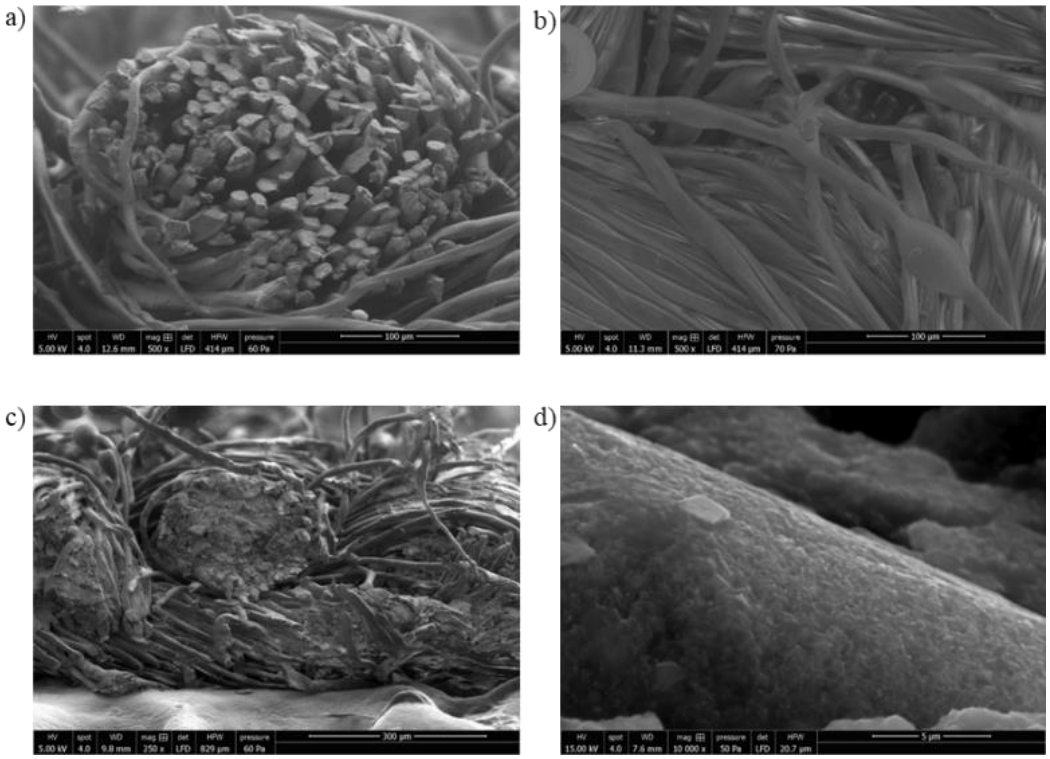


Figure 5-7 ESEM images illustrating the morphological and material deposition characteristics of **a)** the untreated fabric substrate **b)** 50-layer TPGDA printed onto fabric substrate **c)** 50-layer TPGDA printed onto fabric substrate, cross-sectioned to display inter-strand material deposition **d)** deposited graphene flakes resting on individual strands, a result of 50-layers graphene being printed on fabric-TPGDA samples. Images produced at the nmRC by Dr Nicola Weston.

5.2.2 IPL annealing of iGr

This work developed an IPL annealing protocol for inkjet-printing of graphene-EC ink on flexible and stretchable polymeric substrates. Based on the literature, IPL offers the potential for low-temperature annealing for iGr films, whereby substrate integrity is preserved during treatment, enabling deposition onto highly flexible and stretchable polymeric films. Raman spectroscopy was used to provide a comparison against previous results achieved with thermal annealing, confirming an increased reduction in defects and improved structural ordering of IPL-iGr films.

To better understand the effects of IPL-iGr, the process was systematically studied; investigating the number of printed layers, n_L, the number of IPL flashes, n_F, and the

iGr ink concentration effect upon sheet resistance of IPL printed films (**Figure 5-8 a, b**). Samples were printed with both the 1.2 wt% and 2.4 wt% graphene ink formulations onto Kapton film ($T_{substrate}$ = 60 °C) and subject to up to 25 flashes of IPL immediately after printing, with electrical measurements performed periodically. Increasing the number of flashes improved electrical conductivity for all samples. It was found that sample electrical conductivity increased with the number of flashes, attributable to cumulative annealing effects from IPL. This was observed across both graphene ink formulations, demonstrating the suitability of this annealing strategy for different printing systems. For each printed sample, when n_f reaches a certain point, the achieved sheet resistance saturates. This is dependent on the ink formulation and number of printed layers, e.g., for $n_{L\text{-}1.2wt\%}$ = 5, the saturation point occurs at n_f = 5, $n_{L\text{-}2.4wt\%}$ = 10, this is at n_f = 10. This was attributed to the reduced thickness of the printed samples and the penetration depth of the IPL system.

Optical microscopy was used to investigate the surface morphology of as-printed and IPL annealed samples (**Figure 5-8 c**) produced with the DMC (2.4 wt%) formulation with n_L = 10, 20. The as-printed samples appeared to still be wet, indicating incomplete evaporation of the solvents. After IPL annealing, samples appear dry, confirming that IPL treatment stimulates evaporation. Small splash marks can be observed around the edges of the IPL graphene samples, which may be a result of the rapid evaporation caused by IPL pulses. Due to the very short time duration of each flash (~ 4 ms), solvent could evaporate quickly, causing bubbling along the sample surface, and hence causing the splatter marks observed.

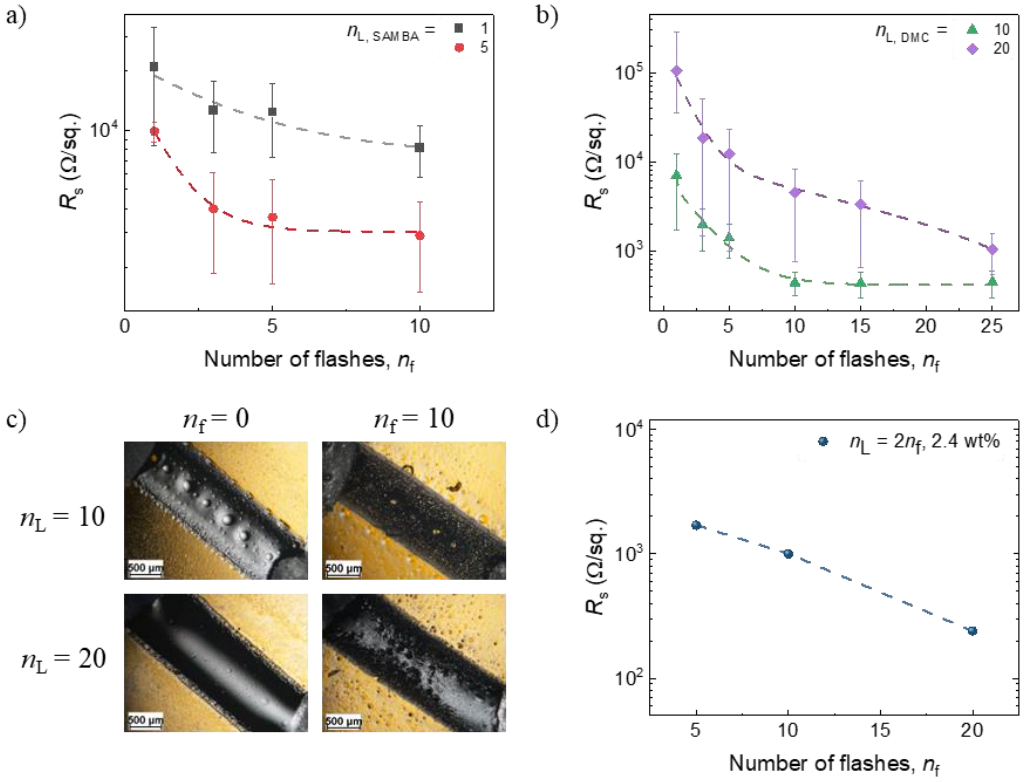


Figure 5-8 Dependence of sheet resistance of IPL annealed iGr samples vs number of printed layers, n_L for different numbers of IPL flashes, with $n_f = 1$ to $n_f = 25$, for **a**) Samba formulation (1.2 wt%) and **b)** DMC formulation. Error bars represent the standard deviation between sampes used for measurement. The dashed lines are a guide to an eye. **c)** Optical images of DMC formulation (n_L = 10, 20) as-printed (left) and after IPL annealing n_f = 10 (right) **d)** samples annealed with in-situ IPL process (2.4 wt% DMC), where instead of flashing samples with IPL after printing, the samples are flashed once every two printed layers.

The effectiveness of n_f on sample electrical conductivity is significantly affected by the print thickness. It was thought that for increasingly thicker samples, there would be a cut-off point for where IPL annealing is effective, due to a maximum optical penetration depth through the film. To overcome this effect, the IPL annealing was applied on a layer-by-layer basis during the printing process. As such, 1 IPL flash was delivered for every 2 printed layers (**Figure 5-8 d**) for up to $n_f = 20$ and $n_L = 40$ (iGr 2.4 wt%, DMC). For samples with $n_f = 10$ and $n_L = 20$, there appeared to be no benefit compared to cumulative IPL annealing, where the sheet resistances obtained were 1000 and 440 Ω/sq. respectively. When the number of flashes and layers exceeds this,

$n_f = 20$ and $n_L = 40$, sheet resistance $R_S = 240$ Ω/sq., demonstrating the benefit of the *in situ* layer-by-layer IPL treatment. No significant changes of R_S after $n_f = 20$ occur after saturation is reached, and sheet resistance does not improve on 440 Ω/sq.

The effectiveness of IPL annealing was evaluated on a range of substrates, both polymeric and non-polymeric. For all samples, 10 layers of the 2.4 wt% DMC formulation were deposited, and 10 flashes of IPL applied. The IPL annealing method was effective for iGr on PEN, PET, Kapton, and Beyolex, achieving sheet resistance values, $R_s < 10^3$ Ω/sq (**Figure 5-9**). On rigid, non-polymeric substrates, including glass, Si/SiO_2, and Sapphire, IPL annealing of iGr was ineffective resulting in poor electrical conductivity, with $R_s \approx 10^4$, $\approx 10^7$, and $\approx 10^9$ Ω/sq, respectively (**Figure 5-9**). The sheet resistance of iGr scales with substrate thermal conductivity, as $R_S \sim k_{substrate}^2$, suggesting that heat dissipation plays an important role in IPL annealed efficiency.[259]

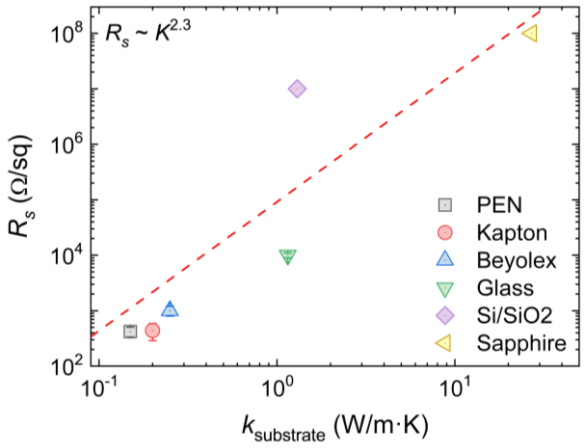


Figure 5-9 Dependence of Sheet resistance of IPL annealed graphene ($n_L = 10$, $n_f = 10$, 2.4 wt% DMC formulation) on substrate thermal conductivity, $k_{substrate}$. Error bars represent the standard deviation between sampes used for measurement.

To better understand the changes that occur in iGr during IPL annealing, micro Raman spectroscopy was performed. Printed iGr samples on Kapton were investigated, before

and after IPL annealing with $n_f = 1$ and $n_f = 20$ (**Figure 5-10 a**). In all spectra, peaks were observed at 1350 cm^{-1} (D-band), 1580 cm^{-1} (G-band), and 2700 cm^{-1} (2D-band), which are attributed to the presence of few-layer graphene in the printed films.[347,348] Following successive IPL flashes, a slight broadening of the 2D peak is observed along with an increase in its symmetry, and the emergence of a broad peak under the D and G bands (**Figure 5-10 a)**. This broad peak is attributed to the emergence of an amorphous carbon phase resulting from the formation of carbon char following the degradation of EC during IPL annealing.[349]

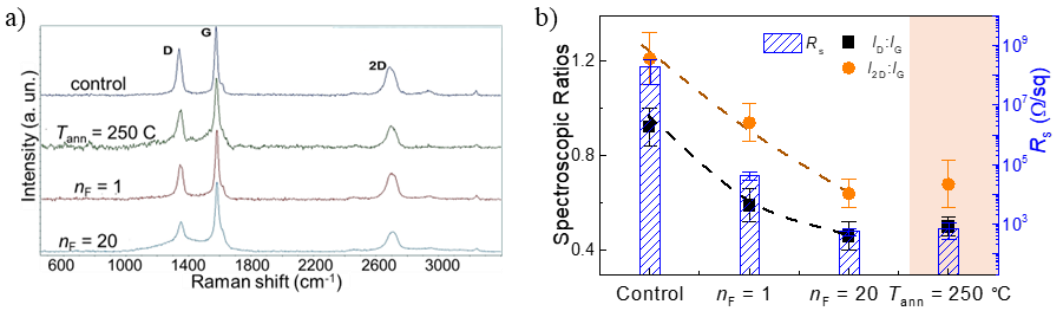


Figure 5-10 a) Raman spectra of iGr films (n_L = 10 printed layers, 1.2 wt%) on Kapton substrate, before annealing, following thermal annealing at T_{ann} = 250 C for 2 hours, and following IPL annealing with n_f = 1 and n_f = 20. **b)** Graph showing average spectroscopic ratios and sheet resistances for of iGr films (n_L = 10 printed layers, 1.2 wt% Samba) on Kapton substrate as printed and then with increasing degrees of IPL annealing with n_f = 1 and n_f = 20, and thermal annealing (T_{anneal} = 300 °C). Error bars represent the standard deviation between sampes used for measurement. The dashed lines provide a guide to follow for each trend.

The spectroscopic ratio is the intensity ratio of the D to G and 2D to G peaks measured by Raman spectroscopy. The ratios I_D:I_G and I_{2D}:I_G provide quantitative descriptors indicating the number of structural defects (the extent of deviation of the crystalline arrangement from a perfect hexagonally organized planar network of carbon atoms) and the length scale of graphitic ordering (symptomatic of interlayer organization), respectively.[159,349,350] Prior to annealing, the iGr films displayed an average I_D:I_G ratio of 0.92 ± 0.08 and an I_{2D}:I_G ratio of 1.21 ± 0.11 (**Figure 5-10 b**). Both of these ratios decreased after IPL annealing at n_f = 1: to I_D:I_G = 0.59 ± 0.07 and I_{2D}:I_G = 0.94 ± 0.08.

These values are comparable to those previously measured for thermally annealed iGr films using T_{anneal} = 250 °C, t_{anneal} = 1 hour.[159] However, with successive IPL flashes, a further reduction in these ratios was observed, to I_D:I_G = 0.46 ± 0.06 and I_{2D}:I_G = 0.64 ± 0.06 for n_f = 20 (**Figure 5-10 b**). The decrease of both spectroscopic ratios indicates a reduction in the defect density within the graphitic lattice and a decrease in interlayer organisation.[350,351] Hence, it was noted that when n_f > 1, there is greater structural ordering in the iGr films than was demonstrated for any thermal annealing condition up to T_{ann} = 400 °C.[156]

Due to improved structural ordering of graphene and an increase in the amount of carbon char with successive IPL flashes, the sheet resistance of the iGr films improves down to R_s = 560 ± 150 Ω/sq. for n_f = 20 IPL flashes (**Figure 5-10 b**, blue bars). As suggested by the Raman studies undertaken, this is an improvement on thermal annealing, where identical samples annealed at T_{ann} = 250 °C for 2 hours achieved R_s = 800 ± 300 Ω/sq.. Raman mapping over a 50 μm^2 (**Figure 5-10 c)** area showed good uniformity of the composition of the graphene layer; however, optical microscopy showed the presence of small circular features on the iGr film surface following IPL annealing (8.3 ± 1.5 μm in diameter), which are likely formed due to rapid solvent evaporation during IPL annealing.

Further examination of the Raman maps (**Figure 5-11**) supports the previous results detailing the effectiveness of IPL annealing upon different substrates. In this case, significant reductions in the I_D:I_G and I_{2D}:I_G ratios for IPL-iGr on both Kapton and PEN were observed. However, for the IPL-iGr sample produced on sapphire, which possesses a much higher thermal conductivity than the polymer counterparts in this study, there is no observed change in these ratios. As such, this further quantifies the

relationship between substrate thermal conductivity and the effectiveness of IPL annealing.

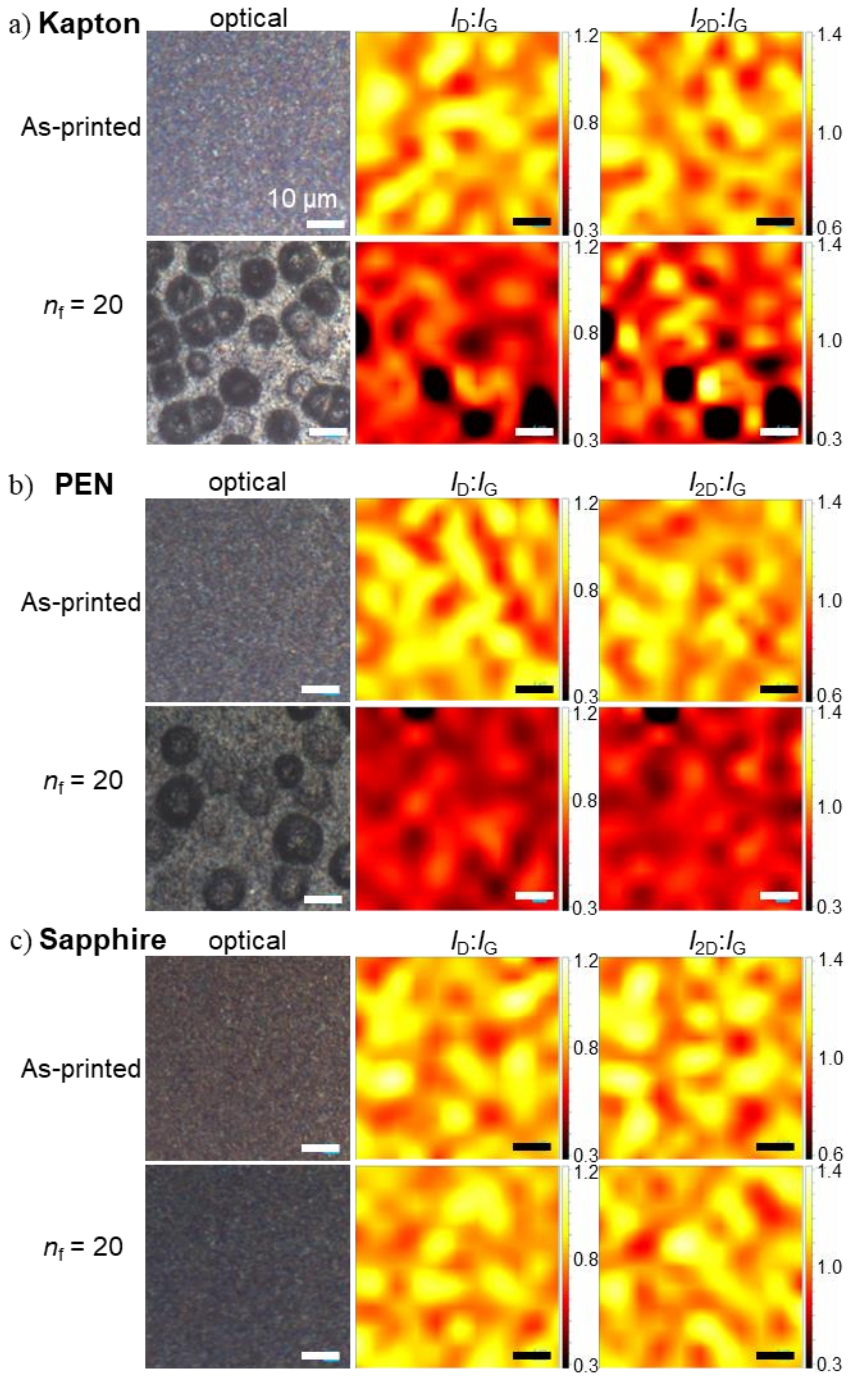


Figure 5-11 Optical images (left) and Raman maps of I_D:I_G (middle) and I_{2D}:I_G (right) ratios of iGr films on **a)** Kapton, **b)** PEN and **c)** Sapphire (n_L = 5 printed layers, 2.4 wt% ink printed with DMC cartridge) before (top) and after (bottom) IPL annealing with n_f = 20 of IPL. Black pixels in the bottom images correspond to locations where fluorescence was dominant and it was not possible to extract structural information on iGr. Scale bar in all images is 10 µm. Images produced at the nmRC by Dr Graham Rance.

3D optical profilometry was carried out on an IPL annealed iGr sample (n_L = 10, $T_{substrate}$ = 60 °C, n_f = 10, Kapton). Curvature of the Kapton substrate was observed at the edges of the *xyz* profile (**Figure 5-12 a**). To allow for calculation of the film thickness, a polynomial fit was applied to the curved section of the *yz*-profile and then subtracted to effectively baseline the dataset (**Figure 5-12 b**). This enabled the film thickness to be estimated as 0.94 ± 0.08 µm.

In agreement with the Raman mapping observations (**Figure 5-11 a, b**), circular features were observed on the surface of the iGr film. It was estimated that these features reach 4.0 ± 1.0 µm in height and have a diameter of 7.2 ± 1.9 µm from profilometry observations. As previously stated, this is most likely caused by rapid solvent evaporation during IPL annealing, due to the short pulsing duration (~4 ms).

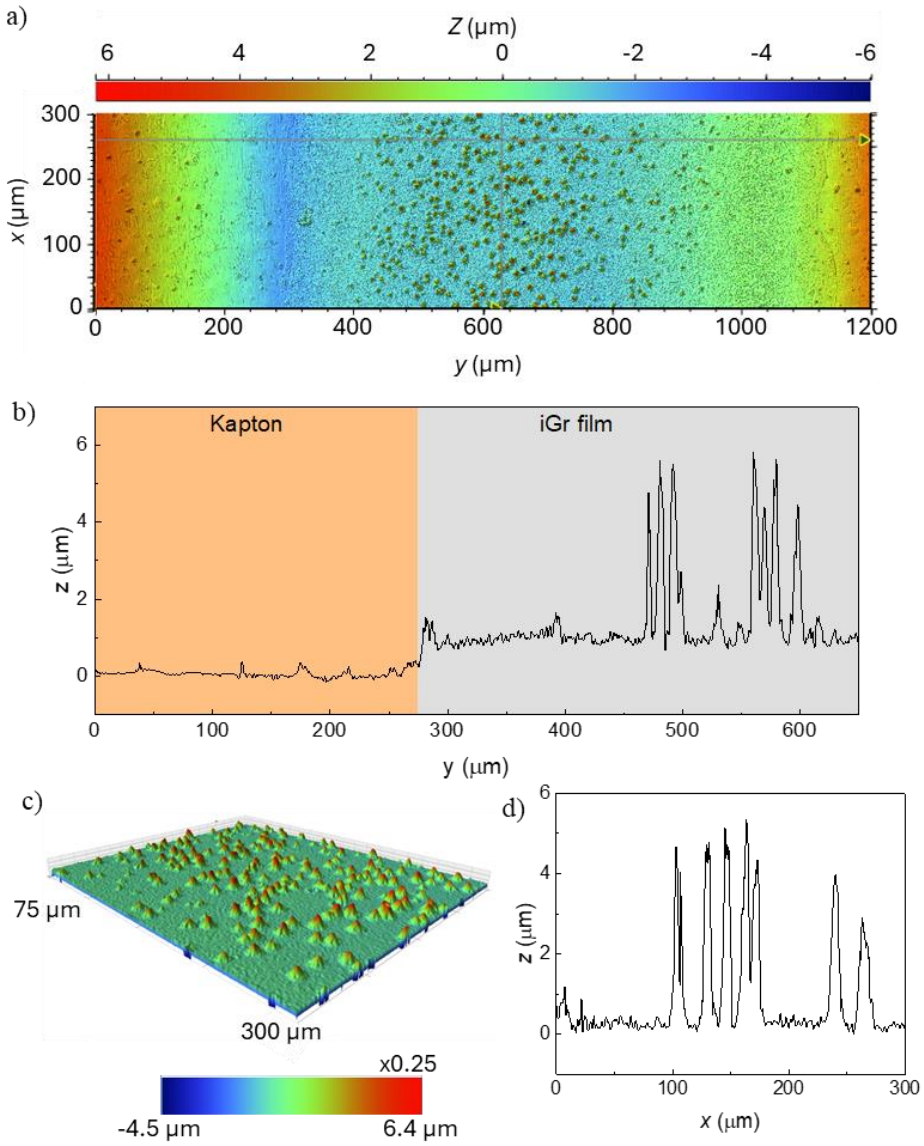


Figure 5-12 Optical profilometry of IPL annealed iGr (n_L = 10, $T_{substrate}$ = 60 °C, n_f = 10). **a)** 2D surface map showing height variation across the sample. **b)** y-z profile of section across sample with regions for Kapton (orange) and iGr (grey) highlighted. **c)** 3D surface reconstruction of iGr surface detailing protrusions. **d)** x-z profile of section across sample, detailing height of surface protrusions.

SEM was performed on samples of iGr, that were both thermally and IPL annealed, to further investigate the surface morphology to determine whether the presence of the small protrusions was dependent on the annealing strategy, whilst also comparing the differences in surface morphology between the different annealing techniques. Samples were prepared with n_L = 10 , then either thermally or (T_{anneal} = 250 °C, t_{anneal}

= 1 hour) IPL annealed (n_f = 25). The thermally annealed iGr was very smooth in appearance, with no distinct surface features (**Figure 5-13 a, b**). In contrast, the IPL sample exhibited a much more disrupted surface morphology, with large features up to 50 µm in size. Circular shapes, similar to those previously seen in Raman mapping (**Figure 5-11 a**) and profilometry (**Figure 5-12 c**) could also be observed via SEM (**Figure 5-13 c, d**). These were measured to have a diameter of 8.3 ± 2.3 µm.

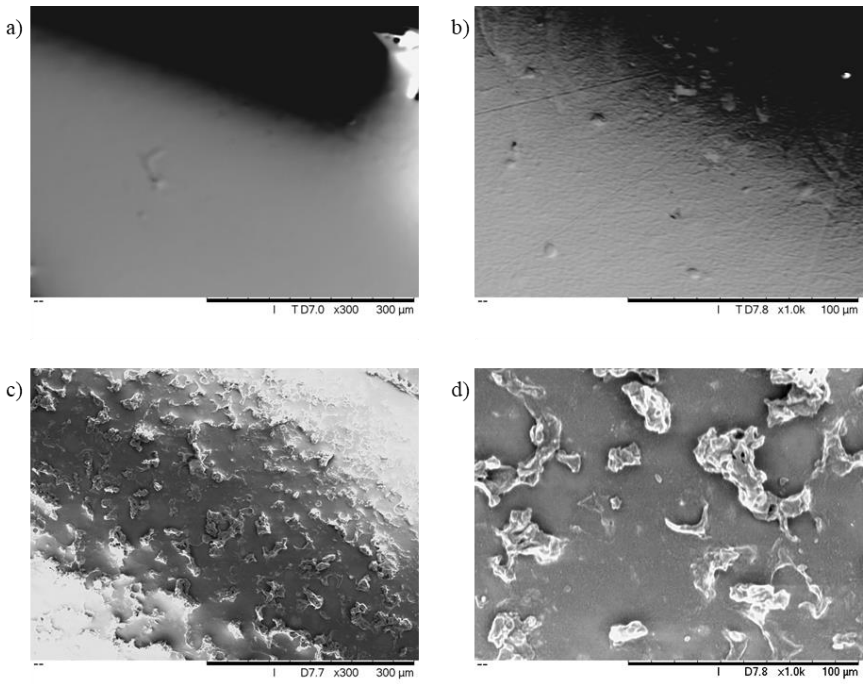


Figure 5-13 SEM images of iGr films (n_L = 10, 2.4 wt%, DMC) that are **a,b)** thermally (T_{anneal} = 250 °C, t_{anneal} = 1 hour) and **c,d)** IPL annealed (n_f = 25).

There is good agreement among the three techniques used to characterise surface morphology: IPL produces a unique surface geometry in the form of circular protrusions. Furthermore, the measurements for diameter from each technique are largely consistent, with significant overlap of the error bars suggesting good agreement (**Figure 5-14**).

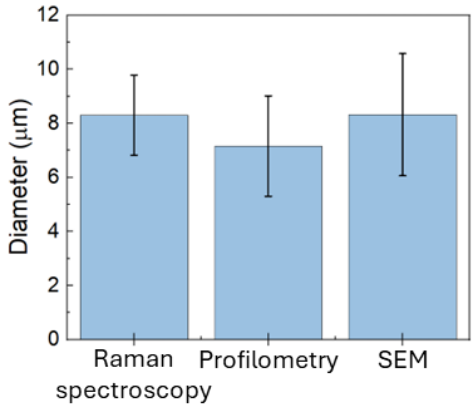


Figure 5-14 Feature diameter as measured with different characterisation methods. Error bars represent the standard deviation between sampes used for measurement.

The long-term stability of IPL annealed graphene films was measured, indicating the suitability of printed devices for sustained operation. It was observed that after 12 months storage in air, at room temperature (~ 20 °C) and in a dark container, there was no deterioration seen in printed samples (**Figure 5-15**). There was, in fact, a small increase in electrical resistance for each sample monitored.

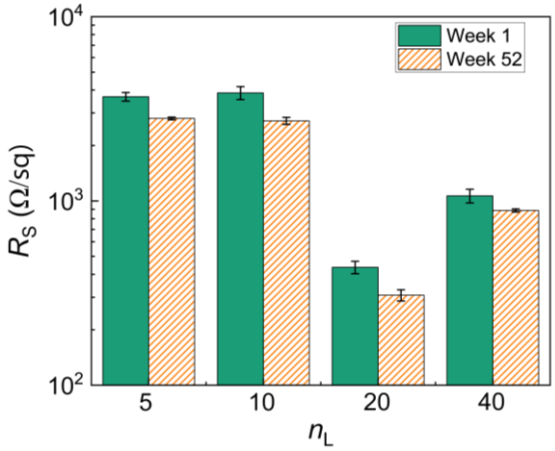


Figure 5-15 Sheet resistance of IPL-iGr films on Kapton annealed (2.4 wt% ink with DMC cartridge, n_f = 25) measured at the time of printing and after 1 year storage in in air, at room temperature (~ 20 °C) and in a dark container. Error bars represent the standard deviation between samples used for measurement.

5.2.3 UV annealing of graphene/PEDOT:PSS

Previous studies have shown an enhancement of electrical properties of PEDOT:PSS following exposure to UV light[285] and so the effects of UV exposure on the sheet resistance of the inkjet-printed Gr/PEDOT:PSS ink was explored. Samples were inkjet-printed on Kapton (n_L = 20; $T_{substrate}$ = 30 °C) and subjected to UV exposure (365 nm, 282 mW cm^{-2}) for a duration of up to 60 minutes. Electrical measurements were performed after UV exposure times of t_{UV} = 0, 0.5, 1, 3, 5, 10, 30, 60 minutes. A DHT22 temperature sensor was placed adjacent to the sample during UV exposure, recording a maximum temperature of T = 80 °C. Even short time exposure to UV light (for 30 sec) led to decrease in sheet resistance of the printed film from 625 ± 23 Ω/sq. to 373 ± 25 Ω/sq. After t_{UV} = 30 min no significant change occurred, where the sheet resistance saturated at 254 ± 44 Ω/sq. (**Figure 5-16 a**). A large uncertainty at t_{UV} = 60 min can be observed, suggesting a possible degradation in the printed films after this time, which could be due to prolonged heating from the UV lamp. This is in agreement with the earlier results (**Chapter 5.1.2**) showing that thermal annealing at T_{anneal} = 100 °C leads to a small increase in sheet resistance by ~ 40 Ω/sq.. Note, the boiling point of the solvent, DMF ($T_{boiling}$ = 153 °C), is higher than the maximum temperature induced by UV light, so no compositional changes are expected. Further studies are needed to fully evaluate the mechanism of annealing in these samples, such as Raman spectroscopy on samples before and after UV irradiation which could provide information on structural changes in the PEDOT:PSS.

Optical microscopy was used to investigate for morphological surface changes in the printed films before and after UV annealing (**Figure 5-16 b, c**). No significant macroscopic defects, such as cracks and peeling, were observed in the

Gr/PEDOT:PSS, suggesting there are no detrimental effects to the morphology of the printed films after UV exposure up to 60 minutes.

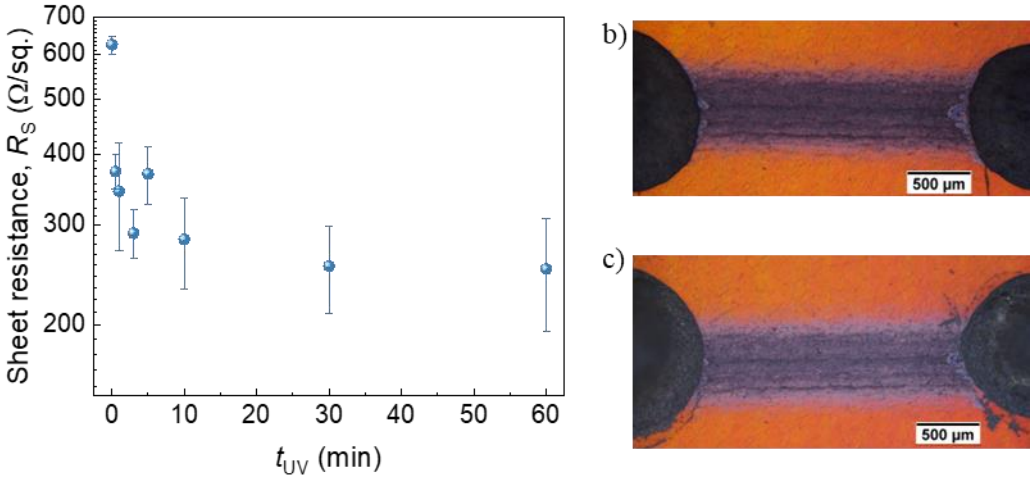


Figure 5-16 a) Effect of UV exposure (395 nm) on the electrical properties of inkjet-printed Gr/PEDOT:PSS on Kapton (n_L = 20; $T_{substrate}$ = 30 °C). Optical microscopy images of the Gr/PEDOT:PSS sample following. Error bars represent the standard deviation across all samples used. **b)** t_{UV} = 0 min and **c)** t_{UV} = 60 min.

5.2.4 UV annealing of GO

The reduction of GO has commonly been achieved through chemical or thermal methods, with both approaches having drawbacks. Chemical reduction can leave behind chemical residues in the GO, whilst thermal reduction requires heating to high temperatures (500-1000 °C) limiting substrate selection, and is more time-consuming.[282,352] Photonic reduction of GO has seen an emergence in recent years, whereby exposing the material to IPL can achieve low-temperature sintering.[353] UV irradiation is demonstrated here as an effective photonic sintering tool, facilitated by the high absorption presented by GO in the region of 365 nm.

The GO ink, containing 4 mg/ml dispersion of GO flakes (~ 5 - 7 µm in diameter) in deionised water, was printed using the Dimatix/Samba system to establish printability

and electrical properties with respect to the number of printed layers and optimal UV exposure post-deposition. An initial sample of 10 × 10 mm with 10 printed layers was prepared in order to optimise the duration of UV exposure with respect to film damage. UV exposure to a 365 nm UV lamp was performed for 0, 30, 60, and 120 s to determine the optimal duration. It was determined that 30 s was sufficient, as UV exposure beyond this point resulted in deterioration of the printed film, with loss of adhesion to the substrate. Samples were prepared at 1, 3, 5, 10, 15 and 20 printed layers (5 x 1 mm). Sheet resistance of 628 ± 178 Ω/sq. was observed with n_L=10 (**Figure 5-17**).

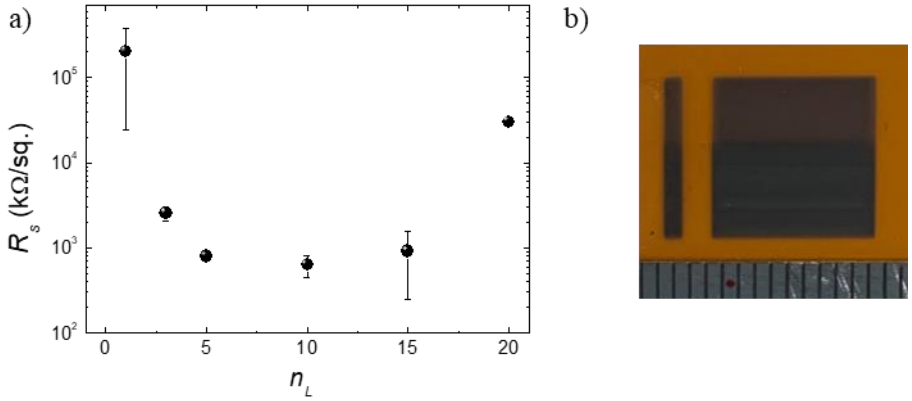


Figure 5-17 a) Dependence of sheet resistance of printed GO on the number of printed layers (5 x 1 mm, n_L=1, 3, 5, 10, 15, 20, Dimatix/Samba). Error bars represent the standard deviation between sampes used for measurement. **b)** optical image of inkjet-printed GO (n_L = 30, 1 x 1 cm).

This study demonstrates UV irradiation as a suitable method for the reduction of inkjet-printed GO, offering low temperature and low power conditions. It was found that n_L = 10 provided the lowest resistance when subject to 30 s UV irradiation. For n_L < 10, it is likely that the coverage of GO flakes on the substrate is sparse, resulting in reduced conductive pathways. For samples produced with n_L > 10, the absorbance of the printed film is higher, resulting in reduced exposure of the bottom layers to UV light. Therefore, for thicker printed sample (n_L > 10), *in situ* UV irradiation is

beneficial, for example after every 10 printed layers to ensure consistent annealing throughout the sample volume.

5.2.5 UV sintering of AuNPs

Thermal sintering is typically performed at T = 140 °C to 300 °C,[17,354] which is not suitable for materials with low thermal degradation temperature, such as PEN (T_{glass} = 120 °C).[355] This work evaluates the use of the photocleavable ligand, *o*-nitrobenzyl thiol (NT), functionalised on the surface of AuNPs, enabling ultralow-power UV-induced nanoparticle sintering.

The NT-AuNP ink, as received from Dr Jisun Im (University of Warwick), was printed onto PEN in a rectangular (7 mm x 0.1 mm) pattern. Samples were prepared with n_L = 1, 5 and 5 printed layers. Post-deposition, the printed AuNP patterns were exposed to 365 nm UV light (282 mW cm^{-2}) for a duration of up to 5 minutes. Electrical measurements were performed after 0.5, 1, 2, 3 and 5 minutes of cumulative UV sintering.

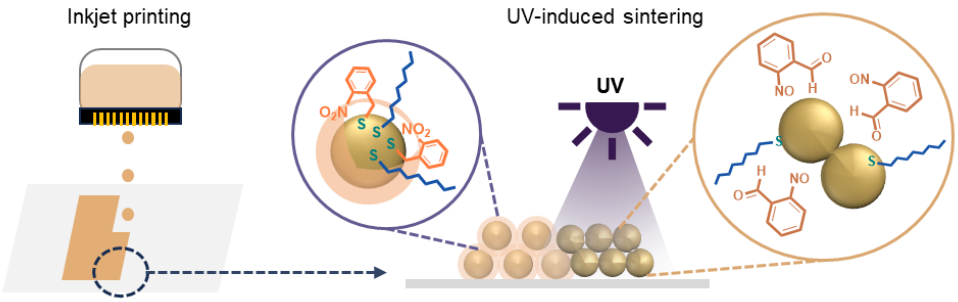


Figure 5-18 UV-induced photonic sintering of the inkjet-printed NT-AuNPs on a flexible polymer substrate. Schematic description of inkjet printing the nano-ink and UV-induced NT ligand cleavage and nanoparticle sintering.[356]

The sheet resistance of the printed AuNPs decreased with increasing the number of printed layers. This can be attributed to an improvement of uniformity and coverage

of the AuNP film on the PEN. The sheet resistance when $n_L = 5$ for the printed NT-AuNP pattern on a PEN substrate decreased from insulating ($R_S > 10^9$) to 7.23 ± 6.60 Ω/sq. after 30 seconds of UV irradiation and further decreased to 3.86 ± 3.24 Ω/sq. after 5 minutes of UV irradiation (**Figure 5-19 a**). When compared with alternative photonic sintering methods for other highly conductive metals, electrical conductivity values observed for samples ($\sigma = 7.0 \times 10^6$ S/m, $n_L = 5$, t_{UV} = 5 min) are comparable with NIR (36 W/cm^2), laser ($1.47 \times 10^6 – 1.63 \times 10^7$ W/cm^2) and IPL (371 – 4099 W/cm^{-1}) sources, with peak power densities 4 to 6 orders of magnitude higher than the UV LED source used in this work (0.28 W/cm^2) (**Figure 5-19 b**). AgNPs were effectively sintered using NIR, IPL and laser sources, with achieved conductivities in the range of ~10^7 – 10^8 S/m. Whilst the electrical conductivity is higher than achieved with the NT-AuNPs, the power densities used in these works are significantly higher (50 - 10^4 W/cm^2).[262,270,357] Conductivities of a more similar range were demonstrated with copper and zinc (~$2 \times 10^6 – 2 \times 10^7$ S/m), both using IPL, but again the power densities required exceed those used in this work.[225,266,267,269,358] This demonstrates the efficacy of the photocleavable ligands for ultralow-power UV-induced AuNP fusion, especially when compared with other highly conductive metals and different photonic sintering methods.

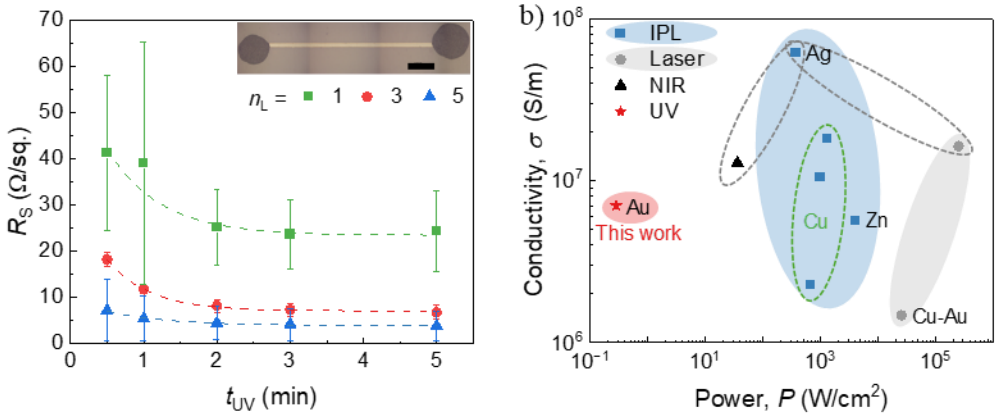


Figure 5-19 UV-induced photonic sintering of the inkjet-printed NT-AuNPs on a flexible polymer substrate. **a)** Sheet resistance (R_s) of inkjet-printed NT-AuNP conductive patterns on a polymer substrate as a function of UV irradiation time (t_{UV}). Error bars represent the standard deviation between samples used for measurement. The dashed lines provide a guide to follow for each trend (Inset: An optical image of the inkjet-printed NT-AuNP pattern with a single printed layer on a polymer substrate. The scale bar represents 1 mm). **b)** Electrical conductivity (σ) versus peak power density (P) for the comparison of ultralow-power UV sintering (this work) with other photonic sintering results.[225,262,266–270,357,358]

The suitability of this ink formulation for long-term usage was investigated. Electrical measurements were performed 24 months after the initial printing, on samples (n_L = 5, t_{UV} = 5 min). Samples were stored in air, at room temperature (~ 20 °C) and in a dark container. It was found that samples saw an increase in sheet resistance from 3.86 ± 3.24 Ω/sq. to 5.40 ± 1.77 Ω/sq., however, as this is within the error of the as-printed measurements and the same order of magnitude as the original value. It is therefore concluded that the samples are stable with respect to electrical properties in storage.

SEM was performed to confirm sintering effects from the application of UV light. Two drop casts of the NT-AuNP ink were prepared on glass slides, with one being subject to 5 minutes of UV sintering and the other left as deposited. In the sample without UV sintering, there is no evidence of a unified network of AuNPs (**Figure 5-20 a**), supporting the requirement for post-processing, and that no electrical conductivity should be expected at this time. The sample prepared with 5 minutes of UV sintering shows the formation of a continuous film of connected NPs (**Figure 5-20 b**).

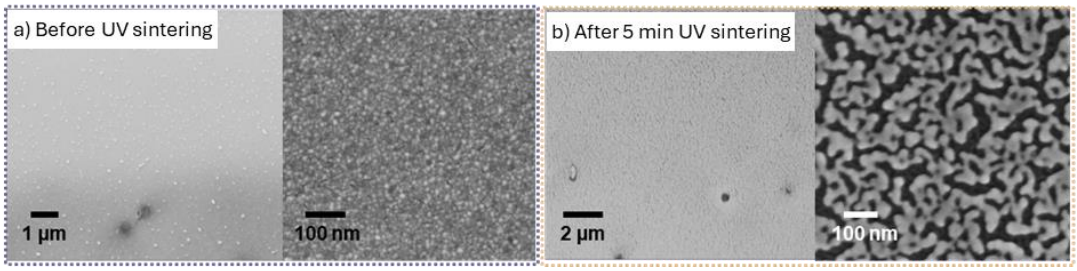


Figure 5-20 Representative SEM images of inkjet-printed NT-AuNPs patterns **a)** before and **b)** after UV irradiation for 5 min.

Transmission electron microscopy was performed on samples of the NT-AuNPs ink, prepared on TEM grids, exposed to UV sintering at intervals of 0, 0.5, 1, 5 and 30 minutes (**Figure 5-21**). This study revealed that fusion of the NPs becomes increasingly more significant with further application of UV sintering. This supports the observation of **Figure 5-19 a**, whereby improving the fusion of NPs increases the available pathways for electrical conductivity.

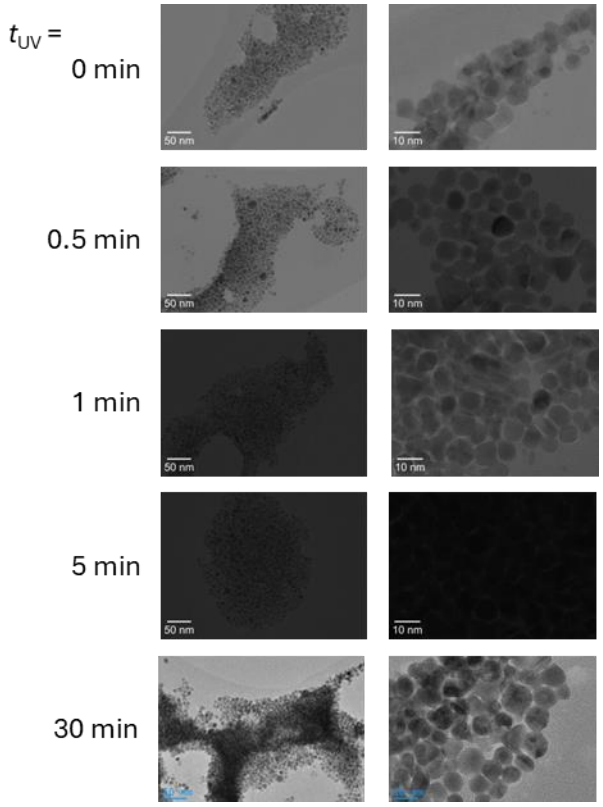


Figure 5-21 TEM analysis of areas with high density of NT-AuNPs exposed to UV irradiation for 0, 0.5, 1, 5, and 30 minutes.

TGA analysis confirmed desorption of the NT ligands under UV irradiation. Octane thiol functionalised gold nanoparticles (OT-AuNPs) synthesised by the modified Brust method were received from Ms Ashleigh Murray (University of Nottingham). The octane thiol ligands would remain unchanged under UV irradiation, and as such could act as the control sample for this work. In order to investigate the effects of UV, samples were dispersed in dichloromethane (DCM) and deposited onto a glass slide. Once dried, both the NT-AuNP and OT-AuNP deposits were subject to 30 minutes of UV irradiation (365 nm). The UV sintered AuNPs were then mechanically removed from the glass slide, ready for TGA. NT-AuNP and OT-AuNP samples were also prepared for TGA without UV irradiation, enabling measurement of the mass loss from UV sintering and ligand desorption (**Figure 5-22**).

No significant difference was observed in the TGA mass loss of the OT-AuNPs before and after UV sintering. The NT-AuNPs exhibited a 10 % change in mass before and after UV irradiation, confirming desorption of the *o*-nitrobenzyl thiol ligands, as expected for these photocleavable ligands.

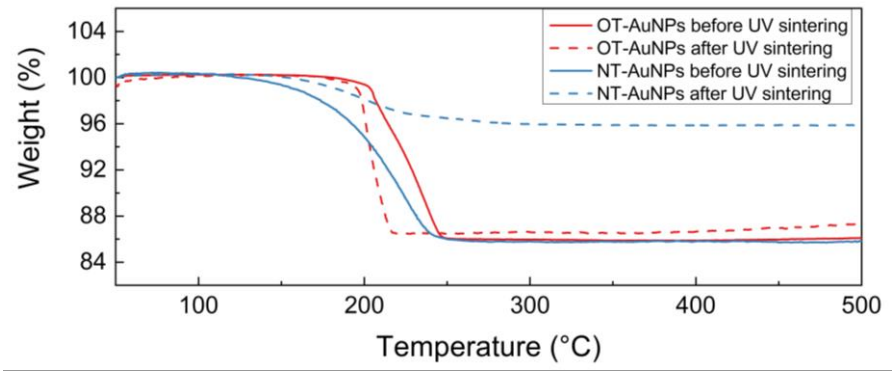


Figure 5-22 TGA analysis of OT-AuNPs and NT-AuNPs before and after UV irradiation.

TGA confirmed the UV-induced desorption of the photocleavable ligands from AuNPs, enabling low-power and low-temperature sintering. This validates the results of the inkjet-printed NT-AuNPs, where a significant decrease in sheet resistance was observed on exposure to the UV source, whilst also achieving electrical conductivity comparable to alternative photonic methods, but at a significantly lower power.

5.3 Material suitability for printed wearable electronics

The evaluation of the electrical properties of inkjet-printed functional materials enables analysis of their suitability for wearable electronic devices and the effectiveness of post-processing methods. The UV curable AuNPs exhibited high electrical resistance when deposited on PEN, whilst maintaining performance when subject to mid-range cyclic bending. Due to the high electrical conductivity observed, the AuNPs would be well-suited to function as a connecting circuitry for fully printed devices.

For sensing applications, two inks were explored: the iGr and Gr/PEDOT:PSS. The iGr ink requires an annealing process, in which the effectiveness of IPL is demonstrated, superseding the conventionally used thermal process for deposition onto polymer substrates with low-temperature resistance. Whilst effectiveness of IPL annealing on substrates with high thermal conductivity ($k_{substrate} < 10$ W/m.K) was low, this post-processing method offers significant benefit for wearable devices. The Gr/PEDOT:PSS was not affected by thermal post-processing, hence can be used as-printed, demonstrating high suitability for the flexible and stretchable substrates, which do not permit thermal annealing.

In this work, effect of post deposition treatment on electrical properties of printed graphene was evaluated on the following samples: iGr (TA-iGr), IPL-annealed iGr (IPL-iGr) and the Gr/PEDOT:PSS ink. All samples had sheet resistance of R_S in the range from 300 to 700 Ω/sq. (**Figure 5-23**). Important factors for this assessment are the number of printed layers and the solid content of the inks. While the Gr/PEDOT:PSS ink was typically deposited with $n_L = 20$ and the iGr ink with $n_L = 10$, they contain significantly different amounts of graphene (iGr = 1.2 wt%; Gr/PEDOT:PSS = 0.11 wt%). Whilst fewer printed layers are desirable for a faster printing process, the Gr/PEDOT:PSS ink would lead to thinner printed films due to low solid content and may be better suited for printing of flexible devices. Overall, both graphene-based inks are suitable for use in sensing devices.

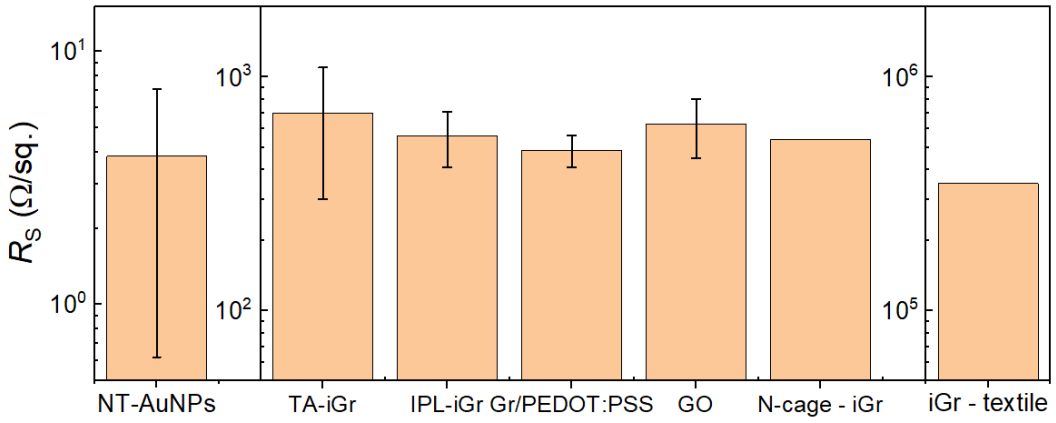


Figure 5-23 Comparison of sheet resistance for inkjet-printed functional materials used in this work, post processed using UV, TA and IPL annealing. Error bars represent the standard deviation between sampes used for measurement. Samples were produced with $n_{L\text{-NT-AuNPs}}$ =5, $n_{L\text{-TA-iGR}}$ = 10, $n_{L\text{-IPL-iGr}}$ = 10, $n_{L\text{-Gr/PEDOT:PSS}}$ = 20, $n_{L\text{-GO}}$ = 10, $n_{L\text{-Nitschke}}$ = 1, $n_{L\text{-iGr (Nitshcke)}}$ = 10, $n_{L\text{-TPGDA (textile)}}$ = 50, $n_{L\text{-iGr (textile)}}$ = 50.

Whilst the Nitschke cage devices showed promise in terms of sensing capabilities, the printed N-cage layers developed significant cracking following drying, presenting challenges for their use as surface decoration and encapsulation layer in graphene sensors. Any macroscopic crack would diminish the capping effects of the N-cage

layer, thereby allowing molecules to reach graphene surface interfering with selective sensing. Therefore, further work on optimization of the ink formulation is required.

In this work, a successful strategy was implemented for printing iGr onto textiles, whereby an interface layer largely improved the achievable electrical resistance. Further exploration of the deposition and UV curing strategy of the interface layer led to significant improvements in the electrical properties, establishing a methodology for reducing surface roughness and porosity of alternative materials. The textile-based iGr samples demonstrate suitability for wearable devices and, as such, warrant exploration of their sensing capabilities.

6 Substrates for inkjet-printed electronics

One distinct advantage of inkjet-printed electronics is the range of available substrates, which are generally unavailable in conventional manufacturing. The growing availability of functional materials as well as low-temperature photonic annealing and sintering techniques enables inkjet printing onto stretchable and flexible polymeric films, offering opportunities for printing of wearable electronic devices. Inkjet deposition of electronic devices onto different substrates was developed and their performance under mechanical deformation was evaluated.

The work included in this chapter, based on photonically annealed iGr, is published in *Heaton et al., "*Photonic Annealing of Inkjet-printed Graphene for Stretchable Wearable Healthcare Monitoring Devices*", Adv. Mater. Technol., 2025, e00913*.

6.1 Flexible and stretchable devices

To evaluate the suitability of printed low-dimensional materials for wearable devices, their performance under mechanical strain was studied. Printed samples were subject to incremental and cyclic bending and /or stretching tests to establish the effect of mechanical deformation on morphological and electrical properties.

6.1.1 AuNPs deposited on PEN

The AuNP ink formulation was received from Dr Jisun Im (University of Warwick) (**Chapter 4.1.1**). AuNPs were functionalised with the photo-cleavable ligand, o-nitrobenzyl Thiol (NT), and dispersed in 2-butoxyethyl acetate at 30 wt %. AuNP ink was deposited onto PEN and UV sintered (n_L = 5, $T_{substrate}$ = 60 °C, t_{UV} = 5 min). The sample was subject to repeated bending to an angle of 150° for up to 1000 cycles. Prior

to bending, the measured sheet resistance, R_S, was 3.84 Ω/sq.. No significant change in sheet resistance was observed for the first 100 cycles, after 500 cycles increase of R_S to 7.14 Ω/sq. was observed, with further increase to > 10^3 Ω/sq. after n_C = 1000 (**Figure 6-1 a**). Major degradation in the electrical conductivity of the printed AuNP film was achieved at n_C = 1000, where $R_S > 10^3$. Optical microscopy was used to visually investigate the sample before and after bending (**Figure 6-1 b, c**). It was observed that cracks, ~ 1 µm in width, presented at the edges of the printed line after n_C = 1000 (**Figure 6-1 d, e**), likely causing the increase in electrical resistance.

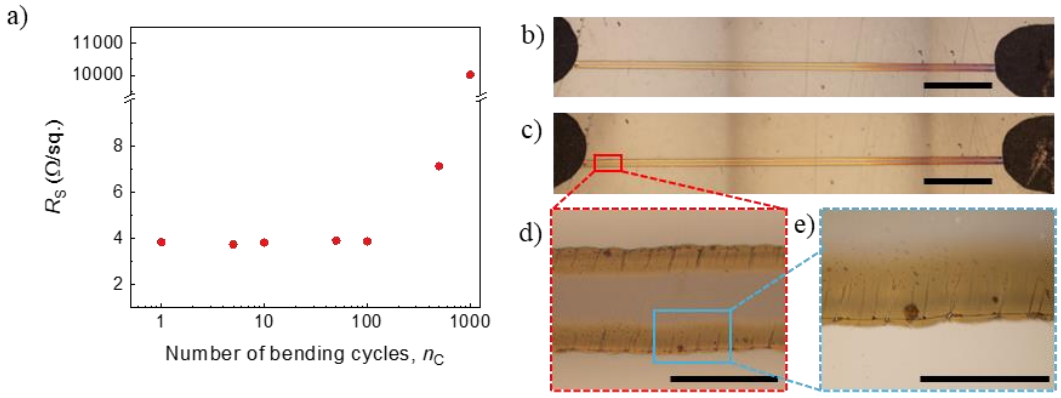


Figure 6-1 Response to cyclic bending of AuNPs printed onto PEN (n_L = 5, $T_{substrate}$ = 60 °C, t_{UV} = 5 min) **a)** Sheet resistance after cyclic bending. Optical microscope images of printed AuNP sample **b)** before (scale bar = 1000 µm) and **c)** after n_C = 1000 (scale bar = 1000 µm). **d)** 20x (scale bar = 100 µm) and **e)** 50x (scale bar = 50 µm) optical microscope images of printed AuNP sample after n_C = 1000.

These results demonstrate the suitability of the AuNP ink for wearable electronics, where repeated mechanical deformation up to 100 cycles does not affect the device performance. Some cracking at the edges of the printed line can be seen following large number of cycles (> 500). Morphological changes of the printed MeNP films were reported previously[359,360] and likely arise from poor adhesion of the MeNP film to the substrate and limited cohesion between the un-sintered NPs within the film. These results provide a tentative guide for the lifecycle of electronic devices with

AuNP films, however, could also offer options for their use in structural health sensing to detect repeated motion and /or deterioration after more detailed characterisation and calibration.

6.1.2 Graphene deposited on Kapton film

An iGr sample was produced on Kapton film and photonically annealed (n_L = 10, n_f = 10, 2.4 wt%, DMC, 50 x 0.5 mm). The sample was subjected to bending to an angle of 160°, both incrementally and cyclically, up to 1000 cycles, to evaluate the performance of iGr under repeated deformation. Under incremental bending, there was no significant change in resistance with R_S = 5.01 ± 0.13 kΩ/sq. (**Figure 6-2 a**). This demonstrates the suitability of such fabrication methods towards wearable electronics, where bending should not affect the operation of the device. When subjected to cyclic bending, the initial sheet resistance was 6.12 kΩ/sq.. No significant deterioration was observed with increasing bending cycles. After 1000 cycles, it was observed that the sheet resistance had increased to 6.34 Ω/sq. (**Figure 6-2 b**). Thus, exhibiting the durability of iGr manufactured using photonic annealing onto flexible polymer films, and that repeated mechanical deformation will not reduce device performance.

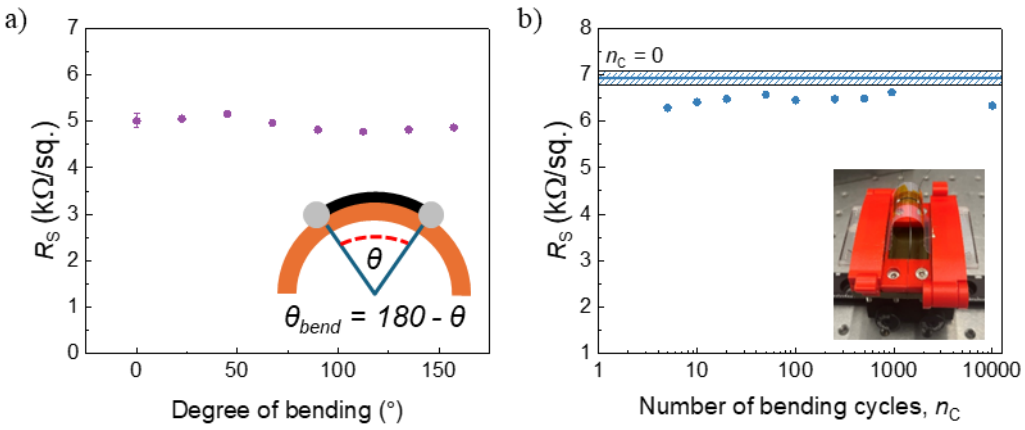


Figure 6-2 Bending data for iGr sample (n_L = 10, n_f = 10, 2.4 wt%, DMC) printed on Kapton subject to bending > 150°. **a)** incrementally (Inset: schematic for measurement of bending angle) and **b)** cyclically (Inset: image of iGr sample placed in bend testing equipment).

Stability of the printed graphene film after bending can be explained by the nature of flake network formation, where conduction mechanism is defined by inter-flake charge hopping. The film consists of a percolating network of overlapping graphene flakes. This structure can therefore be considered better suited to mechanical deformation, as the flakes can move under bending without causing catastrophic deformation. In contrast, in MeNPs films, sintered nanoparticles form continuous film, with metallic charge transport, and mechanical deformation can lead to irreversible damage of metallic layer.

6.1.3 IPL-graphene on stretchable Beyolex

Beyolex is a stretchable polymer film,[361] enabling fabrication of inkjet-printed devices with high durability to mechanical deformation and elongation. Due to the low thermal properties of Beyolex ($T_{operation} \leq 150$ °C), samples produced using the graphene ink would be photonically annealed to prevent substrate deterioration, as seen in **Chapter 5.2.2**.

Samples were printed with $n_L = 10$ and size of 50 x 0.5 mm then photonically annealed with $n_f = 10$. Initial testing incrementally stretched the samples up to an elongation, $\Delta L = 20$ % (**Figure 6-3 a**) with approximately 1 minute between measurements. The sheet resistance of iGr increased linearly from 4.84 kΩ/sq. at $\Delta L = 0$ % to 11.92 kΩ/sq. at $\Delta L = 21$ %. This change corresponds to a sensitivity of 1250 Ω/%. Continuous stretching to the same elongation was also applied to the sample, with a temporal response measured. An initial sharp increase of sheet resistance was observed with fast response (< 1 s), when the sample is reached $\Delta L = 21$ %, followed by a slow recovery back to the initial R_S value with recovery time ~ 50 s (**Figure 6-3 b**). The recovery is largely governed by the viscoelastic properties of the Beyolex film,[362] rather than the

printed graphene film. This is confirmed by images of the sample before and immediately after stretching (**Figure 6-3 c**). In both images the position of the stretch testing rig is the same. In the first image, the Beyolex film exhibits a taught configuration, whereas the second image presents noticeable sagging at the edges, suggesting incomplete elastic recovery and failure to return to its original dimensions following strain.

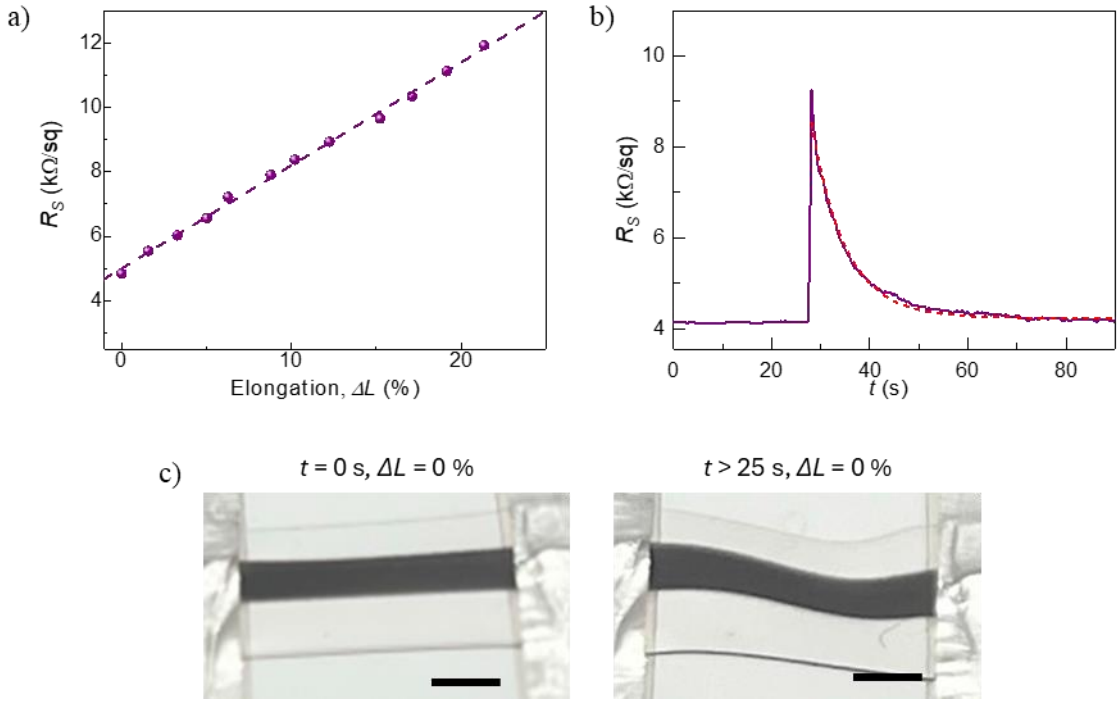


Figure 6-3 a) Sheet resistance of graphene (n_L = 10, n_f = 10, 2.4 wt%, DMC) printed on Beyolex subject to incremental stretching. **b)** Temporal response and recovery of graphene (n_L = 10, n_f = 10, 2.4 wt%, DMC) printed on Beyolex subject to 20 % elongation. **c)** Optical images of printed Gr/PEDOT:PSS films on Beyolex at ΔL = 0 %, before (left) and immediately after (right) stretching. (Scale bar = 1 mm).

This work demonstrates graphene as a suitable material for inkjet-printed wearable electronics. It shows minimal change in electrical properties under both incremental and cyclic bending, suggesting that functionality would not be impaired. Change in resistance due to stretching is not excessive, remaining within 1 order of magnitude,

thus, the response to mechanical deformation as such could be applied for strain sensing.

6.1.4 Stretch response of Gr/PEDOT:PSS on Beyolex

The Gr/PEDOT:PSS ink is an excellent material for printing onto flexible and stretchable substrates, such as Beyolex, as it does not require thermal annealing. In this work, the effect of elongation on the performance of devices produced with different printing parameters and print designs was investigated. Samples were printed by Dr Jonathan Austin (University of Nottingham)

The effect of the number of layers on the change of resistance under mechanical deformation was initially investigated to determine whether a thicker layer of Gr/PEDOT:PSS would reduce changes of film morphology, which leads to an increase in electrical resistance during elongation. Samples were printed with n_L= 10, 20 and 40, at $T_{substrate}$ = 35 °C and with dimensions of 50 x 5 mm. Samples were subject to incremental stretching, up to an elongation of 40 %. The maximum strain used in this experiment is intended to assess the device's suitability for high-mobility areas of the human body, such as the knee and elbow. Electrical measurements were performed, enabling us to evaluate the suitability of Gr/PEDOT:PSS for devices operating under strain. Initial electrical measurements (ΔL = 0 %) were in agreement with previous observations, where an increased number of layers yields improved electrical resistance (**Figure 6-4 a**). The sample with n_L = 10 demonstrated a significant increase in sheet resistance, especially for ΔL > 15 %. This can be attributed to the reduced coverage of Gr/PEDOT:PSS in the printed film, and the reduced packing density elongation. Changes in resistance were observed with R_S increasing by about 4 orders of magnitude. The n_L = 20 and 40 samples had comparable results, with no significant

increase of resistance at ΔL = 15 %, and maximum change of R_S < 100 times. In order to better compare the effects of elongation on the number of printed layers, the resistance was normalised against the initial value (ΔL = 0 %) (**Figure 6-4 b**). This analysis revealed that all samples had comparable performance at small elongation (ΔL < 20%), with the 10-layer sample experiencing a smaller overall change but a significant increase in resistance after ΔL = 15 %, whereas the n_L = 20 and 40 samples performed similarly. The n_L = 20 sample, in fact, exhibited a slightly smaller degradation in electrical resistance compared to the n_L = 40 sample. Optical microscopy was performed on the n_L = 10 and 40 samples before and after stretching up to 40 % (**Figure 6-4 c, d**) in order to investigate any change in surface morphology to the printed films. Optical microscopy of the n_L = 10-layer sample revealed no change in film morphology as a result of stretching. Optical images of the sample with n_L = 40 revealed the presence of small cracks along its surface after stretching. This can be attributed to delamination among the topmost layers of the printed film. Further work investigating the morphological changes that a printed film undergoes from stretching would be valuable. High-resolution profilometry could be used to characterise microscale surface defects. Additionally, it would be of interest to determine whether such defects are limited to the printed film surface; therefore, cross-sectional analysis would be useful to evaluate structural changes throughout the thickness of the material.

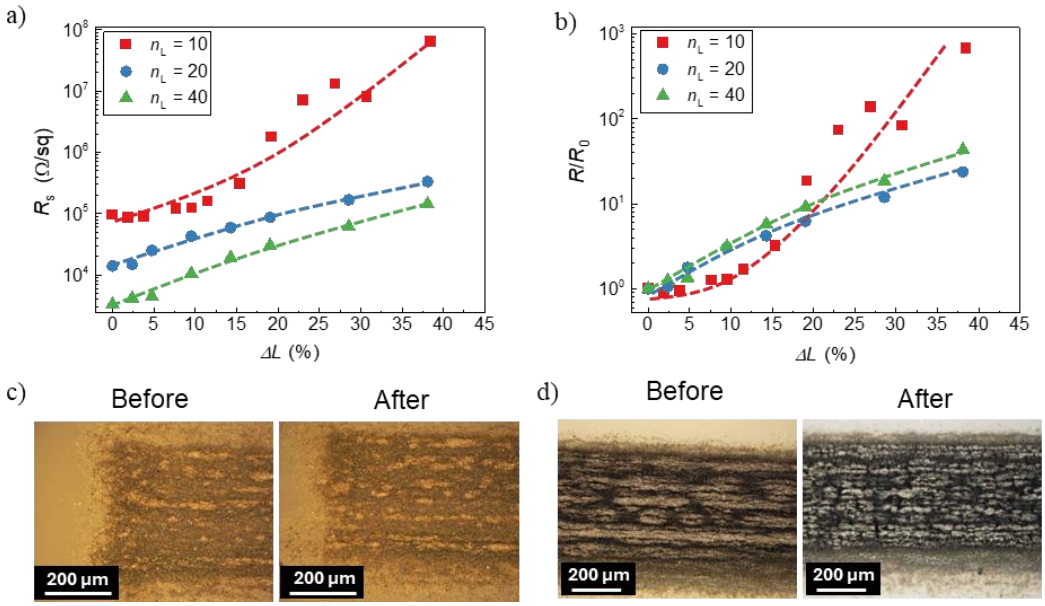


Figure 6-4 a) Sheet resistance vs elongation for Gr/PEDOT:PSS samples on Beyolex. **b)** Normalised resistance vs elongation for Gr/PEDOT:PSS samples on Beyolex. The dashed lines provide a guide to follow for each trend. Optical microscopy of Gr/PEDOT:PSS samples on Beyolex before and after stretching for **c)** n_L = 10 and **d)** n_L = 40.

Published studies have indicated that intentional design can improve resistance to degradation when subject to strain, where concentrations of stress can be better mitigated.[363–365] Therefore, serpentine (**Figure 6-5 a**) and meandering (**Figure 6-5 b**) printed patterns were explored to compare to the previously investigated singular straight line. Both the serpentine and meander patterns have been shown to exhibit high resistance to mechanical deformation and are useful features in the design of wearable and stretchable electronics. The durability of such patterns has been previously demonstrated at elongations exceeding 60 %, with failure often occurring due to substrate damage rather than electrode deterioration.[366]

Samples were printed with n_L = 20 and $T_{substrate}$ = 35 °C and compared to the 20-layer sample from the previous study. Samples were stretched incrementally up to ΔL = 40 %, and the normalised change in resistance was plotted for comparison (**Figure 6-5**

c). It was observed that both patterned samples exhibited less degradation in electrical resistance under stretching. The meander sample (**Figure 6-5 b**) showed approximately 10 % reduced change in resistance compared to the serpentine.

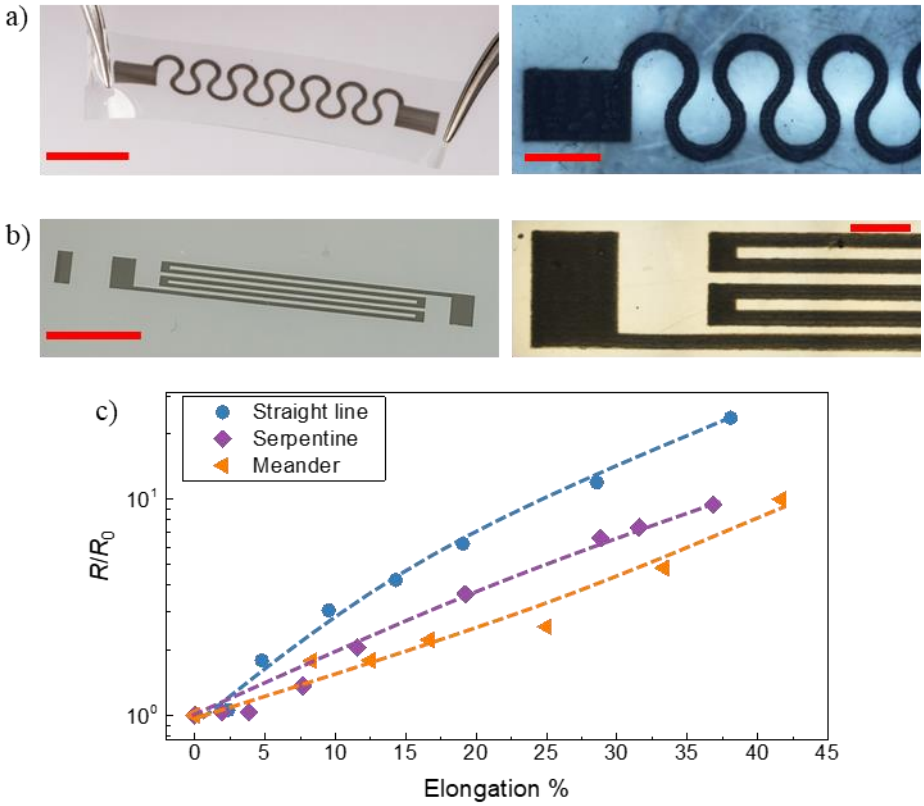


Figure 6-5 Optical and optical microscopy images of Gr/PEDOT:PSS printed on Beyolex (n_L = 20, $T_{substrate}$ = 35 °C) in **a)** serpentine and **b)** meander patterns (left scale bars = 5 mm, right scale bars = 1 mm). **c)** Normalised change in resistance vs elongation of straight line, serpentine and meander Gr/PEDOT:PSS patterns printed on Beyolex.

The length of the sample should also be considered when analysing the performance under strain. Of the samples used, the serpentine and meander possessed similar length, while the straight line was significantly longer. When viewing this data in the context of **Figure 6-5**, it would suggest that longer samples exhibit a higher sensitivity towards elongation. This is most likely due to an increased number of separations in the graphene flake network throughout the printed film. Further work is required to

investigate this relationship, whereby the length of straight samples should be compared, as well as examining patterned and straight samples of equal length. Samples were produced with the following lengths: straight line – 50 mm, serpentine – 31 mm, meander – 29 mm.

6.2 3D printed stretchable substrates

AM offers unique advantages for the development of printed electronics, by utilising complex geometries, surface properties and material combinations which would be challenging to achieve through conventional manufacturing methods. This permits for the addition of functional layers upon a diverse range of substrates, including metallic components, soft elastic polymers and hydrogels. Cross-compatibility of materials poses a challenge: solvents in ink formulations may be unsuitable for certain polymers or hydrogels, and surface finishes may be poorly suited to the deposition of functional inks. Printing onto a silicone formulation suitable for inkjet printing was explored.

6.2.1 Printed silicone substrate

Silicone would typically not be suitable for inkjet printing, as a reactive process is required, where two or more components are mixed, resulting in chemically induced cross-linking. Reactive jetting has been developed to enable 3D printing of such materials, where two or more components can be deposited simultaneously.[367] A custom addition-cure PDMS elastomer was supplied by Added Scientific Ltd. The system follows a standard hydrosilylation mechanism involving vinyl-terminated PDMS chains, a hydride-functional crosslinker, and a platinum catalyst. The exact formulation and component ratios are proprietary. Its suitability as a substrate for the

iGr ink was investigated. Initial work was performed with cast samples of the silicone formulation, rather than printed items.

The iGr ink (1.2 wt%, Samba) was deposited onto the cast Silicone with n_L = 10, $T_{substrate}$ = 60 °C. Samples were annealed both thermally and using IPL. Optical microscopy was performed after IPL annealing (n_f = 10), revealing significant cracking in the printed graphene (**Figure 6-5 a, b**), and no measurable electrical conductivity recorded. The use of thermal annealing ($T_{annealing}$ = 250 °C, $t_{annealing}$ = 2 hours) was more successful, with no cracking or macroscopic defects observed (**Figure 6-5 c, d**) and a sheet resistance R_S = 9.8 ± 0.8 kΩ/sq.. The sample was stretched to 20 % elongation, which saw a significant degradation in the electrical properties (R_S = 64.3 ± 19.8 kΩ). After stretching, significant cracking was observed in the iGr film, with loss of adhesion to the substrate (**Figure 6-5 e**).

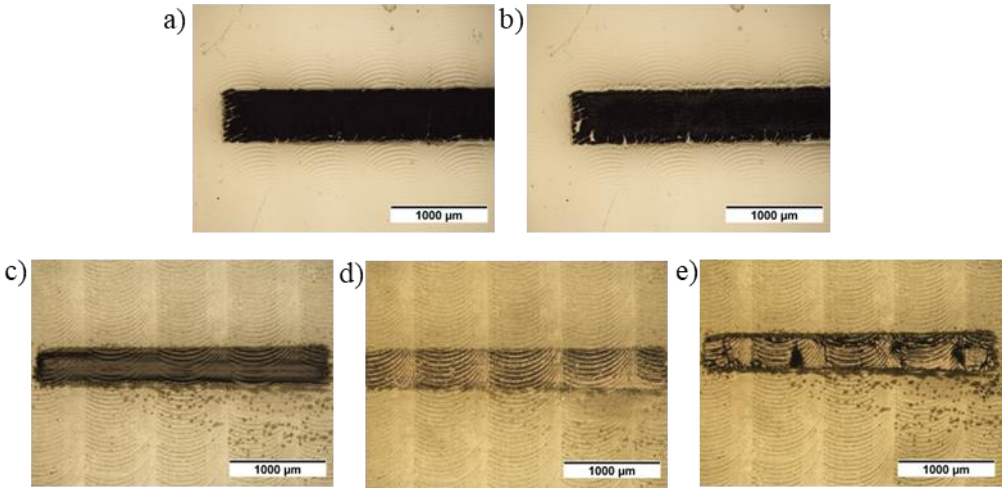


Figure 6-6 Optical images iGr on cast silicone (n_L = 10, $T_{substrate}$ = 60 °C) **a)** before and **b)** after IPL annealing (n_f = 10), **c)** before, **d)** after thermal annealing (T_{anneal} = 250 °C, t_{anneal} = 2 hours) and **e)** after elongation to 20 %.

Silicone has very low surface energy, making inkjet printing a challenge due to the difficulty of obtaining desirable wetting and adhesion of inks to the substrate.[368] This

was seen more evidently during the IPL annealing process, where a small level of delamination occurred after treatment. Further deterioration was observed after bending. Thermal annealing yielded more desirable results and improved adhesion after stretching, although deterioration persisted, as evidenced by a significant increase in sheet resistance. Future work should consider incorporating surfactants into the silicone ink formulation or applying a surface treatment, lowering the silicone surface energy for deposition of inks.

7 Multifunctional sensing devices

This work presents a multifunctional, multimaterial iGr sensor fabricated via inkjet printing that can simultaneously detect multiple stimuli, including temperature, pressure, and humidity. The device architecture combines orthogonal iGr layers separated by a dielectric TPGDA layer. Temperature and humidity are monitored via changes in resistance, whilst pressure is determined from capacitance responses. In the context of wearable electronics, iGr textile-based devices are explored, replicating the previously observed sensitivities to temperature, humidity, and pressure. Highlighting the potential of inkjet-printed electronics towards wearable devices.

The work included in this chapter is based on the multifunctional graphene sensor and graphene fabric devices published in *Wang et. al., "Inkjet-printed Multifunctional Graphene Sensors for Flexible and Wearable Electronics", Adv. Electron. Mater, 2024, 11, 7.*

7.1 Developing simultaneous detection

A graphene-based multifunctional sensor using multimaterial, multilayer inkjet printing technology (**Figure 7-1 a, b**) was designed and printed by Dr Feiran Wang, with initial investigative work carried out characterising the response to individual stimuli, including temperature, pressure and humidity. The work of this thesis was concerned with developing simultaneous detection to multiple stimuli.

In this design, a device comprising two iGr layers separated by an insulating TPGDA layer was printed onto a flexible Kapton substrate. The top and bottom iGr layers were printed perpendicular to each other and consisted of five independent parallel stripes, used for humidity and temperature sensing, respectively. Four electrical contacts

printed with the commercial AgNP ink were used to allow independent measurements of the lateral resistance of the top and bottom iGr tracks as well as the vertical capacitance of the graphene/TPGDA/graphene heterostructure. The device was designed to enable simultaneous sensing of the three external stimuli, temperature (*T*), *RH* and pressure (*P*), providing a proof-of-concept for the technology (Figure 1 c). In this sensor architecture, the electrical conduction of graphene is highly temperature dependent, allowing temperature sensing through measurements of resistance change, *R*(*T*). The top layer of graphene is exposed to the atmosphere, enabling environmental (e.g. humidity, gas) sensing. To demonstrate capability towards simultaneous detection, humidity as the environmental stimulus of interest was chosen to be investigated, *R(RH)*. The electrical resistance between the top and bottom graphene layers are affected by the thickness change of the separating dielectric layer in response to compression, enabling *P*-sensing, *C*(*P*) (**Figure 7-1 c**).

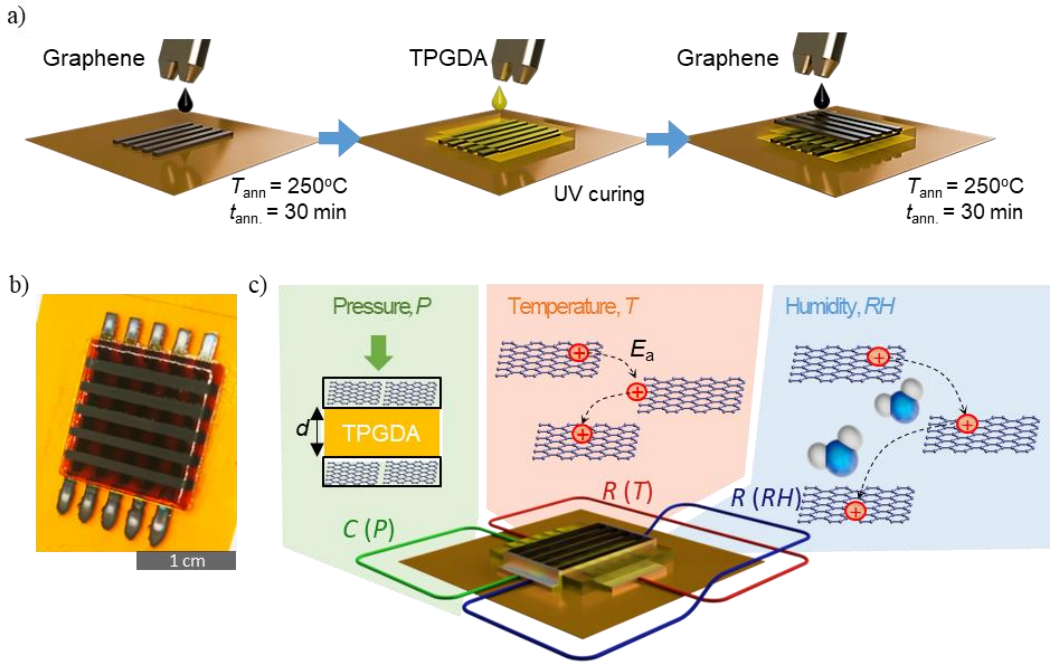


Figure 7-1 a) Schematic illustration of inkjet printing of graphene and polymeric layer (TPGDA) into a multifunctional sensor design and **b)** a photograph of the device. **c)** A diagram of the electrical circuit and corresponding schematics illustrating the response of the sensor to (from left to right) pressure, *P*, temperature, *T*, and relative humidity, *RH*.

In this sensor design, the electrical resistance of the bottom iGr layer is only affected by the sample temperature, as it is capped with the dielectric layer which provides protection from the environment. The five iGr stripes with n_L = 10 are connected in parallel and have a total resistance of ≈ 250 Ω. The response to temperature is fully reversible (**Figure 7-2 a**, Inset) and has ON/OFF times of $t_{on}(T) \approx 30$ s and $t_{off}(T) > 200$ s for an ambient temperature of T = 60 °C.

The top iGr layer is uncapped and exposed to the atmosphere, making it suitable for environmental sensing. In response to 100% *RH*, the resistance of iGr increases by 2.5%. The temporal response is fully reversible over at least ten cycles (**Figure 7-2 b**, Inset) with response times of $t_{on}(RH) \approx 1$ s and $t_{off}(RH) = 5$ s for 2 s exposure to100 % *RH*.

The sensor can also be used to monitor pressure by measuring the capacitance change of the matrix of 25 iGr/TPGDA/iGr parallel plate capacitors (**Figure 7-1 c**). The capacitance of the device can be determined by using **Equation (7-1)**. It is worth noting that the compressive modulus of TPGDA is ~575 MPa.[203]

$$C = \frac{\varepsilon_r \varepsilon_0 A}{d(P)} \quad \textbf{(7-1)}$$

where ε_r = 3.03 is the relative dielectric constant of TPGDA, ε_0 = 1 is the dielectric constant of air, A = 36 mm^2 is the total area, and $d(P)$ is the thickness of the TPGDA layer when the pressure P is applied.

The capacitance of the device increases linearly from 2.5 to 2.8 pF in response to the applied pressure from 0 to 10 kPa (**Figure 7-2 c**). The response is fully reversible with pressure-independent response times of $t_{on}(P) \approx 0.5$ s and $t_{off}(P) = 2$ s. **Equation (7-1)**

provides a good fit to the experimental data (**Figure 7-2 c**) and could be used to guide the material choice and design options for other printed pressure sensors.

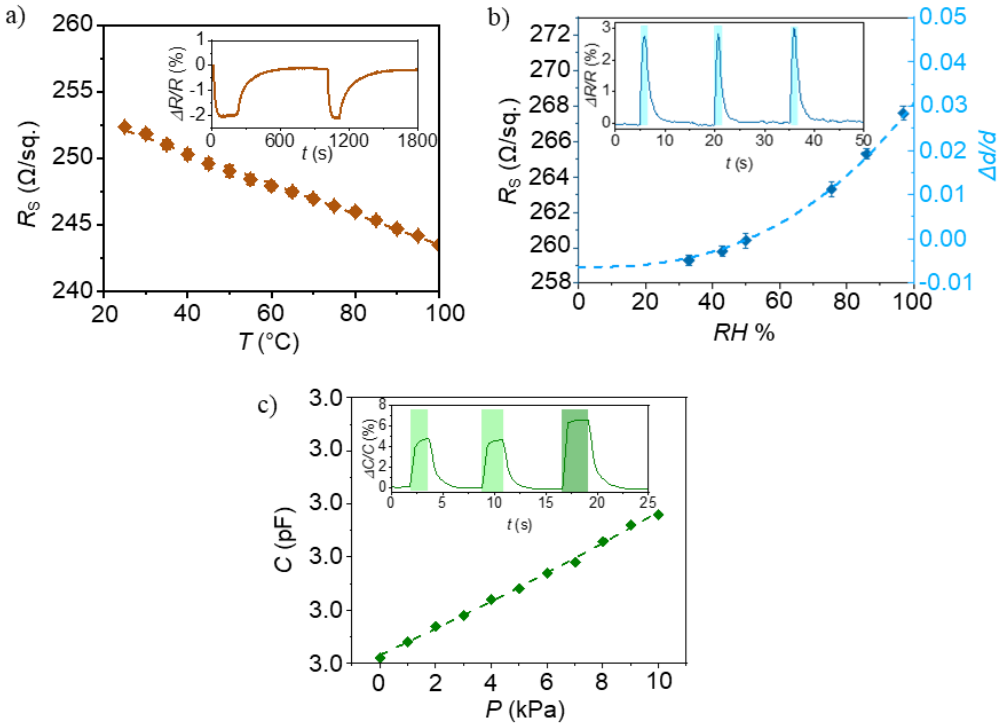


Figure 7-2 a) Temperature dependence of the resistance of bottom iGr stripes of the sensor during two heating/cooling cycles in the temperature 25 °C < T < 80 °C (Inset: temporal response of the temperature sensor at T = 60 °C). **b)** Dependence of iGr resistance on the RH of the environment (Inset: temporal response of iGr-humidity sensor in response to RH = 100%). Dashed line represents the calculated $R \propto 1/d_{eff}$ dependence.

After the preliminary work to characterise the device's sensing properties, a protocol was developed to test simultaneous exposure to multiple stimuli. Due to equipment limitations, it was only possible to investigate the response to two out of three stimuli at the same time. Presented below is strategy to discriminate stimuli in complex environments during simultaneous measurement was developed. Under simultaneous exposure to multiple stimuli, the individual responses were successfully extracted. A temperature sweep was performed by placing the device on a hotplate, whilst blowing across the top layers of the device induced 100 % *RH*, and placing a mass on top of

the device applied pressure. To isolate the *T*-response, the bottom layer of the device is capped with TPGDA and thus is sensitive only to *T*, not to *RH*. Under simultaneous exposure to temperature change and humidity, the *T*-response of the bottom iGr layer can be subtracted from the response of the top layer, providing an *RH* sensing value. The change in capacitance due to the applied pressure is also consistent across different temperatures. To illustrate the simultaneous sensing capabilities, the device was tested at $T = 30$, 40 and 50 °C with simultaneous humidity stimulation ($RH \approx 100$ %) and applied pressure ($P \approx 2$ kPa), where distinguishable and reproducible responses were observed (**Figure 7-3**). It should be noted, that operation of the device would be limited up to the glass transition temperature of TPGDA (80 °C) as severe deformation under pressure may occur and subsequent device damage.

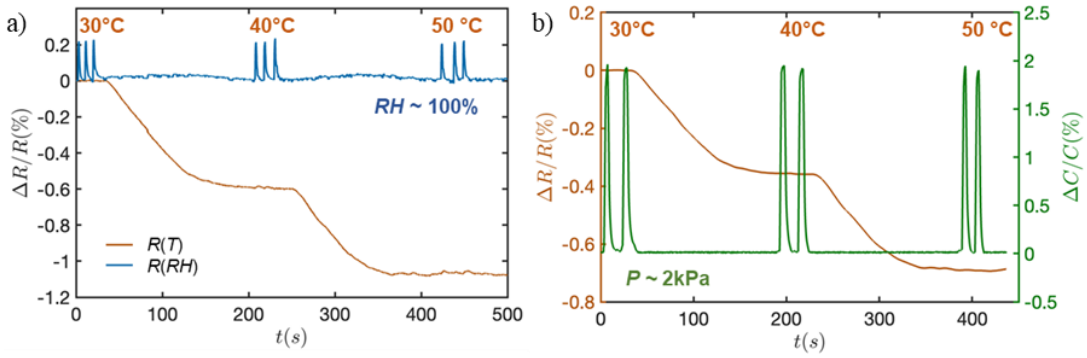


Figure 7-3 Response of the iGr/TPGDA/iGr sensor to simultaneous **a)** *T* (bottom resistance) and *RH* (top resistance) and **b)** *T* (bottom resistance) and *P* (top – bottom capacitance) exposure. The *RH* signal is measured in response to breathing ($RH \sim 100$ %) with respect to $RH = 63$ %. The response to applied *P* is tested as change in capacitance following touch ($P \sim 2$ kPa).

7.2 iGr devices on textile substrates

To demonstrate the potential of this technology for wearable sensors, the sensing capabilities of the previously developed iGr-textile device (**Chapter 5.2.1**) (**Figure 7-4**) was explored. Response to temperature, humidity and pressure of this wearable

device was investigated, and results showed comparable performance to that previously demonstrated on Kapton. Suitability towards wearable devices was also studied, evaluating durability to mechanical deformation.

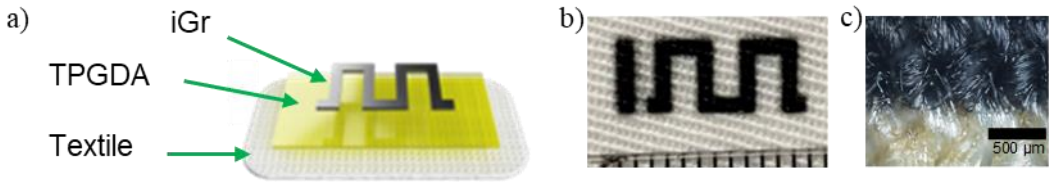


Figure 7-4 a) Schematic illustration, **b)** photograph and **c)** optical microscope images of the iGr-textile device ($n_{\text{L-TPGDA}}$ = 50, $n_{\text{L-iGr}}$ = 50).

Temperature dependent electrical measurements were carried out on the iGr-fabric device, with the electrical resistance being measured at intervals over the temperature range of 20 °C < T < 100 °C. An Arrhenius relationship (**Equation (7-2)**) was exhibited between the device's resistance, R, and local temperature was observed, with a total change of R up to 22 % over the temperature range 20 - 100 °C being observed (**Figure 7-5 a**), comparable to that in **Chapter 7.1**.

$$\sigma \propto \exp\left(\frac{-E_a}{k_B T}\right) \qquad \textbf{(7-2)}$$

Temperature dependence was fitted with an Arrhenius equation, enabling calculation of activation energy, E_a = 20.14 meV. This E_a value is higher than the calculated activation energy for iGr on Kapton (1.8 meV), which is likely due to the reduced packing density from the distribution of graphene flakes throughout the 3D fibrous network of the textile.

Sensitivity towards humidity was explored in an ON/OFF manner, monitoring the response and recovery to humidity change from ambient (~ 50 % *RH*) to 100 % *RH*. An increase of 3.8 % in device resistance was observed across exposures, with a rapid

response and recovery times ($t_{on}(RH) \approx 1$ s and $t_{off}(RH) = 6$ s) similar to those previously observed on the iGr-Kapton device (**Figure 7-5 b**). It is noted that the change of T caused by exhaled air is small (< 5 °C)[337] and does not significantly affect the measured values ($\Delta R < 50$ kΩ), however this temperature change is likely responsible for the small change in resistance observed after recovery.

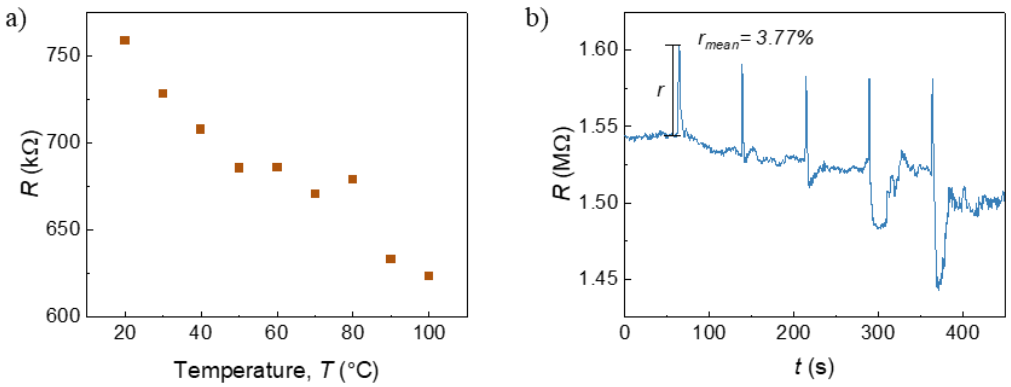


Figure 7-5 a) Temperature dependence of resistance for the iGr-textile device ($n_{L\text{-}TPGDA} = 50$, $n_{L\text{-}iGr} = 50$) for $T = 20$-100 °C. **b)** Temporal humidity dependence of the iGr-textile device ($n_{L\text{-}TPGDA} = 50$, $n_{L\text{-}iGr} = 50$) at $RH = 100$ %.

When printed onto fabric, we envisage the iGr ink forms a 3D network of graphene flakes, throughout the porous structure of the fibres, resulting in a lower packing density compared to iGr on Kapton film. Therefore, when pressure is applied resulting in compression of the fabric, the inter-flake proximity will increase, thereby reducing electrical resistance. To investigate this effect, the pressure was increased incrementally up to 600 kPa, where a decrease in resistance was observed (**Figure 7-6 a**). The dependence of resistance on applied pressure could be fitted exponentially (**Equation (7-3)**), where it can be deduced that the textile structure can only be compressed to a limiting extent, and as such increasing pressure will return diminishing gain in electrical properties.

$$R(P) = a \exp\left(\frac{-P}{b}\right) + j \qquad \textbf{(7-3)}$$

where *R(P)* is the measured resistance at pressure *P*, *a, b* and *j* are fitting parameters (a = 1.28; b = 250.44; j = 3.73).

The temporal response to pressure was investigated for two *P* values, 210 kPa and 567 kPa, with 3 repeats for 10 s, with intervals of 30 s between applications. The device exhibited a fast response and recovery to the applied *P* with $t_{on}(RH)$ and $t_{off}(RH)$ < 0.5 s. Magnitude of resistance decrease scales with *P* observed with change of 13 % and 20 % for the 210 kPa and 357 kPa pressures respectively (**Figure 7-6 b**). It is noted that any change of temperature does not significantly affect this measurement.

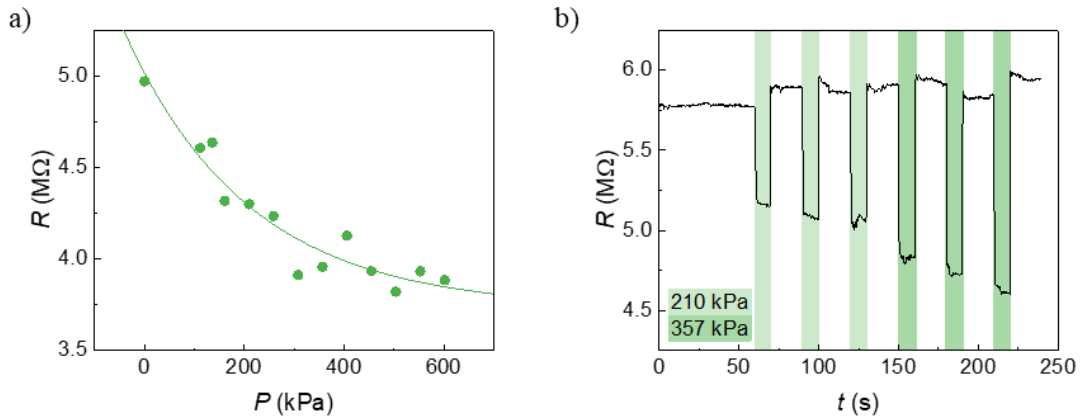


Figure 7-6 a) Pressure dependence of resistance of iGr-TPGDA-textile device ($n_{\text{L-TPGDA}}$ = 50, $n_{\text{L-iGr}}$ = 50). **b)** Temporal response of the iGr-TPGDA-textile when subject to pressures of 210 and 357 kPa.

To assess the viability of these textile-iGr devices for wearable electronics, their performance after cyclic bending was evaluated. The previously used textile device was subject to 1000 bending cycles at an angle of 180°. Electrical measurements were taken periodically throughout. The fabric iGr sensors are suitable for applications on flexible and wearable electronics, as morphology and electrical properties are only

weakly affected by the bending of the substrate up to at least 1000 bending cycles (**Figure 7-7**).

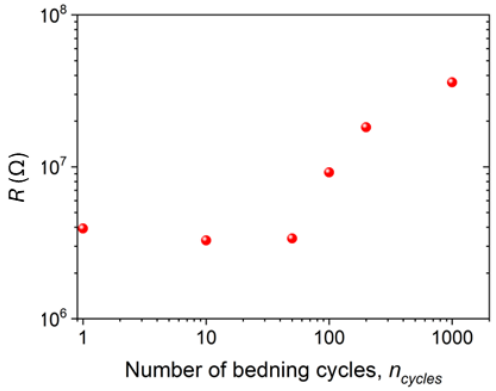


Figure 7-7 Dependence of resistance on the number of bending cycles of textile based iGr-textile device ($n_{\text{L-TPGDA}}$ = 50, $n_{\text{L-iGr}}$ = 50).

These results demonstrate the applicability of inkjet-printed graphene on textiles for wearable electronics. The sensing capabilities have been successfully translated from polymeric films onto a textile substrate, demonstrating responsivity towards temperature, humidity and pressure, as well as reasonable resistance to mechanical deformation. Work is still required to improve the electrical conductivity of iGr-textile devices, where evaluation of the printing strategy and substrate preparation might offer insights. A review of the literature presents a range of strategies to mitigate the challenges associated with printing onto textiles. These include deposition of thick (~200 µm) polymer layers, compression rolling to improve the packing density of functional materials, and the use of close-knit textiles with small fibre diameters, reducing porosity and surface roughness.[19,42,43,369,370]

8 Chemical and environmental sensing

This work utilises the IPL annealing method to fabricate iGr devices on highly flexible and stretchable substrates, exploring their sensing capabilities whilst also considering the effects of mechanical deformation. This chapter reports on the temperature sensitivity of IPL-annealed iGr and assesses its performance under strain. Device design is explored to decouple the effects of mechanical deformation and environmental stimuli and to develop a directional strain sensor. The dual-sensing capabilities of IPL annealed iGr for medical applications in breath sensing was also investigated to demonstrate the ability to simultaneously detect the presence of acetone under varying humid conditions.

The work included in this chapter is based on the IPL annealed graphene devices published in *Heaton et al., "*Photonic Annealing of Inkjet-printed Graphene for Stretchable Wearable Healthcare Monitoring Devices*", Adv. Mater. Technol., 2025, e00913*.

8.1 Temperature dependence of IPL annealed graphene

The temperature dependence of the IPL annealed iGr was investigated. The iGr ink was printed in a Hall bar geometry onto Kapton (n_L = 5) (**Figure 8-1 a,** Inset) and IPL annealed (n_f = 10). Devices were subject to electrical measurements over a broad temperature range (2 K ≤ T ≤ 300 K), whilst mounted in a magneto cryostat (**Chapter 4.7.1**) to enable precise temperature control and application of a magnetic field. Extending measurements to 2 K allows the identification of low-temperature transport regimes typical of printed graphene networks, such as variable-range hopping, which

are not visible at room temperature. Printing of the 6-terminal geometry of the Hall bar device required significant effort to optimise printing parameters to achieve a line width of 150 μm, and spacing between features of less than 450 μm. This device was used to perform Hall effect measurements, where longitudinal (R_{xx}) and transverse resistance (R_{xy}), are measured as a function of applied magnetic field, enabling determination of the carrier concentration.

At low-temperatures (T = 2 K) carrier concentration drops to 0.8×10^{15} cm^{-2}, and mobility stays in the range 7 cm^2/Vs < μ < 13 cm^2/Vs with a maximum around T = 50 K. iGr resistance has rather weak temperature dependence at T > 50 K changing by about factor of 2 in the range 2 K < T < 50 K. Temperature dependence of iGr electrical conductivity (**Figure 8-1 c**) is in good agreement with the 3D variable range hopping model (**Equation (8-1)**), frequently used to model the electrical conductivity of iGr films.[371]

$$\sigma \sim \exp\left[\left(-\frac{T_M}{T}\right)^{\frac{1}{4}}\right] \qquad \textbf{(8-1)}$$

where T_M is Mott temperature.

The IPL annealing method demonstrated strong effectiveness through a high mobility achieved (13 cm^2/Vs). This value is similar to the best results obtained on iGr films of similar thickness fabricated on rigid substrates: ~10 cm^2/Vs of a 20-layer (100 nm) iGr film on quartz, ~13 cm^2/Vs of a 20-layer iGr film on Si/SiO_2.[372] Note, that usual carrier mobilities of thin iGr films is < 1 cm^2/Vs[167] with some state-of-the-art device reaching μ ≈ 100 cm^2/Vs.[373] The observed stable Hall effect in such a thin film also confirms high uniformity of the film and homogeneity of current (**Figure 8-1**). The I–V curves presented in **Figure 8-1 b** are largely linear, indicating ohmic behaviour, although

slight curvature at low temperatures is consistent with junction-limited transport typical of printed graphene films.

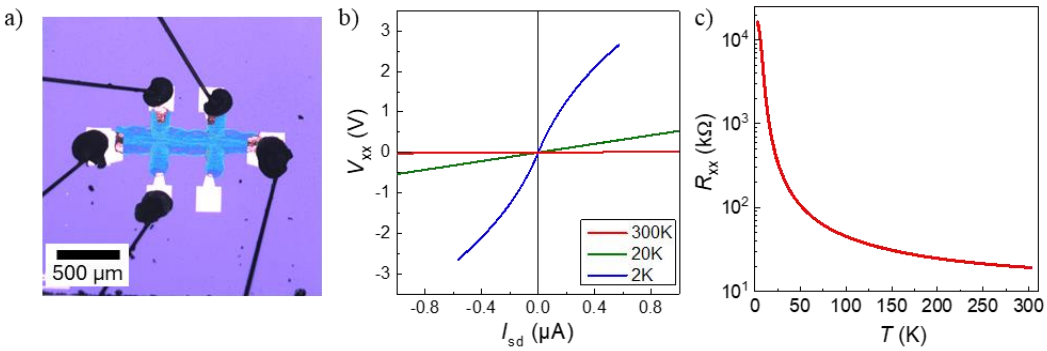


Figure 8-1 Electrical-transport properties of iGr films on Kapton (*n*L = 5 printed layers, 2.4 wt% ink printed with DMC cartridge) **a)** *I(V)* dependences of iGr at *T* =2, 10, 50 and 300 K. (Inset: microscope image of the iGr Hall bar device). **b)** Hall effect measured at different temperatures. **c)** Temperature dependence of IPL annealed iGr sample. Measurements were performed by Mr Leo Ruer and Dr Nathan Cottam.

8.2 Sensing performance of IPL annealed graphene under strain

The development of stretchable sensors demands materials with stable electrical responses under mechanical deformation, and whilst the stretching of iGr films influences their electrical resistance, the temperature dependence remains independent of the elongation (**Figure 8-2**). Electrical measurements were performed on iGr-Beyolex at increasing elongation up to ΔL = 30% across a range of temperatures (305 ≤ T ≤ 325 °C), exhibiting behaviour consistent with previously observed graphene-temperature dependencies[162,374].

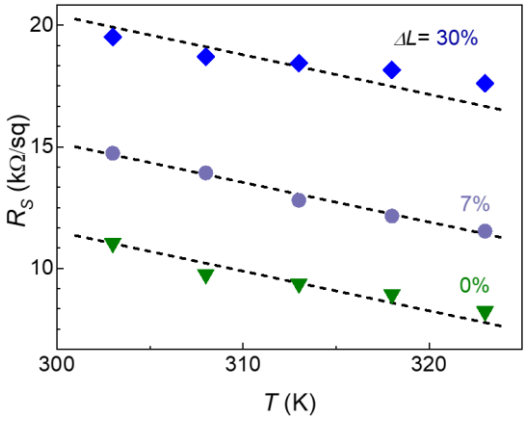


Figure 8-2 Temperature dependence of photonically annealed iGr sample (n_L = 10, 1.2 wt.%, Samba, n_F = 10) on Beyolex under ΔL = 0 (triangle), 7 (circle) and 30 % (square), with linear fit applied (slope ~ -0.16 (Ω/sq)/K) for all stretch conditions.

One difficulty in analysing the sensing performance of single-electrode devices under strain is decoupling the effects and determining the cause of any electrical changes. Device design was found to provide a solution to this challenge, whereby a single printed device composed of orthogonal, yet connected lines could be used (**Figure 8-3 a**). It was proposed that the *x*-section of the device would experience the effects of strain, whilst the *y*-section could provide environmental sensing. For this device, the iGr ink (1.2 wt%, DMC) was printed onto Beyolex (n_L = 10, $T_{substrate}$ = 60 °C) and IPL annealed (n_F = 10) (**Figure 8-3 b**) with dimensions *x*: 30 x 1.5 mm, *y*: 15 x 1.5 mm. The device was subject to stretching in the direction of the *x*-section, up to elongation of 20 %, with electrical measurements taken periodically (**Figure 8-3 c**). The *x*-section of the device exhibits change in sheet resistance which can be fitted exponentially (**Equation (8-2)**) against elongation, showing increasingly significant changes in R_S as ΔL increases, where the sensitivity coefficient, k is 0.5776 $\%^{-1}$.

$$R_S = R_{S0} e^{k\Delta L} \quad \textbf{(8-2)}$$

where R_S is sheet resistance due to stretching, R_{S0} is the initial sheet resistance, and ΔL is the applied elongation.

In comparison, the y-section shows a very low, approximately linear response, with a sensitivity of 21 (Ω/sq.)/%. This demonstrates an effective decoupling method for the effects of strain upon the *x*-section and is suitable for environmental sensing.

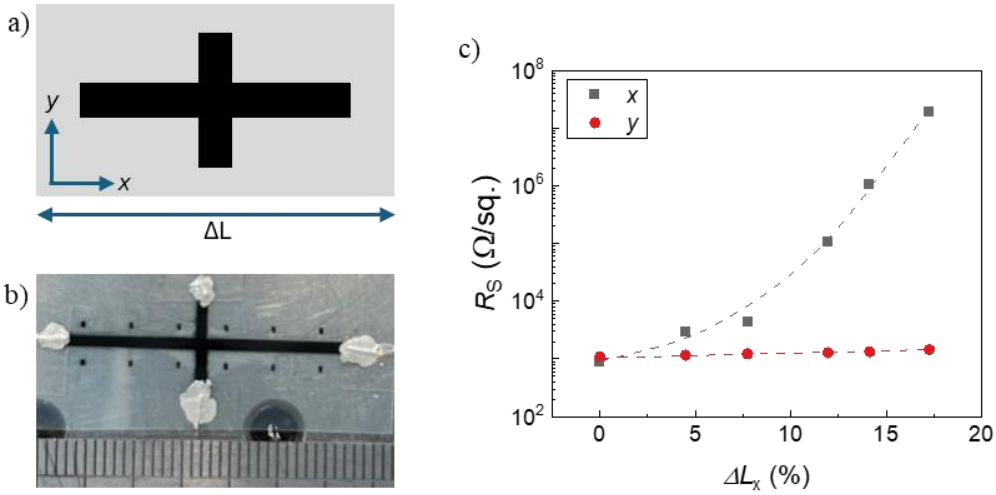


Figure 8-3 a) Schematic of orthogonal device for stretching and environmental sensing. **b)** Optical image of the iGr orthogonal device (1.2 wt%, DMC, $n_L = 10$, $T_{substrate} = 60$ °C, $n_F = 10$). **c)** Sheet resistance dependence on elongation (in the *x* direction) for the *x*- and *y*-sections of the iGr orthogonal device.

One limitation of this device is its ability to operate only under one-dimensional stretching. In order to take into account stretching from any direction, a multi-segment device could be produced (**Figure 8-4 a**), whereby there is always one section significantly perpendicular to the direction of stretching. Increasing the number of segments, $n_{segments}$, will improve the opportunities for strain decoupling if the direction of elongation cannot be known. Furthermore, such a device would enable the direction of stretching to be determined within a 45° arc by measuring the change in sheet resistance across the segments. To investigate this further, a device was produced with $n_{segments} = 4$. (**Figure 8-4 b**). Each segment of the device had dimensions of 25 x 1 mm and was rotated by 45° about the centre relative to the previous segment.

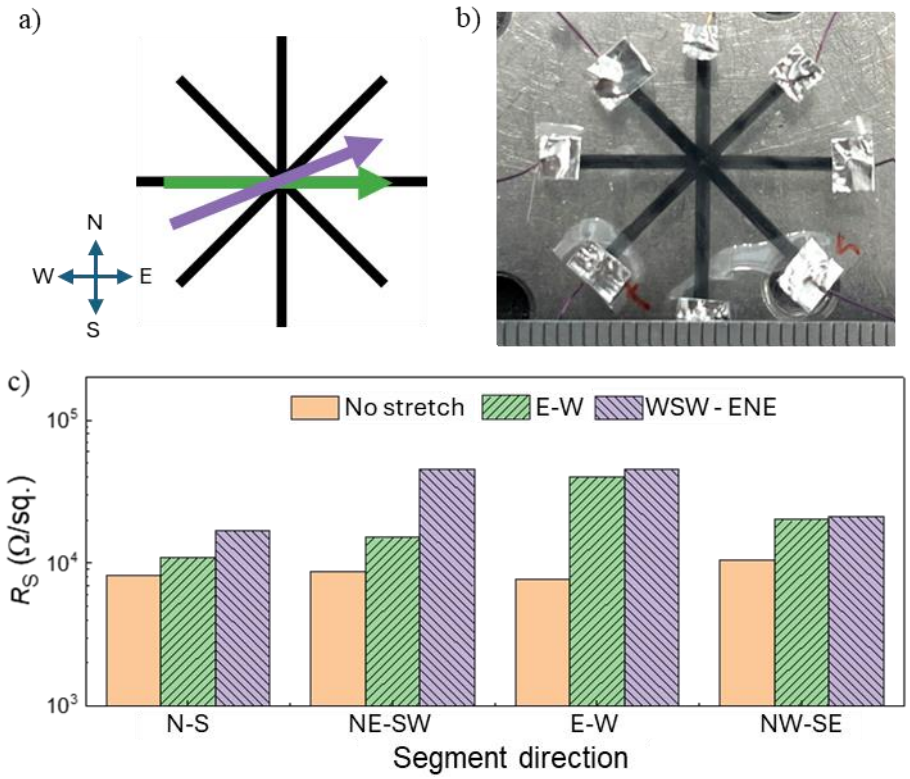


Figure 8-4 a) Diagram of 4 segment device, detailing segment labelling as well as directions of stretching applied (green and purple arrows). **b)** Inkjet-printed iGr 4 segment device on Beyolex, IPL annealed (n_L = 10, $T_{substrate}$ = 60 °C, n_f = 10). **c)** Dependence of sheet resistance on stretching in different states for 4 segment iGr device.

Electrical measurements were performed on the device in 3 states: at rest, stretched in the E-W direction (green), and the WSW-ENE direction (purple) (**Figure 8-4 a**). All segments exhibited comparable sheet resistance in the at rest state ($R_{S\text{-mean}}$ = 8.7 ± 1.1 kΩ) (**Figure 8-4 c**, orange). When stretched in the E-W direction, the sheet resistance of the E-W segment significantly increased by about ~6x, whilst the perpendicular section, N-S, saw a much smaller change (**Figure 8-4 c**, green). The segments at 45° to the direction of stretching exhibited an intermediate response, as they still possess reasonable alignment with the stretch direction. Lastly, the device was stretched in the WSW-ENE direction (**Figure 8-4 c**, purple). As expected, the E-W and NE-SW segments saw the largest increases in sheet resistance, whilst N-S and

NW-SE exhibited a smaller response. Overall, this approach demonstrates a method for directional strain sensing, enabling an approximation of orientation (± 45°) based on the magnitude of the response of different segments.

An important consideration in inkjet printing of stretchable devices is the printing direction, owing to anisotropy between deposited swathes. Inkjet printing has been shown to produce anisotropic devices, with distinctive separation between swathes of printed material.[132] As such, it should be considered that if the printing and strain directions are perpendicular, electrical performance is likely to deteriorate more so than if they are parallel, as separation between printed swathes can increase under mechanical deformation.

8.3 Acetone and humidity sensing

Inkjet-printed devices have been demonstrated for breath monitoring, providing real-time data on respiratory rate via temperature and humidity sensing.[297,298] Whilst breathing rate is a useful diagnostic, there is further benefit for inkjet-printed devices through chemical-sensing capabilities. Exhaled breath contains a range of chemical species, which can be indicative of various conditions. Devices exist that are capable of providing chemical sensing of ammonia but do not account for the effects of humidity, in which water is a major component of exhaled breath.[303] The following experimental work aims to evaluate the suitability of inkjet-printed graphene sensors for chemical detection in a dynamic humid environment.

To explore the gas-sensing capabilities of IPL-iGr with a medically relevant focus, the response to acetone vapour was investigated under the simultaneous application of *RH*. Initial response to an increase of *RH* from 60 - 100 % was observed until saturation of

the iGr signal, displaying a gradual increase in resistance over time, totalling to 80 Ω/sq. (**Figure 8-5 a**). The iGr response to acetone over a range of concentrations (0.2 - 3.2 ppm) was measured. (**Figure 8-5 b**).

At higher acetone concentrations, the iGr sample exhibited a progressively larger response, reaching a maximum change in resistance of 19.7 % at 3.2 ppm acetone. It was found that this behaviour was consistent at both 65 % and 100 % *RH* (**Figure 8-5 c**). The sensitivity exhibited by the IPL-iGr device significantly exceeds that demonstrated by alternative graphene-based devices,[375] whilst the correlation between gas concentration and ΔR_S increase is comparable.[303]

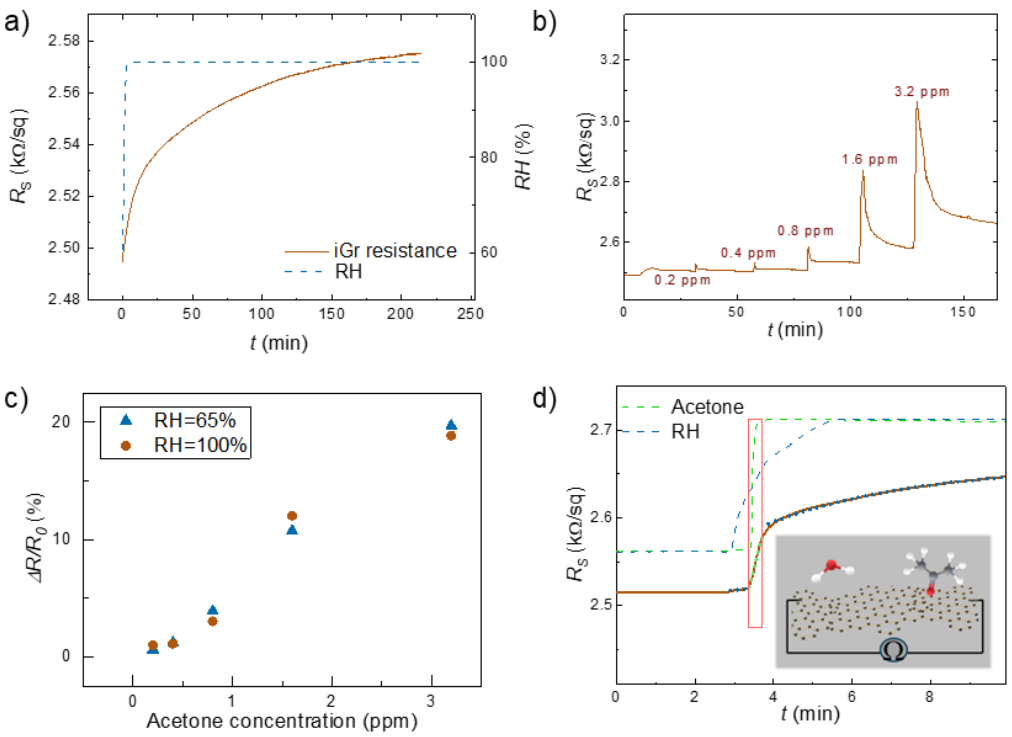


Figure 8-5 Response of IPL annealed iGr sample (n_L = 10, 2.4 wt% printed with SAMBA, n_F = 10, printed onto Kapton) to *RH* and acetone vapour **a)** Temporal response of iGr to humidity increase from 60 - 100 %*RH* **b)** Temporal response of iGr to increasing acetone concentration at *RH* = 100 %. **c)** Dependence of iGr on acetone concentration under different humid conditions. **d)** Temporal response of iGr to increasing humidity level (60 - 100 % *RH*) and increasing acetone concentration (0 - 1.6 ppm).

When assessing the relevance of iGr sensitivity to acetone in a clinical setting, it would be appropriate to use such a device for breath monitoring. Specifically identifying high acetone presence, as this can be symptomatic of diabetic ketoacidosis, a serious complication of type 1 diabetes. Consequently, it was sought to monitor changes in acetone concentration with increasing *RH*, with breath concentrations in the range of 1.76 - 3.73 ppm.[376] The iGr sensor distinguishes acetone humidity based on both the magnitude and rate of change of its electrical response, with acetone producing a faster and more intense response. **Figure 8-5 d** displays an initial increase in response to a rise in humidity, upon acetone being introduced, where the gradient of response is seen to steeply increase. This is in agreement with the previous temporal response seen in **Figure 8-5 b**, distinct to that of more gradual *RH* response. Once the acetone response is complete, the gradient returns to the gradual slope characteristic of the RH response. The distinguishable nature of this simultaneous sensing can be attributed to the differing effects of humidity and acetone upon graphene electrical resistance. When exposed to humidity, the adsorption of water molecules into the iGr film increases flake-to-flake distance, increasing electrical resistance.[183] The observed increase in graphene electrical resistance upon exposure to acetone can be attributed to adsorption of acetone molecules and the subsequent interaction between the C=O bond on acetone molecules and graphene flake edges, influencing charge behaviour.[27] Acetone produces a faster response because it diffuses more rapidly and interacts more strongly with the sensing film than water.[377] Thus, explaining the fast response time observed, enabling the successful distinguishing of the acetone response in changing *RH* and may also be applicable to other gases and chemicals.

9 Sensing of biologically relevant molecules

This chapter builds directly on the multifunctional sensing capabilities established in Chapters 7 and 8. Having demonstrated that printed graphene-based devices can respond selectively to multiple physical and chemical stimuli, we now explore their applicability to biological biomarkers. Two experimental studies are presented: detection of quorum-signalling molecules associated with bacterial infection, and the measurement of ionic composition changes in hydrogels relevant to wound monitoring. These studies evaluate whether the sensing strategies developed earlier in the thesis can be extended to biologically meaningful environments. Gr/PEDOT:PSS devices were developed to investigate their electrical response to thermal, chemical and biological stimuli. This chapter reports on the high temperature sensitivity of the Gr/PEDOT:PSS ink, exceeding values observed with the previously studied iGr ink. The capacitive sensing capabilities of the IDE design are explored through response to a hydrogel interface, enabling signalling of chemical changes from within. Lastly, multimaterial device design is utilised to investigate the applicability of printed electronics towards sensing biological compounds. In this case, artificial quorum signalling molecules are used, provided by Dr Nigel Halliday, with relevant application towards the detection of biofilm growth.

9.1 Temperature dependence of Gr/PEDOT:PSS

Temperature dependence of the commercial inkjet-printed Gr/PEDOT:PSS was investigated to confirm results observed within the literature, as well as determine the specific sensitivity of this ink. A Hall bar geometry was printed (n_L = 5, $T_{substrate}$ =

35 °C) onto an SiO_2/Si wafer (**Figure 9-1 a**). The voltage-current dependence of the Gr/PEDOT:PSS Hall bar device was recorded at 2, 20 and 300 K (**Figure 9-1 b**), exhibiting a strong temperature dependence. Electrical resistance decreased exponentially with increasing temperature (**Figure 9-1 c**), exhibiting an Arrhenius-like behaviour with activation energy E_a = 5.1 meV.

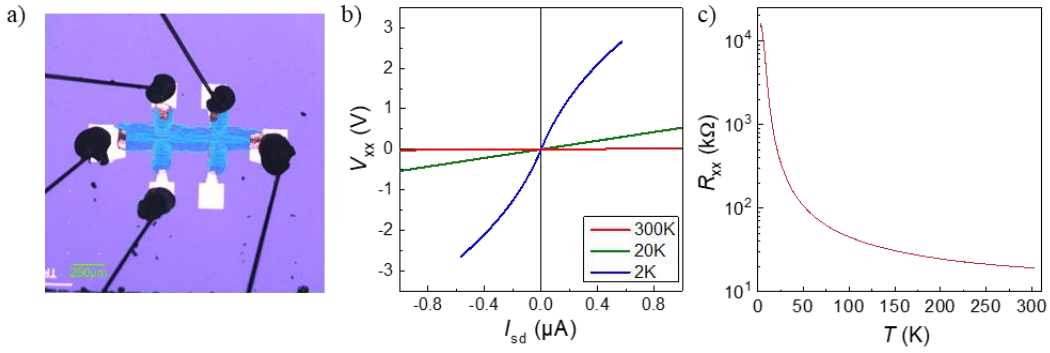


Figure 9-1 a) Inkjet-printed Gr/PEDOT:PSS Hall bar (n_L = 5, $T_{substrate}$ = 35 °C) on SiO_2/Si. **b)** Voltage-current dependence of Gr/PEDOT:PSS. **c)** Temperature dependence of resistance for Gr/PEDOT:PSS ink.

This is in agreement with the temperature dependence studies performed in **Chapter 7.1** and **Chapter 8.1**, although the Gr/PEDOT:PSS ink exhibits significantly higher sensitivity (~ 2x) compared to the iGr ink (**Table 9-1**). This increased sensitivity can be attributed to the larger number of thermally responsive conduction pathways introduced by the PEDOT:PSS component. PEDOT:PSS itself exhibits strongly temperature-dependent transport, and its incorporation into the graphene ink therefore enhances the overall thermal sensitivity of the composite film.[295]

Table 9-1 Temperature sensitivity comparison for iGr – thermally and IPL annealed, and Gr/PEDOT:PSS.

Sample	Relative sensitivity ($°C^{-1}$)
iGr – TA (n_L = 5, T_{anneal} = 250 °C, t_{anneal} = 1 hour)	0.081 %
iGr – IPL annealed (n_L = 5, n_f = 10)	0.096 %
Gr/PEDOT:PSS (n_L = 5)	0.180 %

9.2 Detection of Quorum signalling molecules

Quorum signalling is a fundamental communication mechanism used by bacteria to control population density during biofilm growth through the release and detection of quorum signalling molecules (QSMs).[378] Thus these molecules are highly relevant for biomedical sensing, enabling indication of bacterial presence. Conventional methods for QSM detection include chromatography and spectroscopy, requiring complex sample preparation, and are not well-suited towards *in situ*, real time measurements. In this work, inkjet-printed Gr/PEDOT:PSS as a method of detection for 4 QSMs was explored: pseudomonas quinoline signal 2-heptyl-3-hydroxy-4(1H)-quinolone (PQS), 2-heptyl-4(1H)-quinolone (NHQ), 2-nonyl-4-hydroxyquinoline (HHQ) and 2-heptyl-4-hydroxyquinoline N-oxide (HQNO). Synthetic QSMs were received from Dr Nigel Halliday (University of Nottingham). All these molecules are based off a 4-quinoline scaffold, with variations in alkyl chain length and functional group (**Figure 4-16**).

Gr/PEDOT:PSS devices were produced (n_L = 20, $T_{substrate}$ = 60 °C, 3 x 0.5 mm) with a TPGDA overlay (n_L = 5) providing a window for quorum molecule deposition of 4.4 x 0.4 mm (**Figure 9-2 c**). QSM were dissolved in methanol at a range of concentrations (1 pg/mL – 1 mg/mL). Solutions were deposited onto the Gr/PEDOT:PSS devices 3 times with a droplet volume of 2 μL, whilst the Gr/PEDOT:PSS samples were placed on a heated platform (T = 60 °C) facilitating methanol evaporation and device

recovery. A constant voltage was applied (V = 0.1 V) to devices during exposure, and current, I, was recorded. An interval of ~ 400 s was used between droplet deposition. The Gr/PEDOT:PSS response to methanol was first investigated as a control (**Figure 9-2 a**). After each subsequent exposure to methanol, a decrease in sheet resistance was observed, suggesting that methanol has a drying effect on the Gr/PEDOT:PSS, facilitating the removal of any H_2O adsorbed. Samples were exposed to multiple exposures of methanol (~ 10) until a stable R_S was recorded.

Initially, the PQS molecule was investigated, with the temporal response to 1 ng/mL and 1 µg/ml exposures shown in **Figure 9-2 a**. Exposure to methanol and PQS solutions was very rapid in response ($t_{ON\text{-}methanol}$ = 22.4 ± 2.7 s, $t_{ON\text{-}1\ \mu g/ml\ PQS}$ = 19.8 ± 2.7 s), and recovery times ($t_{OFF\text{-}methanol}$ = 49.1 ± 8.8 s, $t_{OFF\text{-}1\ \mu g/ml\ PQS}$ = 0.8 s) (**Figure 9-2 a**). The change in resistance, ΔR_S, was observed to decrease with an increase in C_{PQS} (**Figure 9-2 b**), with methanol providing the largest response ($\Delta R_{S\text{-}methanol}$ = 55.7 ± 5.2 Ω/sq.).

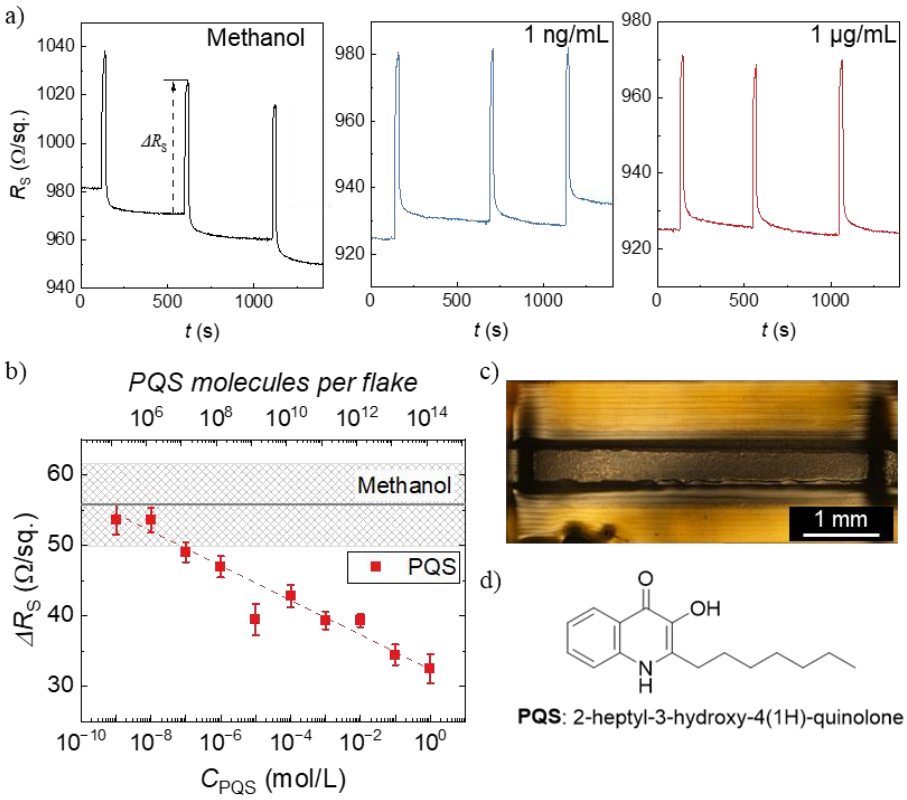


Figure 9-2 a) Representative temporal responses for Gr/PEDOT:PSS (n_L = 20, $T_{substrate}$ = 60 °C) samples when subjected to 2 µL deposits of methanol (black), 1 ng/mL PQS in methanol (blue) and 1 µg/mL PQS in methanol (red). **b)** Dependence of Gr/PEDOT:PSS (n_L = 20, $T_{substrate}$ = 60 °C) change of resistance on PQS concentration in methanol and on the number of PQS molecules deposited per surface-level graphene flake. **c)** Optical image of Gr/PEDOT:PSS-TPGDA ($n_{L\text{-}Gr/PEDOT:PSS}$ = 20, $T_{substrate}$ = 60 °C) samples used for PQS responses with TPGDA window overlay ($n_{L\text{-}TPGDA}$ = 5). **d)** Chemical structure for PQS molecule.

To further explore why the Gr/PEDOT:PSS shows an inverse relationship with PQS concentration, the number of molecules deposited per flake was estimated. Using the molecular weight and known concentration, the number of molecules contained within a 2 µL droplet can be estimated. From manufacturer specifications, it is stated that the average graphene flake size is 10 µm, so the approximate sheet area is 100 µm^2, and thus, for the TPGDA window of 4.4 x 0.4 mm, there would be ~1.7 × 10^4 flakes of graphene. Hence, the coverage of PQS molecules per surface flake was estimated, assuming that molecules are distributed evenly across the Gr/PEDOT:PSS film.

When plotting this against the observed changes in resistance, it can be seen that there are a large number of PQS molecules per surface flake (< 1.36×10^5 molecules per flake) (**Figure 9-2 b**). It is thought that the extensive coverage of PQS molecules causes a screening effect, preventing interaction between the Gr/PEDOT:PSS film and methanol. This could be further aided by π-π stacking occurring between molecules and graphene flakes, due to the presence of aromatic rings in the PQS structure (**Figure 9-2 d**). Thus, as C_{PQS} increases, the interaction between methanol molecules and the Gr/PEDOT:PSS film will be reduced, explaining the inverse relationship observed in **Figure 9-2 b**.

To mitigate potential risks of solution accumulation at the edges of the TPGDA window, which may have been present in the previous work, samples were placed in curved device holders (**Figure 9-3 a**). Devices were prepared with Gr/PEDOT:PSS (n_L = 20, $T_{substrate}$ = 60 °C), with inkjet-printed AgNP electrical contacts ($n_{L\text{-}AgNP}$ = 3, $T_{substrate}$ = 90 °C, T_{anneal} = 150 °C, t_{anneal} = 1 hour), as well as a TPGDA overlay (n_L = 5, $T_{substrate}$ = 25 °C).

Upon exposure to 2 µL methanol deposits, a significant annealing effect was again observed, exhibited by a decrease in sheet resistance (**Figure 9-3 b**). Sample response was first investigated against the effects of the PQS molecule, where a significantly increased response magnitude (~ 10x) was observed when compared to the flat devices (**Figure 9-3 c**). This is likely a result of reduced accumulation of methanol and PQS molecules towards the edges of the sample, hence molecular coverage over Gr/PEDOT:PSS film. Devices were then exposed to different QSM as well as PQS; HHQ, NHQ and HQNO. Different devices were used for each QSM to prevent contamination effects. A similar trend to **Figure 9-2 b** was observed, whereby increasing the concentration of QSM resulted in a decreased response magnitude. It is

proposed that the same screening effect previously described also occurs with curved devices, albeit with a greater magnitude, as evidenced by the increased sensitivity observed. At medium to low concentrations of QSM solutions tested (**Figure 9-3 d**), (10^{-6} – 10^{-12} mol/L), the largest response was observed for PQS (red), then HQNO (blue), NHQ (green) and HHQ (purple). Response sensitivity and variability decreased with concentration, and differences among molecules were insufficient when C < 10^{-5} mol/L.

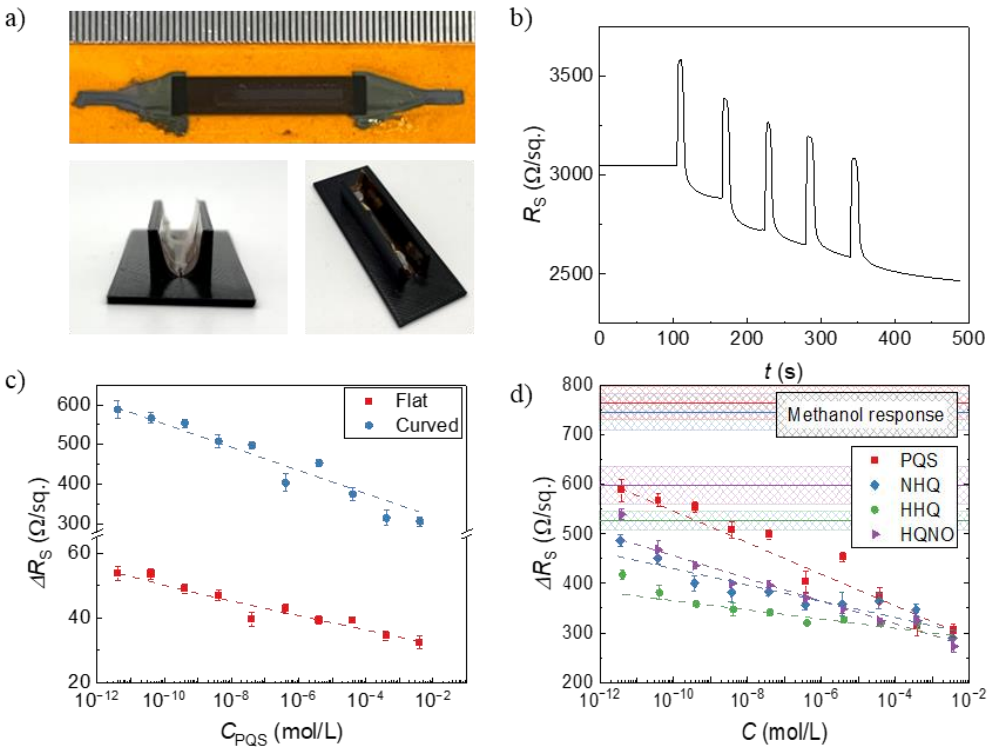


Figure 9-3 a) Optical images of AgNP ($n_{L\text{-}AgNP}$ = 3, $T_{substrate}$ = 90 °C, T_{anneal} = 150 °C, t_{anneal} = 1 hour) Gr/PEDOT:PSS (n_L = 20, $T_{substrate}$ = 60 °C) TPGDA ($n_{L\text{-}TPGDA}$ = 5, $T_{substrate}$ = 25 °C) device as-printed (top) and in a curved holder (bottom). **b)** Temporal responses for Gr/PEDOT:PSS (n_L = 20, $T_{substrate}$ = 60 °C) samples when subject to 2 µL deposits of methanol. **c)** Comparison between of Gr/PEDOT:PSS flat and curved devices' (n_L = 20, $T_{substrate}$ = 60 °C) sheet resistance dependence on PQS concentration in methanol. **d)** Dependence of Gr/PEDOT:PSS (n_L = 20, $T_{substrate}$ = 60 °C) change in resistance on different QSM (PQS, HHQ, NHQ, HQNO) concentration in methanol. Methanol responses (C_{QSM} = 0 mol/L) are given by dashed boxes (colour coded) for each device used in testing.

The sheet resistance value of the samples used in the curved devices was ~ 5x higher than the flat ones ($R_{S\text{-flat}}$ = 657 ± 218 Ω/sq. compared to $R_{S\text{-curved}}$ = 3525 ± 623 Ω/sq.). It could be argued that the sensitivity of such devices, in terms of ΔR_S would be larger due to the increased initial resistance. However, to verify this, a comparison was made of the PQS datasets for both device types, in which the response was normalised to the initial resistance, $\Delta R/R_0$ (**Figure 9-4**). It is evident that the curved sample exhibits higher sensitivity, especially at lower concentrations. This difference decreases as the PQS concentration increases, likely due to increased molecular surface coverage that inhibits methanol interaction with the printed film.

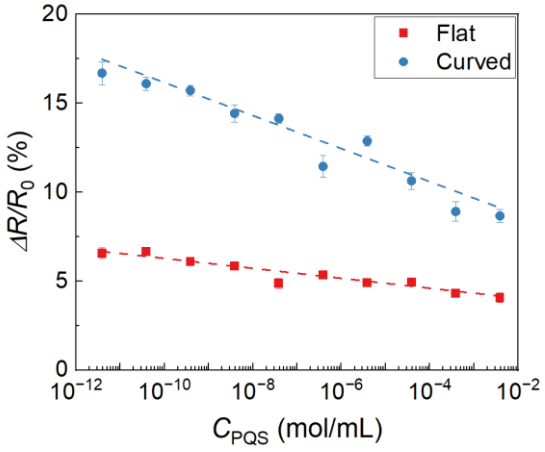


Figure 9-4 Normalised dependence of flat and curved Gr/PEDOT:PSS devices (n_L = 20, $T_{substrate}$ = 60 °C) to methanol-PQS solutions.

The previous results in this chapter have explained the dependence of Gr/PEDOT:PSS on QSM concentration through the shielding effect of molecules upon the film's surface, assuming minimal molecule penetration. The effect of film thickness upon the QSM dependence was investigated. Curved samples were prepared as previously described($n_{L\text{-Gr/PEDOT:PSS}}$ = 20 & 40, $T_{substrate}$ = 60 °C), with AgNP contacts ($n_{L\text{-AgNP}}$ = 3, $T_{substrate}$ = 90 °C, T_{anneal} = 150 °C, t_{anneal} = 1 hour) and a TPGDA window overlay (n_L

= 5, $T_{substrate}$ = 25 °C). Devices were subjected to methanol-NHQ deposits, and electrical measurements were performed as previously described. As the work in **Chapter 5** shows, reduced electrical conductivity for higher n_L was expected, hence a larger ΔR_S would be observed. Initial resistance measurements supported this expectation, whereby $R_{S\text{-}20L}$ = 572 Ω/sq. and $R_{S\text{-}40L}$ = 321 Ω/sq.. To effectively compare the dependence of these devices, the response to NHQ solution was normalised against the initial resistance (**Figure 9-5**). The 20-layer device exhibited greater sensitivity to NHQ by ~ 5 %. These results imply that penetration of NHQ molecules throughout the depth of the Gr/PEDOT:PSS film is minimal, as a greater portion of the 40-layer print remains unaffected. This is shown by the lower sensitivity observed, suggesting that the NHQ molecules effectively cover the surface layer and prevent penetration of methanol throughout the whole printed film.

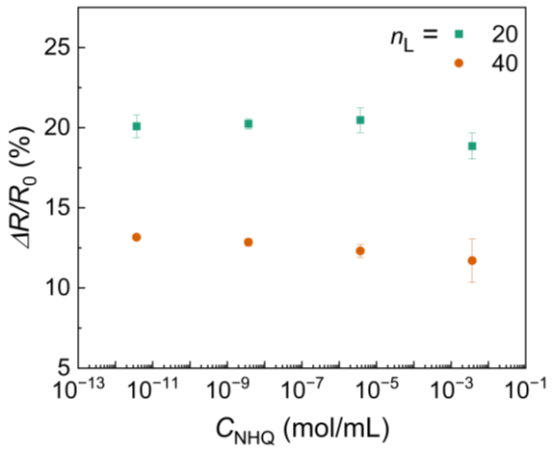


Figure 9-5 Normalised dependence of curved Gr/PEDOT:PSS devices (n_L = 20 & 40, $T_{substrate}$ = 60 °C) to methanol-NHQ solutions.

It should be noted that for these samples, no effective trend was observed in terms of the ΔR_S dependence on NHQ concentration. UV-vis spectroscopy was used to determine whether the QSMs were still in solution. QSM solutions were stored for 6 months at -20 °C. Solutions previously prepared at a concentration of 1 mg/mL were

diluted to 10 µg/mL. This was due to the high absorbance observed at 1 mg/ml, exceeding the readable range of the equipment. Hence, 5 samples were used to investigate, NHQ, PQS, HHQ, HQNO at 10 µg/mL, and the methanol used to prepare the original solutions. Peaks were observed at 230 and 320 nm (NHQ), 250 and 350 nm (PQS), 230 and 320 nm (HHQ), 240 and 330 nm (HQNO). Within the literature, peaks for PQS dissolved in PBS have been observed at 215, 240 and 340 nm, corroborating the data observed in this work.[379,380] No peaks were observed in the methanol spectra, confirming the presence of QSM in the prepared solutions.

9.3 Chemical sensing through a hydrogel medium

In order to perform sensing beyond the surface level of the printed devices, interdigitated electrodes (IDEs) were used due to the capacitive field produced.[381,382] In this work, Gr/PEDOT:PSS IDEs were prepared on glass substrates (n_L = 20, $T_{substrate}$ = 60 °C) for the overprinting of hydrogels with dimensions of 5 x 4 mm, finger width of ~100 µm and finger spacing of ~200 µm. It was intended for the IDE to detect compositional changes throughout the hydrogel with the addition of different aqueous salt solutions. High resolution was achieved by printing the IDEs such that each electrode 'finger' was oriented perpendicular to the printhead travel direction. When printing with this orientation, line widths of 117 ± 12 µm were achieved, and it was possible to maintain a spacing of 187 ± 10 µm (**Figure 9-6 a**).

The hydrogels used in this work were formulated from thiolated gelatine (5 w/v%), norbornene-modified gelatine (5 w/v%) and 0.5 w/v% lithium phenyl (2,4,6-trimethylbenzoyl) phosphinate (LAP) dissolved in phosphate-buffered saline (PBS).

The hydrogels had approximate dimensions of 5 x 5 x 5 mm. These were provided by Dr Nathan Carpentier (University of Nottingham).

The gelatine hydrogel was printed on top of the Gr/PEDOT:PSS electrode by Dr Nathan Carpentier using an Elegoo Mars 4 SLA printer. Upon visual inspection, it appeared that the Gr/PEDOT:PSS IDE had suffered damage during the overprinting process, with macroscopic damage on the surface (**Figure 9-6 b**). When attempting to measure capacitance, values did not surpass 0.01 pF, suggesting that the electrical properties of the IDE were severely impaired.

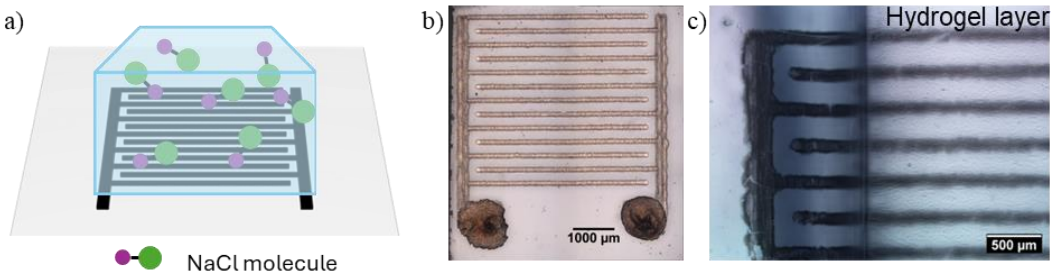


Figure 9-6 a) Schematic of NaCl doped hydrogel deposited on Gr/PEDOT:PSS IDE **b)** Gr/PEDOT:PSS (n_L = 20, $T_{substrate}$ = 60 °C) IDE inkjet-printed on glass. **c)** Gelatine hydrogel overprinted onto Gr/PEDOT:PSS IDE.

In order to further investigate whether compositional changes could be detected through hydrogels, the printed hydrogel was placed on top of a new Gr/PEDOT:PSS (n_L = 20, $T_{substrate}$ = 60 °C). The baseline capacitance of the Gr/PEDOT:PSS electrode, at room temperature in air was 8.83 pF. To investigate the ability of such a device to detect compositional changes within a hydrogel, the hydrogel was soaked in DI water and aqueous NaCl solutions and 0.1 M and 1.0 M concentrations. The concentration of electrolytes, or salt ions, within sweat can be indicative of multiple health conditions, for instance, NaCl is crucial in the body for regulating fluid balance, nerve signal transmission and muscle function. It also helps to maintain blood pressure,

whilst ensuring cells remain hydrated, acting as a vital electrolyte. Insufficient NaCl intake can indicate low blood pressure and dehydration, whereas excessive NaCl intake can have the opposite effects. Physiological levels of NaCl in cells, blood and sweat are in the region of 0.01 – 0.15 M.[383–385] Whilst the concentrations used in this work include and exceed these values, it is a preliminary step in understanding the response of printed Gr/PEDOT:PSS devices towards NaCl presence. The hydrogel was soaked for 1 hour in each solution before being placed on the IDE. The capacitance of the device increases with NaCl concentration (**Figure 9-7 a**). This would likely be as a result of an increase in ionic concentration from the NaCl composition within the hydrogel, raising the number of charge carriers.

Hydrogels were placed and left on the IDE for a duration of 5 minutes, and the temporal capacitance response was observed (**Figure 9-7 b**). The hydrogel soaked in DI water exhibited the most rapid response and stabilisation, and a slow decline thereafter. This is likely due to the hydrogel beginning to dry out, thereby altering its dielectric properties. The time for saturation of the IDE capacitance increased with the NaCl concentration. It is envisaged that this is due to prolonged redistribution and diffusion of the NaCl ions within the hydrogel.[386] These results demonstrate that the ionic concentration of the medium governs the capacitive response and also defines the temporal response.

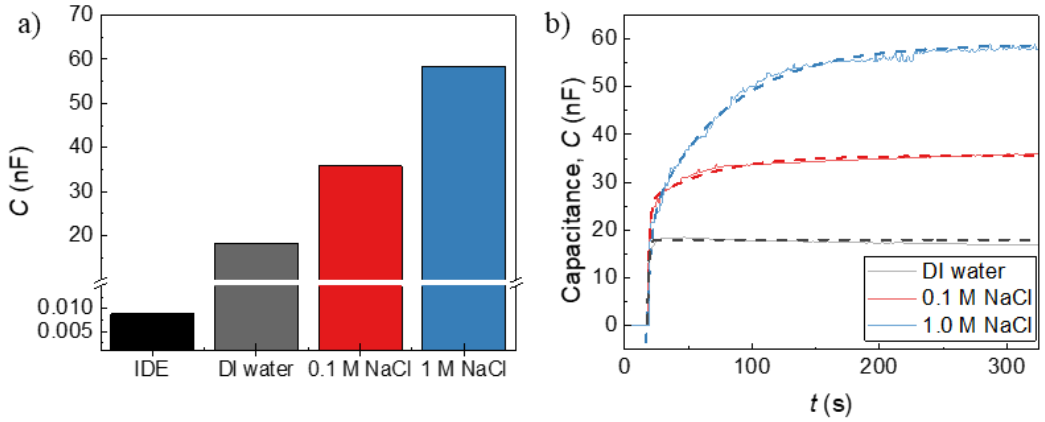


Figure 9-7 a) Maximum capacitance value achieved when depositing hydrogel and NaCl hydrogels onto Gr/PEDOT:PSS IDE on glass (n_L = 20, $T_{substrate}$ = 60). **b)** Temporal responses towards hydrogel and NaCl hydrogels, with exponential fits (dashed lines).

The temporal responses were fitted using exponential functions (**Figure 9-7**). For DI water, a single-term exponential fit was sufficient, as expected for response to individual stimuli. The response to NaCl-soaked hydrogels required a two-term exponential fit, indicating more complex behaviour. The extracted time constants are summarised in **Table 9-2**. They indicate a region of fast response (τ_1 < 4 s), which becomes slower with increased NaCl concentration. The presence of NaCl introduces a slower secondary component, τ_2, representing a gradual increase in capacitance that intensifies with higher salt concentrations.

Table 9-2 Time constants for Gr/PEDOT:PSS (n_L = 20, $T_{substrate}$ = 60 °C) IDE temporal response to hydrogel contact.

Sample	τ_1 (s)	τ_2 (s)
Hydrogel	0.95	-
0.1 M NaCl	1.48	49.43
1.0 M NaCl	3.23	61.85

These results highlight the suitability of inkjet printed IDEs for penetrative sensing; being able to detect compositional changes in media extending above the printed device. Comparatively the devices previously presented in this thesis are only able to detect stimuli at the surface level. Further work should be carried out to investigate the effects of IDE geometry on sensing capabilities, as well as to produce a fully printed device and hydrogel.

10 Conclusions and future work

The primary aims of this PhD were largely met: effective deposition of functional materials onto textile substrates, the development of low-temperature post-processing methods that enable the use of thermally sensitive substrates, and the exploration of simultaneous multifunctional sensing with applications to wearable devices.

With reference to the research questions outlined in the introduction, this work successfully established low temperature photonic annealing/sintering as an effective method for post processing of inkjet printed material compared with thermal techniques. Compatibility with flexible and stretchable thermally sensitive substrates was also proven. Mechanical robustness was shown by inkjet printed graphene devices, where high resilience to bending and stretching was observed, confirming the suitability for wearable. Whilst a method was investigated to offer sensing solutions whilst subject to strain. Lastly, biologically relevant biomarkers were successfully investigated through detection of breath-borne analytes, ionic changes in hydrogels and quorum-signalling molecules associated with bacterial activity. Together, these findings show that the approaches developed in this thesis directly address the challenges identified in the Introduction and contribute to the advancement of multifunctional wearable healthcare technologies.

The key findings from this work are presented below:

A strategy for negating the high surface roughness and porosity of textile substrates was effectively implemented through the use of a polymeric interface layer through post-deposition UV curing. This enabled the deposition of a commercially available graphene ink that exhibited responses to temperature, humidity, and pressure. Although the achieved resistance of the iGr-textile was high (350 kΩ), future work

should consider revising the interface layer to improve substrate deposition or utilising textiles with a tighter weave, thereby reducing porosity. It should also be noted that the number of printed iGr layers was very high (n_L = 50), so the use of higher-drop-volume and increased nozzle-count printing systems may improve process efficiency.

Photonic post-processing methods were successfully employed on inkjet-printed films of iGr, AuNPs and Gr/PEDOT:PSS, permitting the use of highly flexible and stretchable polymeric substrates previously unavailable to thermal methods. IPL was found to be effective on iGr on a range of polymeric substrates, including Kapton, PEN, PET, and Beyolex; however, this was not transferred to rigid substrates with high thermal conductivity, where rapid dissipation of heat away from the printed material reduced annealing effects. The effective range for operation appears to be for substrates with thermal conductivity < 0.5 W/m.K. The achieved sheet resistance of iGr was very low (240 Ω/sq.), comparable with previous studies utilising thermal annealing. UV irradiation was applied to an AuNP ink formulation modified with UV-cleavable ligands. The process was shown to operate with power density several orders of magnitude lower compared with other photonic-based methods applied to MeNPs whilst achieving a competitive electrical conductivity (7.0×10^6 S/m). Whilst the Gr/PEDOT:PSS ink used in this work was conductive as-printed, the application of UV irradiation (t_{UV} = 30 min) was shown to reduce sheet resistance by 60 %, with improvements of 40 % attainable after 30 s exposure.

The application of low-temperature photonic post-processing methods enabled the production of inkjet-printed electronics onto flexible and stretchable substrates, exhibiting durability towards mechanical deformation. This was demonstrated with the following combinations of inkjet-printed functional materials and flexible or stretchable substrates: iGr-textile, iGr-Kapton, iGr-Beyolex, AuNPs-PEN and

Gr/PEDOT:PSS-Beyolex. Modification of the pattern design was shown to improve response to strain, both incrementally and cyclically, through the use of serpentine or meandering geometries. Device design, incorporating orthogonally printed lines, effectively decoupled strain effects in the segment perpendicular to the stretch direction. Further refinement of this design enabled the detection of the strain direction. There remains scope for additional investigation of the orthogonal device, to determine whether it can respond to environmental stimuli independently to the degree of strain.

Multimaterial printing was used to develop an iGr based device, capable of providing selective simultaneous sensing towards temperature, humidity and pressure. An iGr layer was encapsulated by TPGDA, with an additional iGr layer on top of the dielectric. The base iGr would provide temperature sensing and be sealed against humidity. The temperature response recorded from the bottom layer was subtracted from that of the top, isolating the humidity response, whereas pressure was determined from the capacitance change between the two iGr layers and was found to be independent of other stimuli. The device was demonstrated to be effective when subject to temperature-pressure and temperature-humidity.

The performance of a single electrode iGr device in a complex environment was explored, with reference to breath sensing. It was possible to distinguish the acetone response from the iGr in a changing humid environment due to differences in response rate and magnitude. Future work in this area should consider implementing chemical-species-selective membranes on top of printed devices to further enhance selectivity.

Initial efforts have been made to combine different AM techniques, using 3D printed materials as a substrate for inkjet printing. iGr was deposited onto a cast silicone

formulation suitable for inkjet printing, yielding a relatively high sheet resistance of 9.8 kΩ/sq, which exhibited severe degradation upon bending and stretching. There remains significant room to improve deposition on silicone with respect to electrical properties, as well as to explore potential devices enabled by cross-AM technologies.

An attempt was made to overprint a gelatin-based hydrogel onto Gr/PEDOT:PSS IDEs using SLA. However, the electrical properties of the IDE deteriorated during the overprinting process. Instead, a hydrogel was placed on top of an IDE after being soaked in aqueous NaCl solutions of increasing concentration. The capacitance was found to increase with salt concentration, demonstrating detection of compositional changes. To further explore the capabilities of such a sensing method, it would be valuable to achieve an overprinted hydrogel without degradation to IDE electrical properties, and to investigate the addition of geometrical features to the gel for different sensing applications.

Sensitivity of Gr/PEDOT:PSS was demonstrated towards quorum signalling molecules down to picomolar concentrations. These show relevance for wound care, where the presence of quorum molecules is associated with the formation of biofilms, and thus infection.

A formulation for inkjet printing Nitschke cages was successfully developed, and material was printed on top of iGr devices. Increasing the number of N-cage layers was found to increase iGr electrical conductivity and damage the printed film surface through cracking. N-cages are appealing due to their potential for highly selective gas and chemical sensing; however, this work did not include the completion of such sensing studies, which remain a focus of future research.

Whilst in a broader context, the findings of this thesis present a foundation for the development of wearable healthcare technologies, primarily regarding wound monitoring and breath analysis. The demonstrated low-temperature post processing methods in conjunction with the multifunctional sensing capabilities achieved with both simple and heterostructure devices exhibit strong affinity towards the previously mentioned healthcare applications. These findings have the potential to enhance earlier diagnosis, personalised healthcare monitoring and enable high throughput, scalable, low-cost manufacture of devices. By realising conformal and multifunctional sensing, the approaches developed in this thesis directly address the growing demand for wearable, real-time healthcare monitoring systems.

Despite these opportunities, several challenges still remain for the widespread adoption of this technology for device manufacture and operation. The long-term performance of devices in both a sensing and mechanical deformation capacity require investigating, and how these factors might be dependent upon each other. Whilst improving selectivity of devices is still relatively unexplored, in this work and the wider literature. Where true selectivity might be employed through the use of selective membranes, or by functionalising the surface of inkjet printed films. These directions represent significant avenues for future research within this sphere and would be essential for achieving translation of this technology into reliable wearable systems.

In summary, this thesis advances the materials, processing strategies and device applications necessary to realise flexible, multifunctional wearable healthcare devices. The approaches developed and used within this work address fundamental barriers that have limited the translated of printed electronics to wearable devices, and as the field continues to evolve the insights and methodologies presented here should serve to guide future development of healthcare technologies.

11 References

(1) Davaji, B.; Cho, H. D.; Malakoutian, M.; Lee, J. K.; Panin, G.; Kang, T. W.; Lee, C. H. A Patterned Single Layer Graphene Resistance Temperature Sensor. Sci. Rep. 2017, 7 (1). https://doi.org/10.1038/s41598-017-08967-y.

(2) Andò, B.; Baglio, S.; Pasquale, G. Di; Pollicino, A.; Graziani, S.; Gugliuzzo, C.; Lombardo, C.; Marletta, V. Direct Printing of a Multi-Layer Sensor on PET Substrate for CO 2 Detection. Energies (Basel). 2019, 12 (3). https://doi.org/10.3390/en12030557.

(3) Andò, B.; Baglio, S.; Di Pasquale, G.; Pollicino, A.; D'Agata, S.; Gugliuzzo, C.; Lombardo, C.; Re, G. An Inkjet Printed CO2 Gas Sensor. In Procedia Engineering; Elsevier Ltd, 2015; Vol. 120, pp 628–631. https://doi.org/10.1016/j.proeng.2015.08.755.

(4) Xu, G.; Lu, Y.; Cheng, C.; Li, X.; Xu, J.; Liu, Z.; Liu, J.; Liu, G.; Shi, Z.; Chen, Z.; Zhang, F.; Jia, Y.; Xu, D.; Yuan, W.; Cui, Z.; Low, S. S.; Liu, Q. Battery-Free and Wireless Smart Wound Dressing for Wound Infection Monitoring and Electrically Controlled On-Demand Drug Delivery. Adv. Funct. Mater. 2021, 31 (26). https://doi.org/10.1002/adfm.202100852.

(5) Chehade, J. A.; Bhattacharya, S.; Iezzi, R. Inkjet-Printed Graphene Sensors for the Bedside Detection of Tear Film Ph. Transl. Vis. Sci. Technol. 2021, 10 (3). https://doi.org/10.1167/tvst.10.3.10.

(6) Santra, S.; Hu, G.; Howe, R. C. T.; De Luca, A.; Ali, S. Z.; Udrea, F.; Gardner, J. W.; Ray, S. K.; Guha, P. K.; Hasan, T. CMOS Integration of Inkjet-Printed Graphene for Humidity Sensing. Sci. Rep. 2015, 5 (1). https://doi.org/10.1038/srep17374.

(7) Austin, J. S.; Cottam, N. D.; Zhang, C.; Wang, F.; Gosling, J. H.; Nelson-Dummet, O.; James, T. S. S.; Beton, P. H.; Trindade, G. F.; Zhou, Y.; Tuck, C. J.; Hague, R.; Makarovsky, O.; Turyanska, L. Photosensitisation of Inkjet Printed Graphene with Stable All-Inorganic Perovskite Nanocrystals. Nanoscale 2022, 15 (5), 2134–2142. https://doi.org/10.1039/D2NR06429D.

(8) Austin, J. S.; Xiao, W.; Wang, F.; Cottam, N. D.; Rivers, G.; Ward, E. B.; James, T. S. S.; Luan, W.; Tuck, C. J.; Hague, R.; Makarovsky, O.; Turyanska, L. Developing Colloidal Nanoparticles for Inkjet Printing of Devices with Optical Properties Tuneable from the UV to the NIR. J. Mater. Chem. C Mater. 2024, 12 (29), 10992–11000. https://doi.org/10.1039/D4TC01917B.

(9) Haverinen, H. M.; Myllylä, R. A.; Jabbour, G. E.; Jabbour, G. E. Inkjet Printed RGB Quantum Dot-Hybrid LED. IEEE/OSA Journal of Display Technology 2010, 6 (3), 87–89. https://doi.org/10.1109/JDT.2009.2039019.

(10) Lin, Y.; Chang, Y. W.; Hyun, B. R.; Sher, C. W.; Kuo, H. C.; Liu, Z. P-12.2: Inkjet-Printed Quantum-Dots Photopolymers for Full-Color Micro-LED Displays. SID Symposium Digest of Technical Papers 2021, 52 (S1), 597–600. https://doi.org/10.1002/SDTP.14568.

(11) Park, M.; Kim, Y. Il; Jung, Y. K.; Kang, J. G.; Kim, S.; Ha, J.; Yoon, Y. G.; Lee, C. All Inkjet-Printed 6.95″ 217 Ppi Active Matrix QD-LED Display with RGB Cd-Free QDs in the Top-Emission Device Structure. J. Soc. Inf. Disp. 2022, 30 (5), 433–440. https://doi.org/10.1002/JSID.1126.

(12) Worsley, R.; Pimpolari, L.; McManus, D.; Ge, N.; Ionescu, R.; Wittkopf, J. A.; Alieva, A.; Basso, G.; Macucci, M.; Iannaccone, G.; Novoselov, K. S.; Holder, H.; Fiori, G.; Casiraghi, C. All-2D Material Inkjet-Printed Capacitors: Toward Fully Printed Integrated Circuits. ACS Nano 2019, 13 (1), 54–60. https://doi.org/10.1021/acsnano.8b06464.

(13) Graddage, N.; Chu, T. Y.; Ding, H.; Py, C.; Dadvand, A.; Tao, Y. Inkjet Printed Thin and Uniform Dielectrics for Capacitors and Organic Thin Film Transistors Enabled by the Coffee Ring Effect. Org. Electron. 2016, 29, 114–119. https://doi.org/10.1016/J.ORGEL.2015.11.039.

(14) Leng, T.; Parvez, K.; Pan, K.; Ali, J.; McManus, D.; Novoselov, K. S.; Casiraghi, C.; Hu, Z. Printed Graphene/WS2 Battery-Free Wireless Photosensor on Papers. 2d Mater. 2020, 7 (2). https://doi.org/10.1088/2053-1583/ab602f.

(15) Jung, J.; Kim, D.; Lim, J.; Lee, C.; Yoon, S. C. Highly Efficient Inkjet-Printed Organic Photovoltaic Cells. Jpn. J. Appl. Phys. 2010, 49 (5 PART 2), 05EB03. https://doi.org/10.1143/JJAP.49.05EB03.

(16) Trung, T. Q.; Tien, N. T.; Kim, D.; Jung, J. H.; Yoon, O. J.; Lee, N. E. High Thermal Responsiveness of a Reduced Graphene Oxide Field-Effect Transistor. Advanced Materials 2012, 24 (38), 5254–5260. https://doi.org/10.1002/adma.201201724.

(17) Bastola, A.; He, Y.; Im, J.; Rivers, G.; Wang, F.; Worsley, R.; Austin, J. S.; Nelson-Dummett, O.; Wildman, R. D.; Hague, R.; Tuck, C. J.; Turyanska, L. Formulation of Functional Materials for Inkjet Printing: A Pathway towards Fully 3D Printed Electronics. Materials Today Electronics 2023, 6, 100058. https://doi.org/10.1016/j.mtelec.2023.100058.

(18) Htwe, Y. Z. N.; Mariatti, M. Printed Graphene and Hybrid Conductive Inks for Flexible, Stretchable, and Wearable Electronics: Progress, Opportunities, and Challenges. Journal of Science: Advanced Materials and Devices. Elsevier B.V. June 1, 2022. https://doi.org/10.1016/j.jsamd.2022.100435.

(19) Karim, N.; Afroj, S.; Leech, D.; Abdelkader, A. M. Flexible and Wearable Graphene‐Based E‐Textiles. In Oxide Electronics; Wiley, 2021; pp 21–49. https://doi.org/10.1002/9781119529538.ch2.

(20) Yan, K.; Li, J.; Pan, L.; Shi, Y. Inkjet Printing for Flexible and Wearable Electronics. APL Materials. American Institute of Physics Inc. December 1, 2020. https://doi.org/10.1063/5.0031669.

(21) Grillo, A.; Toral-Lopez, A.; Marian, D.; Pelella, A.; Peng, Z.; Wang, J.; Faella, E.; Passacantando, M.; Di Bartolomeo, A.; Fiori, G. Effects of Temperature Annealing on the Intrinsic Transport Mechanisms of Solution Processed Graphene Nanosheet Networks. Adv. Funct. Mater. 2025, 2501534. https://doi.org/10.1002/ADFM.202501534.

(22) Vandevenne, G.; Marchal, W.; Verboven, I.; Drijkoningen, J.; D'Haen, J.; Van Bael, M. K.; Hardy, A.; Deferme, W. A Study on the Thermal Sintering Process of Silver Nanoparticle Inkjet Inks to Achieve Smooth and Highly Conducting Silver Layers. Physica Status Solidi (A) Applications and Materials Science 2016, 213 (6), 1403–1409. https://doi.org/10.1002/PSSA.201533007.

(23) Secor, E. B.; Gao, T. Z.; Hersam, M. C.; Ahn, B. Y.; Lewis, J. A. Rapid and Versatile Photonic Annealing of Graphene Inks for Flexible Printed Electronics. Advanced Materials 2015, 27 (42), 6683–6688. https://doi.org/10.1002/ADMA.201502866.

(24) Ying-Jie, X.; Min-Fang, Q.; Deng-Zhu, G.; Geng-Min, Z. Increased Work Function in PEDOT：PSS Film under Ultraviolet Irradiation. Chinese Physics B 2014, 23 (3), 38504–038504. https://doi.org/10.1088/1674-1056/23/3/038504.

(25) Pop, E.; Varshney, V.; Roy, A. K. Thermal Properties of Graphene: Fundamentals and Applications. MRS Bull. 2012, 37 (12), 1273–1281. https://doi.org/10.1557/mrs.2012.203.

(26) Štulík, J.; Musil, O.; Josefík, F.; Kadlec, P. Graphene-Based Temperature Sensors–Comparison of the Temperature and Humidity Dependences. Nanomaterials 2022, 12 (9). https://doi.org/10.3390/nano12091594.

(27) Mohammed, M. H.; Ajeel, F. N.; Khudhair, A. M. Adsorption of Gas Molecules on Graphene Nanoflakes and Its Implication as a Gas Nanosensor by DFT Investigations. Chinese Journal of Physics 2017, 55 (4), 1576–1582. https://doi.org/10.1016/j.cjph.2017.05.013.

(28) Yuan, T.; Yin, R.; Li, C.; Wang, C.; Fan, Z.; Pan, L. Fully Inkjet-Printed Dual-Mode Sensor for Simultaneous Pressure and Temperature Sensing with High Decoupling. Chemical Engineering Journal 2023, 473 (28), 145475. https://doi.org/10.1016/j.cej.2023.145475.

(29) Yang, R.; Zhang, W.; Tiwari, N.; Yan, H.; Li, T.; Cheng, H. Multimodal Sensors with Decoupled Sensing Mechanisms. Advanced Science 2022, 9 (26), 2202470. https://doi.org/10.1002/advs.202202470.

(30) Patel, S.; Ershad, F.; Zhao, M.; Isseroff, R. R.; Duan, B.; Zhou, Y.; Wang, Y.; Yu, C. Wearable Electronics for Skin Wound Monitoring and Healing. Soft Science 2022, 2 (2), 9. https://doi.org/10.20517/ss.2022.13.

(31) Cima, M. J. Next-Generation Wearable Electronics. Nature Biotechnology 2014 32:7 2014, 32 (7), 642–643. https://doi.org/10.1038/nbt.2952.

(32) Nardini, C.; Osmani, V.; Cormio, P. G.; Frosini, A.; Turrini, M.; Lionis, C.; Neumuth, T.; Ballensiefen, W.; Borgonovi, E.; D'Errico, G. The Evolution of Personalized Healthcare and the Pivotal Role of European Regions in Its Implementation. Per. Med. 2021, 18 (3), 283–294. https://doi.org/https://doi.org/10.2217/pme-2020-0115.

(33) Peng, H. Wearable Electronics. Natl. Sci. Rev. 2023, 10 (1). https://doi.org/10.1093/NSR/NWAC193.

(34) Dhinesh, S. K.; Joshua Robert, J.; Tushar Nair, S.; Sharne Moni, D. H.; Sona Fowzeya, S.; Senthil Kumar, K. L.; Raghunath, M.; Nagarajan, P. Recent Trends in Additive Manufacturing of Electronics Devices. Mater. Today Proc. 2022, 66, 928–941. https://doi.org/10.1016/j.matpr.2022.04.654.

(35) Rao, C. H.; Avinash, K.; Varaprasad, B. K. S. V. L.; Goel, S. A Review on Printed Electronics with Digital 3D Printing: Fabrication Techniques, Materials, Challenges and Future Opportunities. Journal of Electronic Materials 2022 51:6 2022, 51 (6), 2747–2765. https://doi.org/10.1007/S11664-022-09579-7.

(36) Hussin, H.; Soin, N.; Wan Muhamad Hatta, S. F.; Md Rezali, F. A.; Abdul Wahab, Y. Review—Recent Progress in the Diversity of Inkjet-Printed Flexible Sensor Structures in Biomedical Engineering Applications. J. Electrochem. Soc. 2021, 168 (7), 077508. https://doi.org/10.1149/1945-7111/ac0e4b.

(37) Mavuri, A.; Mayes, A. G.; Alexander, M. S. Inkjet Printing of Polyacrylic Acid-Coated Silver Nanoparticle Ink onto Paper with Sub-100 Micron Pixel Size. Materials 2019, 12 (14), 2277. https://doi.org/10.3390/MA12142277.

(38) Kao, Z. K.; Hung, Y. H.; Liao, Y. C. Formation of Conductive Silver Films via Inkjet Reaction System. J. Mater. Chem. 2011, 21 (46), 18799–18803. https://doi.org/10.1039/C1JM13506F.

(39) Arapov, K.; Abbel, R.; De With, G.; Friedrich, H. Inkjet Printing of Graphene. Faraday Discuss. 2014, 173, 323–336. https://doi.org/10.1039/c4fd00067f.

(40) Nayak, L.; Mohanty, S.; Nayak, S. K.; Ramadoss, A. A Review on Inkjet Printing of Nanoparticle Inks for Flexible Electronics. J. Mater. Chem. C Mater. 2019, 7 (29), 8771–8795. https://doi.org/10.1039/c9tc01630a.

(41) Karim, N.; Afroj, S.; Malandraki, A.; Butterworth, S.; Beach, C.; Rigout, M.; Novoselov, K. S.; Casson, A. J.; Yeates, S. G. All Inkjet-Printed Graphene-Based Conductive Patterns for Wearable e-Textile Applications. J. Mater. Chem. C Mater. 2017, 5 (44), 11640–11648. https://doi.org/10.1039/c7tc03669h.

(42) Karim, N.; Afroj, S.; Tan, S.; Novoselov, K. S.; Yeates, S. G. All Inkjet-Printed Graphene-Silver Composite Ink on Textiles for Highly Conductive Wearable Electronics Applications. Sci. Rep. 2019, 9 (1). https://doi.org/10.1038/s41598-019-44420-y.

(43) Mitra, K. Y.; Sowade, E.; Martínez-Domingo, C.; Ramon, E.; Carrabina, J.; Gomes, H. L.; Baumann, R. R. Potential Up-Scaling of Inkjet-Printed Devices for Logical Circuits in Flexible Electronics. AIP Conf. Proc. 2015, 1646 (1), 106–114. https://doi.org/10.1063/1.4908590.

(44) Liew, Q. J.; Abdul Rashid, N.; Lee, H. W.; Hawari, H. F.; Md Khir, M. H. Inkjet-Printed Flexible Temperature Sensor Using Hybrid Reduced Graphene Oxide - Silver Nanoparticles(RGO/AgNPs) Conductive Ink and Silver Nanoparticles Ink. In Journal of Physics: Conference Series; IOP Publishing Ltd, 2021; Vol. 1878. https://doi.org/10.1088/1742-6596/1878/1/012059.

(45) Zeumault, A.; Ma, S.; Holbery, J. Fully Inkjet-Printed Metal-Oxide Thin-Film Transistors on Plastic. physica status solidi (a) 2016, 213 (8), 2189–2195. https://doi.org/10.1002/PSSA.201600077.

(46) Gillan, L.; Leppäniemi, J.; Eiroma, K.; Majumdar, H.; Alastalo, A. High Performance Solution Processed Oxide Thin-Film Transistors with Inkjet Printed Ag Source–Drain Electrodes. J. Mater. Chem. C Mater. 2018, 6 (13), 3220–3225. https://doi.org/10.1039/C7TC05679F.

(47) Zhang, Q.; Shao, S.; Chen, Z.; Pecunia, V.; Xia, K.; Zhao, J.; Cui, Z. High-Resolution Inkjet-Printed Oxide Thin-Film Transistors with a Self-Aligned Fine Channel Bank Structure. ACS Appl. Mater. Interfaces 2018, 10 (18), 15847–15854. https://doi.org/10.1021/acsami.8b02390.

(48) Karuwan, C.; Wisitsoraat, A.; Chaisuwan, P.; Nacapricha, D.; Tuantranont, A. Screen-Printed Graphene-Based Electrochemical Sensors for a Microfluidic Device. Analytical Methods 2017, 9 (24), 3689–3695. https://doi.org/10.1039/C7AY00379J.

(49) Aflatoonian, M. R.; Tajik, S.; Aflatoonian, B.; Beitollahi, H.; Zhang, K.; Le, Q. Van; Cha, J. H.; Jang, H. W.; Shokouhimehr, M.; Peng, W. A Screen-Printed Electrode Modified With Graphene/Co3O4 Nanocomposite for Electrochemical Detection of Tramadol. Front. Chem. 2020, 8, 1065. https://doi.org/10.3389/FCHEM.2020.562308.

(50) Mackenzie, D. M. A.; Smistrup, K.; Whelan, P. R.; Luo, B.; Shivayogimath, A.; Nielsen, T.; Petersen, D. H.; Messina, S. A.; Bøggild, P. Batch Fabrication of

Nanopatterned Graphene Devices via Nanoimprint Lithography. Appl. Phys. Lett. 2017, 111 (19). https://doi.org/10.1063/1.5010923.

(51) Kumar, S.; McEvoy, N.; Kim, H. Y.; Lee, K.; Peltekis, N.; Rezvani, E.; Nolan, H.; Weidlich, A.; Daly, R.; Duesberg, G. S. CVD Growth and Processing of Graphene for Electronic Applications. Phys. Status Solidi B Basic Res. 2011, 248 (11), 2604–2608. https://doi.org/10.1002/pssb.201100179.

(52) Saeed, M.; Alshammari, Y.; Majeed, S. A.; Al-Nasrallah, E. Chemical Vapour Deposition of Graphene—Synthesis, Characterisation, and Applications: A Review. Molecules. MDPI AG September 1, 2020. https://doi.org/10.3390/molecules25173856.

(53) Choi, A.; Hoang, A. T.; Ngoc Van, T. T.; Shong, B.; Hu, L.; You Thai, K.; Ahn, J. H. Residue-Free Photolithographic Patterning of Graphene. Chemical Engineering Journal 2022, 429, 132504. https://doi.org/10.1016/J.CEJ.2021.132504.

(54) Wiklund, J.; Karakoç, A.; Palko, T.; Yigitler, H.; Ruttik, K.; Jäntti, R.; Paltakari, J. A Review on Printed Electronics: Fabrication Methods, Inks, Substrates, Applications and Environmental Impacts. Journal of Manufacturing and Materials Processing 2021, 5 (3). https://doi.org/10.3390/JMMP5030089.

(55) Del, S. K.; Bornemann, R.; Bablich, A.; Schäfer-Eberwein, H.; Li, J.; Kowald, T.; Östling, M.; Haring Bolívar, P.; Lemme, M. C. Optimizing the Optical and Electrical Properties of Graphene Ink Thin Films by Laser-Annealing. 2d Mater. 2015, 2 (1), 011003. https://doi.org/10.1088/2053-1583/2/1/011003.

(56) Roshanghias, A.; Krivec, M.; Baumgart, M. Sintering Strategies for Inkjet Printed Metallic Traces in 3D Printed Electronics. Flexible and Printed Electronics 2017, 2 (4). https://doi.org/10.1088/2058-8585/aa8ed8.

(57) Gu, W.; Lin, J.; Chen, Z.; Cui, Z. Research Progress of Photonic Sintering Technology in Printable Electronics. Yingxiang Kexue yu Guanghuaxue/Imaging Science and Photochemistry 2014, 32 (4), 303–313. https://doi.org/10.7517/j.issn.1674-0475.2014.04.303.

(58) Medina-Plaza, C.; García-Hernández, C.; de Saja, J. A.; Fernández-Escudero, J. A.; Barajas, E.; Medrano, G.; García-Cabezón, C.; Martin-Pedrosa, F.; Rodriguez-Mendez, M. L. The Advantages of Disposable Screen-Printed Biosensors in a Bioelectronic Tongue for the Analysis of Grapes. LWT - Food Science and Technology 2015, 62 (2), 940–947. https://doi.org/10.1016/J.LWT.2015.02.027.

(59) Cruys-Bagger, N.; Tatsumi, H.; Borch, K.; Westh, P. A Graphene Screen-Printed Carbon Electrode for Real-Time Measurements of Unoccupied Active Sites in a Cellulase. Anal. Biochem. 2014, 447 (1), 162–168. https://doi.org/10.1016/J.AB.2013.11.024.

(60) He, P.; Cao, J.; Ding, H.; Liu, C.; Neilson, J.; Li, Z.; Kinloch, I. A.; Derby, B. Screen-Printing of a Highly Conductive Graphene Ink for Flexible Printed Electronics.

ACS Appl. Mater. Interfaces 2019, 11 (35), 32225–32234. https://doi.org/10.1021/acsami.9b04589.

(61) Ostfeld, A. E.; Deckman, I.; Gaikwad, A. M.; Lochner, C. M.; Arias, A. C. Screen Printed Passive Components for Flexible Power Electronics. Sci. Rep. 2015, 5. https://doi.org/10.1038/srep15959.

(62) Kim, D. S.; Jeong, J. M.; Park, H. J.; Kim, Y. K.; Lee, K. G.; Choi, B. G. Highly Concentrated, Conductive, Defect-Free Graphene Ink for Screen-Printed Sensor Application. Nano-Micro Letters 2021 13:1 2021, 13 (1), 1–14. https://doi.org/10.1007/S40820-021-00617-3.

(63) Islam, M. R.; Afroj, S.; Beach, C.; Islam, M. H.; Parraman, C.; Abdelkader, A.; Casson, A. J.; Novoselov, K. S.; Karim, N. Fully Printed and Multifunctional Graphene-Based Wearable e-Textiles for Personalized Healthcare Applications. iScience 2022, 25 (3). https://doi.org/10.1016/j.isci.2022.103945.

(64) Wu, Y.; Zou, X.; Sun, M.; Cao, Z.; Wang, X.; Huo, S.; Zhou, J.; Yang, Y.; Yu, X.; Kong, Y.; Yu, G.; Liao, L.; Chen, T. 200 GHz Maximum Oscillation Frequency in CVD Graphene Radio Frequency Transistors. ACS Appl. Mater. Interfaces 2016, 8 (39), 25645–25649. https://doi.org/10.1021/acsami.6b05791.

(65) Stolyarov, M. A.; Liu, G.; Rumyantsev, S. L.; Shur, M.; Balandin, A. A. Suppression of 1/f Noise in Near-Ballistic h-BN-Graphene-h-BN Heterostructure Field-Effect Transistors. Appl. Phys. Lett. 2015.

(66) Ouyang, S.; Xie, Y.; Wang, D.; Zhu, D.; Xu, X.; Tan, T.; Fong, H. H. Surface Patterning of PEDOT:PSS by Photolithography for Organic Electronic Devices. J. Nanomater. 2015, 2015 (1), 603148. https://doi.org/10.1155/2015/603148.

(67) Bravo-Vasquez, J. P.; Hill, R. H. Photolithographic Deposition of Conducting Gold Films from Thin Amorphous Films of AuPR3X (X=NO3, RCO2) on Silicon Surfaces. Polyhedron 2000, 19 (3), 343–349. https://doi.org/10.1016/S0277-5387(99)00364-2.

(68) Chekkaramkodi, D.; Jacob, L.; C, M. S.; Umer, R.; Butt, H. Review of Vat Photopolymerization 3D Printing of Photonic Devices. Addit. Manuf. 2024, 86, 104189. https://doi.org/10.1016/J.ADDMA.2024.104189.

(69) Tilve-Martinez, D.; Poulin, P. Vat Photopolymerization 3D Printing of Conductive Nanocomposites. Acc. Mater. Res. 2025, 6 (5), 661–671. https://doi.org/10.1021/ACCOUNTSMR.5C00060.

(70) Choudhary, H.; Vaithiyanathan, D.; Kumar, H. A Review on Additive Manufactured Sensors. Mapan - Journal of Metrology Society of India. Springer June 1, 2021, pp 405–422. https://doi.org/10.1007/s12647-020-00399-w.

(71) Kwon, K. S.; Rahman, M. K.; Phung, T. H.; Hoath, S. D.; Jeong, S.; Kim, J. S. Review of Digital Printing Technologies for Electronic Materials. Flexible and Printed

Electronics. IOP Publishing Ltd December 15, 2020. https://doi.org/10.1088/2058-8585/abc8ca.

(72) Hoath, S. D. Fundamentals of Inkjet Printing; 2015.

(73) Rivers, G.; Lion, A.; Putri, N. R. E.; Rance, G. A.; Moloney, C.; Taresco, V.; Crucitti, V. C.; Constantin, H.; Evangelista Barreiros, M. I.; Cantu, L. R.; Tuck, C. J.; Rose, F. R. A. J.; Hague, R. J. M.; Roberts, C. J.; Turyanska, L.; Wildman, R. D.; He, Y. Enabling High-Fidelity Personalised Pharmaceutical Tablets through Multimaterial Inkjet 3D Printing with a Water-Soluble Excipient. Mater. Today Adv. 2024, 22, 100493. https://doi.org/10.1016/J.MTADV.2024.100493.

(74) Dybowska-Sarapuk, L.; Kielbasinski, K.; Arazna, A.; Futera, K.; Skalski, A.; Janczak, D.; Sloma, M.; Jakubowska, M. Efficient Inkjet Printing of Graphene-Based Elements: Influence of Dispersing Agent on Ink Viscosity. Nanomaterials 2018, 8 (8). https://doi.org/10.3390/NANO8080602.

(75) Lemarchand, J.; Bridonneau, N.; Battaglini, N.; Carn, F.; Mattana, G.; Piro, B.; Zrig, S.; Noël, V. Challenges, Prospects, and Emerging Applications of Inkjet-Printed Electronics: A Chemist's Point of View. Angewandte Chemie - International Edition. John Wiley and Sons Inc May 9, 2022. https://doi.org/10.1002/anie.202200166.

(76) Pei, L.; Li, Y.-F. Rapid and Efficient Intense Pulsed Light Reduction of Graphene Oxide Inks for Flexible Printed Electronics. RSC Adv. 2017, 7 (81), 51711–51720. https://doi.org/10.1039/C7RA10416B.

(77) Lo, L. W.; Zhao, J.; Wan, H.; Wang, Y.; Chakrabartty, S.; Wang, C. An Inkjet-Printed PEDOT:PSS-Based Stretchable Conductor for Wearable Health Monitoring Device Applications. ACS Appl. Mater. Interfaces 2021, 13 (18), 21693–21702. https://doi.org/10.1021/ACSAMI.1C00537/ASSET/IMAGES/LARGE/AM1C00537_0006.JPEG.

(78) Shang, J.; Mohammadi, M.; Strandberg, J.; Petsagkourakis, I.; Åhlin, J.; Hagel, O.; Yi, Y.; Herlogsson, L.; Tybrandt, K. Fully Screen Printed Stretchable Liquid Metal Multilayer Circuits Using Green Solvents and Scalable Water-Spray Sintering. npj Flexible Electronics 2025 9:1 2025, 9 (1), 1–9. https://doi.org/10.1038/s41528-025-00394-8.

(79) Lopez-Larrea, N.; Criado-Gonzalez, M.; Dominguez-Alfaro, A.; Alegret, N.; Agua, I. Del; Marchiori, B.; Mecerreyes, D. Digital Light 3D Printing of PEDOT-Based Photopolymerizable Inks for Biosensing. ACS Appl. Polym. Mater. 2022, 6749–6759. https://doi.org/10.1021/ACSAPM.2C01170/SUPPL_FILE/AP2C01170_SI_001.MP4.

(80) Jurinovs, M.; Barkane, A.; Platnieks, O.; Grase, L.; Gaidukovs, S. Three Dimensionally Printed Biobased Electrodes: Ionic Liquid and Single-Walled Carbon Nanotube Hybrids in a Vegetable Oil Matrix for Soft Robotics. ACS Appl. Polym.

Mater. 2023, 5 (9), 7120–7131. https://doi.org/10.1021/ACSAPM.3C01136/SUPPL_FILE/AP3C01136_SI_003.MP4
.

(81) Dominguez-Alfaro, A.; Mitoudi-Vagourdi, E.; Dimov, I.; Picchio, M. L.; Lopez-Larrea, N.; de Lacalle, J. L.; Tao, X.; Serrano, R. R. M.; Gallastegui, A.; Vassardanis, N.; Mecerreyes, D.; Malliaras, G. G. Light-Based 3D Multi-Material Printing of Micro-Structured Bio-Shaped, Conducting and Dry Adhesive Electrodes for Bioelectronics. Advanced Science 2024, 11 (27), 2306424. https://doi.org/10.1002/ADVS.202306424.

(82) Cruz, S. M. F.; Rocha, L. A.; Viana, J. C. Printing Technologies on Flexible Substrates for Printed Electronics. In Flexible Electronics; InTech, 2018. https://doi.org/10.5772/intechopen.76161.

(83) Jose, M.; Vijjapu, M. T.; Neumaier, L.; Rauter, L.; Chakkunny, A. H.; Corzo, D.; Thoelen, R.; Picard, A.; Kosel, J.; Deferme, W. Convergence of Biocompatible Printed Electronics and Sensing in Wound Dressings: A Leap Forward in Sustainable Health Monitoring. npj Flexible Electronics 2025 9:1 2025, 9 (1), 46-. https://doi.org/10.1038/s41528-025-00421-8.

(84) Tabriz, A. G.; Douroumis, D. Recent Advances in 3D Printing for Wound Healing: A Systematic Review. J. Drug Deliv. Sci. Technol. 2022, 74 (4), 103564. https://doi.org/10.1016/j.jddst.2022.103564.

(85) Tsegay, F.; Elsherif, M.; Butt, H. Smart 3D Printed Hydrogel Skin Wound Bandages: A Review. Polymers (Basel). 2022, 14 (5), 1012. https://doi.org/10.3390/polym14051012.

(86) Farooqui, M. F.; Shamim, A. Low Cost Inkjet Printed Smart Bandage for Wireless Monitoring of Chronic Wounds. Scientific Reports 2016 6:1 2016, 6 (1), 1–13. https://doi.org/10.1038/srep28949.

(87) Thi Ngoc Nga, D.; Mattana, G.; Thu, V. T.; Roussel, R.; Piro, B. A Simple Flexible Printed Capacitive Pressure Sensor for Chronic Wound Monitoring. Sens. Actuators A Phys. 2022, 338. https://doi.org/10.1016/j.sna.2022.113490.

(88) Ju, B.; Kim, I.; Li, B. M.; Knowles, C. G.; Mills, A.; Grace, L.; Jur, J. S. Inkjet Printed Textile Force Sensitive Resistors for Wearable and Healthcare Devices. Adv. Healthc. Mater. 2021, 10 (20), 2100893. https://doi.org/10.1002/ADHM.202100893.

(89) Wei, Q.; Rojas, D.; Wang, Q.; Zapata-Pérez, R.; Xuan, X.; Molinero-Fernández, Á.; Crespo, G. A.; Cuartero, M. Wearable 3D-Printed Microneedle Sensor for Intradermal Temperature Monitoring. ACS Sens. 2025, 10 (6), 4027–4037. https://doi.org/10.1021/ACSSENSORS.4C03681.

(90) Ngoc Nga, D. T.; Thu, V. T.; Noel, V.; Piro, B.; Mattana, G. All-Printed Smart Dressing for Chronic Wound Monitoring. IFETC 2023 - 5th IEEE International

Flexible Electronics Technology Conference, Proceedings 2023. https://doi.org/10.1109/IFETC57334.2023.10254815.

(91) Sandry, C. T.; Shila, S.; Gonzalez-Jimenez, L.; Martinez, S.; Sekhar, P. K. Progress in Inkjet-Printed Sensors and Antennas. Electrochemical Society Interface 2023, 32 (4), 61–71. https://doi.org/10.1149/2.F12234IF/PDF.

(92) Ahmad, W.; Budimir, D. Inkjet-Printed Antennas for 28 GHz 5G Applications. Asia-Pacific Microwave Conference Proceedings, APMC 2017, 0. https://doi.org/10.1109/APMC.2016.7931475.

(93) Alex-Amor, A.; Palomares-Caballero, Á.; Moreno-Núñez, J.; Tamayo-Domínguez, A.; García-García, C.; Fernández-González, J. M. Ultrawideband Inkjet-Printed Monopole Antennas for Energy Harvesting Application. Microw. Opt. Technol. Lett. 2021, 63 (6), 1719–1726. https://doi.org/10.1002/MOP.32803.

(94) Chen, C. B.; Kao, H. L.; Chang, L. C.; Lin, Y. C.; Chen, Y. Y.; Chung, W. H.; Chiu, H. C. Wound-Dressing-Based Antenna Inkjet-Printed Using Nanosilver Ink for Wireless Medical Monitoring. Micromachines 2022, Vol. 13, Page 1510 2022, 13 (9), 1510. https://doi.org/10.3390/MI13091510.

(95) Gounden, V.; Singh, M. Hydrogels and Wound Healing: Current and Future Prospects. Gels 2024, 10 (1), 43. https://doi.org/10.3390/GELS10010043.

(96) Tsegay, F.; Hisham, M.; Elsherif, M.; Schiffer, A.; Butt, H. 3D Printing of PH Indicator Auxetic Hydrogel Skin Wound Dressing. Molecules 2023, 28 (3), 1339. https://doi.org/10.3390/MOLECULES28031339.

(97) Huang, T.; Sun, Z.; Heath, D. E.; O'Brien-Simpson, N.; O'Connor, A. J. 3D Printed and Smart Alginate Wound Dressings with PH-Responsive Drug and Nanoparticle Release. Chemical Engineering Journal 2024, 492, 152117. https://doi.org/10.1016/J.CEJ.2024.152117.

(98) Nande, A.; Kalyani, N. T.; Tiwari, A.; Dhoble, S. J. Exploring the World of Functional Materials. Functional Materials from Carbon, Inorganic, and Organic Sources: Methods and Advances 2023, 1–19. https://doi.org/10.1016/B978-0-323-85788-8.00014-8.

(99) Mahamuda, S.; Swapna, K.; Venateswarlu, M.; Srinivasa, M. V. V. K.; Sailaja, P. A Review on Applications of Various Functional Materials. International Journal of Scientific & Technology Research 2020, 9 (1), 3756–3759.

(100) Thanjavur, N.; Bugude, L.; Kim, Y. J. Integration of Functional Materials in Photonic and Optoelectronic Technologies for Advanced Medical Diagnostics. Biosensors 2025, Vol. 15, Page 38 2025, 15 (1), 38. https://doi.org/10.3390/BIOS15010038.

(101) Zhang, X.; Shao, J.; Yan, C.; Qin, R.; Lu, Z.; Geng, H.; Xu, T.; Ju, L. A Review on Optoelectronic Device Applications of 2D Transition Metal Carbides and Nitrides. Mater. Des. 2021, 200, 109452. https://doi.org/10.1016/J.MATDES.2021.109452.

(102) Kamyshny, A.; Ben-Moshe, M.; Aviezer, S.; Magdassi, S. Ink-Jet Printing of Metallic Nanoparticles and Microemulsions. Macromol. Rapid Commun. 2005, 26 (4), 281–288. https://doi.org/10.1002/MARC.200400522.

(103) Xiang, C.; Wu, L.; Lu, Z.; Li, M.; Wen, Y.; Yang, Y.; Liu, W.; Zhang, T.; Cao, W.; Tsang, S. W.; Shan, B.; Yan, X.; Qian, L. High Efficiency and Stability of Ink-Jet Printed Quantum Dot Light Emitting Diodes. Nature Communications 2020 11:1 2020, 11 (1), 1–9. https://doi.org/10.1038/s41467-020-15481-9.

(104) Fu, M.; Santaella, J. J.; Evans, S. D.; Critchley, K. Inkjet Printing of Cadmium-Free Quantum Dots-Based Electroluminescent Devices. ACS Appl. Mater. Interfaces 2025, 17 (15), 22952–22962. https://doi.org/10.1021/ACSAMI.5C01588.

(105) Hu, Y.; Wang, Y.; Yao, Y. Molecular Dynamics on the Sintering Mechanism and Mechanical Feature of the Silver Nanoparticles at Different Temperatures. Mater. Today Commun. 2023, 34, 105292. https://doi.org/10.1016/J.MTCOMM.2022.105292.

(106) Leong, K. H.; Chin, Y. H.; Sim, L. C.; Tan, B.; Dai, C.; Saravanan, P. Physical Properties of Quantum Dots. Graphene, Nanotubes and Quantum Dots-Based Nanotechnology: Fundamentals and Applications 2022, 687–709. https://doi.org/10.1016/B978-0-323-85457-3.00017-7.

(107) Galář, P.; Kopenec, J.; Král, R.; Matějka, F.; Zemenová, P.; Dopita, M.; Hapala, P.; König, D.; Vrbka, P.; Kůsová, K. Engineering the Thermal and Energy-Storage Properties in Quantum Dots Using Dominant Faceting: The Case Study of Silicon. ACS Nano 2025, 19 (2), 2196–2212. https://doi.org/10.1021/ACSNANO.4C11376/SUPPL_FILE/NN4C11376_SI_001.MP4.

(108) Zhang, M. K.; Liu, W. Di; Gong, Y. P.; Liu, Q.; Chen, Z. G. Graphene/Quantum Dot Heterostructure Photodetectors: From Material to Performance. Adv. Opt. Mater. 2022, 10 (24), 2201889. https://doi.org/10.1002/ADOM.202201889;REQUESTEDJOURNAL:JOURNAL:21951071;WGROUP:STRING:PUBLICATION.

(109) Ahmed, S.; Annu; Ikram, S.; Yudha, S. Biosynthesis of Gold Nanoparticles: A Green Approach. J. Photochem. Photobiol. B 2016, 161, 141–153. https://doi.org/10.1016/J.JPHOTOBIOL.2016.04.034.

(110) Sati, A.; Ranade, T. N.; Mali, S. N.; Ahmad Yasin, H. K.; Pratap, A. Silver Nanoparticles (AgNPs): Comprehensive Insights into Bio/Synthesis, Key Influencing

Factors, Multifaceted Applications, and Toxicity—A 2024 Update. ACS Omega 2025, 10 (8), 7549−7582. https://doi.org/10.1021/ACSOMEGA.4C11045.

(111) Ali, M.; Sajjad, U.; Ali, A.; Ali, H. M.; Hamid, K. Metallic Nanoparticles-Based Additive Manufacturing: A Review of Recent Advances on Progress, Prospects, and Challenges. Mater. Des. 2025, 257, 114464. https://doi.org/10.1016/J.MATDES.2025.114464.

(112) Pasparakis, G. Recent Developments in the Use of Gold and Silver Nanoparticles in Biomedicine. Wiley Interdiscip. Rev. Nanomed. Nanobiotechnol. 2022, 14 (5), e1817. https://doi.org/10.1002/WNAN.1817.

(113) Valayil Varghese, T.; Eixenberger, J.; Rajabi-Kouchi, F.; Lazouskaya, M.; Francis, C.; Burgoyne, H.; Wada, K.; Subbaraman, H.; Estrada, D. Multijet Gold Nanoparticle Inks for Additive Manufacturing of Printed and Wearable Electronics. ACS Materials Au 2023, 4 (1), 65–73. https://doi.org/10.1021/ACSMATERIALSAU.3C00058.

(114) Vaithilingam, J.; Saleh, E.; Körner, L.; Wildman, R. D.; Hague, R. J. M.; Leach, R. K.; Tuck, C. J. 3-Dimensional Inkjet Printing of Macro Structures from Silver Nanoparticles. Mater. Des. 2018, 139, 81–88. https://doi.org/10.1016/J.MATDES.2017.10.070.

(115) OrelTech Aurum. https://oreltech.com/products (accessed 2025-11-05).

(116) Huang, Y.; Chen, R.; Chen, Y.; Lü, X. Investigation of Molecular Mechanisms in Silver Nanoparticle-Induced Cytotoxicity from Gene to Metabolite Level. Scientific Reports 2025 15:1 2025, 15 (1), 1–14. https://doi.org/10.1038/s41598-025-12477-7.

(117) Benkovičová, M.; Végsö, K.; Šiffalovič, P.; Jergel, M.; Majková, E.; Luby, Š.; Šatka, A. Preparation of Sterically Stabilized Gold Nanoparticles for Plasmonic Applications. Chemical Papers 2013, 67 (9), 1225–1230. https://doi.org/10.2478/S11696-013-0315-Y.

(118) Qi, W. H.; Wang, M. P. Size and Shape Dependent Melting Temperature of Metallic Nanoparticles. Mater. Chem. Phys. 2004, 88 (2–3), 280–284. https://doi.org/10.1016/J.MATCHEMPHYS.2004.04.026.

(119) Buffat, P.; Borel, J. P. Size Effect on the Melting Temperature of Gold Particles. Phys. Rev. A (Coll Park). 1976, 13 (6), 2287. https://doi.org/10.1103/PhysRevA.13.2287.

(120) Ko, S. H.; Pan, H.; Grigoropoulos, C. P.; Luscombe, C. K.; Fréchet, J. M. J.; Poulikakos, D. All-Inkjet-Printed Flexible Electronics Fabrication on a Polymer Substrate by Low-Temperature High-Resolution Selective Laser Sintering of Metal Nanoparticles. Nanotechnology 2007, 18 (34). https://doi.org/10.1088/0957-4484/18/34/345202.

(121) Fuller, S. B.; Wilhelm, E. J.; Jacobson, J. M. Ink-Jet Printed Nanoparticle Microelectromechanical Systems. Journal of Microelectromechanical Systems 2002, 11 (1), 54–60. https://doi.org/10.1109/84.982863.

(122) Table of Resistivity. http://hyperphysics.phy-astr.gsu.edu/hbase/Tables/rstiv.html (accessed 2025-12-01).

(123) Gold - Physical, Mechanical, Thermal, and Electrical Properties. https://www.azom.com/article.aspx?ArticleID=5147 (accessed 2025-12-01).

(124) Han, L.; Zhao, Y. X.; Liu, C. M.; Li, L. H.; Liang, X. J.; Wei, Y. The Effects of Nanoparticle Shape on Electrical Conductivity of Ag Nanomaterials. Journal of Materials Science: Materials in Electronics 2014 25:9 2014, 25 (9), 3870–3877. https://doi.org/10.1007/S10854-014-2101-1.

(125) Trindade, G. F.; Wang, F.; Im, J.; He, Y.; Balogh, A.; Scurr, D.; Gilmore, I.; Tiddia, M.; Saleh, E.; Pervan, D.; Turyanska, L.; Tuck, C. J.; Wildman, R.; Hague, R.; Roberts, C. J. Residual Polymer Stabiliser Causes Anisotropic Electrical Conductivity during Inkjet Printing of Metal Nanoparticles. Communications Materials 2021 2:1 2021, 2 (1), 1–10. https://doi.org/10.1038/s43246-021-00151-0.

(126) Burdușel, A. C.; Gherasim, O.; Grumezescu, A. M.; Mogoantă, L.; Ficai, A.; Andronescu, E. Biomedical Applications of Silver Nanoparticles: An Up-to-Date Overview. Nanomaterials 2018, 8 (9), 681. https://doi.org/10.3390/NANO8090681.

(127) Bansal, S. A.; Kumar, V.; Karimi, J.; Singh, A. P.; Kumar, S. Role of Gold Nanoparticles in Advanced Biomedical Applications. Nanoscale Adv. 2020, 2 (9), 3764–3787. https://doi.org/10.1039/D0NA00472C.

(128) Okano, M.; Uemura, S.; Tabe, Y.; Nguyen, B. H.; Nguyen, V. H. Promising Applications of Graphene and Graphene-Based Nanostructures. Advances in Natural Sciences: Nanoscience and Nanotechnology 2016, 7 (2), 023002. https://doi.org/10.1088/2043-6262/7/2/023002.

(129) Nemani, S. K.; Torkamanzadeh, M.; Wyatt, B. C.; Presser, V.; Anasori, B. Functional Two-Dimensional High-Entropy Materials. Communications Materials 2023 4:1 2023, 4 (1), 1–7. https://doi.org/10.1038/s43246-023-00341-y.

(130) Cho, K.; Lee, T.; Chung, S. Inkjet Printing of Two-Dimensional van Der Waals Materials: A New Route towards Emerging Electronic Device Applications. Nanoscale Horiz. 2022, 7 (10), 1161–1176. https://doi.org/10.1039/D2NH00162D.

(131) Shanmugam, V.; Mensah, R. A.; Babu, K.; Gawusu, S.; Chanda, A.; Tu, Y.; Neisiany, R. E.; Försth, M.; Sas, G.; Das, O. A Review of the Synthesis, Properties, and Applications of 2D Materials. Particle and Particle Systems Characterization 2022, 39 (6), 2200031. https://doi.org/10.1002/PPSC.202200031;PAGE:STRING:ARTICLE/CHAPTER.

(132) Li, Z.; Young, R. J.; Backes, C.; Zhao, W.; Zhang, X.; Zhukov, A. A.; Tillotson, E.; Conlan, A. P.; Ding, F.; Haigh, S. J.; Novoselov, K. S.; Coleman, J. N. Mechanisms of Liquid-Phase Exfoliation for the Production of Graphene. ACS Nano 2020, 14 (9), 10976–10985. https://doi.org/10.1021/ACSNANO.0C03916.

(133) Chavalekvirat, P.; Hirunpinyopas, W.; Deshsorn, K.; Jitapunkul, K.; Iamprasertkun, P. Liquid Phase Exfoliation of 2D Materials and Its Electrochemical Applications in the Data-Driven Future. Precision Chemistry 2024, 2 (7), 300–329. https://doi.org/10.1021/PRECHEM.3C00119.

(134) Song, O.; Rhee, D.; Kim, J.; Jeon, Y.; Mazánek, V.; Söll, A.; Kwon, Y. A.; Cho, J. H.; Kim, Y. H.; Sofer, Z.; Kang, J. All Inkjet-Printed Electronics Based on Electrochemically Exfoliated Two-Dimensional Metal, Semiconductor, and Dielectric. npj 2D Materials and Applications 2022 6:1 2022, 6 (1), 64-. https://doi.org/10.1038/s41699-022-00337-1.

(135) Sengupta, J.; Das, K.; Nandi, U. N.; Jacob, C. Substrate Free Synthesis of Graphene Nanoflakes by Atmospheric Pressure Chemical Vapour Deposition Using Ni Powder as a Catalyst. Bulletin of Materials Science 2019, 42 (4), 1–5. https://doi.org/10.1007/S12034-019-1818-0/FIGURES/5.

(136) Krishnamoorthy, R.; Muthumalai, K.; Nagaraja, T.; Rajendrakumar, R. T.; Das, S. R. Chemically Exfoliated Titanium Carbide MXene for Highly Sensitive Electrochemical Sensors for Detection of 4-Nitrophenols in Drinking Water. ACS Omega 2022, 7 (46), 42644–42654. https://doi.org/10.1021/ACSOMEGA.2C06505.

(137) Lin, Z.; Liu, Y.; Moon, K. S.; Wong, C. P. Enhanced Thermal Transport of Hexagonal Boron Nitride Filled Polymer Composite by Magnetic Field-Assisted Alignment. Proceedings - Electronic Components and Technology Conference 2013, 1692–1696. https://doi.org/10.1109/ECTC.2013.6575801.

(138) Novoselov, K. S.; Geim, A. K.; Morozov, S. V; Jiang, D.; Zhang, Y.; Dubonos, S. V; Grigorieva, I. V; Firsov, A. A. Electric Field Effect in Atomically Thin Carbon Films. Science (1979). 2004, 306, 666–669.

(139) Graphene - the Perfect Atomic Lattice; 2010; Vol. 54.

(140) Lin, L. S.; Bin-Tay, W.; Aslam, Z.; Westwood, A. V. K.; Brydson, R. Determination of the Lateral Size and Thickness of Solution-Processed Graphene Flakes. J. Phys. Conf. Ser. 2017, 902 (1). https://doi.org/10.1088/1742-6596/902/1/012026.

(141) Vlassiouk, I.; Fulvio, P.; Meyer, H.; Lavrik, N.; Dai, S.; Datskos, P.; Smirnov, S. Large Scale Atmospheric Pressure Chemical Vapor Deposition of Graphene. Carbon N. Y. 2013, 54, 58–67. https://doi.org/10.1016/J.CARBON.2012.11.003.

(142) Hutapea, J. A. A.; Manik, Y. G. O.; Ndruru, S. T. C. L.; Huang, J.; Goei, R.; Tok, A. I. Y.; Siburian, R. Comprehensive Review of Graphene Synthesis Techniques:

Advancements, Challenges, and Future Directions. Micro 2025, Vol. 5, Page 40 2025, 5 (3), 40. https://doi.org/10.3390/MICRO5030040.

(143) Secor, E. B.; Prabhumirashi, P. L.; Puntambekar, K.; Geier, M. L.; Hersam, M. C. Inkjet Printing of High Conductivity, Flexible Graphene Patterns. Journal of Physical Chemistry Letters 2013, 4 (8), 1347–1351. https://doi.org/10.1021/jz400644c.

(144) Zhang, Y.; Tang, T. T.; Girit, C.; Hao, Z.; Martin, M. C.; Zettl, A.; Crommie, M. F.; Shen, Y. R.; Wang, F. Direct Observation of a Widely Tunable Bandgap in Bilayer Graphene. Nature 2009 459:7248 2009, 459 (7248), 820–823. https://doi.org/10.1038/nature08105.

(145) Balandin, A. A.; Ghosh, S.; Bao, W.; Calizo, I.; Teweldebrhan, D.; Miao, F.; Lau, C. N. Superior Thermal Conductivity of Single-Layer Graphene. Nano Lett. 2008, 8 (3), 902–907. https://doi.org/10.1021/NL0731872.

(146) Urade, A. R.; Lahiri, I.; Suresh, K. S. Graphene Properties, Synthesis and Applications: A Review. JOM 2022 75:3 2022, 75 (3), 614–630. https://doi.org/10.1007/S11837-022-05505-8.

(147) Heaton, C. E. D.; Austin, J. S.; Ruer, L.; Cottam, N. D.; Wang, F.; He, Y.; Rance, G. A.; Rose, F. R. A. J.; Wildman, R. D.; Hague, R. J. M.; Makarovsky, O.; Turyanska, L. Photonic Annealing of Inkjet Printed Graphene for Stretchable Wearable Healthcare Monitoring Devices. Adv. Mater. Technol. 2025, 10 (21), e00913. https://doi.org/10.1002/ADMT.202500913.

(148) Carey, T.; Cacovich, S.; Divitini, G.; Ren, J.; Mansouri, A.; Kim, J. M.; Wang, C.; Ducati, C.; Sordan, R.; Torrisi, F. Fully Inkjet-Printed Two-Dimensional Material Field-Effect Heterojunctions for Wearable and Textile Electronics. Nat. Commun. 2017, 8 (1). https://doi.org/10.1038/s41467-017-01210-2.

(149) Cottam, N. D.; Wang, F.; Austin, J. S.; Tuck, C. J.; Hague, R.; Fromhold, M.; Escoffier, W.; Goiran, M.; Pierre, M.; Makarovsky, O.; Turyanska, L. Quantum Nature of Charge Transport in Inkjet-Printed Graphene Revealed in High Magnetic Fields up to 60T. Small 2024, 20 (30), 2311416. https://doi.org/10.1002/smll.202311416.

(150) Juntunen, T.; Jussila, H.; Ruoho, M.; Liu, S.; Hu, G.; Albrow-Owen, T.; Ng, L. W. T.; Howe, R. C. T.; Hasan, T.; Sun, Z.; Tittonen, I. Inkjet Printed Large-Area Flexible Few-Layer Graphene Thermoelectrics. Adv. Funct. Mater. 2018, 28 (22), 1800480. https://doi.org/10.1002/ADFM.201800480;ISSUE:ISSUE:DOI.

(151) Blau, W.; Hernandez, Y.; Rahman, M.; Parvez, K.; Fugallo, G.; Dun, C.; Read, O.; Alieva, A.; Urban, J. J.; Lazzeri, M.; Casiraghi, C.; Pisana, S. Anisotropic Thermal Conductivity of Inkjet-Printed 2D Crystal Films: Role of the Microstructure and Interfaces. 2022. https://doi.org/10.3390/nano12213861.

(152) Wang, F.; Gosling, J. H.; Trindade, G. F.; Rance, G. A.; Makarovsky, O.; Cottam, N. D.; Kudrynskyi, Z.; Balanov, A. G.; Greenaway, M. T.; Wildman, R. D.;

Hague, R.; Tuck, C.; Fromhold, T. M.; Turyanska, L. Inter-Flake Quantum Transport of Electrons and Holes in Inkjet-Printed Graphene Devices. Adv. Funct. Mater. 2021, 31 (5), 2007478. https://doi.org/10.1002/adfm.202007478.

(153) Farraj, S. A.; Jabari, E.; Naguib, H. E.; Chu, T.-Y. Computational Modelling of Graphene-Ethyl Cellulose Printed Ink: A Reactive Molecular Dynamic Study. In 2021 IEEE International Conference on Flexible and Printable Sensors and Systems (FLEPS); IEEE, 2021; pp 1–4. https://doi.org/10.1109/FLEPS51544.2021.9469752.

(154) Wang, F.; Heaton, C. E. D.; Cottam, N. D.; Austin, J. S.; Im, J.; Fromhold, T. M.; Wildman, R. D.; Hague, R. J. M.; Tuck, C. J.; Makarovsky, O.; Turyanska, L. Inkjet Printed Multifunctional Graphene Sensors for Flexible and Wearable Electronics. Adv. Electron. Mater. 2024, 2400689. https://doi.org/10.1002/aelm.202400689.

(155) Kong, D.; Le, L. T.; Li, Y.; Zunino, J. L.; Lee, W. Temperature-Dependent Electrical Properties of Graphene Inkjet-Printed on Flexible Materials. Langmuir 2012, 28 (37), 13467–13472. https://doi.org/10.1021/la301775d.

(156) Sulaiman, S.; Rashid, N. A.; Aziz, A. S. A.; Jun, L. Q.; Jaafar, S. M. H. S. M. Inkjet-Printed Graphene-Based Flexible Humidity Sensor for Environmental Applications. IEEE International Conference on Semiconductor Electronics, Proceedings, ICSE 2020, 2020-July, 148–151. https://doi.org/10.1109/ICSE49846.2020.9166876.

(157) Sun, J.; Sun, Y.; Jia, H.; Bi, H.; Chen, L.; Que, M.; Xiong, Y.; Han, L.; Sun, L. A Novel Pre-Deposition Assisted Strategy for Inkjet Printing Graphene-Based Flexible Pressure Sensor with Enhanced Performance. Carbon N. Y. 2022, 196, 85–91. https://doi.org/10.1016/j.carbon.2022.04.021.

(158) Travan, C.; Bergmann, A. NO2 and NH3 Sensing Characteristics of Inkjet Printing Graphene Gas Sensors. Sensors 2019, Vol. 19, Page 3379 2019, 19 (15), 3379. https://doi.org/10.3390/S19153379.

(159) Thaibunnak, A.; Rungruang, S.; Pakdee, U. Inkjet-Printed Graphene–PEDOT:PSS Decorated with Sparked ZnO Nanoparticles for Application in Acetone Detection at Room Temperature. Polymers (Basel). 2024, 16 (24), 3521. https://doi.org/10.3390/polym16243521.

(160) Piatti, E.; Arbab, A.; Galanti, F.; Carey, T.; Anzi, L.; Spurling, D.; Roy, A.; Zhussupbekova, A.; Patel, K. A.; Kim, J. M.; Daghero, D.; Sordan, R.; Nicolosi, V.; Gonnelli, R. S.; Torrisi, F. Charge Transport Mechanisms in Inkjet-Printed Thin-Film Transistors Based on Two-Dimensional Materials. Nat. Electron. 2021, 4 (12), 893–905. https://doi.org/10.1038/s41928-021-00684-9.

(161) Xia, X.; Weng, G. J.; Zhang, J.; Li, Y. The Effect of Temperature and Graphene Concentration on the Electrical Conductivity and Dielectric Permittivity of Graphene–

Polymer Nanocomposites. Acta Mech. 2020, 231 (4), 1305–1320. https://doi.org/10.1007/s00707-019-02588-4.

(162) Liu, G.; Tan, Q.; Kou, H.; Zhang, L.; Wang, J.; Lv, W.; Dong, H.; Xiong, J. A Flexible Temperature Sensor Based on Reduced Graphene Oxide for Robot Skin Used in Internet of Things. Sensors (Basel). 2018, 18 (5), 1400. https://doi.org/10.3390/s18051400.

(163) Yao, Y.; Chen, X.; Zhu, J.; Zeng, B.; Wu, Z.; Li, X. The Effect of Ambient Humidity on the Electrical Properties of Graphene Oxide Films; 2012. http://www.nanoscalereslett.com/content/7/1/363.

(164) Tian, W.; Liu, X.; Yu, W. Research Progress of Gas Sensor Based on Graphene and Its Derivatives: A Review. Applied Sciences 2018, 8 (7), 1118. https://doi.org/10.3390/app8071118.

(165) Schedin, F.; Geim, A. K.; Morozov, S. V.; Hill, E. W.; Blake, P.; Katsnelson, M. I.; Novoselov, K. S. Detection of Individual Gas Molecules Adsorbed on Graphene. Nat. Mater. 2007, 6 (9), 652–655. https://doi.org/10.1038/nmat1967.

(166) Zhu, Y.; Murali, S.; Cai, W.; Li, X.; Suk, J. W.; Potts, J. R.; Ruoff, R. S. Graphene and Graphene Oxide: Synthesis, Properties, and Applications. Advanced Materials 2010, 22 (35), 3906–3924. https://doi.org/10.1002/adma.201001068.

(167) Wu, J.; Lin, H.; Moss, D. J.; Loh, K. P.; Jia, B. Graphene Oxide for Photonics, Electronics and Optoelectronics. Nature Reviews Chemistry 2023 7:3 2023, 7 (3), 162–183. https://doi.org/10.1038/s41570-022-00458-7.

(168) Lavin-Lopez, M. D. P.; Romero, A.; Garrido, J.; Sanchez-Silva, L.; Valverde, J. L. Influence of Different Improved Hummers Method Modifications on the Characteristics of Graphite Oxide in Order to Make a More Easily Scalable Method. Ind. Eng. Chem. Res. 2016, 55 (50), 12836–12847. https://doi.org/10.1021/ACS.IECR.6B03533.

(169) Paredes, J. I.; Villar-Rodil, S.; Martínez-Alonso, A.; Tascón, J. M. D. Graphene Oxide Dispersions in Organic Solvents. Langmuir 2008, 24 (19), 10560–10564. https://doi.org/10.1021/la801744a.

(170) Li, P.; Tao, C.-A.; Wang, B.; Huang, J.; Li, T.; Wang, J. Preparation of Graphene Oxide-Based Ink for Inkjet Printing. J. Nanosci. Nanotechnol. 2017, 18 (1), 713–718. https://doi.org/10.1166/jnn.2018.13942.

(171) Xiang, X.; Zhu, Y.; Gao, C.; Du, H.; Guo, C. Study on the Structure of Reduced Graphene Oxide Prepared by Different Reduction Methods. Carbon Letters 2021 32:2 2021, 32 (2), 557–566. https://doi.org/10.1007/S42823-021-00287-6.

(172) Jaafar, E.; Kashif, M.; Sahari, S. K.; Ngaini, Z. Study on Morphological, Optical and Electrical Properties of Graphene Oxide (GO) and Reduced Graphene

Oxide (RGO). Materials Science Forum 2018, 917 MSF, 112–116. https://doi.org/10.4028/WWW.SCIENTIFIC.NET/MSF.917.112.

(173) Chua, C. K.; Pumera, M. Chemical Reduction of Graphene Oxide: A Synthetic Chemistry Viewpoint. Chem. Soc. Rev. 2014, 43 (1), 291–312. https://doi.org/10.1039/C3CS60303B.

(174) Huang, L.; Liu, Y.; Ji, L. C.; Xie, Y. Q.; Wang, T.; Shi, W. Z. Pulsed Laser Assisted Reduction of Graphene Oxide. Carbon N. Y. 2011, 49 (7), 2431–2436. https://doi.org/10.1016/J.CARBON.2011.01.067.

(175) Gengler, R. Y. N.; Badali, D. S.; Zhang, D.; Dimos, K.; Spyrou, K.; Gournis, D.; Miller, R. J. D. Revealing the Ultrafast Process behind the Photoreduction of Graphene Oxide. Nature Communications 2013 4:1 2013, 4 (1), 1–5. https://doi.org/10.1038/ncomms3560.

(176) Borini, S.; White, R.; Wei, D.; Astley, M.; Haque, S.; Spigone, E.; Harris, N.; Kivioja, J.; Ryhänen, T. Ultrafast Graphene Oxide Humidity Sensors. ACS Nano 2013, 7 (12), 11166–11173. https://doi.org/10.1021/nn404889b.

(177) Bi, H.; Yin, K.; Xie, X.; Ji, J.; Wan, S.; Sun, L.; Terrones, M.; Dresselhaus, M. S. Ultrahigh Humidity Sensitivity of Graphene Oxide. Scientific Reports 2013 3:1 2013, 3 (1), 1–7. https://doi.org/10.1038/srep02714.

(178) Muchharla, B.; Narayanan, T. N.; Balakrishnan, K.; Ajayan, P. M.; Talapatra, S. Temperature Dependent Electrical Transport of Disordered Reduced Graphene Oxide. 2d Mater. 2014, 1 (1), 011008. https://doi.org/10.1088/2053-1583/1/1/011008.

(179) Soni, M.; Bhattacharjee, M.; Ntagios, M.; Dahiya, R. Printed Temperature Sensor Based on PEDOT: PSS-Graphene Oxide Composite. IEEE Sens. J. 2020, 20 (14). https://doi.org/10.1109/JSEN.2020.2969667.

(180) Shamkhalichenar, H.; Choi, J.-W. Review—Non-Enzymatic Hydrogen Peroxide Electrochemical Sensors Based on Reduced Graphene Oxide. J. Electrochem. Soc. 2020, 167 (3), 037531. https://doi.org/10.1149/1945-7111/ab644a.

(181) Shaban, M.; Ali, S.; Rabia, M. Design and Application of Nanoporous Graphene Oxide Film for CO2, H2, and C2H2 Gases Sensing. Journal of Materials Research and Technology 2019, 8 (5), 4510–4520. https://doi.org/10.1016/j.jmrt.2019.07.064.

(182) Nezakati, T.; Seifalian, A.; Tan, A.; Seifalian, A. M. Conductive Polymers: Opportunities and Challenges in Biomedical Applications. Chem. Rev. 2018, 118 (14), 6766–6843. https://doi.org/10.1021/ACS.CHEMREV.6B00275.

(183) Liu, Y.; Feig, V. R.; Bao, Z. Conjugated Polymer for Implantable Electronics toward Clinical Application. Adv. Healthc. Mater. 2021, 10 (17), 2001916. https://doi.org/10.1002/ADHM.202001916;WGROUP:STRING:PUBLICATION.

(184) Fan, X.; Nie, W.; Tsai, H.; Wang, N.; Huang, H.; Cheng, Y.; Wen, R.; Ma, L.; Yan, F.; Xia, Y. PEDOT:PSS for Flexible and Stretchable Electronics: Modifications, Strategies, and Applications. Advanced Science 2019, 6 (19), 1900813. https://doi.org/10.1002/ADVS.201900813;ISSUE:ISSUE:DOI.

(185) Rivers, G.; Austin, J. S.; He, Y.; Thompson, A.; Gilani, N.; Roberts, N.; Zhao, P.; Tuck, C. J.; Hague, R. J. M.; Wildman, R. D.; Turyanska, L. Stable Large Area Drop-on-Demand Deposition of a Conductive Polymer Ink for 3D-Printed Electronics, Enabled by Bio-Renewable Co-Solvents. Addit. Manuf. 2023, 66. https://doi.org/10.1016/j.addma.2023.103452.

(186) Girtan, M.; Mallet, R.; Socol, M.; Stanculescu, A. On the Physical Properties PEDOT:PSS Thin Films. Mater. Today Commun. 2020, 22, 100735. https://doi.org/10.1016/J.MTCOMM.2019.100735.

(187) Van Hazendonk, L. S.; Pinto, A. M.; Arapov, K.; Pillai, N.; Beurskens, M. R. C.; Teunissen, J. P.; Sneck, A.; Smolander, M.; Rentrop, C. H. A.; Bouten, P. C. P.; Friedrich, H. Printed Stretchable Graphene Conductors for Wearable Technology. Chemistry of Materials 2022, 34 (17), 8031–8042. https://doi.org/10.1021/ACS.CHEMMATER.2C02007/ASSET/IMAGES/LARGE/CM2C02007_0004.JPEG.

(188) Lee, B. M.; Nguyen, Q. H.; Shen, W. Flexible Multifunctional Sensors Using 3-D-Printed PEDOT:PSS Composites. IEEE Sens. J. 2024, 24 (6), 7584–7592. https://doi.org/10.1109/JSEN.2024.3357655.

(189) Hou, S.; Chen, H.; Lv, D.; Li, W.; Liu, X.; Zhang, Q.; Yu, X.; Han, Y. Highly Conductive Inkjet-Printed PEDOT:PSS Film under Cyclic Stretching. ACS Appl. Mater. Interfaces 2023, 15 (23), 28503–28515. https://doi.org/10.1021/acsami.3c03378.

(190) Song, J.; Wei, Y.; Xu, M.; Gao, J.; Luo, L.; Wu, H.; Li, X.; Li, Y.; Wang, X. Highly Sensitive Flexible Temperature Sensor Made Using PEDOT:PSS/PANI. ACS Appl. Polym. Mater. 2022, 4 (2), 766–772. https://doi.org/10.1021/ACSAPM.1C01224/SUPPL_FILE/AP1C01224_SI_004.MP4.

(191) Shen, L.; Feng, W.; Yu, D.; Wang, W. High Sensitive Humidity Sensor Based on PEDOT:PSS/CMC-Na Coated Polyester Fabric with Directional Moisture Transport Performance. Colloids Surf. A Physicochem. Eng. Asp. 2024, 682, 132880. https://doi.org/10.1016/J.COLSURFA.2023.132880.

(192) Yang, T.; Yang, M.; Xu, C.; Yang, K.; Su, Y.; Ye, Y.; Dou, L.; Yang, Q.; Ke, W.; Wang, B.; Luo, Z. PEDOT:PSS Hydrogels with High Conductivity and Biocompatibility for in Situ Cell Sensing. J. Mater. Chem. B 2023, 11 (14), 3226–3235. https://doi.org/10.1039/D3TB00014A.

(193) Liang, Y.; Offenhäusser, A.; Ingebrandt, S.; Mayer, D. PEDOT:PSS ‐ Based Bioelectronic Devices for Recording and Modulation of Electrophysiological and Biochemical Cell Signals. Adv. Healthc. Mater. 2021, 10 (11), 2100061. https://doi.org/10.1002/ADHM.202100061.

(194) Zhang, F.; Tuck, C.; Hague, R.; He, Y.; Saleh, E.; Li, Y.; Sturgess, C.; Wildman, R. Inkjet Printing of Polyimide Insulators for the 3D Printing of Dielectric Materials for Microelectronic Applications. J. Appl. Polym. Sci. 2016, 133 (18), 43361. https://doi.org/10.1002/APP.43361;SUBPAGE:STRING:FULL.

(195) Li, Y. X.; Wu, L. Y.; Yang, Y.; Lu, Y. Z.; Ji, Z. Y.; Guo, Y. X.; Wang, X. L.; Pu, Q. S. A Dielectric Ink Combining Acrylate and Cyanate Moieties for Inkjet 3D Printing with Good Thermal Stability. Chinese Journal of Polymer Science 2024 42:6 2024, 42 (6), 766–774. https://doi.org/10.1007/S10118-024-3114-8.

(196) He, Y.; Zhang, F.; Saleh, E.; Vaithilingam, J.; Aboulkhair, N.; Begines, B.; Tuck, C. J.; Hague, R. J. M.; Ashcroft, I. A.; Wildman, R. D. A Tripropylene Glycol Diacrylate-Based Polymeric Support Ink for Material Jetting. Addit. Manuf. 2017, 16, 153–161. https://doi.org/10.1016/J.ADDMA.2017.06.001.

(197) Saleh, E.; Zhang, F.; He, Y.; Vaithilingam, J.; Fernandez, J. L.; Wildman, R.; Ashcroft, I.; Hague, R.; Dickens, P.; Tuck, C. 3D Inkjet Printing of Electronics Using UV Conversion. Adv. Mater. Technol. 2017, 2 (10), 1700134. https://doi.org/10.1002/ADMT.201700134;REQUESTEDJOURNAL:JOURNAL:2365709X;ISSUE:ISSUE:DOI.

(198) Chamkouri, H. A Review of Hydrogels, Their Properties and Applications in Medicine. Am. J. Biomed. Sci. Res. 2021, 11 (6), 485–493. https://doi.org/10.34297/AJBSR.2021.11.001682.

(199) Li, J.; Ma, L.; Chen, G.; Zhou, Z.; Li, Q. A High Water-Content and High Elastic Dual-Responsive Polyurethane Hydrogel for Drug Delivery. J. Mater. Chem. B 2015, 3 (42), 8401–8409. https://doi.org/10.1039/C5TB01702E.

(200) Tariq, Z.; Iqbal, D. N.; Rizwan, M.; Ahmad, M.; Faheem, M.; Ahmed, M. Significance of Biopolymer-Based Hydrogels and Their Applications in Agriculture: A Review in Perspective of Synthesis and Their Degree of Swelling for Water Holding. RSC Adv. 2023, 13 (35), 24731–24754. https://doi.org/10.1039/D3RA03472K.

(201) Madduma-Bandarage, U. S. K.; Madihally, S. V. Synthetic Hydrogels: Synthesis, Novel Trends, and Applications. J. Appl. Polym. Sci. 2021, 138 (19). https://doi.org/10.1002/APP.50376.

(202) Palmese, L. L.; Thapa, R. K.; Sullivan, M. O.; Kiick, K. L. Hybrid Hydrogels for Biomedical Applications. Curr. Opin. Chem. Eng. 2019, 24, 143–157. https://doi.org/10.1016/J.COCHE.2019.02.010.

(203) Lu, B.; Yuk, H.; Lin, S.; Jian, N.; Qu, K.; Xu, J.; Zhao, X. Pure PEDOT:PSS Hydrogels. Nature Communications 2019 10:1 2019, 10 (1), 1043-. https://doi.org/10.1038/s41467-019-09003-5.

(204) Albao, M. J. F.; Calsis, J. R. F.; Dancel, J. O.; De Juan-Corpuz, L. M.; Corpuz, R. D. Silver Nanoparticle-Infused Hydrogels for Biomedical Applications: A Comprehensive Review. Journal of the Chinese Chemical Society 2025, 72 (2), 124–162. https://doi.org/10.1002/JCCS.202400303;PAGE:STRING:ARTICLE/CHAPTER.

(205) Khodami, S.; Gharakhloo, M.; Dagdelen, S.; Fita, P.; Romanski, J.; Karbarz, M.; Stojek, Z.; Mackiewicz, M. Rapid Photoinduced Self-Healing, Controllable Drug Release, Skin Adhesion Ability, and Mechanical Stability of Hydrogels Incorporating Linker-Modified Gold Nanoparticles and Nanogels. ACS Appl. Mater. Interfaces 2024, 16 (42), 57659–57671. https://doi.org/10.1021/ACSAMI.4C11908.

(206) Patroklou, G.; Triantafyllopoulou, E.; Goula, P. E.; Karali, V.; Chountoulesi, M.; Valsami, G.; Pispas, S.; Pippa, N. PH-Responsive Hydrogels: Recent Advances in Pharmaceutical Applications. Polymers 2025, Vol. 17, Page 1451 2025, 17 (11), 1451. https://doi.org/10.3390/POLYM17111451.

(207) Klouda, L.; Mikos, A. G. Thermoresponsive Hydrogels in Biomedical Applications - a Review. Eur. J. Pharm. Biopharm. 2007, 68 (1), 34. https://doi.org/10.1016/J.EJPB.2007.02.025.

(208) Htwe, Y. Z. N.; Hidayah, I. N.; Mariatti, M. Performance of Inkjet-Printed Strain Sensor Based on Graphene/Silver Nanoparticles Hybrid Conductive Inks on Polyvinyl Alcohol Substrate. Journal of Materials Science: Materials in Electronics 2020, 31 (18), 15361–15371. https://doi.org/10.1007/s10854-020-04100-4.

(209) Alshammari, A. S.; Shkunov, M.; Silva, S. R. P. Inkjet Printed PEDOT:PSS/MWCNT Nano‐composites with Aligned Carbon Nanotubes and Enhanced Conductivity. physica status solidi (RRL) − Rapid Research Letters 2014, 8 (2), 150−153. https://doi.org/10.1002/pssr.201308231.

(210) Liu, Z.; Parvez, K.; Li, R.; Dong, R.; Feng, X.; Müllen, K. Transparent Conductive Electrodes from Graphene/PEDOT:PSS Hybrid Inks for Ultrathin Organic Photodetectors. Advanced Materials 2015, 27 (4), 669–675. https://doi.org/10.1002/adma.201403826.

(211) Saidina, D. S.; Mariatti, M.; Zubir, S. A.; Fontana, S.; Hérold, C. Performance of Graphene Hybrid-Based Ink for Flexible Electronics. Journal of Materials Science: Materials in Electronics 2019, 30 (22), 19906–19916. https://doi.org/10.1007/s10854-019-02357-y.

(212) Popov, V. I.; Kotin, I. A.; Nebogatikova, N. A.; Smagulova, S. A.; Antonova, I. V. Graphene-PEDOT: PSS Humidity Sensors for High Sensitive, Low-Cost, Highly-

Reliable, Flexible, and Printed Electronics. Materials 2019, 12 (21), 3477. https://doi.org/10.3390/ma12213477.

(213) Seekaew, Y.; Lokavee, S.; Phokharatkul, D.; Wisitsoraat, A.; Kerdcharoen, T.; Wongchoosuk, C. Low-Cost and Flexible Printed Graphene-PEDOT:PSS Gas Sensor for Ammonia Detection. Org. Electron. 2014, 15 (11), 2971–2981. https://doi.org/10.1016/j.orgel.2014.08.044.

(214) Vuorinen, T.; Niittynen, J.; Kankkunen, T.; Kraft, T. M.; Mäntysalo, M. Inkjet-Printed Graphene/PEDOT:PSS Temperature Sensors on a Skin-Conformable Polyurethane Substrate. Sci. Rep. 2016, 6 (1). https://doi.org/10.1038/srep35289.

(215) Htwe, Y. Z. N.; Abdullah, M. K.; Mariatti, M. Water-Based Graphene/AgNPs Hybrid Conductive Inks for Flexible Electronic Applications. Journal of Materials Research and Technology 2022, 16, 59–73. https://doi.org/10.1016/J.JMRT.2021.11.159.

(216) Cook, B.; Gong, M.; Corbin, A.; Ewing, D.; Tramble, A.; Wu, J. Inkjet-Printed Imbedded Graphene Nanoplatelet/Zinc Oxide Bulk Heterojunctions Nanocomposite Films for Ultraviolet Photodetection. ACS Omega 2019, 4 (27), 22497–22503. https://doi.org/10.1021/ACSOMEGA.9B03173.

(217) Kim, K.; Jung, M.; Kim, B.; Kim, J.; Shin, K.; Kwon, O. S.; Jeon, S. Low-Voltage, High-Sensitivity and High-Reliability Bimodal Sensor Array with Fully Inkjet-Printed Flexible Conducting Electrode for Low Power Consumption Electronic Skin. Nano Energy 2017, 41, 301–307. https://doi.org/10.1016/J.NANOEN.2017.09.024.

(218) Wallace, S. G.; Bradshaw, N. P.; Williams, N. X.; Qian, J. H.; Putz, K. W.; Tabor, C. E.; Hersam, M. C. Combustion-Assisted Photonic Sintering of Printed Liquid Metal Nanoparticle Films. Adv. Mater. Technol. 2022, 7 (6). https://doi.org/10.1002/ADMT.202101178.

(219) Secor, E. B.; Gao, T. Z.; Dos Santos, M. H.; Wallace, S. G.; Putz, K. W.; Hersam, M. C. Combustion-Assisted Photonic Annealing of Printable Graphene Inks via Exothermic Binders. ACS Appl. Mater. Interfaces 2017, 9 (35), 29418–29423. https://doi.org/10.1021/acsami.7b07189.

(220) Martin, G. D.; Hoath, S. D.; Hutchings, I. M. Inkjet Printing - The Physics of Manipulating Liquid Jets and Drops. J. Phys. Conf. Ser. 2008, 105 (1). https://doi.org/10.1088/1742-6596/105/1/012001.

(221) Ansell, T. Y. Current Status of Liquid Metal Printing. Journal of Manufacturing and Materials Processing. MDPI AG June 1, 2021. https://doi.org/10.3390/jmmp5020031.

(222) Derby, B. Inkjet Printing of Functional and Structural Materials: Fluid Property Requirements, Feature Stability, and Resolution. Annu. Rev. Mater. Res. 2010, 40, 395–414. https://doi.org/10.1146/annurev-matsci-070909-104502.

(223) Yen, B. Continuous Direct Ink Jet Printing, Queen Mary, University of London, London, 2001. http://qmro.qmul.ac.uk/jspui/handle/123456789/1560.

(224) Hoath, S. D.; Hsiao, W. K.; Jung, S.; Martin, G. D.; Hutchings, I. M.; Morrison, N. F.; Harlen, O. G. Drop Speeds from Drop-on-Demand Ink-Jet Print Heads. Journal of Imaging Science and Technology 2013, 57 (1). https://doi.org/10.2352/J.ImagingSci.Technol.2013.57.1.010503.

(225) Guo, Y.; Patanwala, H. S.; Bognet, B.; Ma, A. W. K. Inkjet and Inkjet-Based 3D Printing: Connecting Fluid Properties and Printing Performance. Rapid Prototyp. J. 2017, 23 (3), 562–576. https://doi.org/10.1108/RPJ-05-2016-0076.

(226) Li, J.; Rossignol, F.; Macdonald, J. Inkjet Printing for Biosensor Fabrication: Combining Chemistry and Technology for Advanced Manufacturing. Lab Chip 2015, 15 (12), 2538–2558. https://doi.org/10.1039/C5LC00235D.

(227) Courbat, J. Gas Sensors on Plastic Foil with Reduced Power Consumption, 2010.

(228) Li, J.; Rossignol, F.; Macdonald, J. Inkjet Printing for Biosensor Fabrication: Combining Chemistry and Technology for Advanced Manufacturing. Lab Chip 2015, 15 (12), 2538–2558. https://doi.org/10.1039/C5LC00235D.

(229) McKinley, G. H.; Renardy, M. Wolfgang von Ohnesorge. Physics of Fluids 2011, 23 (12). https://doi.org/10.1063/1.3663616.

(230) Kim, S.; Cho, M.; Jung, S. The Design of an Inkjet Drive Waveform Using Machine Learning. Sci. Rep. 2022, 12 (1). https://doi.org/10.1038/s41598-022-08784-y.

(231) Tembely, M.; Vadillo, D. C.; Dolatabadi, A.; Soucemarianadin, A. A Machine Learning Approach for Predicting the Maximum Spreading Factor of Droplets upon Impact on Surfaces with Various Wettabilities. Processes 2022, 10 (6). https://doi.org/10.3390/pr10061141.

(232) Huang, Q.; Zhu, Y. Printing Conductive Nanomaterials for Flexible and Stretchable Electronics: A Review of Materials, Processes, and Applications. Adv. Mater. Technol. 2019, 4 (5). https://doi.org/10.1002/ADMT.201800546.

(233) Cummins, G.; Desmulliez, M. P. Y. Inkjet Printing of Conductive Materials: A Review. Circuit World. 2012, pp 193–213. https://doi.org/10.1108/03056121211280413.

(234) Zeng, M.; Zhang, Y. Colloidal Nanoparticle Inks for Printing Functional Devices: Emerging Trends and Future Prospects. J. Mater. Chem. A Mater. 2019, 7 (41), 23301–23336. https://doi.org/10.1039/C9TA07552F.

(235) Li, J.; Ye, F.; Vaziri, S.; Muhammed, M.; Lemme, M. C.; Östling, M. Efficient Inkjet Printing of Graphene. Adv. Mater. 2013, 25 (29), 3985–3992. https://doi.org/10.1002/ADMA.201300361.

(236) Shin, K. Y.; Hong, J. Y.; Jang, J. Micropatterning of Graphene Sheets by Inkjet Printing and Its Wideband Dipole-Antenna Application. Adv. Mater. 2011, 23 (18), 2113–2118. https://doi.org/10.1002/ADMA.201100345.

(237) Soltman, D.; Subramanian, V. Inkjet-Printed Line Morphologies and Temperature Control of the Coffee Ring Effect. Langmuir 2008, 24 (5), 2224–2231. https://doi.org/10.1021/la7026847.

(238) Beedasy, V.; Smith, P. J. Printed Electronics as Prepared by Inkjet Printing. Materials. MDPI AG February 1, 2020. https://doi.org/10.3390/ma13030704.

(239) Tan, H. W.; An, J.; Chua, C. K.; Tran, T. Metallic Nanoparticle Inks for 3D Printing of Electronics. Adv. Electron. Mater. 2019, 5 (5), 1800831. https://doi.org/10.1002/AELM.201800831;ISSUE:ISSUE:DOI.

(240) Gao, Y.; Shi, W.; Wang, W.; Leng, Y.; Zhao, Y. Inkjet Printing Patterns of Highly Conductive Pristine Graphene on Flexible Substrates. Ind. Eng. Chem. Res. 2014, 53 (43), 16777–16784. https://doi.org/10.1021/ie502675z.

(241) Tomaszewski, G.; Wałach, T.; Potencki, J.; Pilecki, M. The Influence of Sintering Conditions on the Inkjet Printed Paths Resistance. International Journal of Electronics and Telecommunications 2016, 62 (2), 135–140. https://doi.org/10.1515/eletel-2016-0018.

(242) Jensen, G. C.; Krause, C. E.; Sotzing, G. A.; Rusling, J. F. Inkjet-Printed Gold Nanoparticle Electrochemical Arrays on Plastic. Application to Immunodetection of a Cancer Biomarker Protein. Physical Chemistry Chemical Physics 2011, 13 (11), 4888–4894. https://doi.org/10.1039/c0cp01755h.

(243) Wang, X.; Mu, B.; Zhang, L.; Zhang, X. Drift Characteristic Analysis of Additive Manufactured Ag NPs-PEDOT:PSS Flexible Temperature Sensor. Results in Engineering 2022, 13. https://doi.org/10.1016/j.rineng.2022.100384.

(244) Sui, Y.; Hess-Dunning, A.; Wei, P.; Pentzer, E.; Sankaran, R. M.; Zorman, C. A. Electrically Conductive, Reduced Graphene Oxide Structures Fabricated by Inkjet Printing and Low Temperature Plasma Reduction. Adv. Mater. Technol. 2019, 4 (12). https://doi.org/10.1002/admt.201900834.

(245) Homola, T.; Pospíšil, J.; Krumpolec, R.; Souček, P.; Dzik, P.; Weiter, M.; Černák, M. Atmospheric Dry Hydrogen Plasma Reduction of Inkjet-Printed Flexible Graphene Oxide Electrodes. ChemSusChem 2018, 11 (5), 941–947. https://doi.org/10.1002/cssc.201702139.

(246) Bollgruen, P.; Mager, D.; Korvink, J. G. Ohmic Curing for Ink-Jet Printed Conductive Silver Tracks on PMMA Foil; 2012; Vol. 41. https://www.researchgate.net/publication/282817049.

(247) Roberson, D. A.; Wicker, R. B.; MacDonald, E. Ohmic Curing of Printed Silver Conductive Traces. J. Electron. Mater. 2012, 41 (9), 2553–2566. https://doi.org/10.1007/s11664-012-2140-4.

(248) Perelaer, J.; Klokkenburg, M.; Hendriks, C. E.; Schubert, U. S. Microwave Flash Sintering of Inkjet-Printed Silver Tracks on Polymer Substrates. Advanced Materials 2009, 21 (47), 4830–4834. https://doi.org/10.1002/adma.200901081.

(249) Le, T. T.; Bui, H. H. T.; Dinh, A. K. P.; Van, D. V.; Ho, Q. D.; Thi, H. A. N.; Nguyen, D. H.; La, D. D. Room Temperature-Sintering Conductive Ink Fabricated from Oleic-Modified Graphene for the Flexible Electronic Devices. ChemistrySelect 2022, 7 (4). https://doi.org/10.1002/slct.202104249.

(250) Majee, S.; Zhao, W.; Sugunan, A.; Gillgren, T.; Larsson, J. A.; Brooke, R.; Nordgren, N.; Zhang, Z. Bin; Zhang, S. L.; Nilsson, D.; Ahniyaz, A. Highly Conductive Films by Rapid Photonic Annealing of Inkjet Printable Starch–Graphene Ink. Adv. Mater. Interfaces 2022, 9 (5), 2101884. https://doi.org/10.1002/ADMI.202101884.

(251) Jang, Y. R.; Joo, S. J.; Chu, J. H.; Uhm, H. J.; Park, J. W.; Ryu, C. H.; Yu, M. H.; Kim, H. S. A Review on Intense Pulsed Light Sintering Technologies for Conductive Electrodes in Printed Electronics. International Journal of Precision Engineering and Manufacturing - Green Technology 2021, 8 (1), 327–363. https://doi.org/10.1007/s40684-020-00193-8.

(252) Schroder, K. A. Mechanisms of Photonic Curing: Processing High Temperature Films on Low Temperature Substrates. In Technical Proceedings of the 2011 NSTI Nanotechnology Conference and Trade Show; Nano Science. In Technical Proceedings of the 2011 NSTI Nanotechnology Conference and Trade Show; Austin, TX, 2011; pp 220–223.

(253) Zhao, Z.; Rose, A.; Kwon, S. J.; Jeon, Y.; Cho, E.-S. Rapid Photonic Curing Effects of Xenon Flash Lamp on ITO–Ag–ITO Multilayer Electrodes for High Throughput Transparent Electronics. Sci. Rep. 2023, 13 (1), 1042. https://doi.org/10.1038/s41598-023-27942-4.

(254) Lee, J.; Kwak, J. H.; Kim, J.; Jeong, S.; Park, J. H.; Jeong, S. Y.; Seo, S. H.; Han, J. T.; Lee, G.; Baeg, K.; Yang, I. H. ‐ S.; Jeong, H. J. Minimizing Temperature Gradient in Photonic Sintering for Defect ‐ Free High ‐ Conductivity Cu ‐ Based Printed Patterns by Bidirectional Irradiation. Adv. Mater. Interfaces 2021, 8 (16). https://doi.org/10.1002/admi.202100769.

(255) Gu, W.; Yuan, W.; Zhong, T.; Wu, X.; Zhou, C.; Lin, J.; Cui, Z. Fast near Infrared Sintering of Silver Nanoparticle Ink and Applications for Flexible Hybrid Circuits. RSC Adv. 2018, 8 (53), 30215–30222. https://doi.org/10.1039/C8RA04468F.

(256) Soltan Dallal, M. M.; Safdari, R.; Emadi Koochak, H.; Sharifi-Yazdi, S.; Akhoondinasab, M. R.; Pourmand, M. R.; Hadayatpour, A.; Sharifi-Yazdi, M. K. A Comparison between Occlusive and Exposure Dressing in the Management of Burn Wound. Burns 2016, 42 (3), 578–582. https://doi.org/10.1016/j.burns.2015.05.001.

(257) Yang, Y.; Bai, N.; Cao, T.; Zhang, X.; Gao, Y.; Zhang, J.; Zhao, P.; Huang, J. Numerical and Experimental Investigations on Intense Pulsed Light Sintering of Silver Nanoparticle Inks for Printed Electronics. International Journal of Thermal Sciences 2022, 176, 107507. https://doi.org/10.1016/J.IJTHERMALSCI.2022.107507.

(258) Meng, F.; Peng, J.; Huang, J.; Ping, B.; Lu, W.; Zhou, J.; Li, P. Computational Analysis Model of Intense Pulsed Sintering of Silver Nanoparticles. Addit. Manuf. 2022, 51, 102594. https://doi.org/10.1016/J.ADDMA.2022.102594.

(259) Kang, H.; Sowade, E.; Baumann, R. R. Direct Intense Pulsed Light Sintering of Inkjet-Printed Copper Oxide Layers within Six Milliseconds. ACS Appl. Mater. Interfaces 2014, 6 (3), 1682–1687. https://doi.org/10.1021/AM404581B.

(260) Fumeaux, N.; Briand, D. Zinc Hybrid Sintering for Printed Transient Sensors and Wireless Electronics. npj Flexible Electronics 2023, 7 (1). https://doi.org/10.1038/S41528-023-00249-0.

(261) Zhao, W.; Rovere, T.; Weerawarne, D.; Osterhoudt, G.; Kang, N.; Joseph, P.; Luo, J.; Shim, B.; Poliks, M.; Zhong, C. J. Nanoalloy Printed and Pulse-Laser Sintered Flexible Sensor Devices with Enhanced Stability and Materials Compatibility. ACS Nano 2015, 9 (6), 6168–6177. https://doi.org/10.1021/ACSNANO.5B02704.

(262) Oh, G. H.; Hwang, H. J.; Kim, H. S. Effect of Copper Oxide Shell Thickness on Flash Light Sintering of Copper Nanoparticle Ink. RSC Adv. 2017, 7 (29), 17724–17731. https://doi.org/10.1039/C7RA01429E.

(263) Balliu, E.; Andersson, H.; Engholm, M.; Öhlund, T.; Nilsson, H. E.; Olin, H. Selective Laser Sintering of Inkjet-Printed Silver Nanoparticle Inks on Paper Substrates to Achieve Highly Conductive Patterns. Sci. Rep. 2018, 8 (1). https://doi.org/10.1038/S41598-018-28684-4.

(264) Arapov, K.; Bex, G.; Hendriks, R.; Rubingh, E.; Abbel, R.; de With, G.; Friedrich, H. Conductivity Enhancement of Binder-Based Graphene Inks by Photonic Annealing and Subsequent Compression Rolling. Adv. Eng. Mater. 2016, 18 (7), 1234–1239. https://doi.org/10.1002/adem.201500646.

(265) Afroj, S.; Tan, S.; Abdelkader, A. M.; Novoselov, K. S.; Karim, N. Highly Conductive, Scalable, and Machine Washable Graphene-Based E-Textiles for Multifunctional Wearable Electronic Applications. Adv. Funct. Mater. 2020, 30 (23), 2000293. https://doi.org/10.1002/adfm.202000293.

(266) Chung, W. Y.; Lai, Y. C.; Yonezawa, T.; Liao, Y. C. Sintering Copper Nanoparticles with Photonic Additive for Printed Conductive Patterns by Intense

Pulsed Light. Nanomaterials 2019, Vol. 9, Page 1071 2019, 9 (8), 1071. https://doi.org/10.3390/NANO9081071.

(267) Yang, Y.; Bai, N.; Cao, T.; Zhang, X.; Gao, Y.; Zhang, J.; Zhao, P.; Huang, J. Numerical and Experimental Investigations on Intense Pulsed Light Sintering of Silver Nanoparticle Inks for Printed Electronics. International Journal of Thermal Sciences 2022, 176, 107507. https://doi.org/10.1016/J.IJTHERMALSCI.2022.107507.

(268) Niittynen, J.; Sowade, E.; Kang, H.; Baumann, R. R.; Mäntysalo, M. Comparison of Laser and Intense Pulsed Light Sintering (IPL) for Inkjet-Printed Copper Nanoparticle Layers. Scientific Reports 2015 5:1 2015, 5 (1), 1–10. https://doi.org/10.1038/srep08832.

(269) Pajor-Świerzy, A.; Szyk-Warszyńska, L.; Duraczyńska, D.; Szczepanowicz, K. UV-Vis Sintering Process for Fabrication of Conductive Coatings Based on Ni-Ag Core–Shell Nanoparticles. Materials 2023, Vol. 16, Page 7218 2023, 16 (22), 7218. https://doi.org/10.3390/MA16227218.

(270) Kim, M.; Jee, H.; Lee, J. Photo-Sintered Silver Thin Films by a High-Power UV-LED Module for Flexible Electronic Applications. Nanomaterials 2021, 11 (11), 2840. https://doi.org/10.3390/NANO11112840.

(271) Johra, F. T.; Lee, J. W.; Jung, W. G. Facile and Safe Graphene Preparation on Solution Based Platform. Journal of Industrial and Engineering Chemistry 2014, 20 (5), 2883–2887. https://doi.org/10.1016/J.JIEC.2013.11.022.

(272) Shang, J.; Ma, L.; Li, J.; Ai, W.; Yu, T.; Gurzadyan, G. G. The Origin of Fluorescence from Graphene Oxide. Scientific Reports 2012 2:1 2012, 2 (1), 1–8. https://doi.org/10.1038/srep00792.

(273) Cote, L. J.; Cruz-Silva, R.; Huang, J. Flash Reduction and Patterning of Graphite Oxide and Its Polymer Composite. J. Am. Chem. Soc. 2009, 131 (31), 11027–11032. https://doi.org/10.1021/JA902348K/SUPPL_FILE/JA902348K_SI_002.AVI.

(274) Park, S. H.; Kim, H. S. Environmentally Benign and Facile Reduction of Graphene Oxide by Flash Light Irradiation. Nanotechnology 2015, 26 (20), 205601. https://doi.org/10.1088/0957-4484/26/20/205601.

(275) Akhavan, O. The Effect of Heat Treatment on Formation of Graphene Thin Films from Graphene Oxide Nanosheets. Carbon N. Y. 2010, 48 (2), 509–519. https://doi.org/10.1016/J.CARBON.2009.09.069.

(276) Bon, S. B.; Valentini, L. Restoring the Electrical Conductivity of Graphene Oxide Films by UV Light Induced Oxygen Desorption. 2010.

(277) Alishah, H. M.; Kazici, M.; Ongül, F.; Bozar, S.; Cantürk Rodop, M.; Kahveci, C.; Arvas, M. B.; Sahin, Y.; Gencten, M.; Kaleli, M.; Akyürekli, S.; Yilmaz, H. U.; Bayram, A. B.; Günes, S. Effect of UV Exposure of ITO/PEDOT:PSS Substrates on the Performance of Inverted-Type Perovskite Solar Cells. Journal of Materials

Science: Materials in Electronics 2020, 31 (10), 7968–7980. https://doi.org/10.1007/S10854-020-03336-4/FIGURES/11.

(278) Wei-Yang Chou, S.; Dove, A.; Richard Walton, P.; Ian Hamley, P.; Neil McKeown, P.; Robertson, N.; Skinner, S.; Robert Cava, P.; Andy Cooper, P.; Clare Grey FRS, P.; Alan Heeger, P.; Allan Hoffman, P.; Samuel Stupp, P.; Tang, F.-C.; Chang, J.; Wu, F.-C.; Cheng, H.-L.; Lien-Chung Hsu, S.; Chen, J.-S.; Chou, W.-Y. Alignment of Poly(3,4-Ethylenedioxythiophene) Polymer Chains in Photovoltaic Cells by Ultraviolet Irradiation. J. Mater. Chem. 2012, 22 (42), 22409–22417. https://doi.org/10.1039/C2JM34556K.

(279) Ban, S.; Nie, X.; Lei, Z.; Yi, J.; Vinu, A.; Bao, Y.; Liu, Y. Emerging Low-Dimensional Materials for Nanoelectromechanical Systems Resonators. Mater. Res. Lett. 2022, 11 (1), 21–52. https://doi.org/10.1080/21663831.2022.2111233.

(280) Rahimi, R.; Ochoa, M.; Tamayol, A.; Khalili, S.; Khademhosseini, A.; Ziaie, B. Highly Stretchable Potentiometric PH Sensor Fabricated via Laser Carbonization and Machining of Carbon−Polyaniline Composite. ACS Appl. Mater. Interfaces 2017, 9 (10), 9015–9023. https://doi.org/10.1021/ACSAMI.6B16228/ASSET/IMAGES/LARGE/AM-2016-16228Z_0006.JPEG.

(281) Huang, L.; Huang, Y.; Liang, J.; Wan, X.; Chen, Y. Graphene-Based Conducting Inks for Direct Inkjet Printing of Flexible Conductive Patterns and Their Applications in Electric Circuits and Chemical Sensors. Nano Res. 2011, 4 (7), 675–684. https://doi.org/10.1007/s12274-011-0123-z.

(282) Fang, Y.; Akbari, M.; Sydänheimo, L.; Ukkonen, L.; Tentzeris, M. M. Sensitivity Enhancement of Flexible Gas Sensors via Conversion of Inkjet-Printed Silver Electrodes into Porous Gold Counterparts. Scientific Reports 2017 7:1 2017, 7 (1), 1–10. https://doi.org/10.1038/s41598-017-09174-5.

(283) Dudala, S.; Srikanth, S.; Dubey, S. K.; Javed, A.; Goel, S. Rapid Inkjet-Printed Miniaturized Interdigitated Electrodes for Electrochemical Sensing of Nitrite and Taste Stimuli. Micromachines (Basel). 2021, 12 (9), 1037. https://doi.org/10.3390/MI12091037.

(284) Molina-Lopez, F.; Briand, D.; De Rooij, N. F. Inkjet Printing of Inter Digitated Capacitive Chemical Sensors with Reduced Size by the Introduction of a Dielectric Interlayer. Procedia Eng. 2012, 47, 1173–1176. https://doi.org/10.1016/J.PROENG.2012.09.360.

(285) Salim, A.; Lim, S. Review of Recent Inkjet-Printed Capacitive Tactile Sensors. Sensors 2017, Vol. 17, Page 2593 2017, 17 (11), 2593. https://doi.org/10.3390/S17112593.

(286) Mass, M.; Veiga, L. S.; Garate, O.; Longinotti, G.; Moya, A.; Ramón, E.; Villa, R.; Ybarra, G.; Gabriel, G. Fully Inkjet-Printed Biosensors Fabricated with a Highly

Stable Ink Based on Carbon Nanotubes and Enzyme-Functionalized Nanoparticles. Nanomaterials 2021, 11 (7), 1645. https://doi.org/10.3390/NANO11071645/S1.

(287) Abe, K.; Kotera, K.; Suzuki, K.; Citterio, D. Inkjet-Printed Paperfluidic Immuno-Chemical Sensing Device. Analytical and Bioanalytical Chemistry 2010 398:2 2010, 398 (2), 885–893. https://doi.org/10.1007/S00216-010-4011-2.

(288) Han, C.; Liang, S.; Liu, H.; Ye, H. Temperature Dependence of Polarons in Conductive PEDOT:PSS Thin Films. J. Appl. Phys. 2025, 137 (6), 63103. https://doi.org/10.1063/5.0233560/3335506.

(289) Chen, R.; Luo, T.; Geng, D.; Shen, Z.; Zhou, W. Facile Fabrication of a Fast-Response Flexible Temperature Sensor via Laser Reduced Graphene Oxide for Contactless Human-Machine Interface. Carbon N. Y. 2022, 187, 35–46. https://doi.org/10.1016/J.CARBON.2021.10.064.

(290) Lim, W. Y.; Goh, C. H.; Yap, K. Z.; Ramakrishnan, N. One-Step Fabrication of Paper-Based Inkjet-Printed Graphene for Breath Monitor Sensors. Biosensors 2023, Vol. 13, Page 209 2023, 13 (2), 209. https://doi.org/10.3390/BIOS13020209.

(291) Lu, R.; Haider, M. R.; Gardner, S.; Alexander, J. I. D.; Massoud, Y. A Paper-Based Inkjet-Printed Graphene Sensor for Breathing-Flow Monitoring. IEEE Sens. Lett. 2019, 3 (2). https://doi.org/10.1109/LSENS.2018.2885316.

(292) Lo, L. W.; Shi, H.; Wan, H.; Xu, Z.; Tan, X.; Wang, C. Inkjet-Printed Soft Resistive Pressure Sensor Patch for Wearable Electronics Applications. Adv. Mater. Technol. 2020, 5 (1). https://doi.org/10.1002/admt.201900717.

(293) Walach, H.; Weikl, R.; Prentice, J.; Diemer, A.; Traindl, H.; Kappes, A.; Hockertz, S. Experimental Assessment of Carbon Dioxide Content in Inhaled Air With or Without Face Masks in Healthy Children: A Randomized Clinical Trial. JAMA Pediatr. 2021. https://doi.org/10.1001/JAMAPEDIATRICS.2021.2659.

(294) Anderson, J. C.; Lamm, W. J. E.; Hlastala, M. P. Measuring Airway Exchange of Endogenous Acetone Using a Single-Exhalation Breathing Maneuver. J. Appl. Physiol. (1985). 2006, 100 (3), 880–889. https://doi.org/10.1152/JAPPLPHYSIOL.00868.2005.

(295) Anderson, J. C. Measuring Breath Acetone for Monitoring Fat Loss: Review. Obesity (Silver Spring). 2015, 23 (12), 2327. https://doi.org/10.1002/OBY.21242.

(296) Wu, T. C.; De Luca, A.; Zhong, Q.; Zhu, X.; Ogbeide, O.; Um, D. S.; Hu, G.; Albrow-Owen, T.; Udrea, F.; Hasan, T. Inkjet-Printed CMOS-Integrated Graphene–Metal Oxide Sensors for Breath Analysis. NPJ 2D Mater. Appl. 2019, 3 (1). https://doi.org/10.1038/s41699-019-0125-3.

(297) Reeves, N.; Phillips, S.; Hughes, A.; Maddocks, S.; Bates, M.; Torkington, J.; Robins, L.; Cornish, J. Volatile Organic Compounds in the Early Diagnosis of Non-Healing Surgical Wounds: A Systematic Review. World Journal of Surgery. Springer

Science and Business Media Deutschland GmbH July 1, 2022, pp 1669–1677. https://doi.org/10.1007/s00268-022-06548-3.

(298) Yang, D. S.; Ghaffari, R.; Rogers, J. A. Sweat as a Diagnostic Biofluid. Science 2023, 379 (6634), 760–761. https://doi.org/10.1126/science.abq5916.

(299) Pei, X.; Sun, M.; Wang, J.; Bai, J.; Bo, X.; Zhou, M. A Bifunctional Fully Integrated Wearable Tracker for Epidermal Sweat and Wound Exudate Multiple Biomarkers Monitoring. Small 2022, 2205061. https://doi.org/10.1002/smll.202205061.

(300) Hashemzadeh, S.; Omidi, Y.; Rafii-Tabar, H. Amperometric Lactate Nanobiosensor Based on Reduced Graphene Oxide, Carbon Nanotube and Gold Nanoparticle Nanocomposite. Microchimica Acta 2019, 186 (10). https://doi.org/10.1007/s00604-019-3791-0.

(301) Lapraz, J. C.; Hedayat, K. M.; Pauly, P. Endobiogeny: A Global Approach to Systems Biology (Part 2 of 2). Glob. Adv. Health Med. 2013, 2 (2), 32–56. https://doi.org/10.7453/GAHMJ.2013.013.

(302) Payne, M. E.; Zamarayeva, A.; Pister, V. I.; Yamamoto, N. A. D.; Arias, A. C. Printed, Flexible Lactate Sensors: Design Considerations Before Performing On-Body Measurements. Scientific Reports 2019 9:1 2019, 9 (1), 13720-. https://doi.org/10.1038/s41598-019-49689-7.

(303) Tsou, K. L.; Chen, K. Y.; Chou, Y. De; Cheng, Y. T.; Tsai, H. E.; Lee, C. K. Inkjet-Printed Flexible Non-Enzymatic Lactate Sensor with High Sensitivity and Low Interference Using a Stacked NiOx/NiOx-Nafion Nanocomposite Electrode with Clinical Blood Test Verification. Talanta 2022, 249. https://doi.org/10.1016/j.talanta.2022.123598.

(304) He, Q.; Das, S. R.; Garland, N. T.; Jing, D.; Hondred, J. A.; Cargill, A. A.; Ding, S.; Karunakaran, C.; Claussen, J. C. Enabling Inkjet Printed Graphene for Ion Selective Electrodes with Postprint Thermal Annealing. ACS Appl. Mater. Interfaces 2017, 9 (14), 12719–12727. https://doi.org/10.1021/ACSAMI.7B00092/SUPPL_FILE/AM7B00092_SI_001.PDF.

(305) Yang, Q.; Rosati, G.; Abarintos, V.; Aroca, M. A.; Osma, J. F.; Merkoçi, A. Wearable and Fully Printed Microfluidic Nanosensor for Sweat Rate, Conductivity, and Copper Detection with Healthcare Applications. Biosens. Bioelectron. 2022, 202, 114005. https://doi.org/10.1016/J.BIOS.2022.114005.

(306) Chakraborthy, A.; Nuthalapati, S.; Nag, A.; Afsarimanesh, N.; Alahi, M. E. E.; Altinsoy, M. E. A Critical Review of the Use of Graphene-Based Gas Sensors. Chemosensors. MDPI September 1, 2022. https://doi.org/10.3390/chemosensors10090355.

(307) Liang, R.; Luo, A.; Zhang, Z.; Li, Z.; Han, C.; Wu, W. Research Progress of Graphene-Based Flexible Humidity Sensor. Sensors (Basel). 2020, 20 (19), 1–17. https://doi.org/10.3390/s20195601.

(308) Xu, L. Y.; Yang, G. Y.; Jing, H. Y.; Wei, J.; Han, Y. D. Ag-Graphene Hybrid Conductive Ink for Writing Electronics. Nanotechnology 2014, 25 (5). https://doi.org/10.1088/0957-4484/25/5/055201.

(309) Wang, Y. H.; Du, D. X.; Xie, H.; Zhang, X. B.; Lin, K. W.; Wang, K.; Fu, E. Printability and Electrical Conductivity of Silver Nanoparticle-Based Conductive Inks for Inkjet Printing. Journal of Materials Science: Materials in Electronics 2021, 32 (1), 496–508. https://doi.org/10.1007/s10854-020-04828-z.

(310) Moujoud, A.; Oh, S. H.; Shin, H. S.; Kim, H. J. On the Mechanism of Conductivity Enhancement and Work Function Control in PEDOT:PSS Film through UV-Light Treatment. physica status solidi (a) 2010, 207 (7), 1704–1707. https://doi.org/10.1002/PSSA.200983711.

(311) Huang, H.; Su, S.; Wu, N.; Wan, H.; Wan, S.; Bi, H.; Sun, L. Graphene-Based Sensors for Human Health Monitoring. Frontiers in Chemistry. Frontiers Media S.A. 2019. https://doi.org/10.3389/fchem.2019.00399.

(312) Yao, S.; Swetha, P.; Zhu, Y. Nanomaterial-Enabled Wearable Sensors for Healthcare. Advanced Healthcare Materials. Wiley-VCH Verlag January 10, 2018. https://doi.org/10.1002/adhm.201700889.

(313) Pandhi, T.; Chandnani, A.; Subbaraman, H.; Estrada, D. A Review of Inkjet Printed Graphene and Carbon Nanotubes Based Gas Sensors. Sensors (Switzerland). MDPI AG October 1, 2020, pp 1–20. https://doi.org/10.3390/s20195642.

(314) Barandun, G.; Gonzalez-Macia, L.; Lee, H. S.; Dincer, C.; Güder, F. Challenges and Opportunities for Printed Electrical Gas Sensors. ACS Sens. 2022, 7 (10), 2804–2822. https://doi.org/10.1021/ACSSENSORS.2C01086.

(315) Kim, I.; Shahariar, H.; Ingram, W. F.; Zhou, Y.; Jur, J. S. Inkjet Process for Conductive Patterning on Textiles: Maintaining Inherent Stretchability and Breathability in Knit Structures. Adv. Funct. Mater. 2019, 29 (7). https://doi.org/10.1002/adfm.201807573.

(316) Wang, Z.; Lowe, T.; Derby, B. Fluid/Fiber Interactions and the Conductivity of Inkjet Printed Ag on Textile Substrates. ACS Appl. Mater. Interfaces 2020, 12 (40), 45516–45524. https://doi.org/10.1021/acsami.0c11535.

(317) Im, J.; Trindade, G. F.; Quach, T. T.; Sohaib, A.; Wang, F.; Austin, J.; Turyanska, L.; Roberts, C. J.; Wildman, R.; Hague, R.; Tuck, C. Functionalized Gold Nanoparticles with a Cohesion Enhancer for Robust Flexible Electrodes. ACS Appl. Nano Mater. 2022, 5 (5), 6708–6716. https://doi.org/10.1021/acsanm.2c00742.

(318) Fogel'son, R. L.; Likhachev, R. H. Temperature Dependence of Viscosity. Technical Physics 2001, 46 (8), 128–131.

(319) Berry, J. D.; Neeson, M. J.; Dagastine, R. R.; Chan, D. Y. C.; Tabor, R. F. Measurement of Surface and Interfacial Tension Using Pendant Drop Tensiometry. J. Colloid Interface Sci. 2015, 454, 226–237. https://doi.org/10.1016/J.JCIS.2015.05.012.

(320) Schneider, C. A.; Rasband, W. S.; Eliceiri, K. W. NIH Image to ImageJ: 25 Years of Image Analysis. Nat. Methods 2012, 9 (7), 671–675. https://doi.org/10.1038/NMETH.2089;SUBJMETA=1647,245,631,794;KWRD=IMAGING,SOFTWARE.

(321) Brugnara, M. Contact Angle Plugin (for ImageJ Software). 2006. https://imagej.net/ij/plugins/contact-angle.html.

(322) Lamour, G.; Hamraoui, A.; Buvailo, A.; Xing, Y.; Keuleyan, S.; Prakash, V.; Eftekhari-Bafrooei, A.; Borguet, E. Contact Angle Measurements Using a Simplified Experimental Setup. J. Chem. Educ. 2010, 87 (12), 1403–1407. https://doi.org/10.1021/ED100468U/SUPPL_FILE/ED100468U_SI_002.DOC.

(323) Chakrabarti, A.; Gunjikar, V. G.; Choudhary, V. R. Thermal Analysis of Ethyl Cellulose: Influence of Atmosphere and Addition of Diethyl Phthalate as Plasticizer. Thermochim. Acta 1989, 145 (C), 173–178. https://doi.org/10.1016/0040-6031(89)85136-6.

(324) Mohammed, A.; Abdullah, A. Scanning Electron Microscopy (SEM): A Review. In 2018 International Conference on Hydraulics and Pneumatics - HERVEX; Băile Govora, 2018; pp 1–9.

(325) Franken, L. E.; Grünewald, K.; Boekema, E. J.; Stuart, M. C. A. A Technical Introduction to Transmission Electron Microscopy for Soft‐Matter: Imaging, Possibilities, Choices, and Technical Developments. Small 2020, 16 (14). https://doi.org/10.1002/smll.201906198.

(326) Jayasooriya, U. A.; Jenkins, R. D. Introduction to Raman Spectroscopy. In An Introduction to Laser Spectroscopy; Springer US: Boston, MA, 2002; pp 77–104. https://doi.org/10.1007/978-1-4615-0727-7_3.

(327) Lin, L.; Bi, X.; Gu, Y.; Wang, F.; Ye, J. Surface-Enhanced Raman Scattering Nanotags for Bioimaging. J. Appl. Phys. 2021, 129 (19), 191101. https://doi.org/10.1063/5.0047578/848955.

(328) Nixdorf, S. L. UV-VIS Spectroscopy : UV-VIS Spectroscopy and Its Application, by H.-H. Perkampus (Translators: H. Charlotte Grinter and T.L. Threlfall) Springer, Berlin, 1992, DM 168 (244 Pp.), ISBN: 0-387-5542 1 - 1. TrAC Trends in Analytical Chemistry 1992, 12 (7), x. https://doi.org/10.1016/0165-9936(93)87010-U.

(329) More, S. S.; Kadam, S. P.; Redasani, V. K. A Comprehensive Review of UV-Visible Spectroscopy. International Journal of Pharmaceutical Research and Applications 10, 114. https://doi.org/10.35629/4494-1003114134.

(330) Mansour, E.; Vishinkin, R.; Rihet, S.; Saliba, W.; Fish, F.; Sarfati, P.; Haick, H. Measurement of Temperature and Relative Humidity in Exhaled Breath. Sens. Actuators B Chem. 2020, 304. https://doi.org/10.1016/j.snb.2019.127371.

(331) Anghel, M.-A.; Fănel Iacobescu, P. The Influence of Temperature and CO2 in Exhaled Breath. In 16th Internation congress of Metrology; 2013. https://doi.org/10.1051/C.

(332) Wu, Z.-S.; Liu, Z.; Parvez, K.; Feng, X.; Müllen, K.; Wu, Z.; Liu, Z.; Parvez, K.; Müllen, K.; Feng, X. L. Ultrathin Printable Graphene Supercapacitors with AC Line-Filtering Performance. Advanced Materials 2015, 27 (24), 3669–3675. https://doi.org/10.1002/ADMA.201501208.

(333) Makaluza, S.; Midzi, N.; Olorundare, F. O. G.; Zwane, B. N.; Nkosi, D.; Arotiba, O. A. An Electrochemical Sensor for Dopamine on a Graphene-Poly(3,4-Ethylenedioxythiophene):Polystyrene Sulphonate Hybrid Ink Nanoplatform. Discover Applied Sciences 2025, 7 (4). https://doi.org/10.1007/S42452-025-06694-Y.

(334) Functional Molecular Cages Through Subcomponent Self–Assembly. Bull. Jpn. Soc. Coord. Chem. 2017, 69 (0), 29–34. https://doi.org/10.4019/bjscc.69.29.

(335) Parvez, K.; Worsley, R.; Alieva, A.; Felten, A.; Casiraghi, C. Water-Based and Inkjet Printable Inks Made by Electrochemically Exfoliated Graphene. Carbon N. Y. 2019, 149, 213–221. https://doi.org/10.1016/J.CARBON.2019.04.047.

(336) Gao, Y.; Shi, W.; Wang, W.; Leng, Y.; Zhao, Y. Inkjet Printing Patterns of Highly Conductive Pristine Graphene on Flexible Substrates. Ind. Eng. Chem. Res. 2014, 53 (43), 16777–16784. https://doi.org/10.1021/ie502675z.

(337) Carey, T.; Alhourani, A.; Tian, R.; Seyedin, S.; Arbab, A.; Maughan, J.; Šiller, L.; Horvath, D.; Kelly, A.; Kaur, H.; Caffrey, E.; Kim, J. M.; Hagland, H. R.; Coleman, J. N. Cyclic Production of Biocompatible Few-Layer Graphene Ink with in-Line Shear-Mixing for Inkjet-Printed Electrodes and Li-Ion Energy Storage. NPJ 2D Mater. Appl. 2022, 6 (1), 1–11. https://doi.org/10.1038/S41699-021-00279-0;SUBJMETA=1005,1007,1055,298,301,638,639,918;KWRD=ELECTRONIC+DEVICES,SYNTHESIS+OF+GRAPHENE.

(338) Dulal, M.; Modha, H. R. M.; Liu, J.; Islam, M. R.; Carr, C.; Hasan, T.; Thorn, R. M. S.; Afroj, S.; Karim, N. Sustainable, Wearable, and Eco-Friendly Electronic Textiles. Energy and Environmental Materials 2024. https://doi.org/10.1002/eem2.12854.

(339) Zólyomi, V.; Koltai, J.; Kürti, J. Resonance Raman Spectroscopy of Graphite and Graphene. physica status solidi (b) 2011, 248 (11), 2435–2444. https://doi.org/10.1002/pssb.201100295.

(340) Wu, J.-B.; Lin, M.-L.; Cong, X.; Liu, H.-N.; Tan, P.-H. Raman Spectroscopy of Graphene-Based Materials and Its Applications in Related Devices. Chem. Soc. Rev. 2018, 47 (5), 1822–1873. https://doi.org/10.1039/C6CS00915H.

(341) Ferrari, A. C.; Robertson, J. Interpretation of Raman Spectra of Disordered and Amorphous Carbon. Phys. Rev. B 2000, 61 (20), 14095–14107. https://doi.org/10.1103/PhysRevB.61.14095.

(342) Ferrari, A. C.; Meyer, J. C.; Scardaci, V.; Casiraghi, C.; Lazzeri, M.; Mauri, F.; Piscanec, S.; Jiang, D.; Novoselov, K. S.; Roth, S.; Geim, A. K. Raman Spectrum of Graphene and Graphene Layers. Phys. Rev. Lett. 2006, 97 (18), 187401. https://doi.org/10.1103/PhysRevLett.97.187401.

(343) Malard, L. M.; Pimenta, M. A.; Dresselhaus, G.; Dresselhaus, M. S. Raman Spectroscopy in Graphene. Phys. Rep. 2009, 473 (5–6), 51–87. https://doi.org/10.1016/j.physrep.2009.02.003.

(344) Park, S.-H.; Kim, H.-S. Environmentally Benign and Facile Reduction of Graphene Oxide by Flash Light Irradiation. Nanotechnology 2015, 26 (20), 205601. https://doi.org/10.1088/0957-4484/26/20/205601.

(345) Gengler, R. Y. N.; Badali, D. S.; Zhang, D.; Dimos, K.; Spyrou, K.; Gournis, D.; Miller, R. J. D. Revealing the Ultrafast Process behind the Photoreduction of Graphene Oxide. Nat. Commun. 2013, 4 (1), 2560. https://doi.org/10.1038/ncomms3560.

(346) Tan, H. W.; An, J.; Chua, C. K.; Tran, T. Metallic Nanoparticle Inks for 3D Printing of Electronics. Adv. Electron. Mater. 2019, 5 (5). https://doi.org/10.1002/aelm.201800831.

(347) Yoon, H. K.; Lee, S. C.; Park, O. O. Thermal Properties of Poly(Ethylene 2,6-Naphthalate) and Poly(Butylene 2,6-Naphthalate) Blends . Polym. J. 1994, 26 (7), 816–821.

(348) Im, J.; Heaton, C.; Putri, N. R. E.; Liu, C.; Usuba, J.; Butler, K.; Fay, M.; Han, G. G. D.; Hooshmand, H.; Thompson, A.; Wildman, R.; Hague, R.; Turyanska, L.; Tuck, C. On-Demand Sintering of Gold Nanoparticles via Controlled Removal of o-Nitrobenzyl Thiol Ligands Under Record-Low Power for Conductive Patterns. Advanced Science 2025, 12 (12), 2415496. https://doi.org/10.1002/ADVS.202415496.

(349) Perelaer, J.; Abbel, R.; Wünscher, S.; Jani, R.; Van Lammeren, T.; Schubert, U. S. Roll-to-Roll Compatible Sintering of Inkjet Printed Features by Photonic and Microwave Exposure: From Non-Conductive Ink to 40% Bulk Silver Conductivity in Less than 15 Seconds. Advanced Materials 2012, 24 (19), 2620–2625. https://doi.org/10.1002/ADMA.201104417.

(350) Lee, J. W.; Kwak, J. H.; Kim, J.; Jeong, S.; Park, J. H.; Jeong, S. Y.; Seo, S. H.; Han, J. T.; Lee, G. W.; Baeg, K. J.; Yang, I. H. S.; Jeong, H. J. Minimizing

Temperature Gradient in Photonic Sintering for Defect-Free High-Conductivity Cu-Based Printed Patterns by Bidirectional Irradiation. Adv. Mater. Interfaces 2021, 8 (16). https://doi.org/10.1002/ADMI.202100769.

(351) Le Druillennec, M.; Mandrillon, V.; Estevez, R.; Parry, G.; Audoit, G.; Poulain, C. Mechanics of Cracking Failure in a Silver Layer Deposited by Inkjet Printing on a Flexible Substrate. 2016 6th Electronic System-Integration Technology Conference, ESTC 2016 2016. https://doi.org/10.1109/ESTC.2016.7764476.

(352) Glushko, O.; Cordill, M. J.; Klug, A.; List-Kratochvil, E. J. W. The Effect of Bending Loading Conditions on the Reliability of Inkjet Printed and Evaporated Silver Metallization on Polymer Substrates. Microelectronics Reliability 2016, 56, 109–113. https://doi.org/10.1016/J.MICROREL.2015.10.007.

(353) Panasonic Industry. BEYOLEXTM Thermosetting Stretchable Film. https://industry.panasonic.eu/products/devices/electronic-materials/beyolextm-thermosetting-stretchable-film.

(354) Kulkarni, S. S.; Din, I. U.; Samad, Y. A.; Khan, K. A. Thermo-Viscoelastic Characterization and Modeling of a High-Temperature Stretchable Film for Foldable Electronics Applications. Int. J. Eng. Sci. 2025, 216, 104352. https://doi.org/10.1016/J.IJENGSCI.2025.104352.

(355) Lee, Y.; Cho, H.; Yoon, H.; Kang, H.; Yoo, H.; Zhou, H.; Jeong, S.; Lee, G. H.; Kim, G.; Go, G. T.; Seo, J.; Lee, T. W.; Hong, Y.; Yun, Y. Advancements in Electronic Materials and Devices for Stretchable Displays. Adv. Mater. Technol. 2023, 8 (20), 2201067. https://doi.org/10.1002/ADMT.202201067;REQUESTEDJOURNAL:JOURNAL:2365709X;WGROUP:STRING:PUBLICATION.

(356) Ma, Q.; Zhang, Y. Mechanics of Fractal-Inspired Horseshoe Microstructures for Applications in Stretchable Electronics. Journal of Applied Mechanics, Transactions ASME 2016, 83 (11). https://doi.org/10.1115/1.4034458/421948.

(357) Gonzalez, M.; Axisa, F.; Bulcke, M. Vanden; Brosteaux, D.; Vandevelde, B.; Vanfleteren, J. Design of Metal Interconnects for Stretchable Electronic Circuits. Microelectronics Reliability 2008, 48 (6), 825–832. https://doi.org/10.1016/J.MICROREL.2008.03.025.

(358) Oldroyd, P.; Oldroyd, S.; Meng, M.; Makwana, R.; Sanger, G.; Bulmer, D.; Malliaras, G. G.; Owens, R. M. Stretchable Device for Simultaneous Measurements of Contractility and Electrophysiology of Neuromuscular Tissue in the Gastrointestinal Tract. Advanced Materials 2024, 36 (19). https://doi.org/10.1002/ADMA.202312735,.

(359) Śliwiak, M.; Bui, R.; Brook, M. A.; Selvaganapathy, P. R. 3D Printing of Highly Reactive Silicones Using Inkjet Type Droplet Ejection and Free Space Droplet

Merging and Reaction. Addit. Manuf. 2021, 46, 102099. https://doi.org/10.1016/J.ADDMA.2021.102099.

(360) Hauer, L.; Naga, A.; Badr, R. G. M.; Pham, J. T.; Wong, W. S. Y.; Vollmer, D. Wetting on Silicone Surfaces. Soft Matter 2024, 20 (27), 5273–5295. https://doi.org/10.1039/D4SM00346B.

(361) Afroj, S.; Islam, M. H.; Karim, N. Multifunctional Graphene-Based Wearable E-Textiles; MDPI AG, 2021; p 11. https://doi.org/10.3390/proceedings2021068011.

(362) Dulal, M.; Afroj, S.; Ahn, J.; Cho, Y.; Carr, C.; Kim, I. D.; Karim, N. Toward Sustainable Wearable Electronic Textiles. ACS Nano. American Chemical Society 2022. https://doi.org/10.1021/acsnano.2c07723.

(363) Piatti, E.; Arbab, A.; Galanti, F.; Carey, T.; Anzi, L.; Spurling, D.; Roy, A.; Zhussupbekova, A.; Patel, K. A.; Kim, J. M.; Daghero, D.; Sordan, R.; Nicolosi, V.; Gonnelli, R. S.; Torrisi, F. Charge Transport Mechanisms in Inkjet-Printed Thin-Film Transistors Based on Two-Dimensional Materials. Nat. Electron. 2021, 4 (12), 893–905. https://doi.org/10.1038/s41928-021-00684-9.

(364) Calabrese, G.; Pimpolari, L.; Conti, S.; Mavier, F.; Majee, S.; Worsley, R.; Wang, Z.; Pieri, F.; Basso, G.; Pennelli, G.; Parvez, K.; Brooks, D.; Macucci, M.; Iannaccone, G.; Novoselov, K. S.; Casiraghi, C.; Fiori, G. Inkjet-Printed Graphene Hall Mobility Measurements and Low-Frequency Noise Characterization. Nanoscale 2020, 12 (12), 6708–6716. https://doi.org/10.1039/C9NR09289G.

(365) Carey, T.; Cacovich, S.; Divitini, G.; Ren, J.; Mansouri, A.; Kim, J. M.; Wang, C.; Ducati, C.; Sordan, R.; Torrisi, F. Fully Inkjet-Printed Two-Dimensional Material Field-Effect Heterojunctions for Wearable and Textile Electronics. Nat. Commun. 2017, 8 (1), 1202. https://doi.org/10.1038/s41467-017-01210-2.

(366) Gosling, J. H.; Morozov, S. V.; Vdovin, E. E.; Greenaway, M. T.; Khanin, Y. N.; Kudrynskyi, Z.; Patanè, A.; Eaves, L.; Turyanska, L.; Fromhold, T. M.; Makarovsky, O. Graphene FETs with High and Low Mobilities Have Universal Temperature-Dependent Properties. Nanotechnology 2023, 34 (12). https://doi.org/10.1088/1361-6528/aca981.

(367) Zhou, H.; Ramaraj, S. G.; Ma, K.; Sarker, M. S.; Liao, Z.; Tang, S.; Yamahara, H.; Tabata, H. Real-Time Detection of Acetone Gas Molecules at Ppt Levels in an Air Atmosphere Using a Partially Suspended Graphene Surface Acoustic Wave Skin Gas Sensor. Nanoscale Adv. 2023, 5 (24), 6999–7008. https://doi.org/10.1039/D3NA00914A.

(368) Deng, C.; Zhang, J.; Yu, X.; Zhang, W.; Zhang, X. Determination of Acetone in Human Breath by Gas Chromatography–Mass Spectrometry and Solid-Phase Microextraction with on-Fiber Derivatization. Journal of Chromatography B 2004, 810 (2), 269–275. https://doi.org/10.1016/j.jchromb.2004.08.013.

(369) Lin, J.; Cheng, J.; Wang, Y.; Shen, X. The Pseudomonas Quinolone Signal (PQS): Not Just for Quorum Sensing Anymore. Front. Cell. Infect. Microbiol. 2018, 8. https://doi.org/10.3389/fcimb.2018.00230.

(370) Zsila, F.; Ricci, M.; Szigyártó, I. C.; Singh, P.; Beke-Somfai, T. Quorum Sensing Pseudomonas Quinolone Signal Forms Chiral Supramolecular Assemblies With the Host Defense Peptide LL-37. Front. Mol. Biosci. 2021, 8, 742023. https://doi.org/10.3389/FMOLB.2021.742023/FULL.

(371) Pezzoni, M.; Meichtry, M.; Pizarro, R. A.; Costa, C. S. Role of the Pseudomonas Quinolone Signal (PQS) in Sensitising Pseudomonas Aeruginosa to UVA Radiation. J. Photochem. Photobiol. B 2015, 142, 129–140. https://doi.org/10.1016/J.JPHOTOBIOL.2014.11.014.

(372) Habboush, S.; Rojas, S.; Rodríguez, N.; Rivadeneyra, A. The Role of Interdigitated Electrodes in Printed and Flexible Electronics. Sensors 2024, Vol. 24, Page 2717 2024, 24 (9), 2717. https://doi.org/10.3390/S24092717.

(373) Yang, W. S.; Han, S.; Lim, G. R.; Kim, H. Y.; Hong, S. H. Effects and Mechanism of Surface Water Wettability and Operating Frequency on Response Linearity of Flexible IDE Capacitive Humidity Sensor. Sensors 2021, Vol. 21, Page 6633 2021, 21 (19), 6633. https://doi.org/10.3390/S21196633.

(374) Bernal, A.; Zafra, M. A.; Simón, M. J.; Mahía, J. Sodium Homeostasis, a Balance Necessary for Life. Nutrients 2023, 15 (2), 395. https://doi.org/10.3390/NU15020395.

(375) Zoroddu, M. A.; Aaseth, J.; Crisponi, G.; Medici, S.; Peana, M.; Nurchi, V. M. The Essential Metals for Humans: A Brief Overview. J. Inorg. Biochem. 2019, 195, 120–129. https://doi.org/10.1016/J.JINORGBIO.2019.03.013.

(376) Baker, L. B. Physiology of Sweat Gland Function: The Roles of Sweating and Sweat Composition in Human Health. Temperature: Multidisciplinary Biomedical Journal 2019, 6 (3), 211. https://doi.org/10.1080/23328940.2019.1632145.

(377) Cai, H.; Tepermeister, M.; Yuan, C.; Silberstein, M. N. Regulating Hydrogel Mechanical Properties with an Electric Field. Mater. Horiz. 2025, 12 (14), 5388–5399. https://doi.org/10.1039/D5MH00308C.